1-1-2012

Optical investigation of ethanol and n-heptane dual-fuel partially premixed combution in s reciprocating engine

Radu Catalin Florea
Wayne State University,

OPTICAL INVESTIGATION OF ETHANOL AND N-HEPTANE DUAL-FUEL PARTIALLY PREMIXED COMBUSTION IN A RECIPROCATING ENGINE

by

RADU-CATALIN FLOREA

DISSERTATION

Submitted to the Graduate School

of Wayne State University,

Detroit, Michigan

in partial fulfillment of the requirements

for the degree of

DOCTOR OF PHILOSOPHY

2012

MAJOR: MECHANICAL ENGINEERING

Approved by,

_____

Advisor Date

_____

_____

_____

_____

_____

DEDICATION

To my son, David A.

ACKNOWLEDGMENTS

My deepest gratitude is extended to Dr. Dinu Taraza for his mentorship throughout this journey. He has provided me with guidance and encouragement when I needed them, as well as lots of great ideas on how to solve the day-to-day research puzzles. His dedication, enthusiasm and kindness helped my growth as a researcher and for this I'll be eternally thankful.

It has been a pleasure spending countless hours with Dr. Marcis Jansons working on various optical diagnostics-related topics and I'm thankful for all those conversations we had that helped me move forward in my graduate school odyssey.

Thank you to Dr. Naeim Henein for sharing his wealth of knowledge related to internal combustion engines. His attention for detail as well as pursuit of fundamental understanding of complex phenomena is inspirational. I consider myself very fortunate to have had the opportunity to have worked in his team.

I wish to thank also Dr. Gregory Auner and Dr. Trilochan Singh for their advice and support as a member of my doctoral committee. I'm indebted to the Mechanical Engineering department chair Dr. Walter Bryzik as well as the entire faculty body for providing a friendly but challenging academic environment filled with opportunities to learn.

I am grateful for the support of my colleagues in the Low Temperature Research Laboratory: Kan "Linda" Zha, Xin Yu, Eric Gingrich, Alex Davidson and Jinqiao "Edward" Wang. Without their support much of my experimental work

would not have been possible. I'd like to especially thank Linda for sharing with me her world-views and culture.

I'm thankful for the help and support of the members of Wayne State's Center for Automotive Research in achieving various research goals. I'd like also to express my sincerest appreciation to the technical support staff (Lidia Nedeltcheva, Eugene Snowden, David Griffiths and Marvin Santure) for manufacturing or maintaining all the equipment that I needed throughout my work and clerical staff (Rosalind Willis and Taquandra Grant) for making sure that everything ran smoothly in our department.

Last but not least I'd like to thank my family; my wife Elena and my son David for their unconditional support and affection as well as my parents whom, while far away, encouraged me every step of the way.

I gratefully acknowledge the financial support of US Army TARDEC, Warren, MI

PREFACE

At the time of the writing of this manuscript, a significant amount of interest exists towards the investigation of dual-fuel combustion modes. Dual-fuel combustion is designed to address existing issues in homogenous charge compression ignition (HCCI) – such as combustion phasing control difficulties as well as limited operating range – while maintaining low engine-out emissions and improve upon engine fuel conversion efficiency. While most of the work currently available within the public domain focuses with good reason on *what* dual-fuel combustion is capable of achieving in terms of improved thermal efficiency, the author believes that an equally important question that needs to be answered is *how* does dual-fuel combustion work?

This work seeks to provide answers for the latter question through the application of a suite of combustion diagnostics techniques.

TABLE OF CONTENTS

Dedication ii

Acknowledgments iii

Preface v

List of Tables xi

List of Figures xii

Nomenclature xviii

Chapter 1. "Introduction" 1

1.1 Biomass-Derived Alternative Fuels 3

1.2 Electrification of the Transportation System 5

1.3 Other Transportation Energy Sources and Recovery Methods 6

1.4 Conclusions 6

Chapter 2. "Review of Literature" 8

2.1 Combustion Modes for Internal Combustion Engines 9

2.1.1 Spark Ignition Combustion (Otto) 11

2.1.2 Compression Ignition Combustion (Diesel) 12

2.1.3 Low Temperature Combustion 13

2.2 Autoignition in Internal Combustion Engines 14

2.2.1 Low Temperature Oxidation of Alkanes 15

2.2.2 High and Intermediate Temperature Oxidation 18

2.2.3 Effect of Autoignition Inhibitors 19

2.2.4 Effect of Autoignition Enhancers 36

2.3 Ethanol-Diesel Dual Fuel Operation 46
2.3.1 Ethanol – Diesel fuel blending 47
2.3.2 Ethanol Intake Fumigation and Port Fuel Injection 51
2.3.3 Neat Ethanol Operation 54
2.3.4 Dual Fuel Compression Ignition 55
2.4 Conclusions 57
Chapter 3. "Experimental Facility" 60
3.1 Engine Systems 61
3.1.1 Optically Accessible Engine 61
3.1.2 Cold Chamber and Camera Support 65
3.1.3 Dynamometer 68
3.1.4 Crank-Angle Encoder 69
3.1.5 Fuel Delivery System 69
3.1.6 Engine Electronic Control 70
3.1.7 Engine Balancing 71
3.1.8 Engine Cooling and Lubrication 71
3.1.9 Swirl Control 72
3.2 Test-Cell Instrumentation 73
3.2.1 High-Speed Data Acquisition System (Indimeter) 73
3.2.2 Low-Speed Data Acquisition System (IFEM) 73
3.2.3 Pressure Transducer 74
3.2.4 Rail Pressure Measurement 74

3.2.5 Needle Lift Measurement 75
3.2.6 Exhaust Gas Analysis (FTIR) 75
3.3 Optical Investigation Equipment 76
3.3.1 High-Speed Camera 76
3.3.2 Intensified Monochromatic Cameras 78
3.3.3 Diffraction Spectroscopy 81
3.3.4 Nd:YAG Pulsed Laser 83
Chapter 4. "Numerical Modeling of Combustion" 87
4.1 Zero-Dimensional Modeling (CHEMKIN) 87
4.2 N-Heptane Oxidation Mechanism Reduction 97
4.3 3D CFD Chemical Kinetic Code KIVA4-WSU 99
4.3.1 The C/O Equivalence Ratio 103
4.3.2 Local Ethanol Energy Fraction 104
4.3.3 Measure of Reactivity Stratification 105
Chapter 5. "Experimental Methods and Results" 107
5.1 Effect of Ethanol on Partially Premixed N-heptane Combustion 107
5.1.1 Introduction 107
5.1.2 Ethanol Intake Mole Fraction Measurement 108
5.1.3 Effect of Ethanol on the In-Cylinder Pressure Measurement 109
5.1.4 High-Speed Spray Imaging 113
5.1.5 High-Speed Visible Range Combustion Imaging 121

5.1.6 UV filtered Images at 307nm (OH transition) 128
5.1.7 Combustion Chemiluminescence Spectral Measurements 130
5.1.8 Planar Laser Induced Fluorescence (PLIF) of Formaldehyde 134
5.2 Effect of ethanol on Partially Premixed ULSD combustion 158
5.2.1 Effect of Ethanol on the In-Cylinder Pressure Measurement 159
5.2.2 Visible High-Speed Imaging of Combustion 162
5.2.3 Planar Laser Induced Fluorescence of Formaldehyde 166
Chapter 6. "Simulation Results" 174
6.1 Model Validation 174
6.2 Modeling Results Discussion 179
6.2.1 Mixture Formation 179
6.2.2 Combustion Evolution 180
6.2.3 Reactivity Stratification 187
Chapter 7. "Summary and Recommendations" 194
7.1 Summary 194
7.2 Recommendations for Future Work 196
Appendix 1 MATLAB routine for reading Phantom CINE file header and frame information 200
Appendix 2 KIVA4-WSU FORTRAN subroutine for TECPLOT 360 CFD output 202

Appendix 3 KIVA4-WSU FORTRAN modified subroutine "chem" replacing previous KIVA4 chemistry handling with a CANTERA interface (master node) 208

Appendix 4 KIVA4-WSU FORTRAN program operating on the "slave" nodes handling chemical kinetics through CANTERA 214

Appendix 5 CANTERA C++ subroutine for chemical kinetic solver 217

Appendix 6 Semi-detailed n-heptane ethanol oxidation mechanism..... 218

References 265

Abstract 281

Autobiographical Statement..... 283

LIST OF TABLES

Table 1. Effect of additives 45

Table 2. Experimental Engine Characteristics 61

Table 3. Optical properties of fused silica and sapphire [84] 63

Table 4. Maximum cool-flame energy release for the top 10 reactions 93

Table 5. Operating Points 107

Table 6. Experimental engine specifications 138

Table 7. Operating points 139

Table 8. ULSD fuel properties 159

Table 9. Operating points 160

LIST OF FIGURES

Fig. 1.1. Cost of oil vs. other indicators. 2

Fig. 1.2. Crude price and consumption. 2

Fig. 2.1. Different modes of combustion 10

Fig. 2.2. Combustion in Spark-Ignition engines 11

Fig. 2.3. Simplified low temperature oxidation mechanism for alkanes 16

Fig. 2.4. Pressure and temperature dependence of the HC oxidation regimes 18

Fig. 2.5. Effect of CO_2 on HCCI combustion 21

Fig. 2.6. Effect of reformer gas on HCCI combustion 23

Fig. 2.7. Rate constants for the possible $H+O_2$ reactions 23

Fig. 2.8. Effect of CO_2 on DME HCCI combustion 24

Fig. 2.9. Enhancing chemical effect of H_2O present in EGR 25

Fig. 2.10. Effect of HCCI combustion additives on LTC and HTC 27

Fig. 2.11. Effect of ethanol on n-heptane HTHR 28

Fig. 2.12. Effect of ethanol on cool-flame chemiluminescence (left) and OH hot ignition chemiluminescence (right) 28

Fig. 2.13. Effect of methanol on DME combustion 29

Fig. 2.14. Effect of formaldehyde addition on pressure 31

Fig. 2.15. PIC correlation with CA50 32

Fig. 2.16. Effect of formaldehyde, wall temperature and equivalence ratio on LPPC 33

Fig. 2.17. Effect of formaldehyde on the distribution of local temperature and equivalence ratio 34

Fig. 2.18. The effect of iron Pentacarbonyl on burning velocity 35

Fig. 2.19. Effect of activation additives on PRF90 ignition delay 37

Fig. 2.20. Molecular structure of iso-octane HCCI additives 38

Fig. 2.21. Effect of diethyl-ether/ethanol mixtures on combustion (RCM) 39

Fig. 2.22 Effect of ozone on DME combustion 40

Fig. 2.23. Effect of ozone on flame lift-off for different fuel jet velocities 42

Fig. 2.24. Flame liftoff 43

Fig. 2.25. Comparison of rate ARHR curves for 3 bar IMEP 48

Fig. 2.26. Cylinder pressure comparison 49

Fig. 2.27. Effect of ethanol fraction on combustion 52

Fig. 2.28. Effect of ethanol on HCCI combustion of PRF25 53

Fig. 2.29. Effect of ethanol addition 53

Fig. 2.30. Cylinder pressure data for maximum load 54

Fig. 2.31. Cylinder pressure data for light load 55

Fig. 2.32. Effect of different dual-fuel strategies 56

Fig. 3.1. Experimental Setup (concept diagram) 60

Fig. 3.2. AVL SCRE5402 Optically accessible engine cross-section 62

Fig. 3.3. Spectral transmissivity for fused silica and sapphire 63

Fig. 3.4. Adapter plate design for PLIF experiments. 65

Fig. 3.5. Optically accessible engine enclosed in the environmental chamber 66

Fig. 3.6. Camera support 67

Fig. 3.7. Engine dynamometer assembly 68

Fig. 3.8 Bosch ECU and ETAS VTK7.1 and AVL solenoid driver *70*

Fig. 3.9. Swirl valve calibration *72*

Fig. 3.10. Vision Research Phantom 7.3 High-Speed CMOS camera *77*

Fig. 3.11. Phantom V7.3 optical response as reported by Zha et al. [88, 89] *78*

Fig. 3.12. PIMAX II 512x512 ICCD camera [90] *79*

Fig. 3.13. PIMAX 3, intensifier concept [92] and quantum efficiency curves [93] *80*

Fig. 3.14. Difraction spectrometer *82*

Fig. 3.15. Beam energy adjustment optical setup *84*

Fig. 3.16. Laser equipment layout (upper) and actual experimental setup (lower) *86*

Fig. 4.1. Ignition delay data comparison for n-heptane/etOH merged mechanism with source mechanism *88*

Fig. 4.2. Formaldehyde evolution (blue) and energy release rate (red, dashed) for the baseline condition (without ethanol addition) *89*

Fig. 4.3. Effect of ethanol on formaldehyde profiles *90*

Fig. 4.4. Effect of ethanol fraction on n-heptane consumption and formaldehyde formation *92*

Fig. 4.5. Effect of ethanol fraction on energy release-formaldehyde mole fraction correlation *93*

Fig. 4.6. Effect of ethanol on hydroxyl radical during the cool-flame stage *94*

Fig. 4.7. Effect of initial temperature on energy release-formaldehyde mole fraction correlation *95*

Fig. 4.8. Effect of equivalence ratio on energy release-formaldehyde mole fraction correlation 96

Fig. 4.9. Comparison of ignition delay data for detailed and semi-detailed mechanism. Φ=0.7, T_{ini}=800K, p_{ini}=30bar 99

Fig. 4.10. KIVA4-WSU parallel operation diagram 100

Fig. 4.11 Computational mesh 102

Fig. 4.12 Computing cluster 103

Fig. 4.13 The Lorenz curve 105

Fig. 5.1. FTIR ethanol spectrum for 2 and 3 msec injector activation time 108

Fig. 5.2. Effect of ethanol addition on n-heptane partially premixed combustion 110

Fig. 5.3. Detail of the Low Temperature Heat Release 110

Fig. 5.4. Effect of intake temperature on ethanol/n-heptane dual fuel combustion 113

Fig. 5.5. Needle lift profile; the crank angle data is reported with respect to the start of injection. 114

Fig. 5.6. Imaging of injection events for the two conditions studied 116

Fig. 5.7. Secondary injections due to needle rebound 117

Fig. 5.8. Sequence of spray locations throughout the injection event 118

Fig. 5.9. a) Back illuminated spray image b) composite image showing liquid and vapor phase 119

Fig. 5.10 Single-cycle high-speed visible range images a) without ethanol b) with ethanol 122

Fig. 5.11a) smokeless JP-8 combustion b) JP-8 combustion with formaldehyde intake addition *124*

Fig. 5.12. Combustion time sequence a) without ethanol scale 1.5..9°aTDC b) without ethanol scale 3.5..7°aTDC c) with ethanol scale 1.5..9°aTDC *125*

Fig. 5.13. Blue Flame Integral signal evolution (dashed line) *127*

Fig. 5.14. Combustion imaging a) w/o etOH, Vis b) w/o etOH, 307 nm c) w/ etOH, Vis d) w/ etOH, 307 nm *129*

Fig. 5.15. Chemiluminescence spectrum time evolution *131*

Fig. 5.16. HTHR Chemiluminescence spectra without ethanol addition *132*

Fig. 5.17. Effect of ethanol on chemiluminescence spectra *133*

Fig. 5.18. ULSD distillation curve *159*

Fig. 5.19. Effect of ethanol on in-cylinder pressure, apparent rate of heat release (ARHR) and cumulative heat release (AHR) *161*

Fig. 5.20. Comparison of in-cylinder pressure and corresponding ARHR between ULSD and n-heptane partially premixed combustion (no ethanol addition). *162*

Fig. 5.21. Single-cycle high-speed visible range images ethanol/ULSD combustion a) without ethanol b) with ethanol *165*

Fig. 5.22. Window deposits transmissivity *167*

Fig. 5.23. Low pressure, low temperature formaldehyde spectrum (not corrected for optics efficiency) *169*

Fig. 5.24. Uncorrected formaldehyde spectrum during cool-flame *170*

Fig. 5.25. a) PLIF images during the LTHR, NTC and HTHR b) ARHR data with a focus on low temperature energy release *172*

Fig. 6.1 Comparison between experimental and modeling pressure and energy release data *175*

Fig. 6.2 Baseline - comparison between experimental formaldehyde LIF data and modeled formaldehyde mass fraction *176*

Fig. 6.3 Ethanol/Heptane - comparison between experimental formaldehyde LIF data and modeled formaldehyde mass fraction *177*

Fig. 6.4 Ethanol energy fraction distribution for ethanol-heptane operation. Left image represents cross-section through the injection plane (shown with dashed line) *179*

Fig. 6.5 Time evolution of equivalence ratio (color coded) and chemical energy release rate (contour levels) *186*

Fig. 6.6 Ignition kernel at 6°aTDC (baseline) and 5.5°aTDC (dual-fuel). Section aligned with spray and energy release isosurfaces. *186*

Fig. 6.7. Time dependence of chemical energy release histograms *188*

Fig. 6.8 Specific energy release standard deviation (above) and coefficient of variation (below) *189*

Fig. 6.9 Lorenz curves for baseline and dual-fuel combustion at several crank positions. Linear scale (upper), Logarithmic scale (lower) *191*

Fig. 6.10 Gini index for baseline and dual-fuel operation *192*

Fig. 6.11 Flame front propagation *193*

NOMENCLATURE

Abbreviations

ARHR	Apparent Rate of Heat Release
AHR	Apparent Heat Release
b/aTDC	before/after Top Dead Center
COV	Coefficient of Variation
CA50	Crank Angle for 50% heat release ATDC
CAD	Crank Angle Degree
CCD	Charge Coupled Device
CI	Compression Ignition
CMOS	Complementary Metal–Oxide–Semiconductor
DEE	Di-ethyl ether
DME	Di-methyl ether
ECU	Engine Control Unit
EGR	Exhaust Gas Recirculation
HCCI	Homogenous Charge Compression Ignition
HTHR	High Temperature Heat Release
ICCD	Intensified Charge Coupled Device
IMEP	Indicated Mean Effective Pressure
LIF	Laser Induced Fluorescence
LPPC	Location Peak Premixed Combustion
LTC	Low Temperature Combustion

LTHR	Low Temperature Heat Release
MK	Modulated Kinetics combustion mode
PAH	Poly-aromatic hydrocarbons
PEG	Poly-ethylene glycol
PIC	Pre-injection Chemiluminescence
PLIF	Planar Laser Induced Fluorescence
PPC	Partially Premixed Combustion
RCCI	Reactivity Controlled Compression Ignition
RCM	Rapid Compression Machine
SI	Spark Ignition
TDC	Top Dead Center
TTL	Transistor–Transistor Logic
UHC	Unburned Hydrocarbons
ULSD	Ultra-Low Sulphur Diesel
UV	Ultra Violet spectral range (10nm to 400nm)
UV-Vis	Ultra Violet and Visible spectral range (10 nm to 800nm)
VCO	Valve Covered Orifice injector nozzle

Symbols

D	Diffusion coefficient
E	laser energy measurement
f_{laser}	Laser correction factor for sheet non-uniformity
f/#	F-stop number (lens aperture)

G	Gini index
h	Plank's constant
h_m	enthalpy of species m
I	Specific internal energy
I	Pixel count (intensity)
L	Lorenz curve
S, **P**	polarization planes
P	Pressure
$\dot{Q}$	Energy source term
T	Temperature
$\boldsymbol{u}$	Velocity vector
δ	Dirac delta function
ε	Turbulence dissipation rate
ϕ	Equivalence ratio
λ	wavelength
$\boldsymbol{\lambda}$	Excess air coefficient
ν	Photon frequency
ρ	Density
σ	Standard deviation
τ	Optical transmissivity

Chapter 1. "Introduction"

Internal combustion engines have become over the past century part of the fabric of the modern society. Along with the availability of relatively inexpensive energy supply, it has completely changed the lifestyle of the human race up to its most basic levels. A review related to the history of the internal combustion engine has been published by Somerscales et.al. [1]. Engines provide mechanical energy to a wide range of applications, starting from miniaturized model airplane engines and going up to large marine diesel engines. However, the application where the internal combustion engine is found most often is by far transportation. Automobiles allow humans to travel large distances in relatively short periods of time and due to this, they have become a symbol of freedom and independence.

However, energy costs have observed a dramatic increase over the past decade (2000-2010) due to a complex set of factors, including - but not limited to – increasing energy demand, political instability in oil producing countries located mainly in the Middle East as well as increased cost of crude extraction. Fig. 1.1 shows the historical trends of crude cost [2] with respect to both the actual value at the time of the trade and to the normalized cost considering the Consumers Price Index [3] while Fig. 1.2 adds information regarding crude consumption for the United States as well as global consumption.

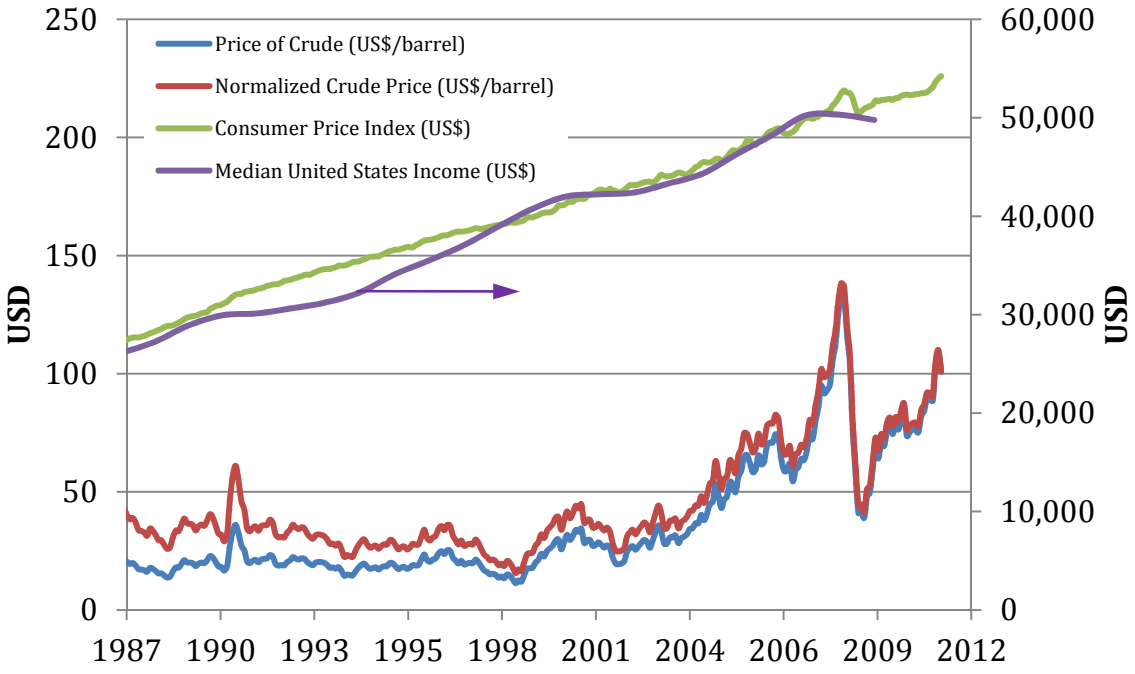

Fig. 1.1. Cost of oil vs. other indicators.
Crude price per barrel [2] normalized considering the CPI [3] and Median Income for the United States [4].

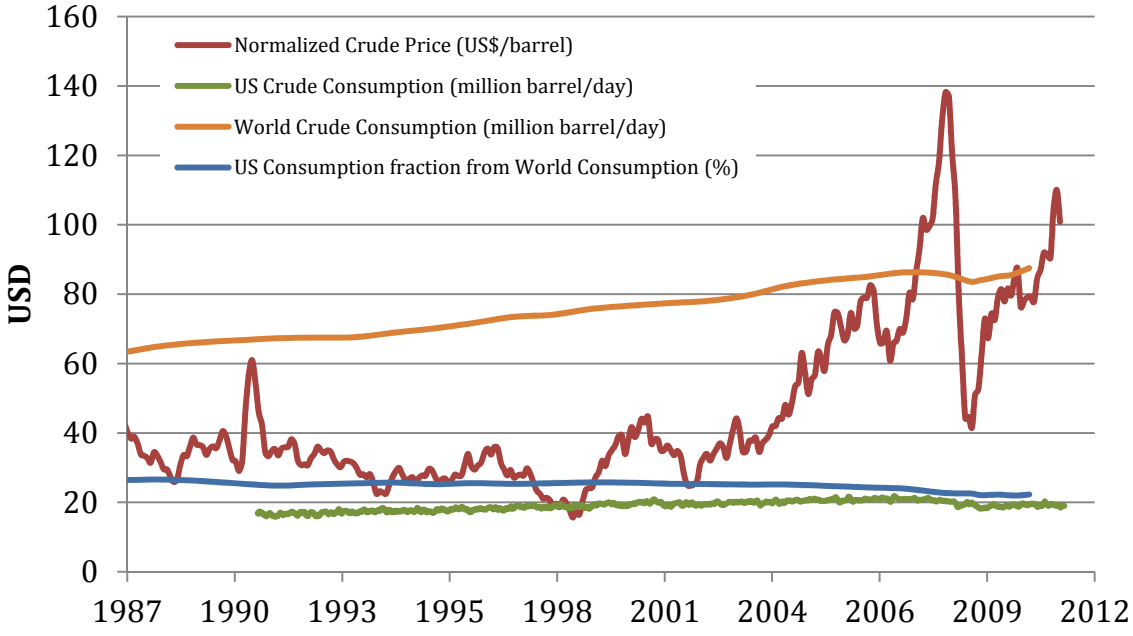

Fig. 1.2. Crude price and consumption.
Normalized crude price [2],[3] and crude petroleum consumption [2]

While during 1990's the normalized crude price did not reflect the increase in global demand, due to a cumulative effect of political, cost and market volatility factors, the normalized crude price increased sharply around 2004 only to drop dramatically as a result of the economic downturn in 2008-2009.

Thus, in order to contain rising crude price and higher fuel price observed by a consumer, it is important to improve the overall efficiency of the power plants which use the fuel. Improved efficiency has also additional benefits related to lowering CO_2 emissions which are thought to be responsible for a global increase in troposheric temperature and adverse effects on changing weather patterns. A discussion related to the available data related to global warming has been published by Keller [5, 6]. Also the Intergovernmental Panel on Climate Change (IPPC) issued its fourth Assessment Report (AR4) [7] in 2007 while AR5 is due in 2013/2014.

As a solution to both issues – energy security and global warming – over the last decade several paths have been pursued, ranging from alternative fuels derived from biomass up to complete electrification of the transportation system. However, each proposed solution comes with its own set of opportunities and challenges.

1.1 Biomass-Derived Alternative Fuels

Different nations decided to invest research and infrastructure funds into different methods of generating transportation-grade fuels from a diverse set of biomass sources. The European nations, as part of the European Union, invested mainly in the use of bio-mass derived fuels in diesel-type internal combustion

engines. A widely used biofuel source within the European Union has been the rapeseed oil. A 2002 report [8] of the U.S. Embassy in Berlin observed that the major method employed by European governments in general and Germany's government in particular is the use of fuel taxation in order to make biofuels commercially attractive. While the production costs for biofuels are generally higher than fossil-based fuels, the tax exemption allows biofuels to be sold for a lower total price than ultra-low sulfur diesel (ULSD).

Other nations, such as the United States and Brazil launched programs for ethanol-based bio-fuel production from various feedstocks. From a combustion technology standpoint, most applications have been focused towards spark-ignition engines, with ethanol being used as a pre-ignition reactions suppressant and consequently octane number improver for gasoline-type fuels. However, several attempts have been made at using ethanol-diesel fuel mixtures in compression ignition engines, which is further detailed in section 2.3, *Ethanol – Diesel fuel blending* section.

While biomass derived fuels present a major benefit in terms of being renewable and, in some cases, carbon neutral, they incur important challenges with respect to their method of production. A significant amount of research as well as political debate has been focused on the conflict between energy/fuel supply demand and human food supply. Some of the proposed feedstock sources, including most notably the corn used for ethanol production, result in direct competition with food supply for direct human consumption as well as feedstock usage in farming [9].

1.2 Electrification of the Transportation System

Electrically driven automobiles have a major benefit related to the lack of gaseous emissions at the vehicle level. The issue of harmful emissions is basically pushed upstream the electrical supply system, at the level of the electric power company where, at least in theory, this issue can be addressed more efficiently as well as the energy production technology can be selected to be carbon neutral (carbon sequestration or use of alternative fuels generated from renewable sources such as algae) or without any carbon involved in the power generation cycle (such as nuclear energy, wind or solar). Use of traditional powerplant fuels such as coal, without carbon sequestration techniques, would be useful in providing decreased demand for crude but would not provide any significant reduction in CO_2 output.

While electrically powered vehicles have been around for close to a century, drawbacks related to battery energy density, limited number of recharging cycles as well as lack of a suitable vehicle charging station network have prevented the widespread adoption of this technology in the automotive market. Recent developments have indicated that hybrid technology can dramatically improve the maximum range an electric vehicle can be driven for by using a smaller, less powerful, internal combustion engine. However, due to increased system complexity and resulting cost, the application of plug-in hybrid technology is restricted to higher-cost luxury models for now and is not expected to have an important market share until market-driven changes result in a higher demand for

powertrains characterized by very low fossil-fuel consumption. A more detailed discussion related to the electric vehicle technology in provided in ref [10].

1.3 Other Transportation Energy Sources and Recovery Methods

Many other alternative ways of propelling vehicles are in various stages of development. While some, such as fuel cell [11] or solar technologies went as far as vehicle demonstrators, others, such as thermo-electric effect for waste heat recovery [12], are quite far away from becoming commercially viable at the time this work has been conducted.

1.4 Conclusions

Current economic, political, environmental and social forces are competing over the future of energy sources for transportation. All of these factors have very strong arguments for favoring one option over another, but they all face the same real-world constraints related to the state of technology, production costs, reliability and safety.

Over the last decade two major directions have emerged towards providing an alternative to the current energy model. The first direction focused on using existing technology and providing renewable energy supply through either bio-mass derived fuels or other fuel types, such as hydrogen. The second direction followed the path of electric drive vehicles. While considerable progress has been made in increasing battery energy density and reliability, production costs are still high and limited range continues to prevent their wide market adoption.

It is therefore a strategic need for nations as well as internal combustion engine manufacturers to improve upon the existing transportation technology by pursuing improved fuel efficiency for internal combustion engines while maintaining low engine-out emissions. Recent breakthroughs in combustion technology detailed in Chapter 2 related to Low Temperature Combustion (LTC) have obtained promising results in achieving this target.

Chapter 2. "Review of Literature"

Any attempt to control combustion in internal combustion engines through chemical kinetic means requires a deep understanding of the underlying elementary reactions taking place at molecular level. This fundamental understanding has been helped considerably over the past couple of decades, with the advent of relatively inexpensive computing capabilities as well as political and economic pressure to reduce pollutants produced by internal combustion engines, by the development of ever larger and more comprehensive chemical kinetic models for alkanes, alkenes, cycloalkanes and aromatic compounds. In the 1997 study by Curran et.al. [13], an important step has been made towards modeling and understanding the oxidation chemistry for alkanes up to seven carbon atoms. Other studies aimed at expanding the description of the oxidation chemistry for compounds typically encountered in hydro-carbon based fuels have been included in a 2007 comprehensive review by Battin-Leclerc [14].

In the first part of this chapter is presented a brief overview of different combustion modes currently employed in internal combustion engines as well as the main reactions responsible for the oxidative behavior of alkanes during autoignition under different temperature regimes. This literature review is focused on combustion and combustion chemistry details relevant for the overall goal of the research, i.e. active control of the combustion process through chemical kinetic combustion additives. The introduction is followed by a survey of the body of literature available to date regarding the chemical kinetic effect of different

combustion additives on ignition delay relevant for engine-related pressure and temperature conditions.

2.1 Combustion Modes for Internal Combustion Engines

Combustion has been traditionally split along two major approaches. The first one, and also the most widely used, ignites the combustible mixture by providing a localized high-energy pulse, most of the times in the form of a spark, thus its name: Spark Ignition combustion mode. The second mode involves fuel delivery, typically in the form of a spray, in a high-pressure environment. While this combustion mode lacks an ignition source, it relies on fuel decomposition reactions subsequently followed by a rapid release of energy in the form of a thermal explosion.

These two combustion modes, illustrated in Fig. 2.1 a) and b), have dominated the use of internal combustion engines for most commercial applications over the last century and have recently come under two distinct but concurrent challenges.

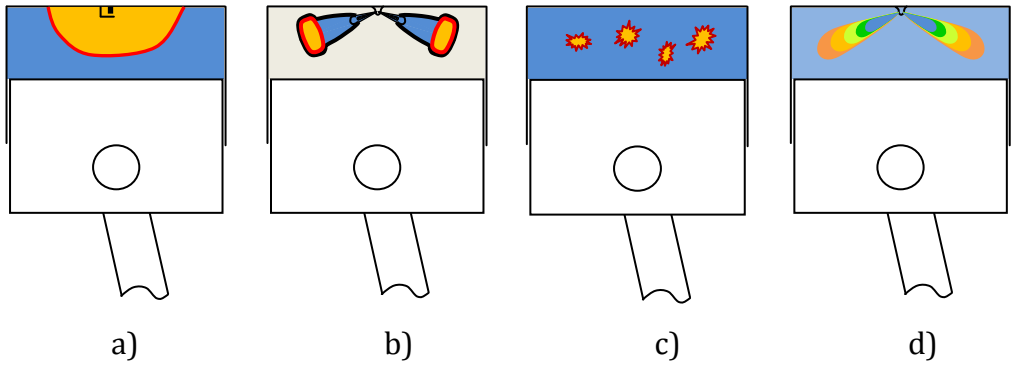

Fig. 2.1. Different modes of combustion
a) Spark Ignition b) Compression Ignition [15] c) Homogenous Charge Compression Ignition (HCCI) d) Reactivity Controlled Compression Ignition (RCCI)

Firstly, most governments recognized, based on increasing scientific evidence, that some of the gaseous and particulate emissions from internal combustion engines represent a health hazard for humans as well as a destabilizing factor for our environment. In a couple of review papers, Johnson discussed the issue of diesel emissions [16, 17]. Secondly, previously discussed issues related to the driving forces behind improvements in powerplant efficiency have increased the need to improve upon the existing combustion technology. A complete description of these traditional combustion modes is provided by Heywood [18].

2.1.1 Spark Ignition Combustion (Otto)

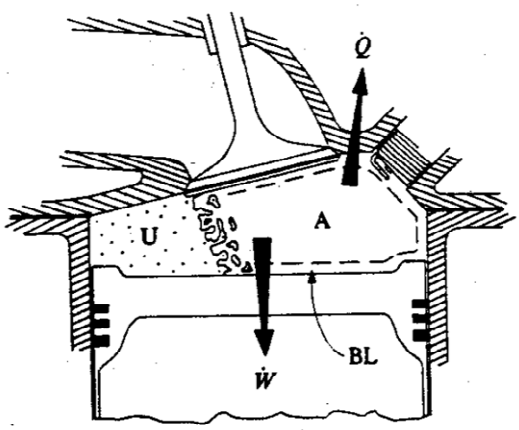

Fig. 2.2. Combustion in Spark-Ignition engines
(reproduced from ref. [18])

In a spark-ignition engine, the fuel which is either premixed with air or injected in the combustion chamber well before the combustion event is ignited by a spark. Reactions initiated in the ignition kernel quickly form a flame front typically a few fractions of a millimeter thick, which propagates throughout the combustion chamber in a quasi-spherical pattern. Due to the large temperatures experienced by the combustible mixture within the flame-front as well as in the burned gas zone, conditions favorable for formation of NO and other oxides of nitrogen arise. Additionally, as the flame-front propagates and compresses the end-gas zone, elevated temperatures are experienced by the un-burned mixture, which results in increased rate of fuel decomposition and auto-ignition. This self-ignition process occurring ahead of the flame front occurs in a volumetric fashion, with a sudden release in thermal energy and known as *knock*. As a result, in order to limit the occurrence of knock in spark-ignition engines, the in-cylinder pressure and

temperature are limited to a level where the auto-ignition reactions are not significant, thus effectively limiting the maximum allowable compression ratio and engine efficiency.

Additionally, as a result of engine emissions and exhaust aftertreatment considerations, the equivalence ratio of spark-ignition engines has to be maintained within a narrow range around stoichiometry. This effectively mandates a requirement for either displacing existing oxygen from the mixture with EGR or, more commonly, throttling the engine intake system with further impacts on engine efficiency.

For spark-ignition engines combustion phasing control is achieved through the adjustment of the spark timing.

2.1.2 Compression Ignition Combustion (Diesel)

During Compression Ignition combustion mode, commonly referred to as Diesel combustion, fuel is injected in a high-pressure and high-temperature air. As the fuel evaporates, it undergoes fuel decomposition reactions and subsequent thermal explosion, commonly referred to as premixed phase of the combustion. As the pre-evaporated fuel is depleted, the combustion process becomes rate-limited by the speed with which fuel is evaporating from spray droplets and impinged surfaces, thus the name of diffusion controlled combustion.

In this combustion regime, high temperature zones of the flame result in increased formation of NO and other oxides of nitrogen, while the equivalence ratio stratification implies that an overall lean mixture has to be used. This renders the

three-way catalyst technology unusable, as the catalytic reduction reactions are not efficient in the predominantly oxidative exhaust gas.

Also, diffusion controlled combustion is characterized by important amounts of particle matter formation due to fuel oxidation under rich conditions as well as fuel molecules pyrolysis.

Modern diesel engines equipped with advanced injection systems have been shown to be high-efficiency methods of converting chemical energy stored in hydrocarbon chemical bonds into useful mechanical work.

2.1.3 Low Temperature Combustion

In response to emissions and energy efficiency concerns, recent work (references provided in paragraph below) has focused on different types of low-temperature combustion modes. These combustion modes are typically characterized by relatively lean or dilute mixtures which undergo autoignition rather than being ignited by an external ignition source. This avoids the formation of high-temperature flame-fronts as well as it alleviates the need for stoichiometric mixtures and the associated high combustion temperatures. Additionally, through certain degrees of fuel premixing, diffusion-controlled phase of the combustion process can be greatly reduced with significant reductions in particulate matter production.

Among the most important combustion modes falling under the general Low Temperature Combustion category are: Homogenous Charge Compression Ignition (HCCI) [19] which is shown in Fig. 2.1 d), Premixed Charge Compression Ignition

(PCCI) [20], Modulated Kinetics (MK) [21] as well as the more recently proposed Reactivity Controlled Compression Ignition (RCCI) [22].

While the traditional combustion modes (SI and CI) have provided methods for direct control over the combustion process, some of the LTC combustion modes, such as HCCI, exhibit difficulty in controlling combustion phasing as well as being load-limited by excessive rates of pressure rise [23],[24]. The presence of NTC for some of the practical fuels, such as diesel fuel, makes temperature control increasingly difficult [24] due to inverse response of ignition delay with increase in temperature for certain temperature ranges.

Thus, premixed combustion modes that lack complete charge homogeneity in favor of charge equivalence ratio stratification are capable of extended load capability as well as reduced combustion noise [25].

2.2 Autoignition in Internal Combustion Engines

Currently available automotive fuels are most of the times distillates comprised of hundreds of hydrocarbon species ranging from one carbon atom for methane-fueled engines up to about twenty carbon atoms per molecule for some of the recently proposed bio-derived fuels. Under most applications relevant for this work, the fuel is available in liquid form for easier storage and is vaporized as needed for combustion purposes. The liquid fuel can be either evaporated outside the cylinder, by fuel injection in the engine intake system and other means, or it can be vaporized within the cylinder by direct injection of the fuel. As these fuel molecules transfer to the gas phase, they are exposed to an oxidative environment.

If the ambient pressure and temperature are low, the rate of the oxidation reactions will be low with respect to the rate of heat transfer with the surroundings and only slow decomposition reactions will take place thus lacking any runaway exothermic heat release and explosion. However, as the temperature of the environment increases beyond 500-600K, the oxidation reactions become significant and usually thermal explosions will occur with certain ignition delays. For homogenous gas-phase reactors the ignition delay is completely controlled by chemical kinetic effects. In diesel engine-related terminology, this combustion phase is called premixed combustion and occurs mostly due to the fuel available as gas-phase. A more detailed description of the combustion process in traditional diesel engines is provided by Heywood [18].

2.2.1 Low Temperature Oxidation of Alkanes

As shown by Battin-Leclerc [14] and Pilling et.al.[26], under low temperature conditions (below 900K for engine-relevant pressures), the hydrocarbon oxidation reactions are initiated by hydrogen atom abstraction by direct reaction with molecular oxygen and by reaction with hydroxyl radicals (·OH). These reactions result in the formation of alkyl radicals and hydroperoxy radicals (RH → ·R or RH → ·OOH). A simplified outline of the reaction pathways is shown in Fig. 2.3. If the temperature is sufficiently high (500-600K), the alkyl radicals (·R) further react with oxygen to form conjugate alkanes (with the same number of carbon atoms) along with HO_2· radicals as well as smaller alkyl radicals. Due to the relatively low reactivity of HO_2· compared to more active radicals, such as ·OH or ·H, this is in most

cases considered to be a termination reaction path which does not lead to the conditions favorable for runaway energy release. The peroxides (ROO·) radicals shown in Fig. 2.3 will be converted to hydroperoxides through internal isomerisation, where, due to the cyclic molecular structure, a proton is transferred from the CH bond to an oxygen atom.

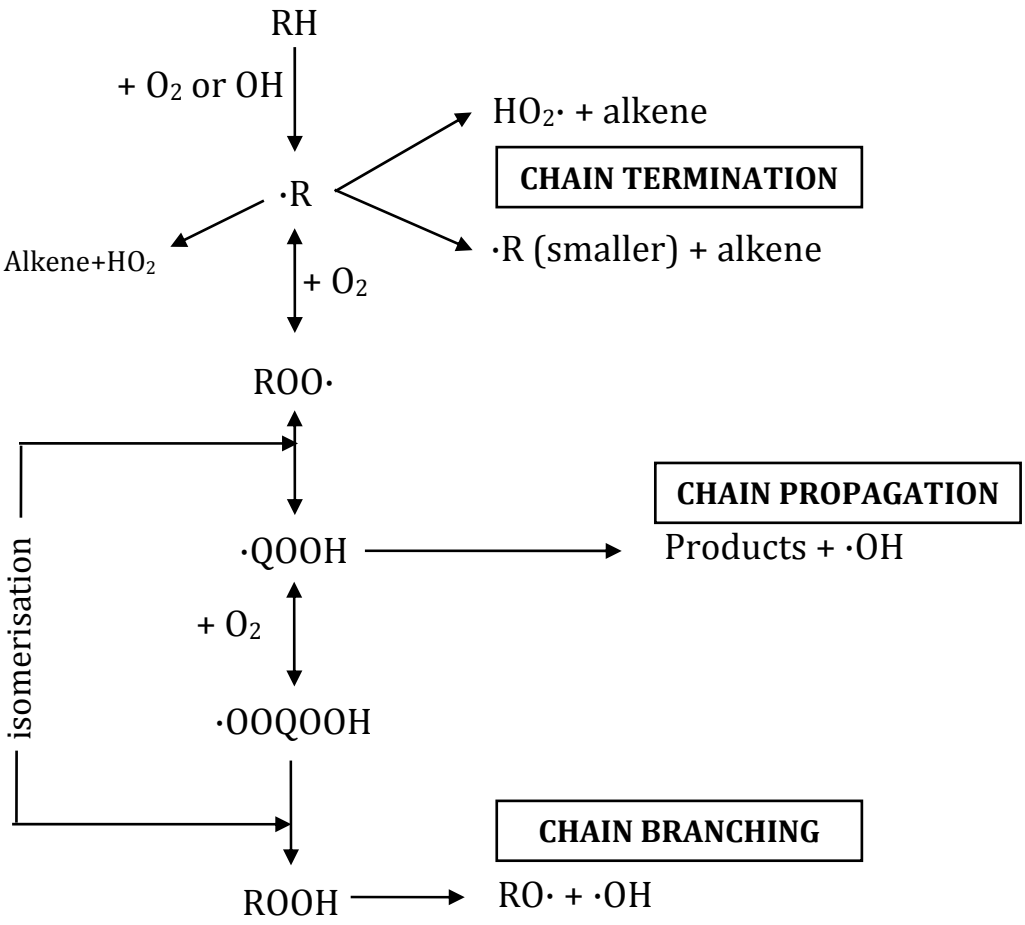

Fig. 2.3. Simplified low temperature oxidation mechanism for alkanes (adapted from [26] and [14])

The hydroperoxide easily reacts with O_2 to form another peroxy radical, ·OOQOOH, which, though an additional isomerisation is converted to a more stable hydroperoxide molecule (ROOH) along with an ·OH radical. The ROOH, which can have a fairly long lifetime, will be converted to two radicals, RO· and another hydroxyl radical, thus effectively providing the chain branching responsible for the rapid thermal release (exponential growth) characteristic of most auto-ignition processes.

Due to the importance peroxide radicals and peroxides have during the low temperature ignition process, the low temperature regime is sometimes called the "peroxy chemistry zone".

An important phenomenon that occurs during low-temperature combustion is the shift in the equilibrium of the reversible reaction $\cdot R + O_2 \leftrightarrow ROO\cdot$ as temperature is increased, which leads to an alkene-forming reaction type to be favored (Fig. 2.3). Thus, an apparent decrease in reaction rates as well as thermal heat release is observed, which is generally known as the Negative Temperature Coefficient (NTC) regime. This regime generally results in depressed energy release and cool-flames are observed to occur.

The pressure and temperature dependence of the different combustion modes is shown in Fig. 2.4.

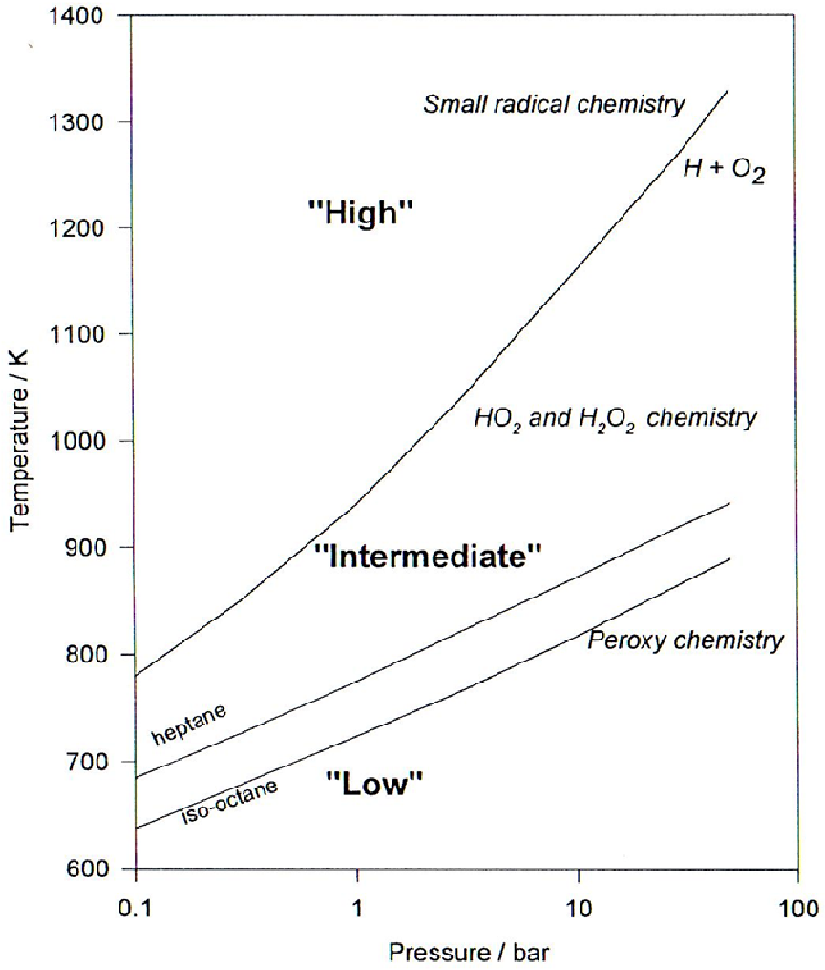

Fig. 2.4. Pressure and temperature dependence of the HC oxidation regimes (reproduced from ref [26])

2.2.2 High and Intermediate Temperature Oxidation

At the other side of the spectrum, for high temperature ignition, the main branching reaction is:

$$\cdot H + O_2 \rightarrow \cdot OH + \cdot O$$

In engine applications this region starts at about 900-1000K for most alkanes. However, as temperature decreases, another reaction is favored:

$$\cdot H + O_2 + M \rightarrow HO_2\cdot + M$$

Again, due to the relatively low reactivity of the hydroperoxyl radical, this reaction behaves as a termination reaction rather than a chain propagation reaction, effectively suppressing the high-temperature branching path.

At this relatively lower temperature, but still above the previously discussed low-temperature oxidation processes, the high-temperature branching mechanism is largely inhibited while the equilibrium of the previously discussed peroxide forming reaction:

$$\cdot R + O_2 \leftrightarrow ROO\cdot$$

is biased towards the left of the reaction. This results in a void of branching reactions which is filled by the hydrogen peroxide decomposition reactions:

$$RH + \cdot OOH \rightarrow R\cdot + H_2O_2$$

$$H_2O_2 + M \rightarrow \cdot OH + \cdot OH + M$$

where RH can be either the original hydrocarbon, as well as an aldehyde or alkene.

2.2.3 Effect of Autoignition Inhibitors

This section focuses on the data available in literature regarding the use of combustion additives targeted towards delaying the combustion process. While this section covers a fairly large range of combustion additives, this list is not meant to be exhaustive and concentrates mostly on additives of practical interest. Again, the ultimate research goal is the control of the active combustion process through combustion additives.

In more generalized treatments of ignition reaction inhibition, Gray *et al.* [27] and Lazarovici *et al.* [28] have studied from a theoretical standpoint a simplified

second-order reacting system in which flame quenching by endothermic reactions as well as radical quenching are considered. The results point towards enhanced inhibition of the considered premixed flame when radical scavenging is considered.

2.2.3.1 H_2, CO, CO_2 and EGR

In an HCCI related work, Eng *et al.* [29] reported the influence of POx (Partial Oxidation Gas) on n-heptane and iso-octane autoignition. POx contains H_2 and CO obtained by gasoline partial oxidation. The experimental work has considered a synthetic version of this gas, by mixing bottled CO/N_2 with H_2. The results obtained showed that POx had a strong influence on the n-heptane autoignition, but little effect on iso-octane. Based on chemical kinetic reasoning and simulation, the team concluded that the lack of effect observed in the case of the iso-octane fuel is due to its molecular structure, which is more compact than straight-chained n-heptane and thus less prone to low-temperature fuel decomposition. Thus, as a remark, it can be hypothesized that the best candidates for chemical control of autoignition process are fuels which exhibit low-temperature chemistry.

In attempting to explain the way POx affects n-heptane auto-ignition, the authors point towards the initial fuel decomposition reactions which rely heavily on the formation of OH radicals in order to initiate the reaction chain. However, the reactions sequence:

$$H_2 + OH \leftrightarrow H_2O + H$$

$$H + O_2 + M \leftrightarrow HO_2 + M$$

seems to be favored with POx addition, thus yielding a radical of much lower reactivity. Therefore H_2 effectively slows down the reactions occurring during the cool-flame phase of the auto-ignition.

The effect of reformer gas (H_2 and CO) of different compositions on HCCI combustion of dimethyl ether (DME - CH_3OCH_3) has been studied by Shudo *et al.* [30]. The authors concluded that there are two fundamental effects of the reformer gas on the HCCI combustion that they were observing experimentally. First, there was the thermodynamic effect of the inert specie CO_2.

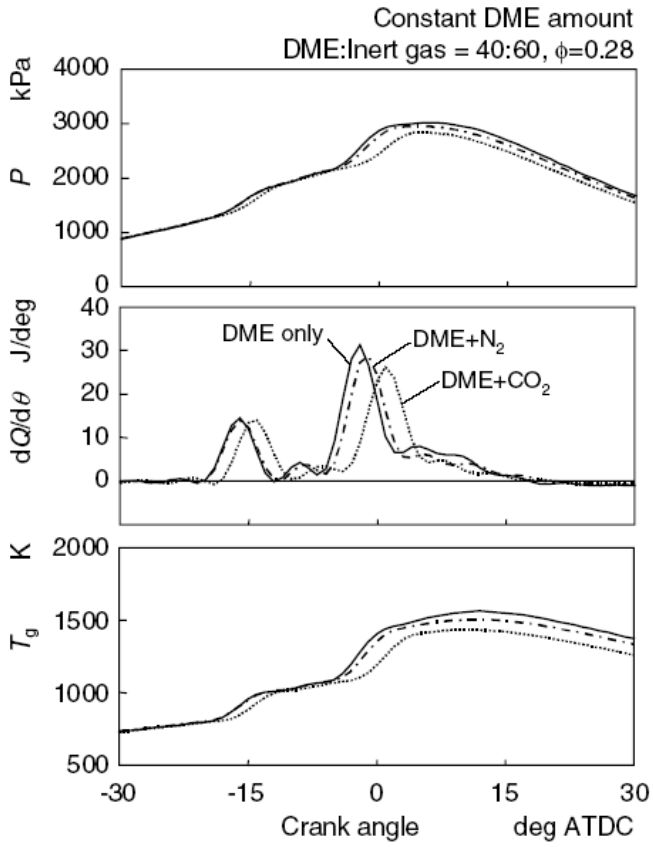

Fig. 2.5. Effect of CO_2 on HCCI combustion (reproduced from [30])

It affects combustion by shifting the temperatures at which combustion takes place; due to the high sensitivity of key auto-ignition reactions to variations in temperature, CO_2 had a strong effect (as much as 5 CAD) as shown in Fig. 2.5.

It is important to note that both the low and the high temperature heat release rates are affected by the CO_2 content. The second effect of the reformer was due to H_2. This species is believed to have a strong effect on auto-ignition of hydrocarbon fuels due to the fact that the reaction

$$H_2 + OH \leftrightarrow H_2O + H$$

is favored with respect to other radical-producing reactions such as H atom abstraction:

$$CH_3OCH_3 + OH \leftrightarrow CH_3OCH_2 + H_2O$$

and formaldehyde consumption:

$$HCHO + OH \leftrightarrow CHO + H_2O$$

thus, fuel decomposition reactions are slowed down and the high-temperature heat release is delayed.

In a follow-up publication, Shudo *et al.* [31] presented chemical kinetic simulation results for the effect of Methanol Reformed Gas (MRG) on HCCI combustion of DME. Essentially, the experimental findings of the previous publication have been backed up by CHEMKIN-based simulations. An interesting observation presented in this publication is related to the reaction paths the

reaction between atomic hydrogen and molecular oxygen can take as a function of temperature.

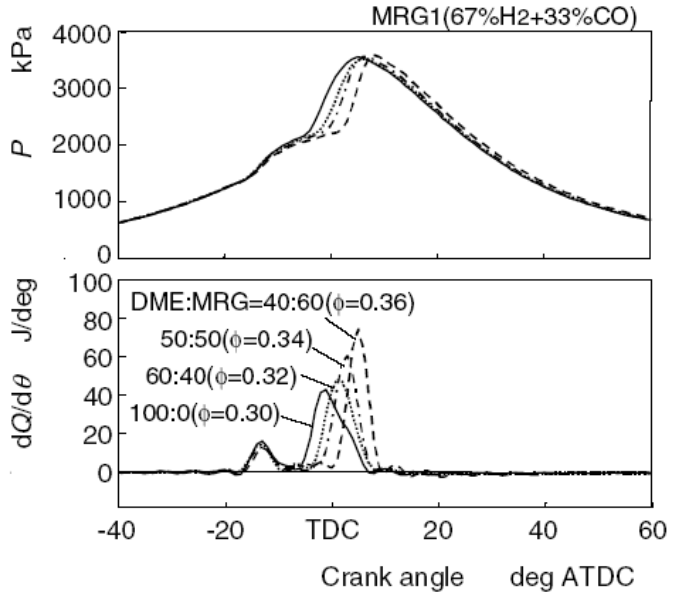

Fig. 2.6. Effect of reformer gas on HCCI combustion (reproduced from ref [30])

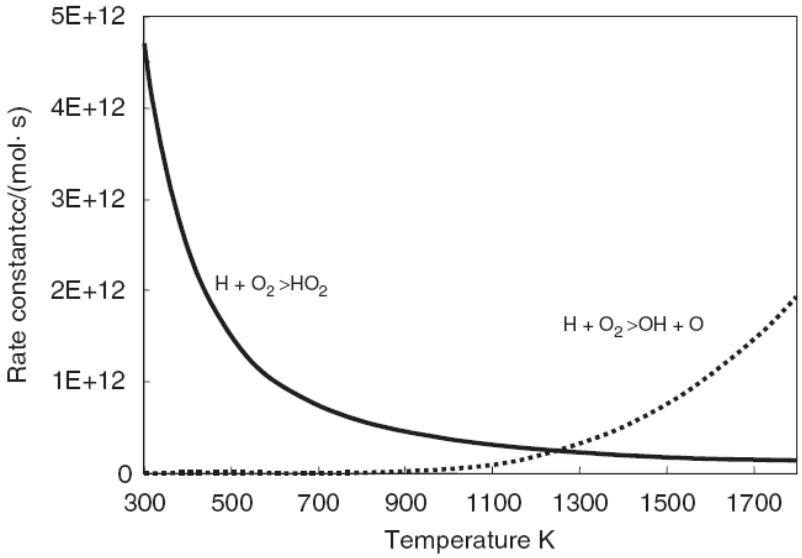

Fig. 2.7. Rate constants for the possible $H+O_2$ reactions (reproduced from ref [31])

The rate constants shown in the figure above indicate that in the low temperature combustion window, $H+O_2$ will result in HO_2, a fairly inactive radical (compared to OH), thus slowing down the reaction chain, while at high-temperature conditions the branching reaction producing OH and O is favored and thus accelerating the combustion process. This observation is consistent with the introductory remarks presented earlier in this chapter.

The effect of CO_2 on DME combustion is presented in another work by Shudo *et al.* [32]. The figure below shows the experimental results obtained.

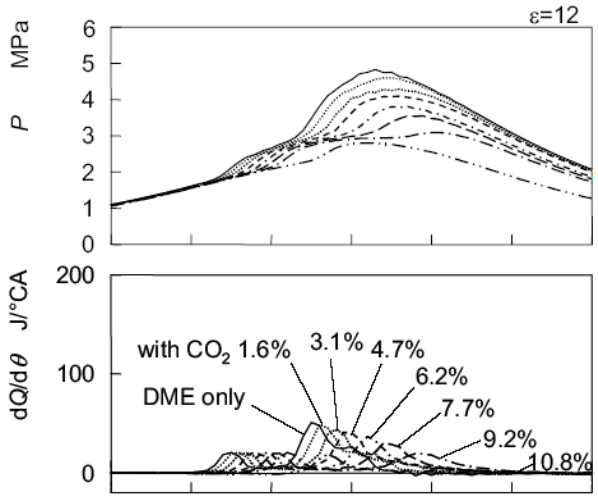

Fig. 2.8. Effect of CO_2 on DME HCCI combustion (reproduced from ref [32])

The CO_2 addition, which could be considered to simulate the effects of EGR, affects both the high temperature and the low-temperature heat releases, delaying them. The authors attribute this retarding effect to the change in heat capacity, which reduces the temperature rise of the charge. Besides the thermal effect, a chemical effect of CO_2 was noticed due to the shift in the equilibrium of reactions

involving CO_2. However, this effect was shown to be small compared to the thermal effect.

Sjoeberg *et al.* [33] investigated the thermodynamic and chemical effects of EGR on HCCI combustion of primary reference fuels. Besides the well known and important thermodynamic effect involving O_2 displacement, two other autoignition phasing control mechanisms are identified. The first one involves the H_2O content in EGR, while the second is residual trace species. The authors state without going into further details that H_2O was observed to chemically enhance the autoignition of primary reference fuel (PRF80). The enhancement was observed experimentally to be strong enough in order to compensate for the thermodynamic effects. Fig. 2.9 shows a zero net effect for this fuel.

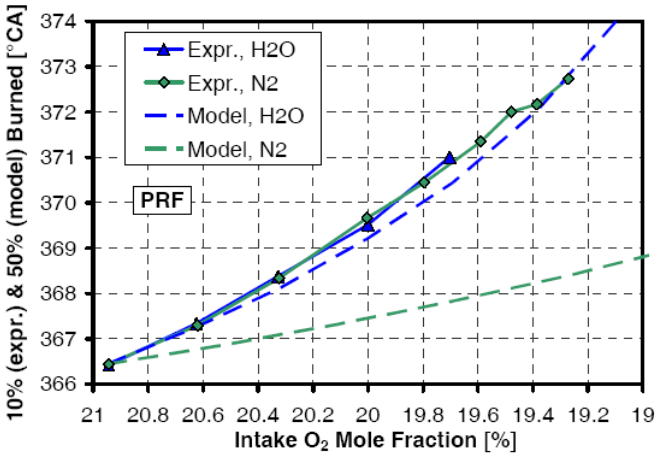

Fig. 2.9. Enhancing chemical effect of H_2O present in EGR (reproduced from ref [33])

Additional work related to the effect of reformer gas, but this time on n-heptane HCCI combustion, was presented by Kongsereeparp *et al.* [34]. This work confirms the delaying effects of H_2 on longer-chain hydrocarbon oxidation. The

authors point towards the inhibition of H_2O forming reactions as the cause of this effect.

2.2.3.2 Alcohols

Xingcai *et al.* [35] investigated the effects of suppression additives on ignition delay for HCCI type combustion. Their research used a modified four-cylinder four-stroke engine for which one of the cylinders was operated in HCCI mode while the others were maintained in classical diesel combustion mode. The direct injection system of the engine delivered n-heptane as baseline test-fuel. Additionally, the intake manifold of the engine was fitted with a low-pressure gasoline-type injector which delivered the fuel additives. The additives considered experimentally were methyl tert-butyl ether (MTBE), propanol, ethanol and methanol. By running experiments at two equivalence ratios and 1800 rpm, the researchers concluded that all additives considered have a retarding effect on the timing of HCCI combustion. It is interesting to notice in Fig. 2.10 that both LTC and HTC stages are affected by almost the same amount. The researchers point out that the effect is stronger for some species than for others, with methanol and ethanol having the largest suppression effects.

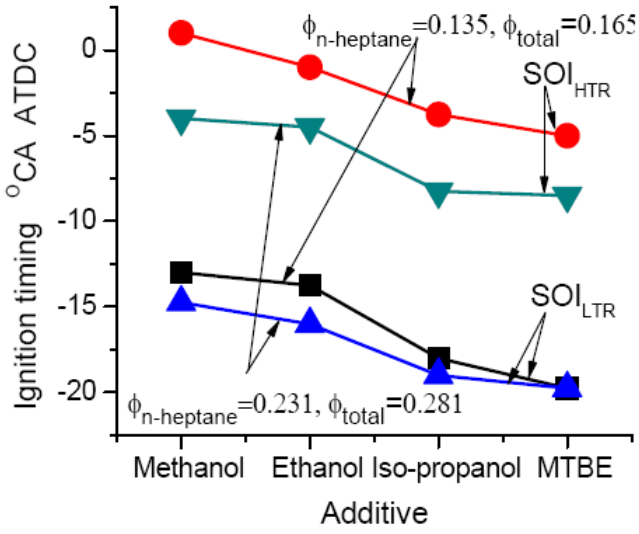

Fig. 2.10. Effect of HCCI combustion additives on LTC and HTC (reproduced from ref [35])

Additional to the experimental work, this research included numerical simulation of a zero-dimensional adiabatic homogenous reacting system where the oxidation of n-heptane supplemented by a set of ethanol reactions was considered. The authors showed the evolution of different important intermediate species but did not indicate the mechanism of reaction suppression responsible for the effect observed experimentally.

More recent work by Hashimoto [36] investigated the effects of ethanol and diethyl-ether (DEE) on n-heptane HCCI combustion in a Rapid Compression Machine (RCM). The experiments carried out with significant amounts of ethanol and diethyl-ether respectively have been observed to impact the ignition timing. Fig. 2.11 shows the effect of ethanol mass fraction on the timing of high-temperature heat release. There is a clear retarding trend with increase in ethanol mass fraction.

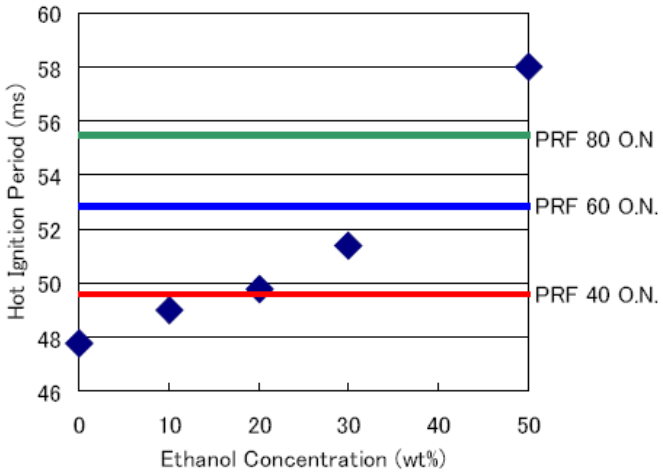

Fig. 2.11. Effect of ethanol on n-heptane HTHR (reproduced from ref [36])

In a subsequent publication [37], Hashimoto conducted numerical simulations related the experimental observations, and a sensitivity analysis of the chemically reacting system confirmed the importance of hydroxyl radical reactions in the overall inhibiting effect. Combustion imaging of the cool-flame within an optically accessible RCM showed a decrease in chemiluminescence.

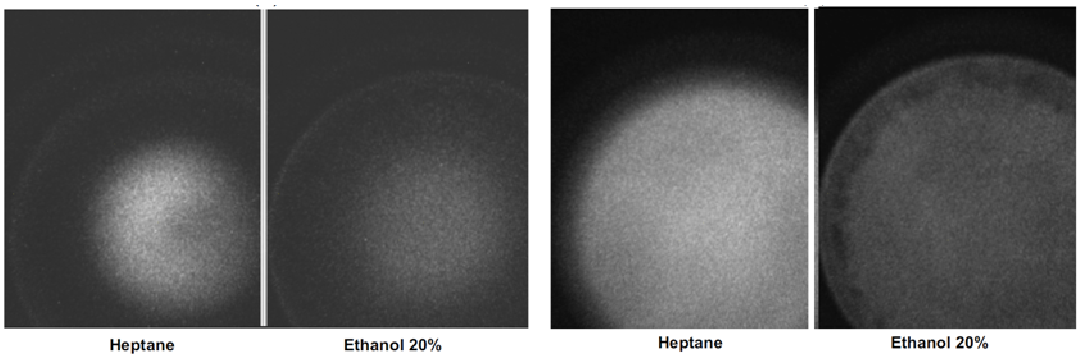

Fig. 2.12. Effect of ethanol on cool-flame chemiluminescence (left) and OH hot ignition chemiluminescence (right) (reproduced from ref [37])

Yamada *et al.* [38, 39] studied the effect of methanol on DME HCCI combustion. Experimental results are shown in Fig. 2.13 where the delaying effect of methanol is apparent. The authors point also towards the suppression of the cool-flame reactions as the main culprit for the overall delaying effect. The hydroxyl scavenging reactions by methanol

$$CH_3OH + OH \rightarrow CH_2OH + H_2O$$

$$CH_3OH + OH \rightarrow CH_3O + H_2O$$

are considered to be responsible for the observed behavior.

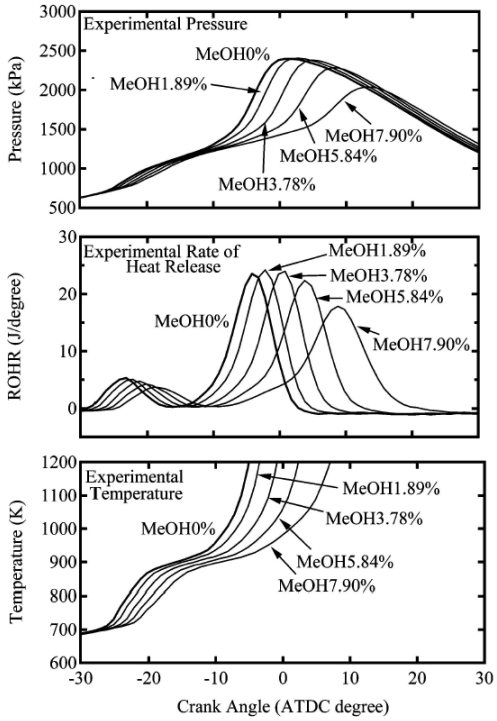

Fig. 2.13. Effect of methanol on DME combustion (reproduced from ref [38])

Observations regarding the effect of ethanol on different combustion modes are presented in further detail in section 2.3.

2.2.3.3 Formaldehyde

Work conducted by Kuwahara *et al.* [40] in CI and SI combustion modes showed the effect of 1900 ppm formaldehyde addition on the autoignition of diesel fuel (CN 52); a similar analysis is presented for gasoline (RON 90). The authors point towards a shift in the effect of formaldehyde from inhibiting the autoignition and suppressing cool-flame reactions at relatively low temperatures to an advancing effect at temperatures exceeding 900 K (intermediate/high temperature combustion). An important additional conclusion can be reached from the data presented in Fig. 2.14; lower compression ratios result in lower in-cylinder temperatures which in turn favor the cool-flame-specific chemical pathways. The effect of formaldehyde in terms of total delay is stronger for the lower-compression ratio case due to the presence of the low-temperature chemistry and its higher sensitivity to the radical scavenging reactions involving formaldehyde.

Work conducted by Jansons *et al.* [41, 42, 43, 44, 45, 46] from Wayne State University's combustion group, identified the role formaldehyde is playing in Low Temperature Combustion as observed during the cold-starting process of diesel engines. Optical investigation in [43] and [44] identified formaldehyde as a potential culprit for combustion instability, typically associated with cold-starting, after removing other effects, such as engine dynamics or transient behavior of the fuel system.

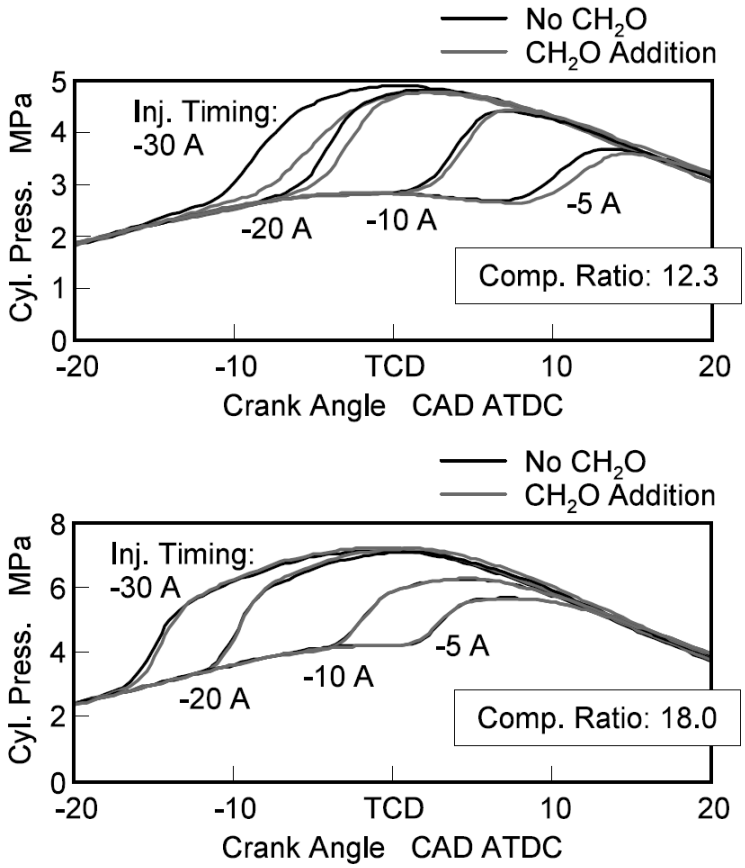

Fig. 2.14. Effect of formaldehyde addition on pressure (reproduced from ref [40])

The combustion instability observed during a starting sequence has been replicated well by the UV-Vis light emitted by reactions that precede the injection event, called Pre-Injection Chemiluminescence (PIC), as shown in the figure below. It has been found that the sensitivity of the combustion process to changes in PIC signal increases as temperature decreases, as indicated decreased slope of the inverse correlation between PIC and CA50.

This suggests that the role formaldehyde plays in cold-starting is significantly amplified under low combustion chamber wall temperature.

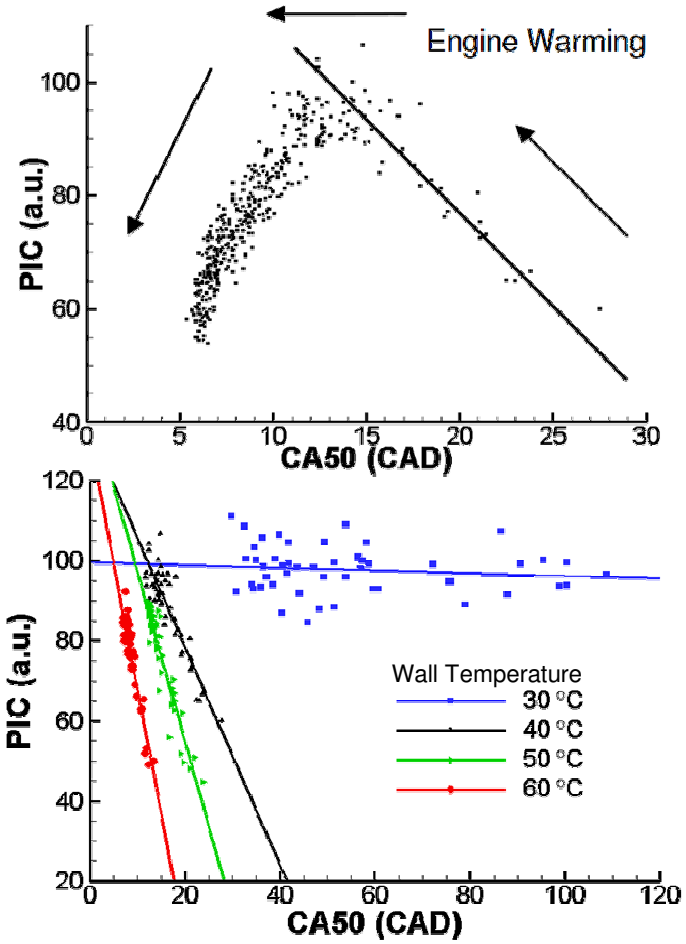

Fig. 2.15. PIC correlation with CA50 (reproduced from ref [42])

The impact of formaldehyde on combustion has been later examined both experimentally [41, 45] and numerically [44, 45, 46] by adding controlled amounts of formaldehyde in the intake system of the engine.

Under the conditions investigated, characterized by low ignition temperatures, formaldehyde has been found to have a strong inhibiting effect which is consistent with previous findings. This effect has been also attributed to OH scavenging by formaldehyde molecules, as the formaldehyde reactions with the

hydroxyl radical are favored compared to other reactions, such as hydrogen abstraction from fuel molecules.

A numerical study reported in ref [44] studied the effect of formaldehyde in a single-zone homogenous reactor and similar results have been obtained.

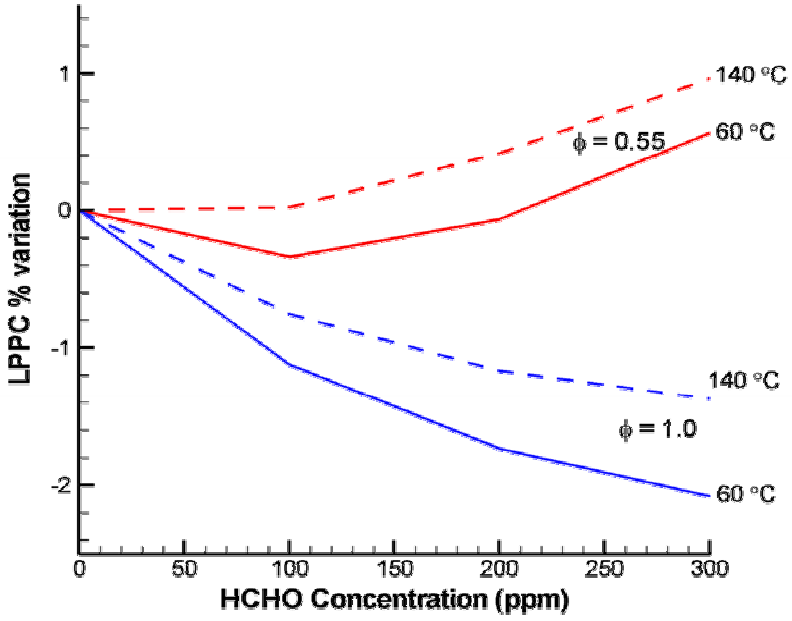

Fig. 2.16. Effect of formaldehyde, wall temperature and equivalence ratio on LPPC (reproduced from ref [44])

This work has been complemented by a CFD investigation [46] regarding the effect of formaldehyde under conditions relevant for the optically accessible engine used in previous investigations.

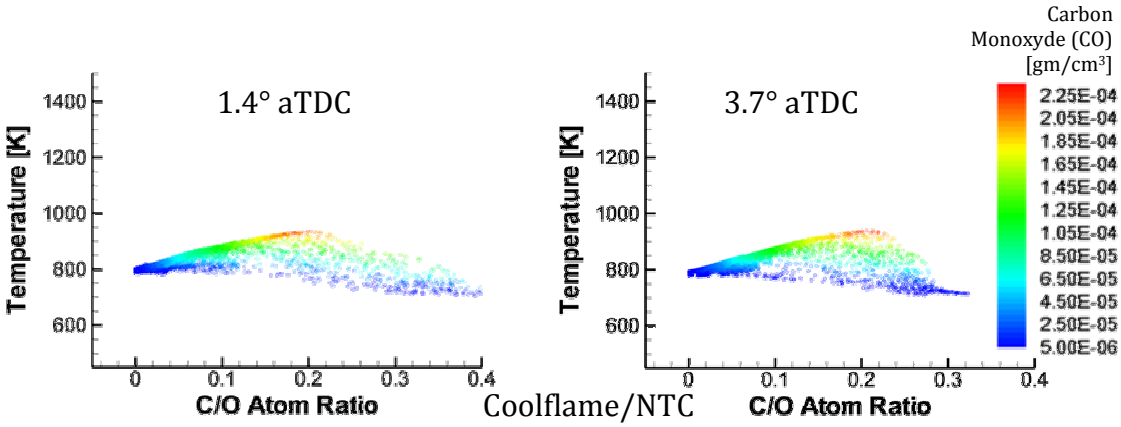

Fig. 2.17. Effect of formaldehyde on the distribution of local temperature and equivalence ratio
(adapted from ref [46])

As shown in the figure above, formaldehyde has a second important retarding effect. Besides the mechanism already identified for ignition suppression, formaldehyde prolongs the ignition delay through a reduction in local equivalence ratio due to diffusion effects.

The observations related to the impact of formaldehyde on LTC, point towards a possible combustion control method, where the inhibiting effect is used actively rather than observed passively. While the use of formaldehyde for combustion control in production engines is impractical due to a number of factors, other combustion additives with similar effect on chemistry could be employed.

2.2.3.4 Iron Pentacarbonyl $Fe(CO)_5$

While iron pentacarbonyl has many drawbacks, including high-toxicity as well as poor lubrication properties which might render it unusable in modern fuel injection systems, it has been observed to be an extremely effective inhibitor of

high-temperature combustion in premixed laminar flames and it is close to the theoretical limit for flame inhibition [47]. Extremely small amounts of iron pentacarbonyl, in the order of magnitude of a few ppm, were required in order to significantly reduce the flame velocity.

Rumminger *et al.* [48] studied the effect of $Fe(CO)_5$ on the burning velocity of premixed CH_4–O2–N2 flames. In a series of follow-up publications [49],[50],[51] the authors extended the research on other types of premixed flames.

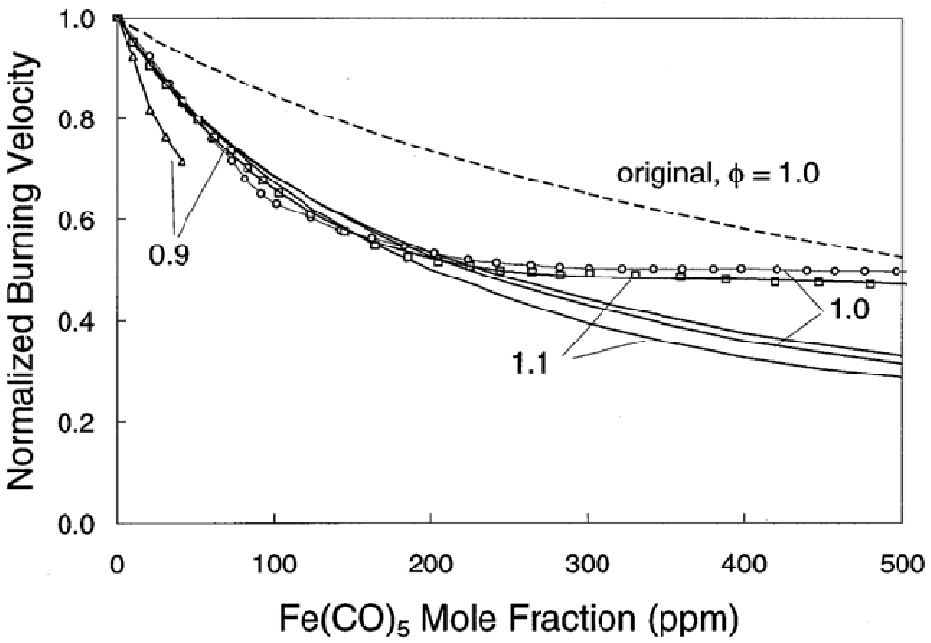

Fig. 2.18. The effect of iron Pentacarbonyl on burning velocity (reproduced from ref [48])

Additional research focused towards the effect of iron pentacarbonyl on the hydrogen-oxygen flames has been reported by Gerasimov *et al.* [52] and by Staude *et al.* [53].

However, preliminary chemical kinetic calculations carried out by the author under low-temperature auto-ignition conditions for n-heptane and iron-

pentacarbonyl failed to yield an increase in ignition delay. The observed behavior can be explained by considering that the mechanism of inhibition of high-temperature oxidation by iron-pentacarbonyl brakes down at low temperature due to the associated change in combustion chemistry associated with low-temperature oxidation of hydrocarbons.

2.2.4 Effect of Autoignition Enhancers

2.2.4.1 DTBP (di-tertiary-butyl-peroxide)

Research performed by Tanaka *et al.* [54] concentrated on the effects of "activation" additives, also known as cetane improvers, where the auto-ignition reactions are accelerated by interaction with these additives. Experiments were carried out using a Rapid Compression Machine (RCM) working in HCCI mode. In order to be able to make accurate chemical kinetics predictions, only pure hydrocarbons have been studied, such as n-heptane, iso-octane, cyclic paraffins, olefins, cyclic olefins and toluene, thus covering a fairly wide range of potential real-fuel components. The additives considered included 2-ethyl-hexyl-nitrate and di-tertiary-butyl-peroxide (DTBP - $(CH_3)_3CO\text{-}OC(CH_3)_3$). The mechanism by which DTBP influences the early autoignition reactions is reported to be related to the production of two alcoxy radicals $(CH_3)_3CO$ by low-temperature decomposition of DTBP. The enhancement of the autoignition process is due to the low activation energy of DTBP decomposition and the high reactivity of the alcoxy-radicals. It is concluded and shown experimentally that small concentrations (2% v/v DTBP as

shown in Fig. 2.19) can have dramatic effects on the autoignition timing, effectively halving the delay from approximately 6ms initially (for the PRF90 fuel) to less than 3ms.

The investigation on the effect of DTBP has further been extended to the effect of DTBP on ethanol and diethyl-ether by Mack *et al.* [55]. The effect of DTBP on primary-reference fuel mixtures has been also the subject of doctoral studies of Gong [56].

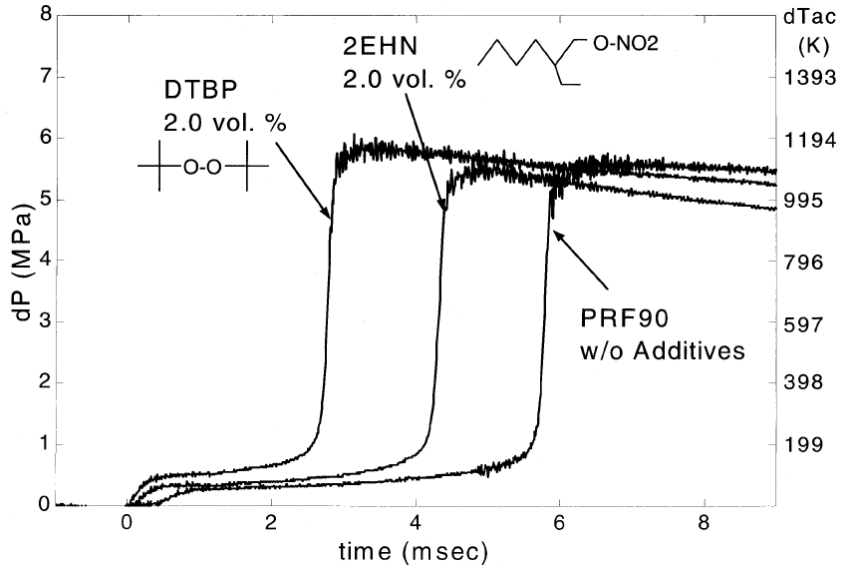

Fig. 2.19. Effect of activation additives on PRF90 ignition delay (reproduced from ref [54])

2.2.4.2 *Peroxides*

Theoretical work conducted by Aceves *et al.* [57] looked at the potential use of intermediate combustion species already included in the iso-octane detailed reaction mechanism (a more recent version of the mechanism is available in [58]). Iso-octane has been observed to exhibit relatively little low-temperature reactivity,

with considerable lower cool-flame energy release and much narrower NTC region [59]. Out of the 913 species available in the mechanism, some species were automatically discarded by imposing stability criteria due to practical reasons. Out of the remaining species, alkylhydroperoxide peroxy radicals (see Fig. 2.20 – additives 1-5) were observed to have the strongest advancing effect with other peroxides exhibiting slightly weaker effects.

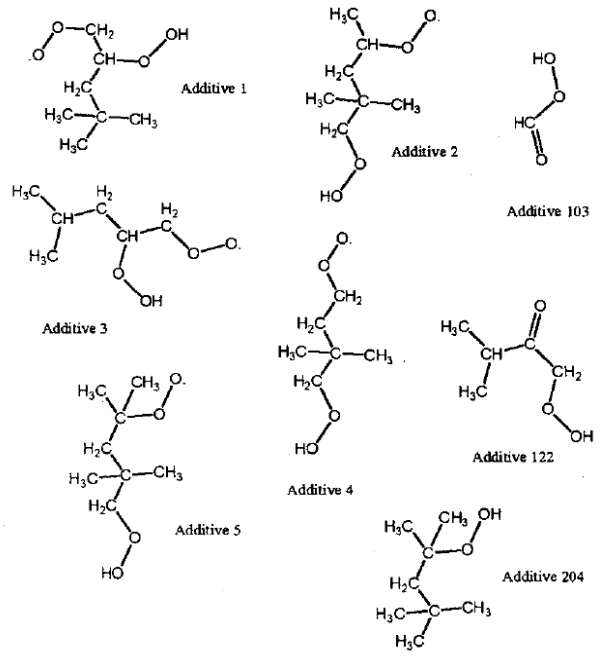

Fig. 2.20. Molecular structure of iso-octane HCCI additives (reproduced from [57])

Alkylhydroperoxide peroxy radicals have been observed to change the combustion timing by as much as 11 CAD for 10ppm of additive added to the mixture. The low amount of additive required in order to obtain a significant effect makes it practical even in a dual-fuel configuration, without the need of onboard

fuel reformulation. However, the simulation results have not been replicated in any experimental work to date.

2.2.4.3 Diethyl-Ether (DEE)

In the previously cited work [36], the effects of diethyl-ether were studied. This species, which may be produced on-board the vehicle by catalytic reformulation of ethanol, has very good low-temperature reactivity.

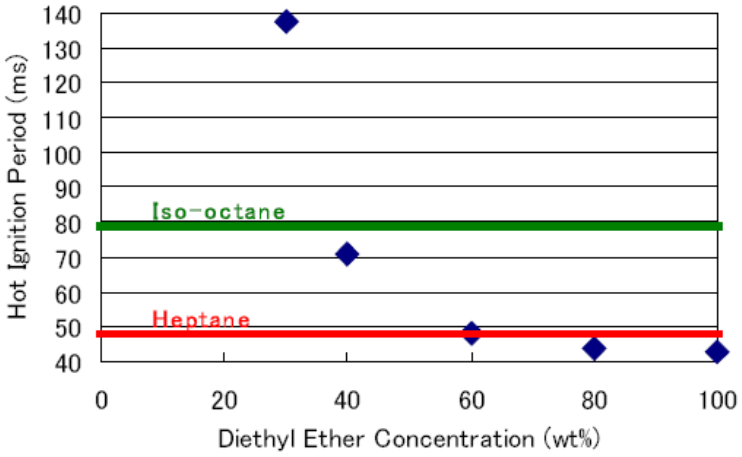

Fig. 2.21. Effect of diethyl-ether/ethanol mixtures on combustion (RCM) (reproduced from ref [36])

DEE was shown to shorten the ignition delay of n-heptane in HCCI combustion (Fig. 2.21). Using chemical kinetic reasoning based on hydrogen abstraction activation energy, the author concluded that diethyl-ether should have improved auto-ignition enhancement capabilities compared to DME.

2.2.4.4 Ozone (O_3)

The effect of ozone on HCCI combustion of DME was studied by Yamada *et al.* [38, 39].

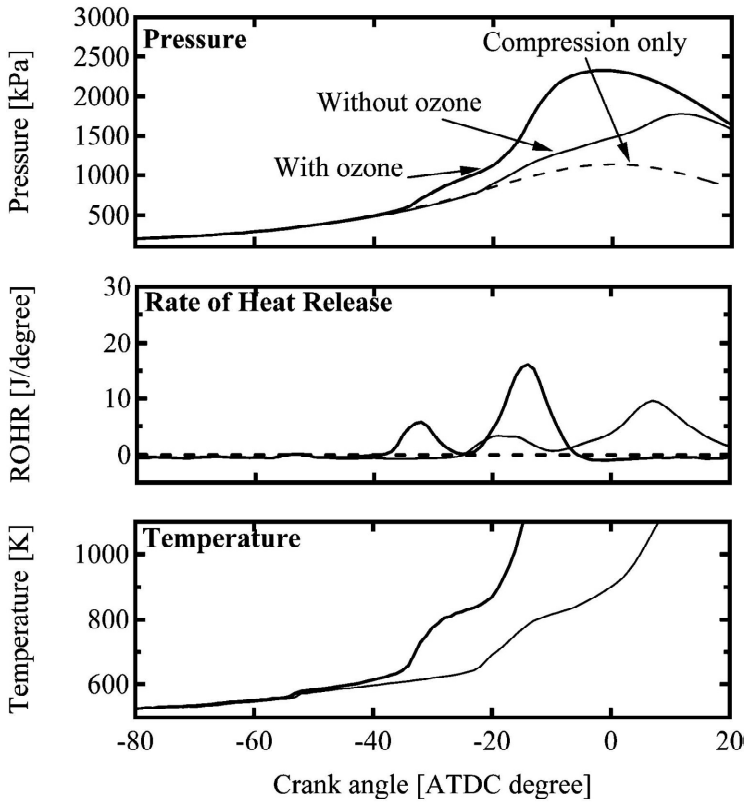

Fig. 2.22 Effect of ozone on DME combustion (reproduced from ref [38])

As shown in Fig. 2.22, ozone has a strong advancing effect. The addition of approximately 6750 ppm O_3 to the fuel mixture resulted in almost 20 CAD advance in the timing of the high-temperature oxidation reactions.

The ozone decomposition reaction

$$O_3 + M \rightarrow O_2 + O + M$$

is identified as being the main path of autoignition reactions enhancement. As ozone decomposition is highly favored at temperatures above 650 K, the supply of oxygen atoms is increased and cool-flame fuel decomposition occurs at lower temperatures than otherwise would be possible without ozone addition. This effect favors branching reactions which produce hydroxyl radicals and also delays the formation of formaldehyde resulting in earlier occurrence of the high-temperature heat release.

Ombrello *et al.* [60] investigated numerically and experimentally the effect of ozone on propane laminar lifted flames. In the experiment conducted by Ombrello *et al.*, ozone was produced by dielectric plasma discharge and subsequently isolated from other products of the plasma discharge to eliminate potential complications in the analysis of its effect. The results obtained are shown in Fig. 2.23 b) and indicate an advancing effect of 1260 ppm ozone addition. In Fig. 2.23 c) a schematic O_3 oxidation reaction enhancement is shown. O_3 is considered as being an atomic oxygen carrier, as O is extremely short-lived due to recombination and wall quenching reactions. As soon as O_3 reaches the higher temperature environment within the flame, it quickly decomposes to O_2 and O. The resulting atomic oxygen participates in oxygen abstraction reactions and OH radical formation which in turn speed up the autoignition process.

a)

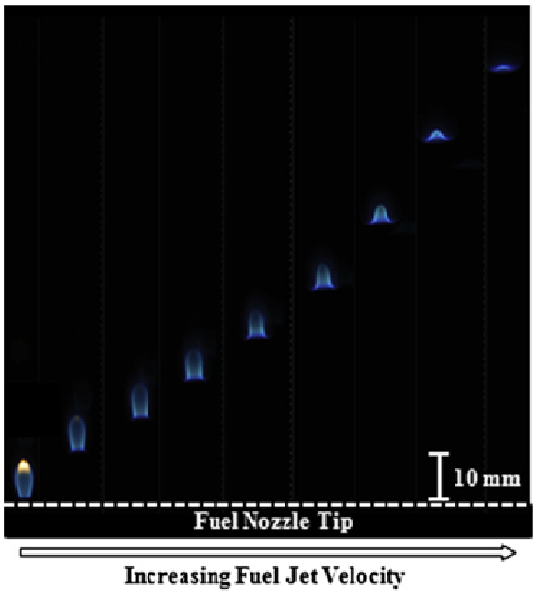

b)

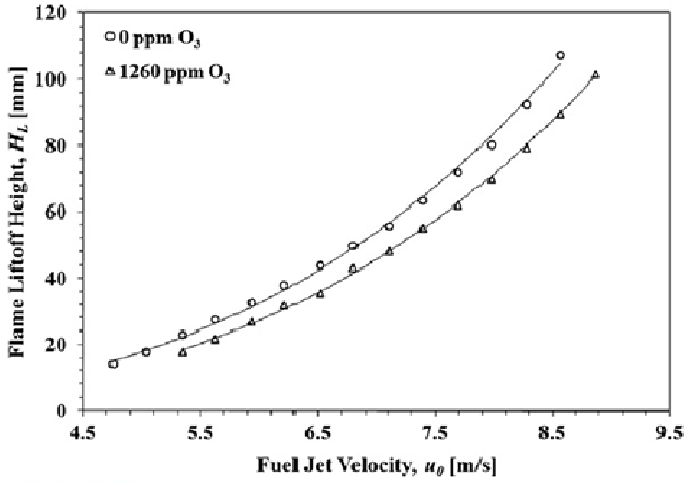

c)

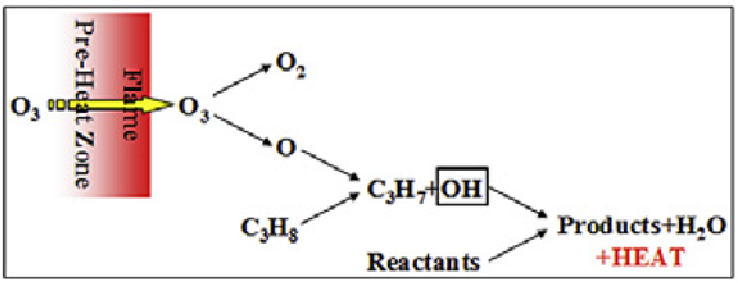

Fig. 2.23. Effect of ozone on flame lift-off for different fuel jet velocities (reproduced from ref [60])

2.2.4.5 Oxygen Singlet $O_2(a^1\Delta_g)$

Ombrello *et al.* [61] studied the effect of $O_2(a^1\Delta_g)$ – oxygen singlet, sometimes denoted by $^1O_2$ – on ethylene lifted flames. $O_2(a^1\Delta_g)$ is the diamagnetic state of oxygen molecule which is characterized by reduced stability compared to its stable counterpart [62], the oxygen triplet, $^3O_2$, the normal state of the oxygen molecule. $O_2(a^1\Delta_g)$ is characterized by increased reactivity compared to the normal state of the oxygen molecule [62].

a)

b)

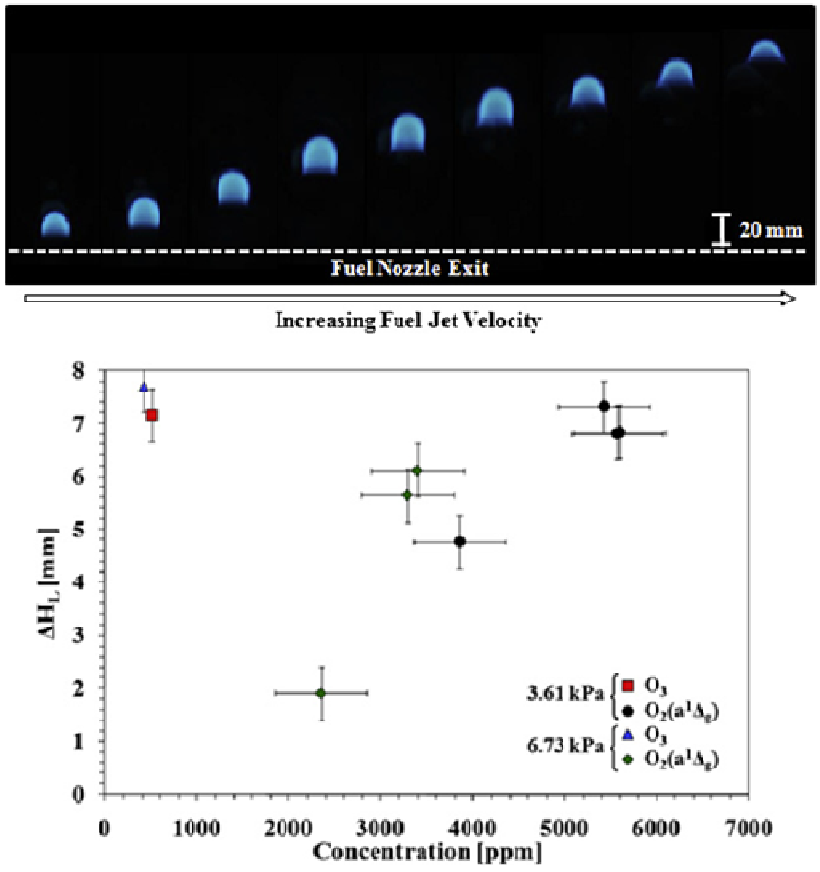

Fig. 2.24. Flame liftoff
a) flame liftoff images for different fuel jet velocities
b) effect of O_3 and $O_2(a1\Delta g)$ on the flame liftoff change
(reproduced from ref [61])

In their study, Ombrello *et al.* produced $O_2(a^1\Delta_g)$ using again a plasma discharge ahead of the flame. By-products of plasma discharge (O and O_3) were removed by NO addition.

From the data presented in Fig. 2.24, it is apparent that in order to obtain the same effect on the flame liftoff, roughly 10 times higher amount of $O_2(a^1\Delta_g)$ is required in order to achieve the same effect as ozone. Beyond this, there are a few other considerations that restrict the practical applicability of this combustion additive.

First, $O_2(a^1\Delta_g)$ is inherently an unstable specie. Although its lifetime is fairly long at normal pressure and temperature, in the order of magnitude of hours, at pressures and temperatures relevant to autoignition in internal combustion engines, this lifetime might be reduced to millisecond level, which will render it ineffective.

Second, wall-, reactive and collisional quenching effects might further reduce its effectiveness at higher temperatures and pressures.

2.2.4.6 *Nitroalkanes*

Cracknell *et al.* [24] investigated the potential use of nitroalkanes as fuel additives with the purpose of increasing iso-octane autoignition sensitivity with respect to autoignition temperature. According to the experimental work performed, the addition of nitroalkanes and especially nitroethane increases the sensitivity of the iso-octane ignition delay to changes in temperature (Table 1). It is

also of interest the observation that the addition of n-heptane reduced the sensitivity of the mixture due to its two-stage autoignition characteristics.

Table 1. Effect of additives

Difference in CA50 between T=523K, P=1 bara intake manifold conditions and 323K 2 bara conditions for various fuels and values of λ. Data is missing for cases of high COV or excessive pressure rise rate [24].

Fuel considered				**Difference between CA50 at high and low temperature conditions (CAD)**				
Iso-octane	**Additive**	**RON**	**MON**	**λ = 3**	**λ = 3.5**	**λ = 4**	**λ = 4.5**	**λ = 5**
100%	0%	95.4	86.4	9.6	9.7	8.7	-	-
95%	5% Nitroethane	92.0	75.8	-	14.6	19.0	19.2	18.4
90%	10% Nitroethane	91.5	71.6	-	15.9	20.2	21.5	20.8
97%	3% Nitromethane	93.3	81.9	-	16.5	19.7	18.4	18.8
90%	10% n-heptane	88.0	82.5	-	1.7	3.2	4.3	1.8

Beyond the risk of explosion involved in the use of the nitroalkanes which was covered by the authors (a risk which is alleviated by the dilution with regular gasoline), there are additional concerns which limit the applicability of these

particular additives. First of all, the presence of nitrogen and oxygen atoms in the nitroethane molecule could become precursors for, if not directly form, oxides of nitrogen, which are one of the main targets of clean combustion concepts and thus eliminate the benefits of low temperature combustion modes. Nitroethane has also mild toxicity and has been found to moderately irritate eyes, nose, throat and skin [63].

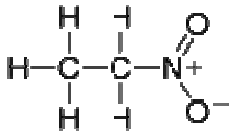

Nitroethane ($C_2H_5NO_2$)

2.3 Ethanol-Diesel Dual Fuel Operation

As described in the previous sections, active combustion control may be achieved by using a combustion additive or a second fuel, such as alcohols, gasoline and others.

In recent work conducted by University of Wisconsin's ERC group [22, 64, 65, 66] an approach to providing practical means of low-temperature combustion control has been proposed. The concept, called Reactivity Controlled Compression Ignition (RCCI), tries to bring improvements to the earlier combustion technology, Homogenous Charge Compression Ignition (HCCI), which has been studied in considerable detail. As it was shown in Chapter 1, HCCI has been shown to be difficult to control. There exists a large body of experimental and theoretical work which attempts to provide an answer to this challenge [67, 68, 69, 70].

Additionally, due to its nature, HCCI tends to have fairly short duration of combustion, as the energy is released in a volumetric fashion. However, while this is desirable from a theoretical thermodynamics point of view, the sudden release of energy is accompanied by a rapid rise in cylinder pressure, acoustic waves, engine "ringing" and eventual engine mechanical failure [71]. The rate of pressure rise becomes a limiting factor for HCCI engine load range as well as engine power density which constitute important barriers against its applicability in commercial applications especially in the medium and heavy duty engine sectors.

2.3.1 Ethanol – Diesel fuel blending

In a review of ethanol blends used in diesel engines, Hansen *et al.* [72] reported the findings of more than two decades of engine and fundamental research related to impacts of ethanol-diesel blends on blend stability, lubricity, materials compatibility, biodegradability and engine emissions and durability. A wide range of investigations surveyed observed a strong reduction in soot emissions (30-41% for 15% etOH blends), consistent with other literature sources considered in the following paragraphs. However, NOx reductions were minimal, ranging from 0 to 4-5%.

Cui *et al.* [73] investigated the use of five fuel blends in a small-bore diesel engine, among which they considered an ultra-low sulfur diesel (ULSD) blend with 10% ethanol and 2% emulsification additive. The ARHR data is shown in Fig. 2.25 for a non-boosted condition and pilot injection (initial heat release most probably due to pilot, not cool-flame). The ethanol-diesel blend is denoted as E-Diesel.

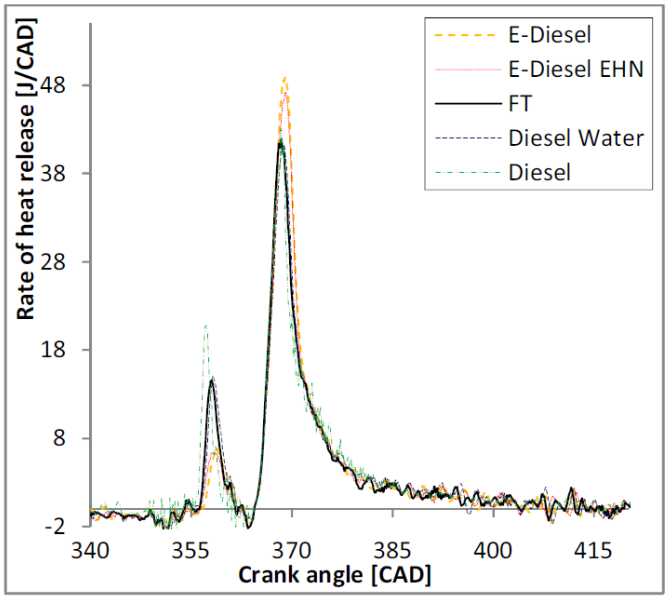

Fig. 2.25. Comparison of rate ARHR curves for 3 bar IMEP (reproduced from ref [73])

One may observe that most blends, including diesel-ethanol blend, have little effect on the ARHR. This can most probably be attributed to the fact that the fuels are blended prior to being injected in the combustion chamber and there is little variation in the percentage of ethanol available at the level of the local mixture. However, this is not the case for ethanol delivery in the intake port or in-cylinder injection through a second fuel system. For the operating conditions considered, the authors observed significant reduction in soot emissions when diesel-ethanol blends were used with slight increase in UHC and CO, while no NOx impact was noticed. Similar results in terms of soot reduction have been obtained in work performed by Cole *et al.* [74], who investigated the use of 10% and 15% ethanol blends in a small light-duty diesel engine. Additional work by Rakopoulos *et al.* [75] observed the same results in a heavy-duty turbocharged engine. However, under

their conditions, the authors observed a slight reduction in NOx emissions as well as reductions in CO output.

Qi *et al.* [76] looked at the effect of ethanol (5%) on bio-diesel blends and found also a strong reduction in soot emissions for a medium-bore (105mm), naturally aspirated engine.

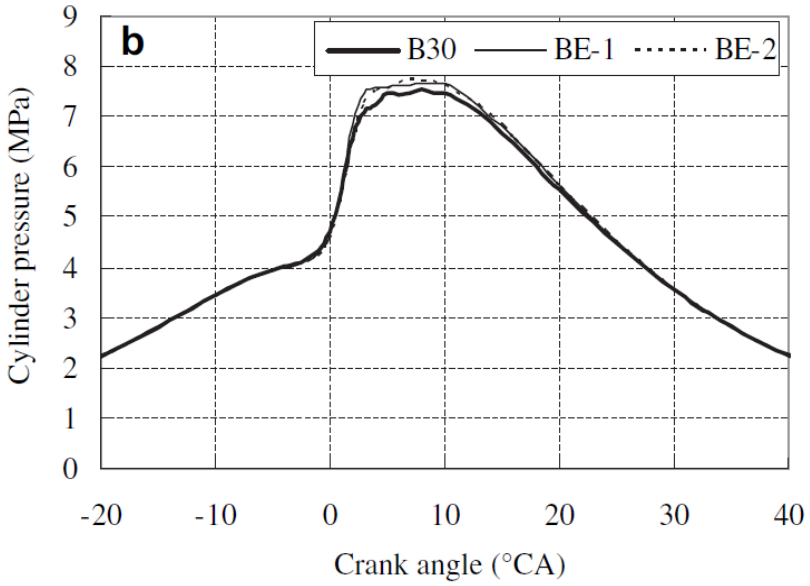

Fig. 2.26. Cylinder pressure comparison (reproduced from ref [76])

As previously observed by Cui *et al.* [73], ethanol has almost an imperceptible effect on cylinder pressure under the conditions studied.

Yan *et al.* [77] investigated the use of ethanol-diesel blends in a diesel engine. The authors observed similar trends with respect to soot and CO emissions reductions. However, a gas chromatograph and an FTIR were used to measure unregulated emissions and ethanol was found to increase formaldehyde, acetaldehyde and formic acid emissions. Although the authors do not specifically

state the precision of the instrumentation used for their determinations, it is quite likely that the measurements observed, which are in the order of magnitude of a few ppm, are close to the measurement errors of the gas chromatograph and FTIR instruments respectively.

Pidol *et al.* [78] discussed the implications of flash point reduction by ethanol-diesel fuel blends and the resulting safety issues related to fuel storage and dispensing. As the authors used the settings of a base ECU, not optimized for the particular fuel blend used, the addition of ethanol resulted in unstable/late combustion.

In an earlier publication, Pidol *et al.* [79] investigated the use of ethanol-diesel blends in HCCI-type combustion. The authors observed very low soot emissions.

Hu *et al.* [80] performed experiments in a constant-volume optically accessible reactor and a 17.5:1 compression ratio diesel engine using blends of ethanol and diesel, while vegetable methyl ester was added to prevent phase separation. In this work, which focused mostly on collecting spray data using the constant-volume reactor and soot data using the diesel engine, it was observed that the ethanol-diesel blend had a slightly smaller spray penetration rate than neat diesel along with an increased spray cone angle; additionally, ethanol was found to reduce the soot particle size along with an overall reduction in soot production.

2.3.2 Ethanol Intake Fumigation and Port Fuel Injection

He *et al.* [81] conducted experiments using a diesel engine with a compression ratio of 17:1 and an optically accessible engine of unspecified compression ratio, both naturally aspirated. Although not clearly stated, the authors considered neat ethanol induction through the intake system and diesel fuel direct injection with ethanol varying from 0 to 100 percent of the total amount of fuel. This combustion mode resembles the characteristics of the dual-fuel combustion.

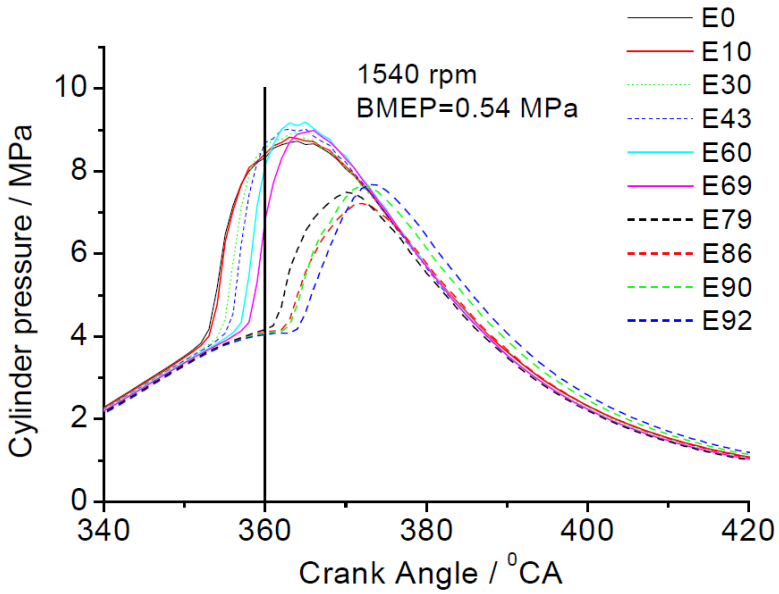

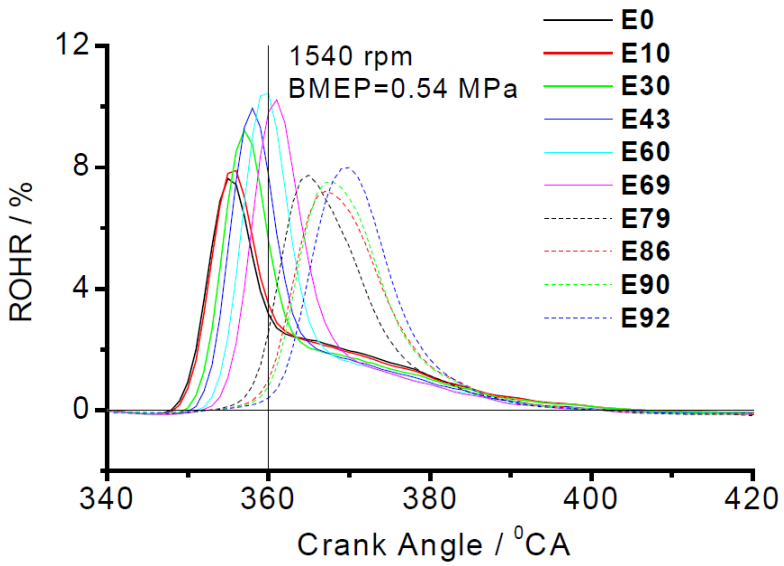

Fig. 2.27. Effect of ethanol fraction on combustion (reproduced from ref [81])

While most conclusions are consistent with previously published data in terms of effect of ethanol on combustion as well as more recent publications [22], the authors observe a reduced duration of combustion and attribute this observation to the increased ethanol intake delivery. However, as shown in the figure below, one may notice that the conditions chosen by the authors result in the variation of multiple parameters as ethanol fraction is varied. Thus, for the lower ethanol fractions shown, as the ethanol fraction increases, so does the ignition delay due to both chemical (OH scavenging) and thermodynamic (latent heat of evaporation higher for ethanol) effects. The increase in ignition delay coupled with the piston motion result in higher in-cylinder bulk temperatures at the time of the high-temperature heat release. This in turn increases the rate of the oxidation reactions with an apparent reduction in duration of combustion.

Kamio *et al.* [82] studied the effect of ethanol port fuel injection on the combustion process of a primary reference fuel (PRF) with an octane rating of 25. The engine considered has a relatively low compression ratio (13:1) and it is naturally aspirated, thus low temperature combustion is evident in the ARHR data shown below.

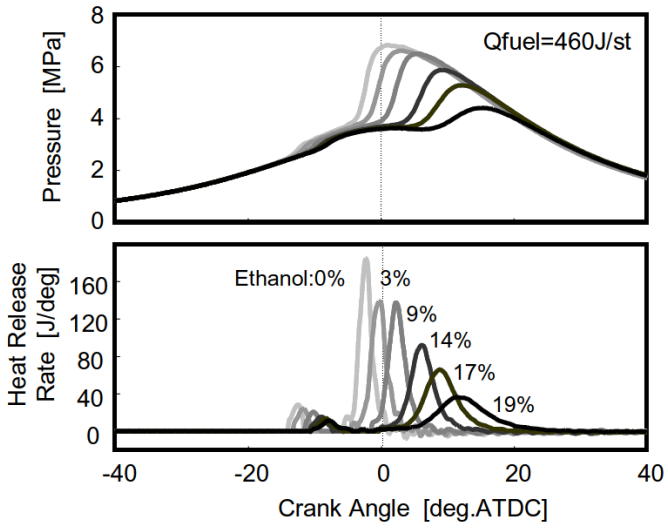

Fig. 2.28. Effect of ethanol on HCCI combustion of PRF25 (reproduced from ref [82])

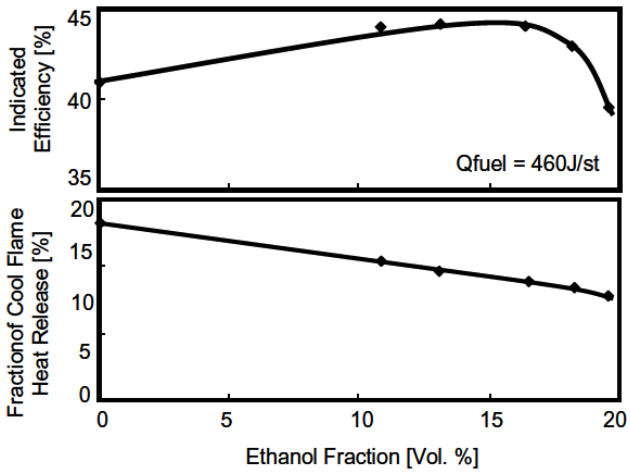

Fig. 2.29. Effect of ethanol addition (reproduced from ref [82])

Ethanol is observed to have a delaying effect on high-temperature heat release phasing. Additionally, it changes both the combustion phasing and energy release fraction of the low temperature heat release (cool-flame). This is consistent with previous observations. Additionally, ethanol is observed to increase the duration of the premixed combustion phase. Due to significantly different CA50 values for different ethanol fraction, it is difficult to separate the chemical effects of ethanol from the cylinder expansion effect.

2.3.3 Neat Ethanol Operation

Gjirja *et al.* [83] operated a heavy-duty Volvo bus engine using neat ethanol which was direct-injected into the combustion chamber while the intake was fumigated with two ignition improvers, DEE and PEG (tradename – Beraid).

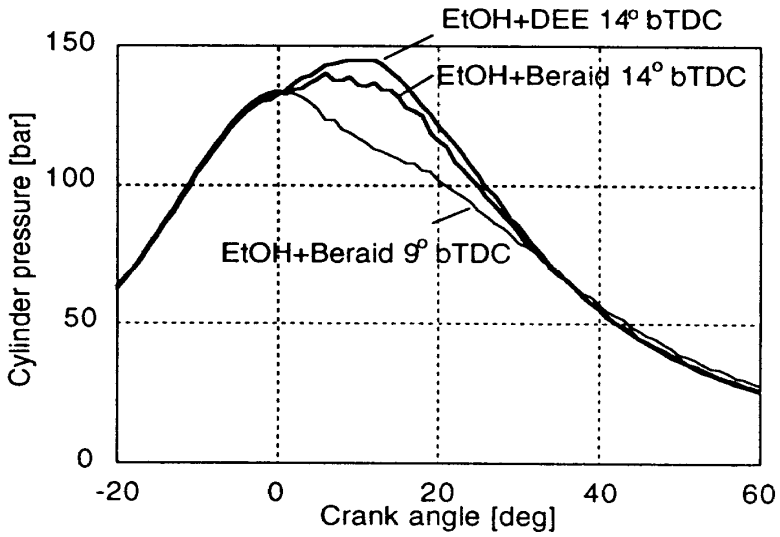

Fig. 2.30. Cylinder pressure data for maximum load (reproduced from ref [83])

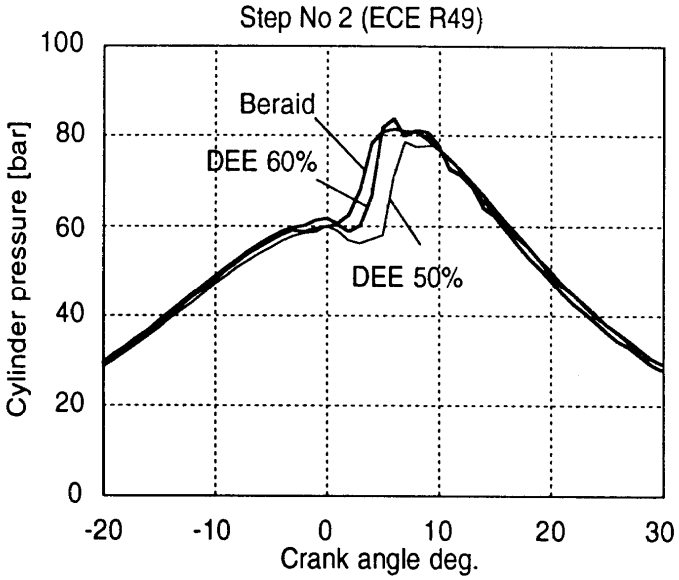

Fig. 2.31. Cylinder pressure data for light load (reproduced from ref [83])

Due to the large ignition delay associated with neat ethanol, large amounts of ignition improvers had to be used.

2.3.4 Dual Fuel Compression Ignition

Research performed by Splitter *et al.* [22] at ERC has focused on medium and high load RCCI combustion in a heavy-duty single-cylinder engine. The engine had a fairly low effective compression ratio (CR=15.1) with respect traditional diesel engines, thus providing an environment suitable for low-temperature chemistry. The authors have investigated experimentally different fueling configurations, including gasoline-diesel, gasoline-gasoline+DTBP (di-tert butyl peroxide cetane number improver), as well as ethanol (E85)-diesel.

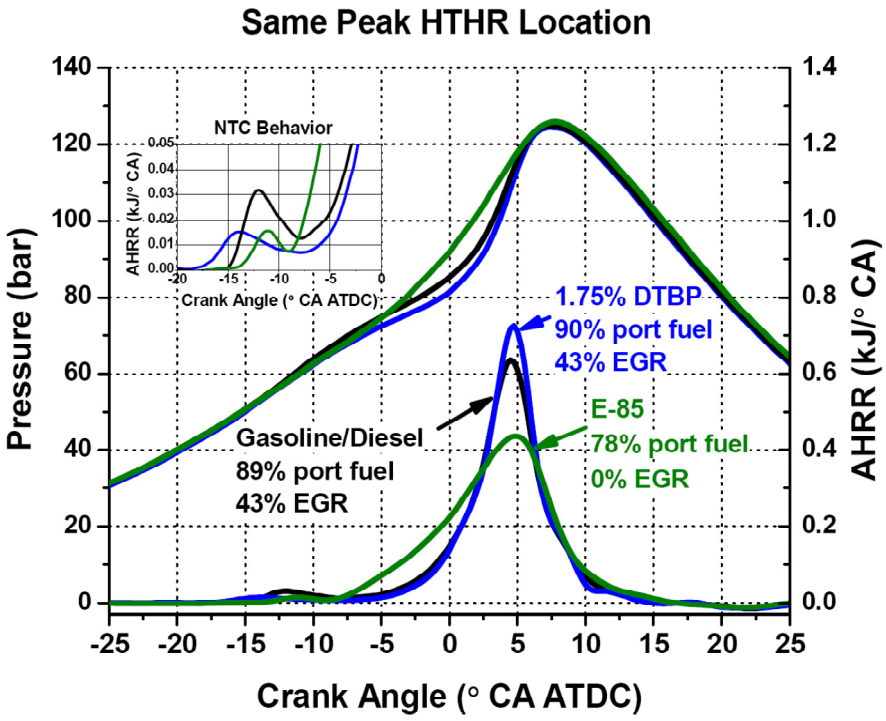

Fig. 2.32. Effect of different dual-fuel strategies (reproduced from ref [66])

The experimental results shown in Fig. 2.32 indicate a high degree of efficacy of ethanol-diesel dual-fuel configuration to extend the duration of the combustion process and limit the maximum rate of pressure rise. The ethanol-diesel configuration obtained a lower peak of rate of heat release although it operates without EGR, while the other fueling strategies required EGR to operate below the maximum allowed rate of pressure rise of 10 bar/deg.

The authors attribute the observed effect to the OH radical scavenging by ethanol molecules, which was previously described by Hashimoto [36, 37]. Thus, ethanol chemical effects are found to be more effective in providing "reactivity

stratification" compared to mixing fuels with different ignition qualities where chemical interaction between fuels is not significant.

2.4 Conclusions

The internal combustion engine has seen over the past 150 years a steady string of improvements. The driving factors behind those improvements have changed over time, from increased power to increased power density, followed by the need for higher fuel efficiency when fuel supply experienced disruptions. Currently the fuel efficiency is one of the major research foci along with reduction in exhaust pollutants.

The pursuit of both targets, better fuel economy and lower emissions, has led to reduced combustion temperatures (Low Temperature Combustion) while maintaining higher compression ratios compared to the traditional spark-ignition engine.

One of the combustion modes that have been recently studied as a promising alternative to CI and SI combustion, the HCCI combustion mode, has faced significant challenges related to combustion phasing control as well as short combustion duration. While short combustion duration around TDC is ideal from a thermodynamic standpoint in order to maximize fuel energy conversion efficiency [18], in practical combustion systems the rate of pressure rise has to be maintained within acceptable limits due to potential hardware damage, accelerated wear and noise considerations.

During HCCI combustion, state parameters and species concentrations within the entire combustion chamber experience relatively small variation. Thus, the combustion event is characterized by a "volumetric" energy release, which causes rapid rates of pressure rise. Additionally, due to the non-linear behavior of chemical reactions involved in LTC, the resulting combustion system is highly sensitive to initial conditions, such as temperature and equivalence ratio. However, the process becomes insensitive to injection events, as the mixture is close to homogeneity at the time of ignition, resulting in a lack of direct combustion phasing trigger and difficult control.

In order to increase the duration of the premixed combustion event, a phase shift in the energy release at specific locations in the combustion chamber is desirable. This is the case for Partially Premixed Combustion (PPC) and Premixed-Charge Compression Ignition (PCCI), where lack of complete homogenization of the air-fuel mixture results in the stratification of fuel conversion reaction rates. Additional benefits can be extracted by combining equivalence ratio stratification with the in-cylinder mixing of fuels of different ignition qualities, as in the case of RCCI. This stratification allows higher engine loads to be achieved along with higher engine efficiency while maintaining emissions, especially oxides of nitrogen, below the allowable limits.

A number of combustion additives capable of changing the autoignition characteristics of typical hydrocarbon based fuels have been reported in literature and reviewed in this publication. While the list of species is not meant to be

comprehensive with regards to possible combustion additive candidates, ethanol showed the best compromise between effectiveness of chemical kinetic control of combustion, supply availability and environmental impact. Additionally, ethanol is a renewable fuel, which made it an attractive option for use in SI engines.

Chapter 3. "Experimental Facility"

Experimental work reported in this work has been conducted in an optically accessible research engine facility at Wayne State University's Center for Automotive Research (CAR). The Low Temperature Research Center is a relatively new facility (commissioning completed in 2006) and the author had the opportunity to be involved in all development stages of the optical engine laboratory.

A general layout of the test-cell and investigation equipment is shown in Fig. 3.1 below.

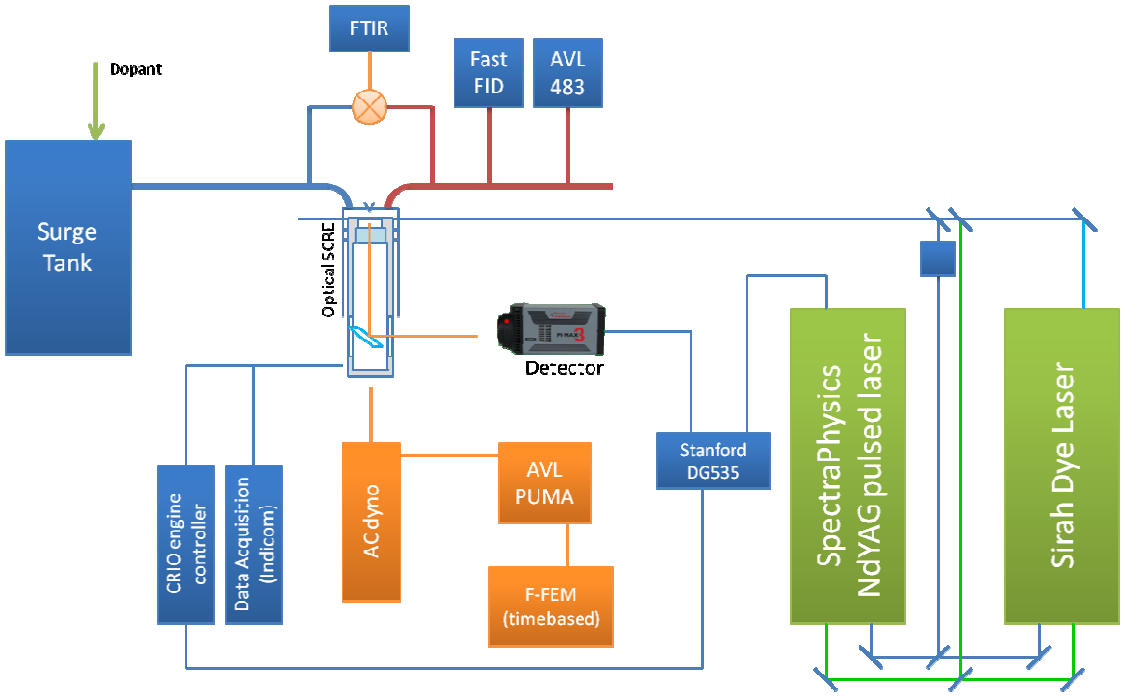

Fig. 3.1. Experimental Setup (concept diagram)

3.1 Engine Systems

3.1.1 Optically Accessible Engine

The engine, an AVL5402 Single Cylinder Research Engine (SCRE), has been provided with optical windows in order to allow the observation of the combustion process. A cross-section through this engine is shown in the figure below.

Table 2. Experimental Engine Characteristics

Optically accessible engine	AVL SCRE5402
Bore x Stroke	85 x 90 mm
Swept Volume	510 cm^3
Compression Ratio	15:1
Engine Speed	Variable (1200 rpm for laser diagnostics)
Injection System	Common Rail CP1
Injection Pressure	Variable (1350 bar max)
Injector Number of Holes, Type, Hole Diameter	5 holes, VCO, 180μm dia
Hole Included Angle	142°

The engine specifications are provided in Table 2 above. As one may observe in Fig. 3.2, the combustion-chamber has a flat pancake design in order to provide non-distorted optical access to the combustion chamber.

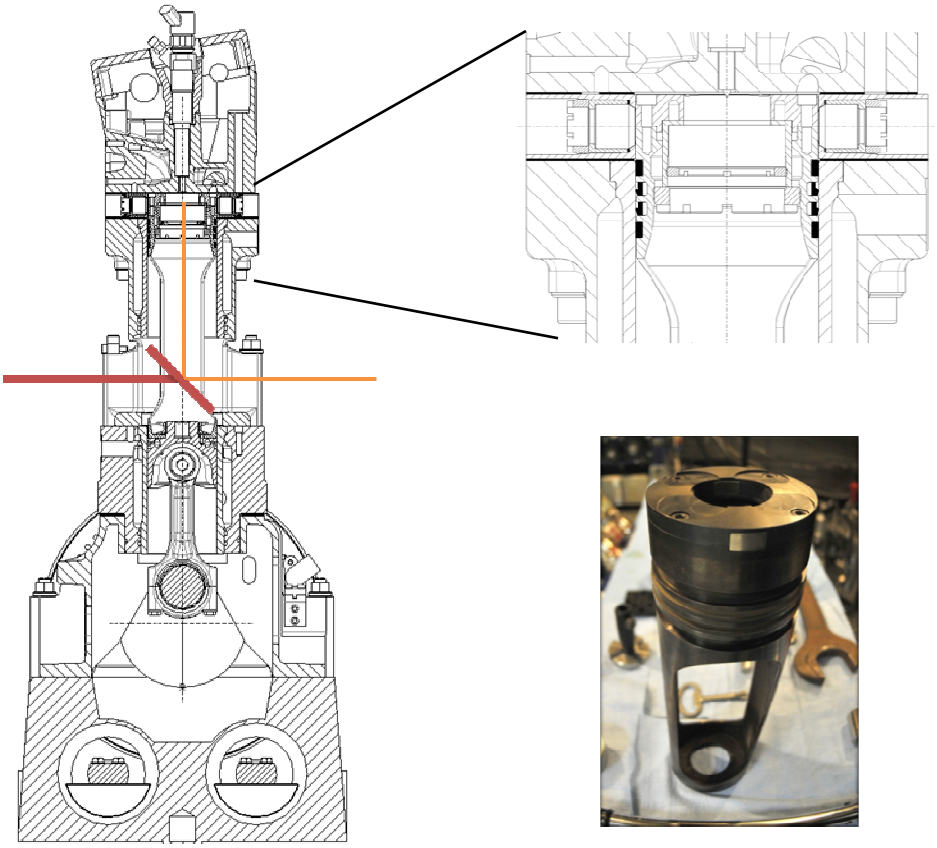

Fig. 3.2. AVL SCRE5402 Optically accessible engine cross-section

Depending upon the conditions investigated, the main window which provides a bottom-up view of the combustion chamber, manufactured either using fused silica or sapphire may be employed. A comparison between typical fused silica and sapphire spectral transmissivities is shown in the figure below.

A comparison regarding optical and mechanical properties of sapphire and fused silica is provided in Table 3. Sapphire, whose hardness is only second to diamond, represents an excellent choice for optical window material in high-pressure and high-temperature applications, such as the internal combustion engine. However, it has a significantly lower transmissivity within the range of

interest (UV-Vis spectrum – see Fig. 3.3) than fused silica, which results in increased signal attenuation.

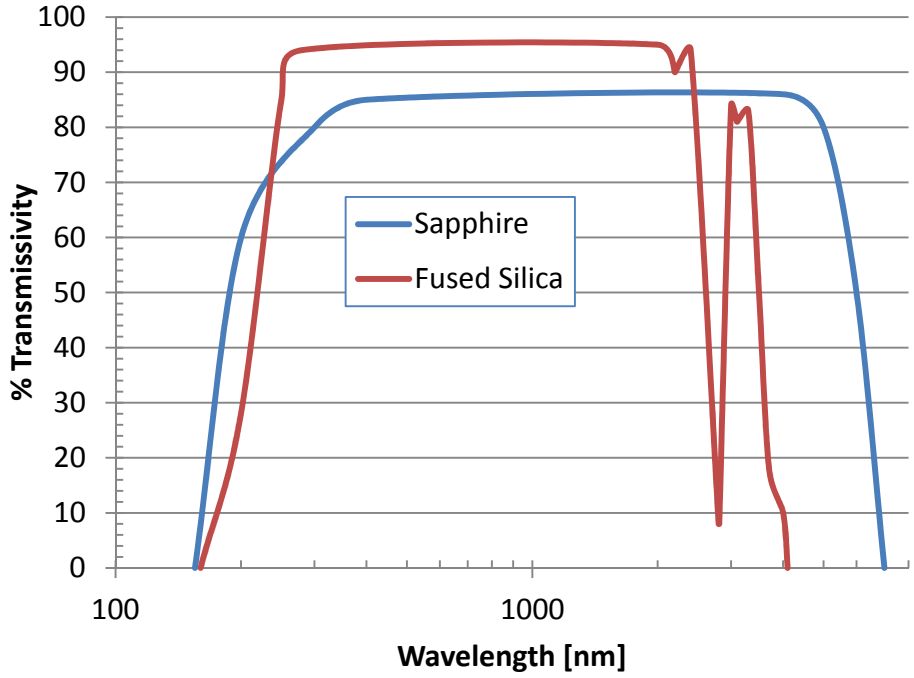

Fig. 3.3. Spectral transmissivity for fused silica and sapphire

Table 3. Optical properties of fused silica and sapphire [84]

Property	**Fused Silica**	**Sapphire**
Chemical Formula		Al_2O_3
Index of refraction @400nm	1.469	1.785
Density @293K [kg/m^3]	2.19	3.98
Thermal Conductivity @300K [W/m.K]	1.4	35.1 ∥ 33.0 ⊥
Thermal Expansion @ 293K [1/K]	0.5e-06	5.6e-06 ∥ 5.0e-06 ⊥
Specific Heat @298K [J/kg.K]	750	753
Mohs Hardness	7 (ref [85])	9
Young's modulus of elasticity E [GPa]	72	335
Poisson's Ratio	0.17	0.25

In order to avoid mounting-related stresses that could potentially damage windows during engine maintenance, optical windows are enclosed in stainless steel cases; the mounting procedure is called “stress-free” mounting and has been observed to successfully eliminate almost completely window failures related to the installation of the window.

Unobstructed optical access for piston positions near TDC is required in order to investigate the auto-ignition characteristics of most combustion modes. Thus, the engine has been provided with optical windows mounted in the piston crown. This method allows maintaining the combustion chamber geometry as close as possible to engines used in commercial applications and minimum interference with fluid flow and combustion. For this purpose, a modified adapter plate has been designed to allow optical access for piston positions in the vicinity of TDC as well as allow the delivery of the laser sheet required for Planar Laser Induced Fluorescence (PLIF) in close proximity to the fire deck. The adapter plate, shown in Fig. 3.4, connects the cylinder head to the extended crankcase and provides the required optical access.

In this design, the optical window, which is manufactured using fused silica, is enclosed in a steel enclosure in order to prevent window damage due to mounting-induced stresses. Also, only one of the two available optical axes for this engine has been provided with this type of optical access. Along the optical axis aligned with the engine crankshaft, due to space constraints, a cylindrical optical access has been employed.

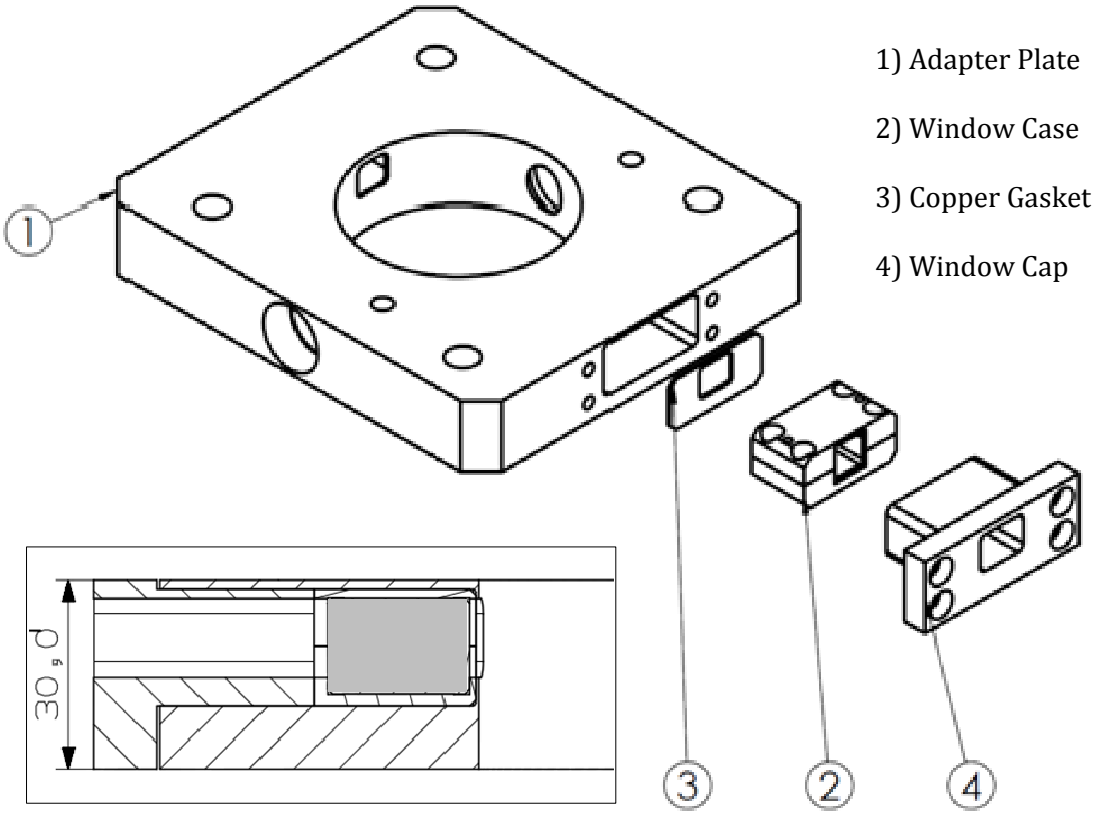

Fig. 3.4. Adapter plate design for PLIF experiments.

3.1.2 Cold Chamber and Camera Support

The test-cell used in the experimental work is intended for studies of the low environmental temperature behavior of engine systems, focused towards the issue of cold-startability of military diesel engines. Thus the facility (Fig. 3.5) includes also an environmental chamber which completely surrounds the single-cylinder engine.

Fig. 3.5. Optically accessible engine enclosed in the environmental chamber

In order to protect camera equipment and other electronics from the low environmental temperatures associated with the engine cold-starting, they are installed and operated outside the cold-chamber. The optical access is provided through a six inch diameter quartz window.

During engine operation, as the engine stand is completely supported by the environmental chamber structure, a significant amount of low-frequency, high amplitude vibrations are transmitted to the walls of the environmental chamber. Thus, in order to reduce the impact of these vibrations on optical measurements, a camera support has been built. This support, which is shown in Fig. 3.6. features an 18”x30” aluminum breadboard meant for optical applications which may accept a large variety of camera and optical equipment configurations. The breadboard is

attached to a set of translational stages which offer full control over the X, Y and Z translations. The system has a total travel distance of 6" for the Z direction, 24" for the Y direction and 6" for the X direction. As the translational stages selected are machine-tool grade, sub-pixel positioning accuracy is possible.

Fig. 3.6. Camera support

Additionally, due to lack of space around the single-cylinder engine as well as interest in the ease of access to the engine for window-cleaning procedures, the entire camera support has been mounted on Bosch-Rexroth linear bearings which allow the support to slide out and then back into position as required by the window cleaning operation with highly repeatable positioning.

3.1.3 Dynamometer

The experimental setup is equipped with an AMK AC dynamometer model number DW13-170-4-A0W capable of delivering up to 38kW output or absorbed power and a maximum torque of 120Nm at a nominal speed of 3000 rpm. The electric motor is rated for a maximum speed of 9000 rpm, while the single-cylinder engine is limited to a maximum speed of 3000 rpm in its optical-diagnostics configuration.

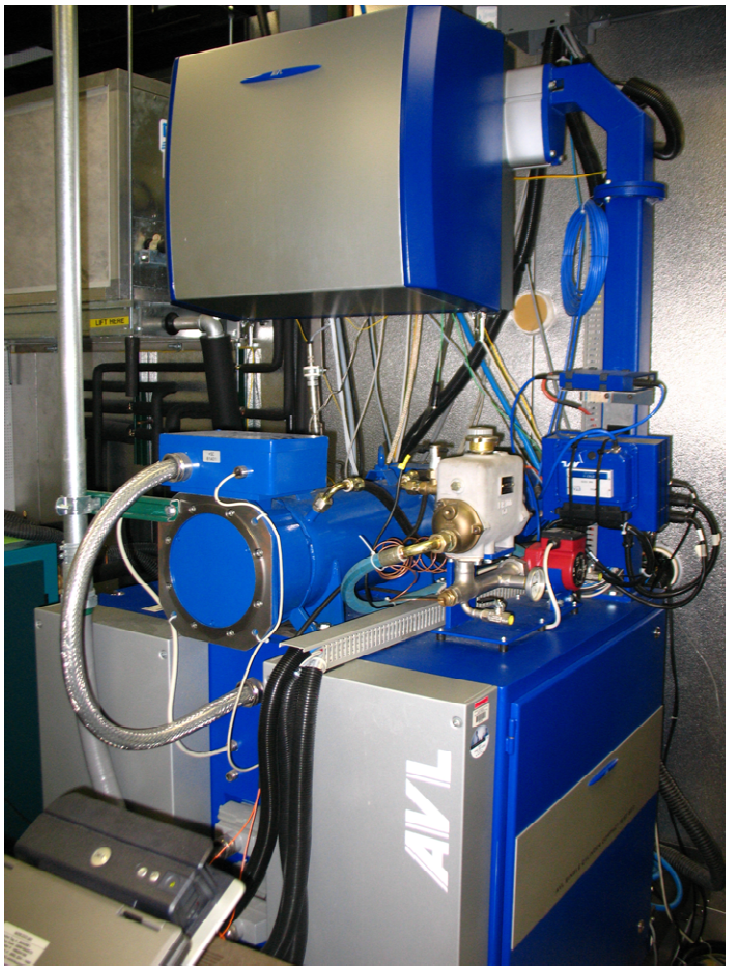

Fig. 3.7. Engine dynamometer assembly

3.1.4 Crank-Angle Encoder

An AVL 365 optical crank-angle encoder has been used for this research. It has an optical resolution of 0.5 CAD (720 pulses/rotation) and is multiplied by a pulse multiplier to achieve a 0.1 CAD resolution assuming both rising and falling signal edges as triggers (~1800 pulses/rotation with 3600 edges/rotation). The crank angle encoder is mounted on the crank-shaft of the single-cylinder engine; thus, the crank angle encoder does not provide information regarding the "firing" versus "exhaust" TDC associated with a four-stroke cycle. For this purpose, the data acquisition system makes use of the pressure signal obtained from the piezo-transducer, thus distinguishing through real-time post-processing (on an FPGA) between "firing" and "exhaust" TDC. Other equipment which makes use of the crank angle signal, such as NI-cRIO based engine and camera controller, are provided with a cam-shaft type TDC pulse.

3.1.5 Fuel Delivery System

The engine is equipped with a prototype (non-production) common-rail injection system. The injection pump is a Bosch generation CP1 capable of achieving up to 1350 bar injection pressure. The fuel is injected using a solenoid-driven injector. Two injector nozzle configurations have been available for experiments; both nozzles have a VCO configuration. Two variants of this nozzle reported in Table 2 have been used in this work. While they are characterized by identical specifications, one of the nozzles was provided with a 36° shift in hole positioning

This shift was necessary due to the requirements of the PLIF experiments, in order to avoid fuel impingement on the input side window mounted in the piston crown. The nozzle holes have an included angle of 142°.

3.1.6 Engine Electronic Control

Control over the injection process is obtained through an ETAS ETK7.1 controller and the associated software, INCA V5.1, along with a modified Bosch ECU designed for diesel applications. The engine control software provides adjustment of injection timing and duration as well as injection pressure. The TTL level pulse delivered by the Bosch ECU (modified using ETK7.1) for injection command is received by an AVL solenoid injector driver, which provides the appropriate pulse for the activation of the needle opening.

Fig. 3.8 Bosch ECU and ETAS VTK7.1 and AVL solenoid driver

However, in order to increase the flexibility of this setup in terms of triggered events, a National Instruments compact RIO (cRIO) real-time controller has been added to the experimental setup. This unit receives the logic-level pulses from the multiplication box of the optical crank-angle encoder and provides triggers under prescribed conditions for the various camera systems as well as laser equipment. Additionally, the TTL pulse controlling the fuel delivery from the injector previously generated by the Bosch ECU has been replaced with a similar pulse generated by cRIO. The control of the rail pressure is currently still maintained by the Bosch ECU.

3.1.7 Engine Balancing

Due to the increased weight of the elongated piston with respect to a classical engine design, the engine needs dynamic balancing. Thus, two additional shafts (Fig. 3.2) rotating at the same speed as the crankshaft are balancing the first order inertia forces and allow the engine to operate safely up to 3000 rpm.

3.1.8 Engine Cooling and Lubrication

The optically accessible research engine is not equipped with a crankshaft driven water or oil pump. Replacing them, an external conditioning unit (AVL 577) allows the circulation of the lubricant and coolant as well as heating/cooling of the respective circuits in order to maintain a specified temperature (60°C). The temperature is controlled using a PID controller built into the AVL Puma system.

For low-temperature testing a bypass system is available, where the AVL 577 unit is replaced by separate oil and coolant pumps. When this configuration is used,

no lubricant or coolant conditioning is provided and the experiment relies on the temperature controller of the environmental chamber to provide the appropriate temperature. This system has not been employed in this work.

3.1.9 Swirl Control

The engine has been provided with an adjustable swirl. This is achieved by throttling the direct intake port while allowing the air to flow freely through the helical intake port. By adjusting the position of the butterfly valve, different swirl levels may be achieved, ranging from 2.0 up to 4.5 swirl number. The calibration of the swirl valve is included in the figure below.

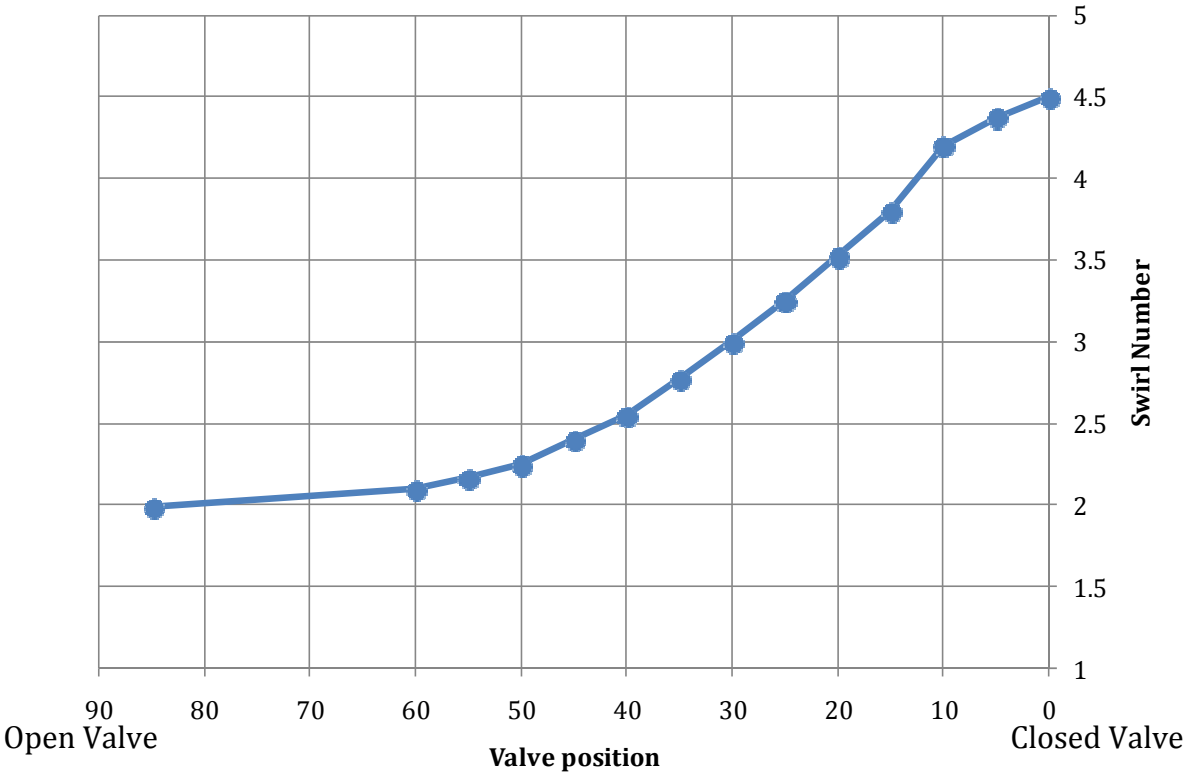

Fig. 3.9. Swirl valve calibration

3.2 Test-Cell Instrumentation

3.2.1 High-Speed Data Acquisition System (Indimeter)

An AVL Indimeter high-speed data acquisition system has been used to acquire cycle-resolved data related to parameters such as in-cylinder pressure, injector needle lift and common-rail pressure. The data acquisition system operates at a maximum frequency of 20 MHz and each data sampling is triggered by the multiplied crank-angle signal. Due to the way in which the signal is multiplied, the data acquisition is performed along both the rising and falling edge of the input crank-angle pulse. Data acquired by the Indimeter hardware is processed by the Indicom computer software which in turn stores the relevant data in a proprietary AVL IFILE format. For the post-processing procedure, a MATLAB script which makes use of the *catool* [86] utility has been developed which allows more flexibility in data analysis.

The Indimeter hardware is equipped with eight input channels and a total memory of 128 MB. For the settings used, typically about 1500 cycles are available to be recorded given the memory available.

3.2.2 Low-Speed Data Acquisition System (IFEM)

Additional slow-varying parameters, such as fluid temperatures, engine speed and others, are recorded by an AVL IFEM (Front End Module). The IFEM has a maximum frequency for data acquisition restricted at 100 Hz, with most measurements performed around 10 Hz to conserve storage. This type of

measurement is not crank-angle synchronized or triggered. For the purposes of synchronizing high-speed data with the data collected by IFEM or other time-based devices such as the FTIR, the test procedure includes when necessary a time-line maintained manually.

3.2.3 Pressure Transducer

The in-cylinder pressure was measured using piezo-resistive pressure transducer (AVL GH12D). The signal was conditioned by a charge amplifier (AVL 621). The pressure transducer was characterized by a calibration constant of 16.25 pC/V along with a data acquisition gain of 13.8942 bar/V.

In order to minimize signal interference due to pressure waves, the pressure transducer was mounted flush with the cylinder head in close proximity to the combustion bowl lip.

Due to the typical drift associated with the piezo crystal and amplification system, a pressure correction scheme was applied, where the absolute in-cylinder pressure was computed based on the relative pressure increase at two distinct times during the compression stroke of each cycle and an assumed value of the polytropic index of compression $n=1.37$.

3.2.4 Rail Pressure Measurement

For the experiments reported, the rail pressure has been measured at two distinct locations. The first pressure transducer, a production Bosch common-rail pressure sensor, is mounted on one end of the common-rail. It is an integral part of

the Bosch Engine Management System modified with ETAS VTK7.1. This sensor provides a common-rail pressure feedback for control purposes. In order to have an increased accuracy of the common-rail pressure measurement as well as cycle-resolved common-rail pressure data, a second pressure transducer has been mounted on the high-pressure fuel line connecting the rail to the injector. This pressure transducer is an AVL SL31D-2000 strain-gage type transducer and its signal is amplified by the AVL 621 strain gage/charge amplifier. The calibration settings for this pressure transducer were 275.95 bar/V and 0.453μV/V.bar.

3.2.5 Needle Lift Measurement

A proximity sensor (Micro-Epsilon ES04) connected with the EC6 cable has been mounted on the body of the fuel injector in order to obtain data regarding instantaneous needle position throughout the injection event. The signal is conditioned by an amplifier (MicroEpsilon eddyNCDT 3300). The sensor measures a displacement in the range 0 up to 0.4 mm and the amplifier provides a signal in the range 0 to 10V.

3.2.6 Exhaust Gas Analysis (FTIR)

Exhaust/Intake gas analysis has been performed using a Thermo-Nicolet Nexus 670 FTIR system connected to an MKS gas conditioning unit. The unit has a 2 Hz maximum sampling frequency (for transient emissions measurements) along with a 10 m absorption cell (gas cell). The gas was sampled from either the intake or the exhaust systems of the engine and routed through switch-box to the infrared

spectrometer. In order to prevent condensation of gaseous species, the lines connecting the engine to the spectrometer were heated to a temperature of 165°C. The total length of heated lines has been measured to be 10 m. Due to its infrared operating spectral range, this technique is limited to measuring concentrations for species which actively absorb infrared radiation, i.e. species that have a dipole moment and a change in bond stretching produces a change in dipole moment [87]. Thus, species such as N_2 and O_2 are "transparent" in the infrared spectral range. Additionally, for long-chained hydrocarbon species, species identification becomes difficult due to the complexity of the absorption spectrum as well as interference from other species, such as CO_2 and H_2O. Thus, the use of an infrared spectrometer will yield a relatively unreliable measurement of heavier hydrocarbon compounds which might be present in diesel engine exhaust. However, relatively small molecules, such as ethanol, are perfect candidates for FTIR quantitative measurements.

3.3 Optical Investigation Equipment

3.3.1 High-Speed Camera

Acquisition of cycle-resolved visible-range images was achieved using a high-speed CMOS camera (Phantom v7.3 from Vision Research Inc) with a 16GB memory and 14bit dynamic resolution for each color. The sensor has a maximum resolution of 800x600 pixels with a pixel size of 22 μm.

With speeds up to about 200,000 frames per second for a chip size of 32x32 pixels, this camera has been found to have the best sensitivity for combustion studies out of a number of tested high-speed cameras.

In a typical experiment, the camera is operated synchronously with the engine, where individual frames are triggered by the crank-angle pulse with a 0.5 CAD resolution. This is achieved by directly feeding the unmodified crank-angle signal to the FSYNC input of the camera. Additionally, in order to conserve memory as well as post-processing time, memory gating has been applied. A TTL pulse delivered by the cRIO controller, about 90CAD long and starting at the time of fuel delivery, specifies the window within the engine cycle when frames acquired are also stored in the memory of the camera. In the absence of this pulse, frames are continuously discarded, allowing only frames that contain relevant signal to be recorded.

Resolution	Frames/s
800 x 600	6,688
640 x 480	10,101
512 x 512	11,527
256 x 256	36,697
128 x 128	88,888
128 x 64	129,032
64 x 64	148,148
32 x 32	190,476

Fig. 3.10. Vision Research Phantom 7.3 High-Speed CMOS camera

In recently published work by Zha *et al.* [88, 89] related to this high-speed camera, the normalized spectral response of the camera has been measured and is shown below. The high-speed CMOS camera has been configured and calibrated for two-color soot pyrometry measurements.

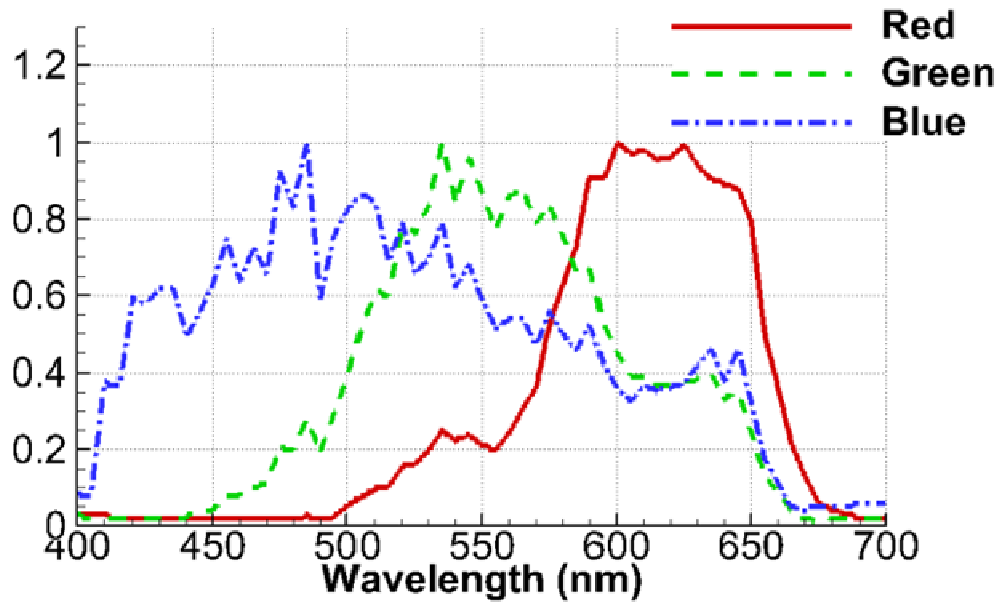

Fig. 3.11. Phantom V7.3 optical response as reported by Zha et al. [88, 89]

3.3.2 Intensified Monochromatic Cameras

Light emission from early stages of autoignition as well as fluorescence signals from PLIF experiments are characterized by low amounts of radiation yield. Additionally, due to experiment requirements, restricted spectral ranges are required (through the use of band-pass filters or combinations of low-pass/high-pass filters). The low-intensity light was measured using two Intensified Charge-Coupled Device (ICCD) cameras manufactured by Princeton Instruments, a subsidiary of Roper Industries.

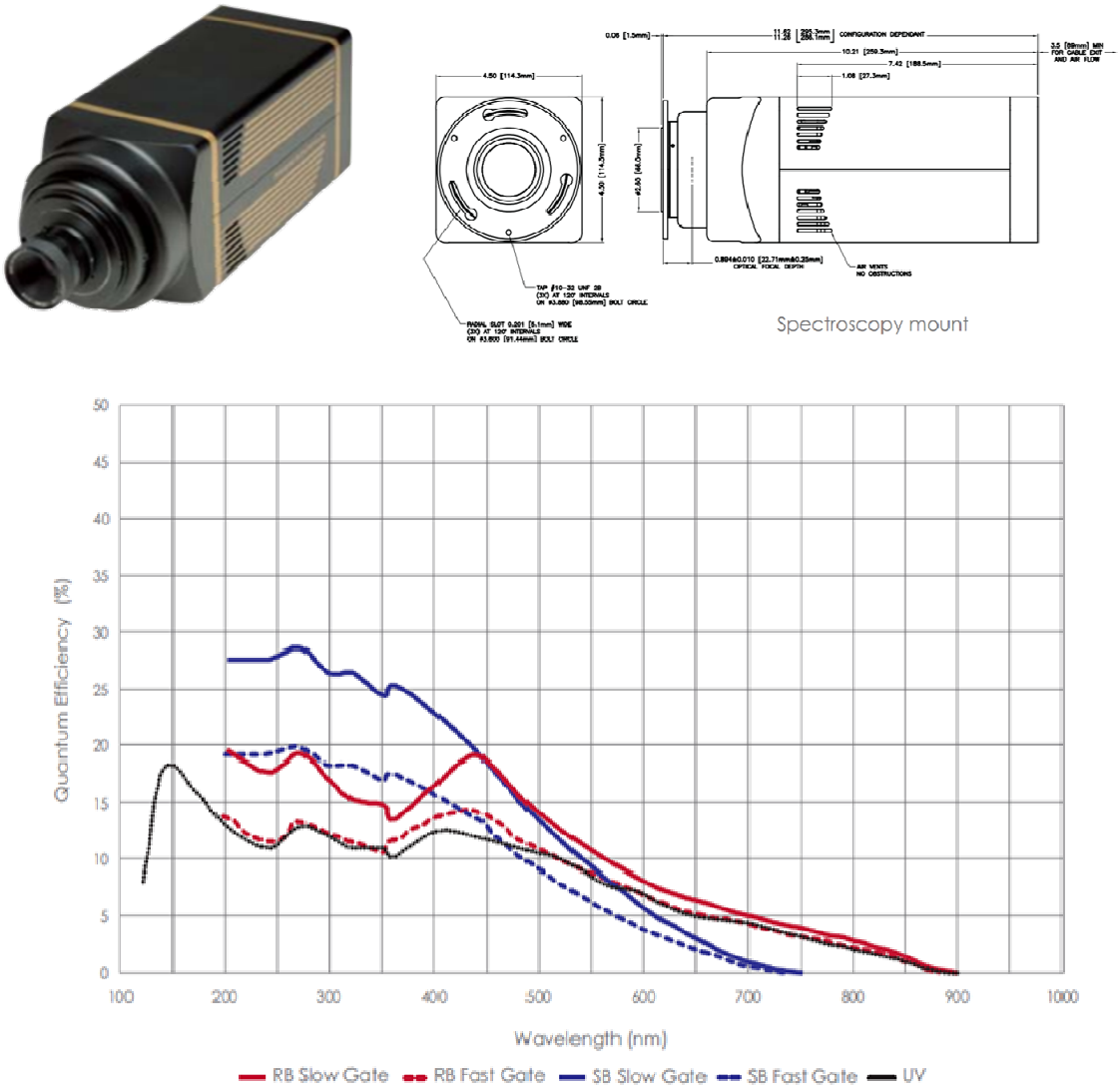

Fig. 3.12. PIMAX II 512x512 ICCD camera [90]

The first ICCD camera is a PIMAX II model, shown in Fig. 3.12 above, with a 2nd generation intensifier and 512x512 available imaging pixels. The pixel size is 19μm with 24μm pixel spacing. The camera used for the investigations reported has been equipped with the "UV" option shown above in the quantum efficiency plot.

During experiments, in order to compensate for chip noise due to factors such as dark current [91], a logical frame size of 540x540 has been selected,

allowing a 28 pixel wide band of readout to occur without actual physical pixels. This method allows for background compensation of camera-electronics related issues.

The camera is capable of acquiring images at a frequency of 17 Hz when operated at full chip size (without a region of interest defined or pixel binning). This speed is sufficient to capture one image every engine cycle when the engine is operated at 1200 rpm (10 Hz, the repetition frequency of the pulsed Nd:YAG laser).

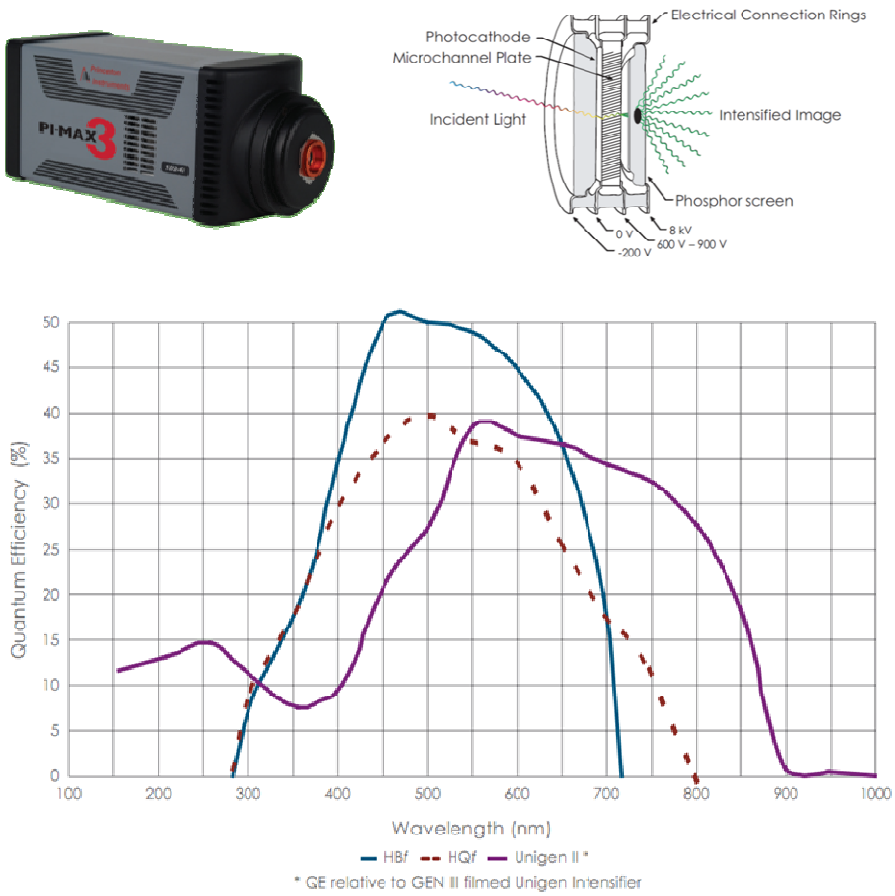

Fig. 3.13. PIMAX 3, intensifier concept [92] and quantum efficiency curves [93]

The second ICCD camera is a PIMAX 3 model with 1024x1024 imaging pixels and GenIII filmless intensifier coupled to the CCD chip using optic fibers. The pixel size is 12.8μm with 13.1μm pixel spacing. The rise time for the intensifier gate is about 2 nsec. The quantum efficiency for this camera is shown in Fig. 3.13 (Unigen II type).

Both cameras are equipped with UV lenses. The first lens is made by Electrophysiscs and has three elements. It has a fixed focal length of 78 mm and the minimum f/# is 3.8. The second lens, also produced by Electrophysiscs, has 105 mm focal length and the minimum f/# is 4.0.

In addition to two-dimensional imaging, both of these cameras can be used for spectroscopic measurements when combined with the diffraction monochromator described in the following section.

Depending upon experimental conditions, the cameras are triggered either by a TTL signal generated by cRIO (Section 3.1.6), or, in instances where the relative triggering of other equipment such as the Nd:YAG laser is important, the triggering is provided by a Stanford Research DG535 delay generator. The DG535 is capable to produce reliably trigger delays down to 5 picoseconds, but most delays that have been considered are in the order of magnitude of a few tens of nanoseconds.

3.3.3 Diffraction Spectroscopy

In order to perform UV-Vis spectroscopy, a PiActon SP2150i diffraction spectrometer has been used. It has a focal length of 150 mm, making it compact

enough to be suitable for engine diagnostics. The spectrometer has a Czerny-Turner design (Fig. 3.14) with a 300 groove/mm grating density.

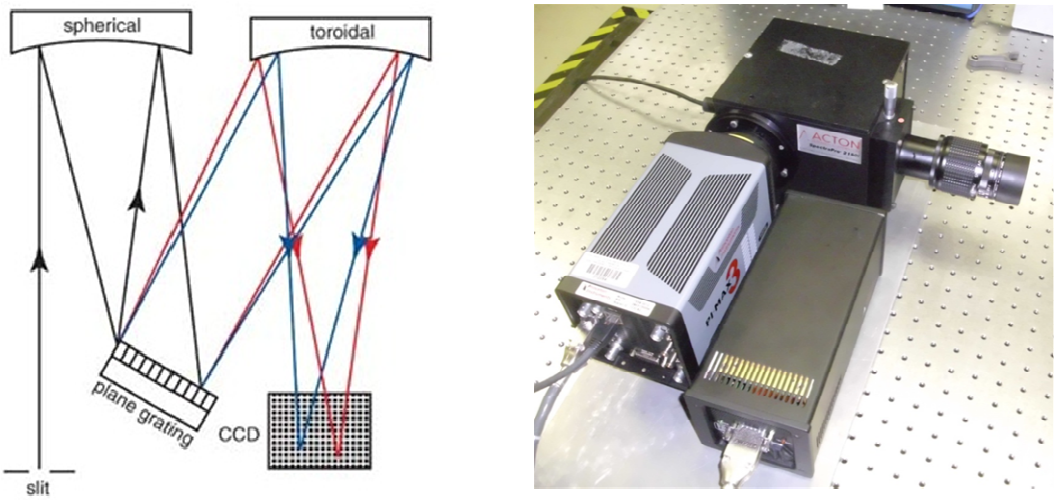

Fig. 3.14. Difraction spectrometer
From left to right: Czerny-Turner spectrometer [94]; Pimax 3 mounted on the PiActon SP2150i monochromator

The spectrometer grating turret accepts two gratings simultaneously. The first grating is characterized by a 300 nm blaze wavelength, while the second has a 500 nm blaze wavelength.

The spectrometer input slit has been set at 150 μm for all experiments reported. The Electrophysics UV lens (78 mm focal length) has been used for focusing the target image on the CCD chip while the spectrometer grating was set in the zero-order position (mirror mode).

The wavelength calibration was performed using a Roper Scientific MS-416 Mercury line light source. While the location of the spectral lines was used for wavelength calibration, the width of these lines helped in ensuring proper positioning of the imaging plane with respect to the spectrometer internal optics.

3.3.4 Nd:YAG Pulsed Laser

In order to conduct PLIF experiments, a high energy SpectraPhysics QuantaRay Pro 270 Q-switched pulsed Nd:YAG laser has been employed. The laser is characterized by a 10 Hz pulse frequency and an off the-shelf energy of 1750mJ/pulse (17.5W average power) at its fundamental wavelength, 1064nm. The fundamental beam is passed through two harmonic generators. In the first non-linear crystal, frequency summation of the same fundamental beam yields a frequency-doubled beam at 532nm. Subsequently, this frequency doubled beam is mixed again with the fundamental beam to yield the third harmonic at 355nm.

The output energy mentioned earlier is decreased in practice by the use of an injection seeder as well as the optimization of the harmonic generator for higher 532nm output. This Nd:YAG output is used to further pump the dye laser described in the next section. The third harmonic of the Nd:YAG laser is used for both mixing with the dye laser output wavelength in the dye laser harmonic generator as well as direct experiments in the optically accessible engine. This 355 nm laser wavelength has been used successfully in a number of previous studies [95, 96, 97] of formaldehyde evolution throughout the autoignition process.

One of the major difficulties associated with the experimental setup used in the current research is the relatively large distance between the actual experiment location in the combustion chamber and the optical table used for the Nd:YAG and dye lasers of approximately 8.5 m. This means that any small imperfection in the collimation of the beam is highly amplified by the time it reaches the combustion

chamber. When the laser is operated at full load, the Nd:YAG rod achieves thermal equilibrium and the Nd:YAG rod expands, focusing the laser beam. However, as the laser energy is reduced by decreasing the intensity of the flash-lamp pulse, the thermal equilibrium of the rod changes and the rod will stabilize at a different length compared to the condition used for beam focusing. This results in beam quality deterioration.

In order to avoid this issue, a laser energy adjustment setup has been used in order to properly control the output energy of the laser.

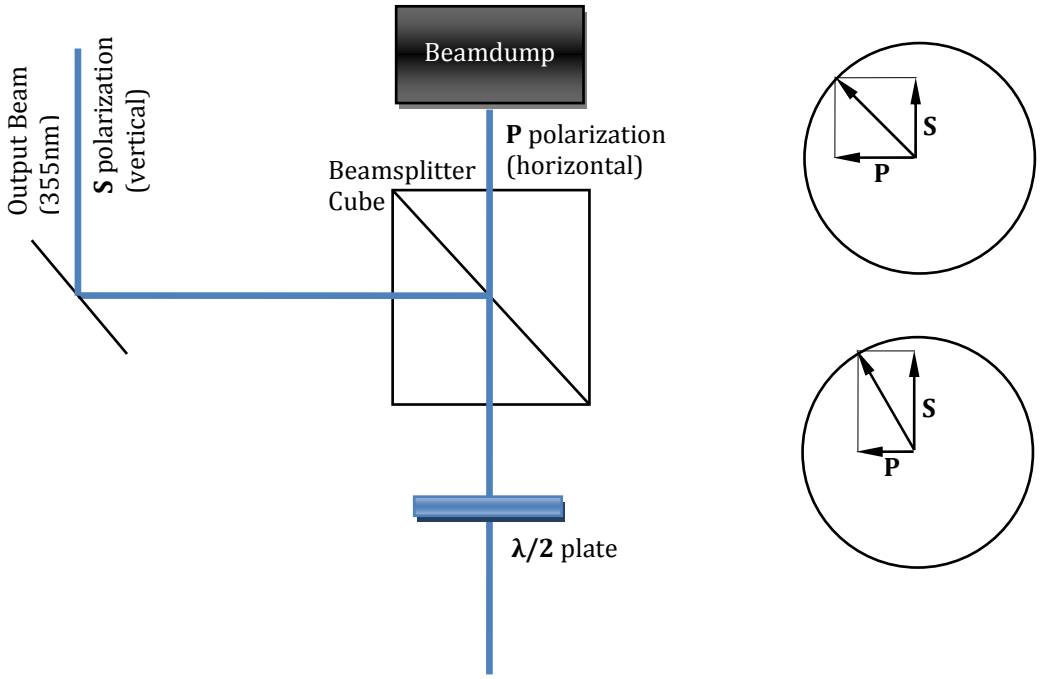

Fig. 3.15. Beam energy adjustment optical setup

The setup, shown in Fig. 3.15, allows output beam energy adjustment by rotating the half-wave plate. The rotation of the half-wave plate changes the polarization angle of the incoming laser beam (which may or may not be already

polarized), thus effectively changing the amount of energy available in the **S** and **P** polarizations respectively (in this case, in the vertical and horizontal polarization). In this setup, the **S** polarization is used for experimental determinations, while the **P** polarization is discarded in a beamdump.

Thus, the energy delivered to the experiment becomes independent of the actual laser output allowing the laser to operate at maximum energy output under all conditions. In order to set the appropriate laser energy, the S polarization component is monitored prior to collecting laser energy data through the Newport 842-PE powermeter connected to the 818P-030-18HP powermeter head. For lower energies a Newport 1918C powermeter along with a 818P-110-19 powermeter head are also available.

A relatively important amount of pulse-to-pulse energy variation occurs in Nd:YAG lasers due to a variety of factors, including the uniformity of the laser triggering frequency. In order to alleviate this issue, a high-speed integration circuit (Stanford Research SR250) was used along with a high-speed laser diode in order to measure the laser energy each pulse.

A layout of the experimental setup, including a dye laser (Sirah PRSC-LG-24) which was not used in the current research, is shown in Fig. 3.16.

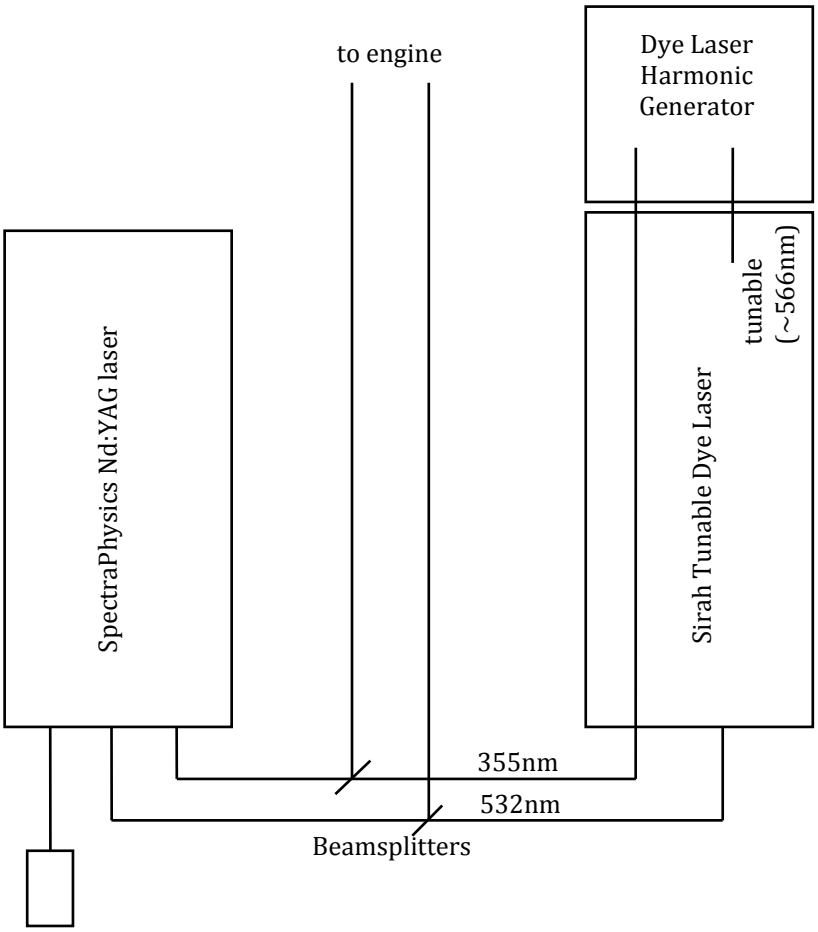

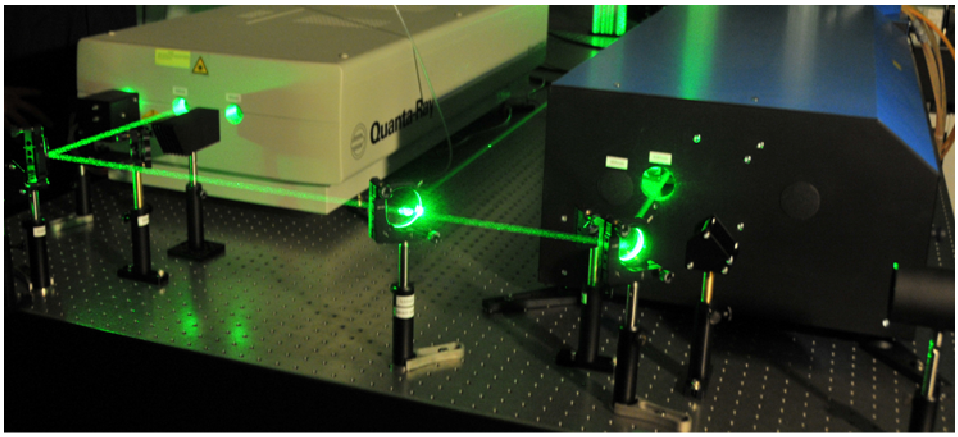

Fig. 3.16. Laser equipment layout (upper) and actual experimental setup (lower)

Chapter 4. "Numerical Modeling of Combustion"

4.1 Zero-Dimensional Modeling (CHEMKIN)

While the combustion phenomena taking place in partially premixed combustion modes are by no means homogenously reacting mixtures where the spatial variation of state parameters could be ignored, useful information can nevertheless be extracted from analysis of zero-dimensional reacting systems that could be directly applied toward improving the understanding the complexity of the process.

In this work, the CHEMKIN PRO chemical kinetic solver (Reaction Design Inc.) was employed for zero-dimensional calculations. A mechanism obtained by merging the Curran *et al.* n-heptane mechanism [13] and Marinov ethanol mechanism [98] was used to model the interaction between ethanol and n-heptane. This approach is similar to previous work performed by Hashimoto [36, 37]. The resulting mechanism has 563 species and 2652 reactions, compared to 561 and 2539 reactions available in the second version of the Curran n-heptane mechanism.

Special attention will be focused on the behavior of formaldehyde. This species has been identified in previous studies as playing a significant role throughout the low temperature decomposition of many hydrocarbons and is of particular interest for studying the combustion of multi-stage fuels such as n-heptane and diesel distillates. Formaldehyde is also fairly easily accessible using optical diagnostics such as PLIF, as it exhibits absorption lines aligned with the third harmonic of the Nd:YAG laser. While the formaldehyde absorption cross-section at

the 355 nm Nd:YAG output is fairly weak, the laser used in the current study provided sufficient energy to overcome this issue.

The figure below shows a comparison between the ignition delay data obtained using the Curran n-heptane mechanism, the Marinov ethanol mechanism and the merged mechanism for an initial pressure of 30bar and an equivalence ratio 0.7. The ignition delay data is reported by considering the location of highest OH mole fraction, which is in close proximity to the peak of LTHR.

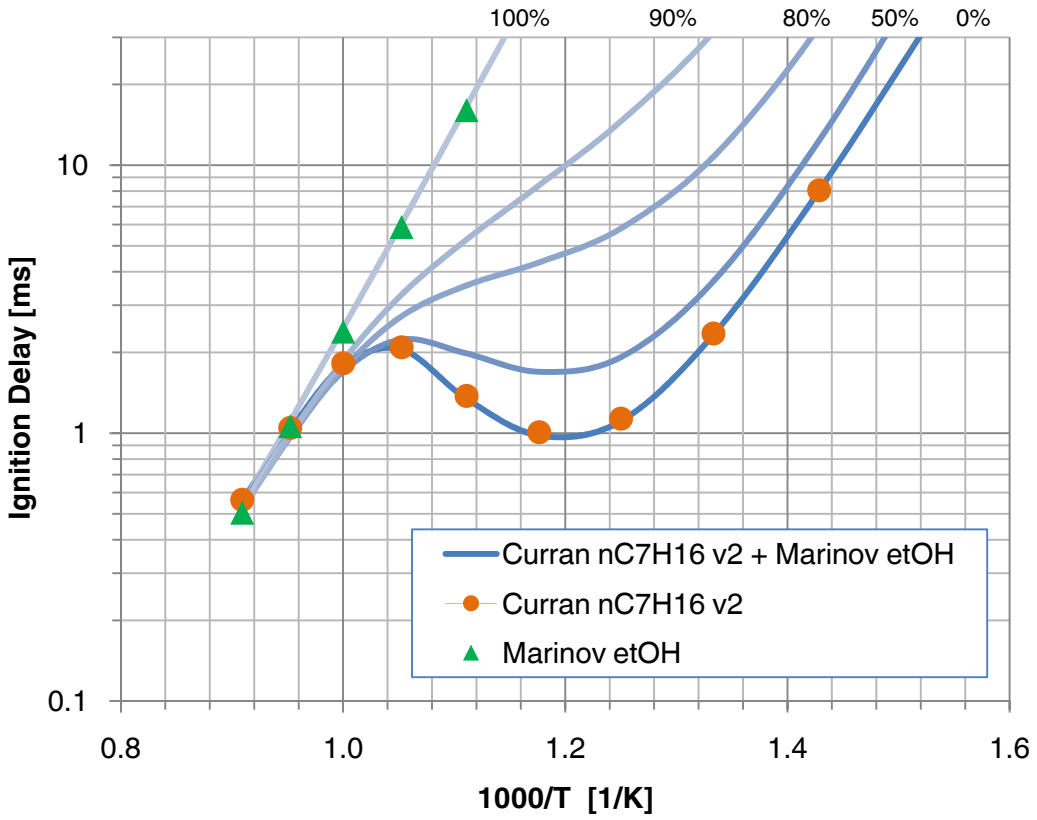

Fig. 4.1. Ignition delay data comparison for n-heptane/etOH merged mechanism with source mechanism

It may be observed that the merged mechanism exhibits excellent agreement with the original mechanisms for the two conditions under which those mechanisms have been validated, i.e. 0% etOH and 100% etOH.

The zero-dimensional model assumes a constant-volume reactor where mass conservation and energy conservation are considered. The simulation base point was assumed to be characterized by an initial temperature T_{ini}=800 K, initial pressure p_{ini}=30bar, and an equivalence ratio ϕ=0.7. The oxidizer was assumed to have a composition N_2-3.76:O_2-1. The results obtained from a series of zero-dimensional simulations are shown in the following paragraphs.

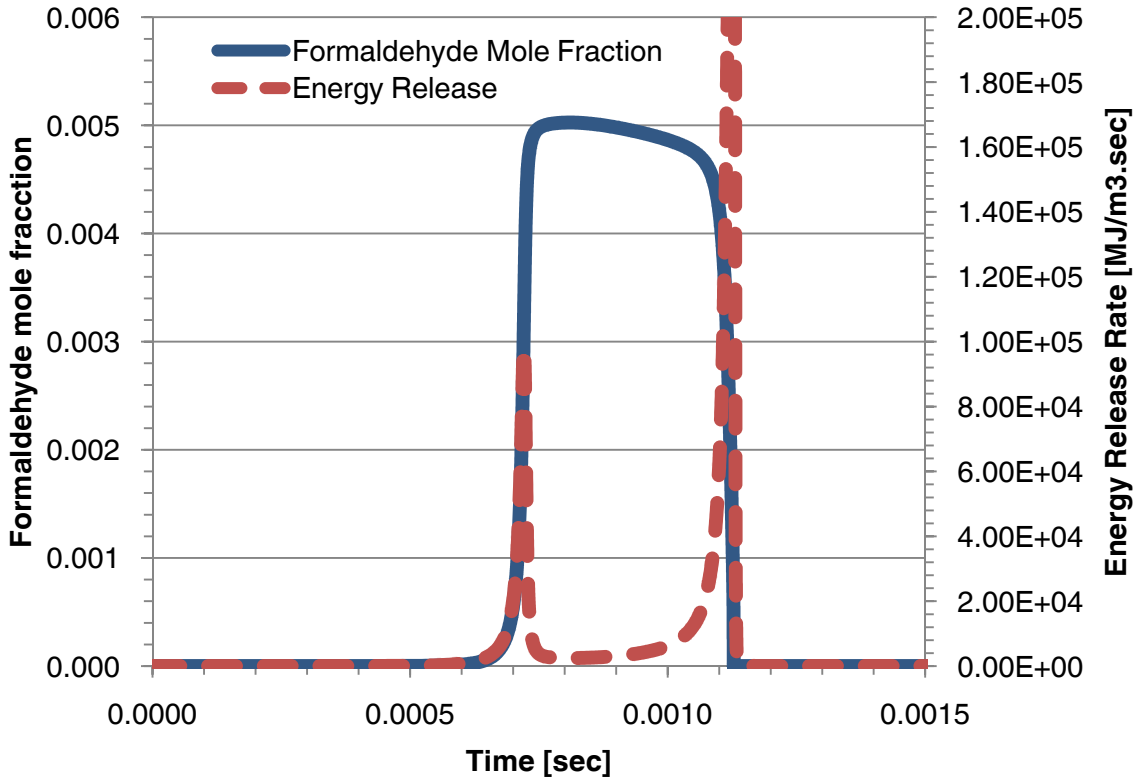

Fig. 4.2. Formaldehyde evolution (blue) and energy release rate (red, dashed) for the baseline condition (without ethanol addition)

The traces above show the typical behavior of a two-stage fuel such as n-heptane during an exclusively kinetically controlled combustion process. The LTHR and HTHR are evident and extremely sharp due to the lack of mixing-rate limited reaction rates. The HTHR is separated from the LTHR by a fairly long NTC region which is characteristic of two-stage combustion. As the LTHR process begins, formaldehyde is quickly formed only to remain relatively constant throughout the NTC region. These observations have been previously confirmed through optical measurements within an optically accessible HCCI engine [95].

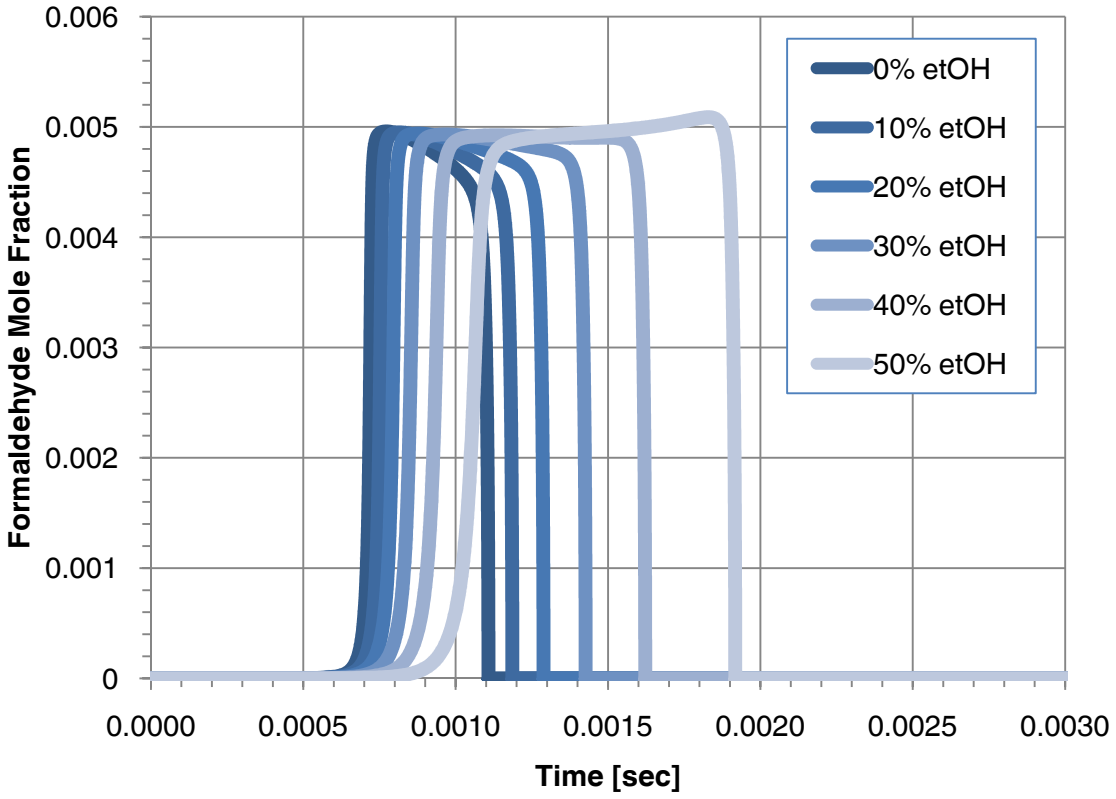

Fig. 4.3. Effect of ethanol on formaldehyde profiles

It can thus be noticed that formaldehyde is expected to be found in significant quantities within the combustion chamber only between the onset of

LTHR and the end of HTHR and this will be the region targeted experimentally by formaldehyde PLIF measurements reported in Chapter 5.

Based on the data presented in the figure above, an interesting phenomenon can be observed. Ethanol is observed to introduce a delay on the start of LTHR as well as an increase in the duration of NTC. This observation may be explained based on the sensitivity analysis performed by Hashimoto [37] pointing towards the OH scavenging as the main mechanism for inhibition of auto-ignition reactions. As the hydroxyl radical plays an important role during both branching reactions as well as propagation reactions associated with the cool-flame and NTC regions respectively, the OH scavenging by ethanol results in the delaying/lengthening of both processes.

However, ethanol has almost no impact on the amount of formaldehyde accumulation throughout the NTC region, suggesting that the formaldehyde mole fraction should be insensitive to ethanol percentage in the fuel mixture for a constant equivalence ratio. However, if one considers a theoretical case where ethanol fraction is stratified throughout the reactor while maintaining a constant equivalence ratio, a stratification of formaldehyde distribution is expected as well due to the phase-shift of the onset of oxidation reactions occurring in the combustion chamber. This phase shift should be introduced by the delaying effect of ethanol.

In the figure below, Fig. 4.4, the previous data is reported in a slightly different way. One may observe that the correlation of formaldehyde mole fraction with fuel decomposition is quite insensitive to ethanol addition. Although n-heptane

initial mole fraction changes as its fraction in the mixture changes, the peak of the cool-flame process occurs at a relatively constant n-heptane mole fraction, which is independent of the ethanol amount.

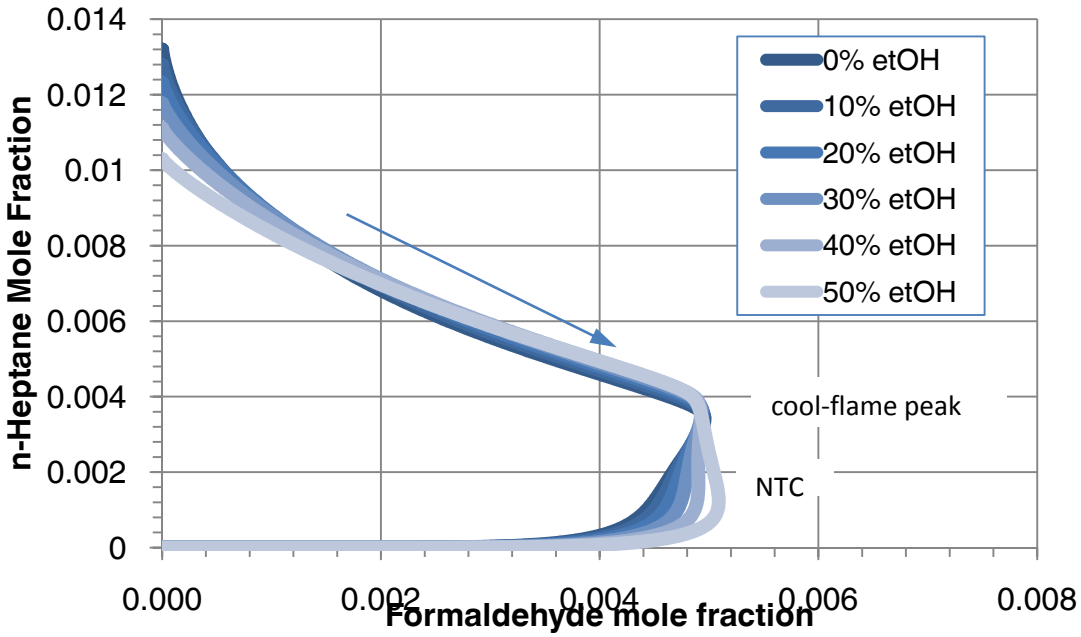

Fig. 4.4. Effect of ethanol fraction on n-heptane consumption and formaldehyde formation

The correlation between formaldehyde mole fraction and energy release associated with chemical reactions can be investigated as well and is shown in Fig. 4.5. Ethanol is observed to have little impact on formaldehyde formation. However, it significantly reduces the energy release. This could be attributed to the indirect effect of OH scavenging which impacts the reaction rates. Table 4 below shows the impact of ethanol on the ten highest energy releasing reactions throughout the cool-flame process for both the base condition as well as a 50% ethanol case. In these reactions hydroxyl, formaldehyde and oxygen seem to play significant roles. Ethanol is observed to have an uneven effect on energy release inhibition, with the hydroperoxyl termination reaction involving the hydroxyl radical seeing the most significant impact.

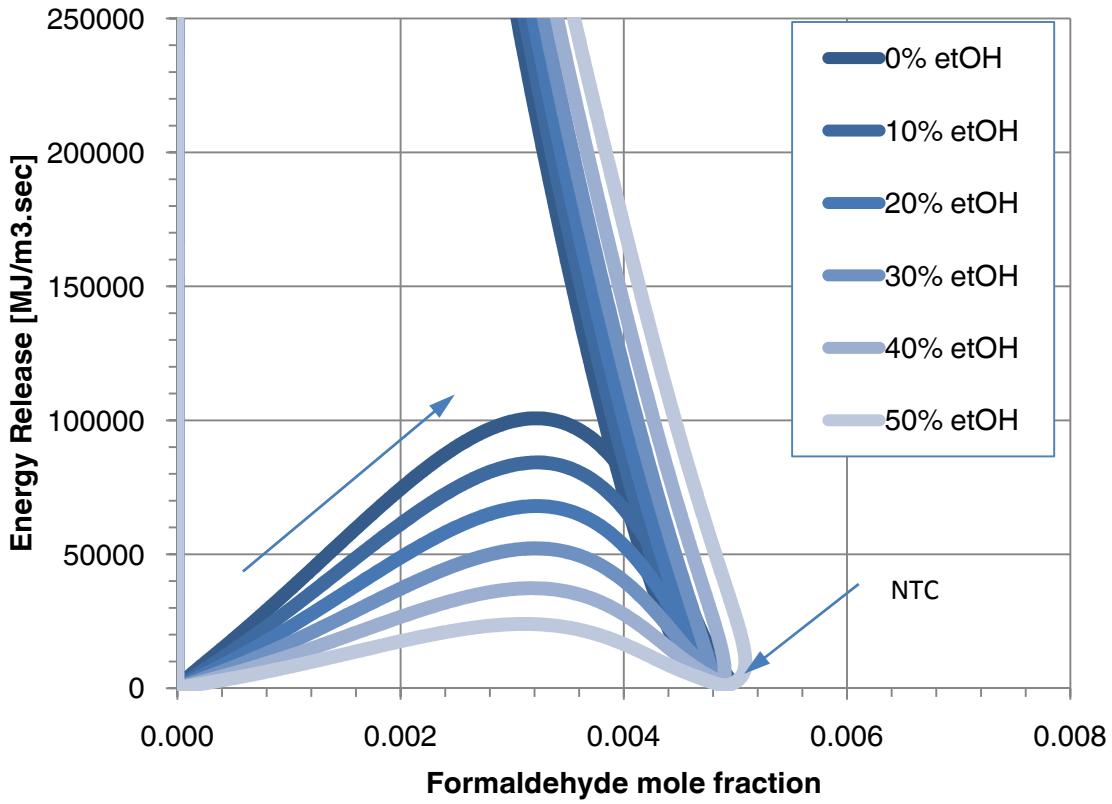

Fig. 4.5. Effect of ethanol fraction on energy release-formaldehyde mole fraction correlation

Table 4. Maximum cool-flame energy release for the top 10 reactions

Reaction				Maximum Cool-Flame energy release [MJ/m3.sec]				Percent Change
				0% etOH	#	50% etOH	#	
26	$H + O_2 (+M)$	↔	$HO_2 (+M)$	$1.432 \cdot 10^4$	1	$3.290 \cdot 10^3$	1	-77%
46	$HCO + O_2$	↔	$CO + HO_2$	$1.073 \cdot 10^4$	2	$2.352 \cdot 10^3$	2	-78%
32	$CH_2O + OH$	↔	$HCO + H_2O$	$7.275 \cdot 10^3$	3	$1.593 \cdot 10^3$	4	-78%
520	$CH_3O_2 + M$	↔	$CH_3 + O_2 + M$	$7.033 \cdot 10^3$	4	$1.916 \cdot 10^3$	3	-73%
49	$HO_2 + OH$	↔	$H_2O + O_2$	$7.012 \cdot 10^3$	5	$1.030 \cdot 10^3$	10	-85%
50	$H_2O_2 + O_2$	↔	$HO_2 + HO_2$	$5.857 \cdot 10^3$	6	$1.581 \cdot 10^3$	5	-73%
2252	$C_7H_{15}O_2$-3	↔	C_7H_{15}-3 + O_2	$5.166 \cdot 10^3$	7	$1.393 \cdot 10^3$	6	-73%
1401	$CH_2CHO + O_2$	↔	$CH_2O + CO + OH$	$5.040 \cdot 10^3$	8	$1.185 \cdot 10^3$	8	-76%
2251	$C_7H_{15}O_2$-2	↔	C_7H_{15}-2 + O_2	$4.943 \cdot 10^3$	9	$1.355 \cdot 10^3$	7	-73%
40	$CH_3O (+M)$	↔	$CH_2O + H (+M)$	$4.816 \cdot 10^3$	10	$1.141 \cdot 10^3$	9	-76%

Indeed, as shown in Fig. 4.6 below, the increase in ethanol fraction results in a decrease in hydroxyl radical mole fractions. While OH is already about four orders of magnitude above its equilibrium mole fraction, the actual value of the OH mole fraction doesn't seem to be correlated with its equilibrium value as the ethanol fraction is changed.

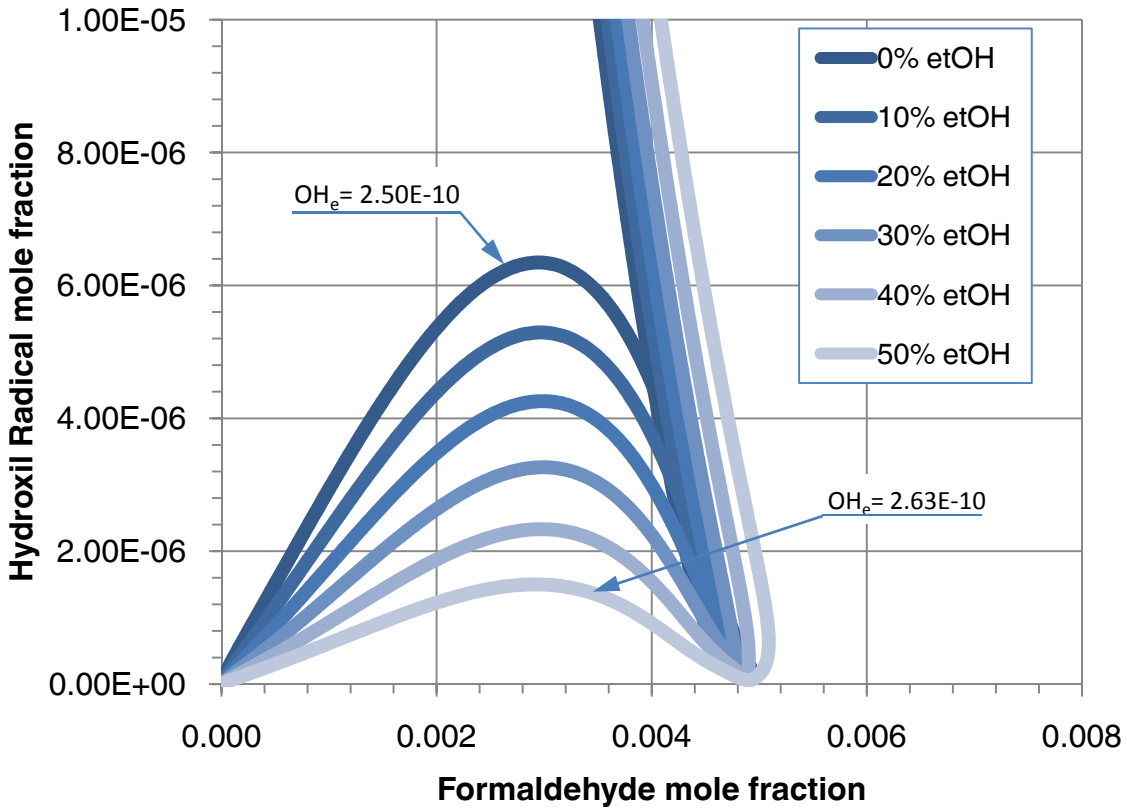

Fig. 4.6. Effect of ethanol on hydroxyl radical during the cool-flame stage

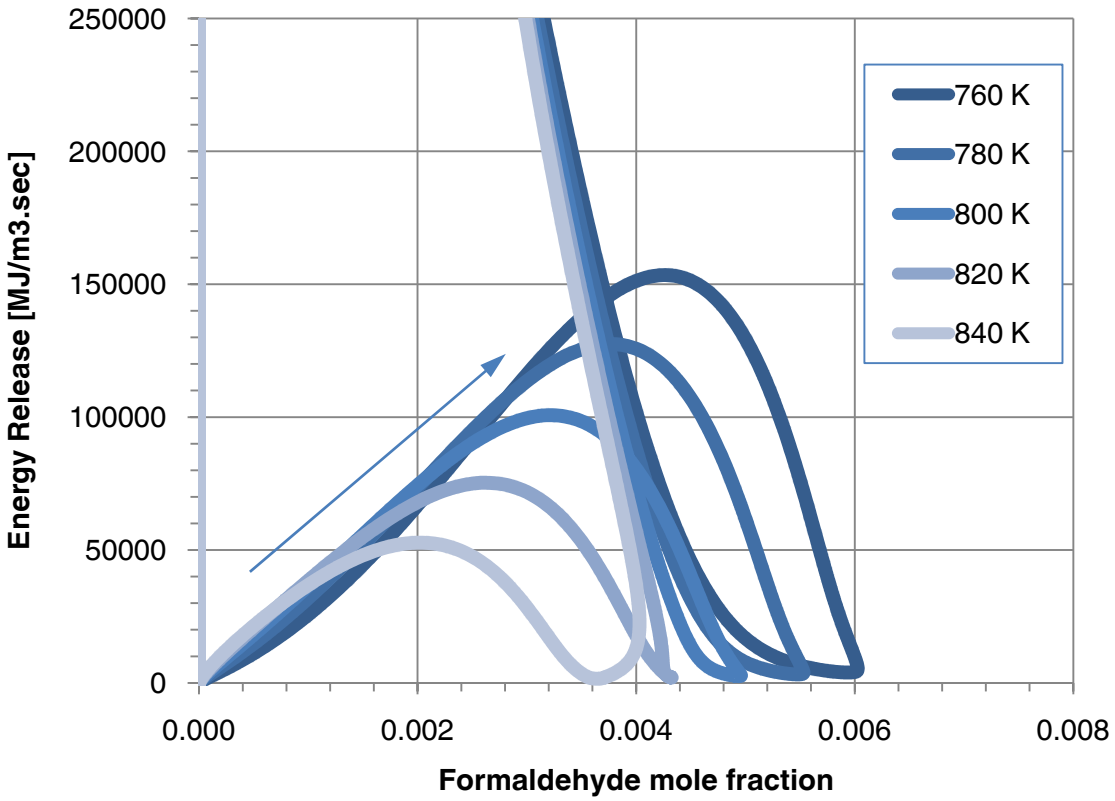

Fig. 4.7. Effect of initial temperature on energy release-formaldehyde mole fraction correlation

A similar analysis is shown in Fig. 4.7 above regarding the effect of varying temperature around the base condition considered, characterized by an initial temperature of 800 K. The LTHR strength is observed to increase with the decrease of temperature. Additionally, the amount of formaldehyde formed during the LTHR and persisting through the NTC region increases with the decrease in initial reactor temperature.

Further, when the effect of equivalence ratio is investigated as shown in Fig. 4.8, the peak amount of formaldehyde observed during the NTC stage is

proportional to the equivalence ratio as is the peak heat release during the cool-flame.

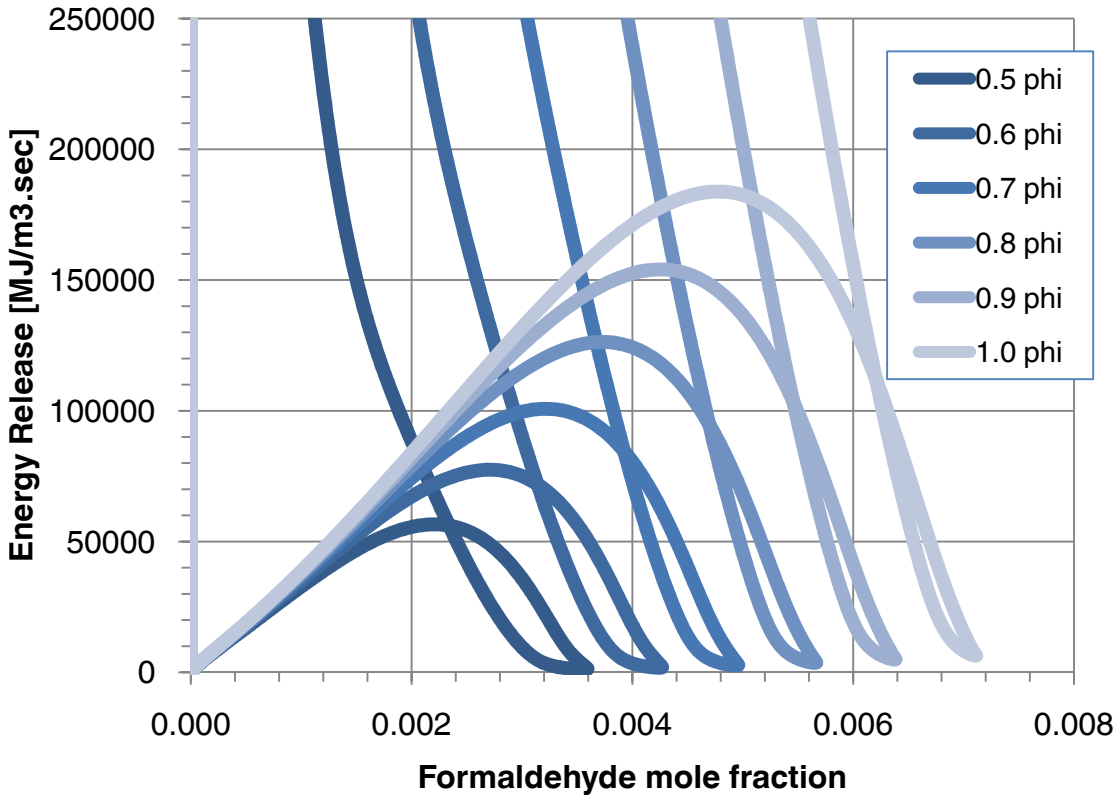

Fig. 4.8. Effect of equivalence ratio on energy release-formaldehyde mole fraction correlation

A conclusion prefacing later discussions regarding experimental results, is that ethanol does not have a direct impact on the amount of formaldehyde formed, although the magnitude of the rate of heat release is considerably affected by ethanol addition. Ethanol does however impact the formaldehyde formation and stratification through at least a couple of mechanisms. The first and most obvious one is the phase shift in the onset and evolution of fuel decomposition reactions which results in a phase shift in formaldehyde formation as well as energy release.

The second mechanism involves the impact of the ethanol delaying effect on mixture formation. As the ignition delay is increased by the presence of ethanol, the local conditions in terms of local equivalence ratio as well as temperature change, resulting in additional stratification of the combustion process. Formaldehyde is observed to increase with the increase of equivalence ratio as well as the decrease in local temperature.

4.2 N-Heptane Oxidation Mechanism Reduction

In order to better understand the impact of mixture heterogeneity on the dual-fuel combustion of ethanol and n-heptane, a 3D CFD analysis was considered, as it will be described in the following sections. However, performing a CFD simulation coupled with chemical kinetics relevant for this type of reacting system is computationally extremely expensive if the entire detailed 563 species, 2652 reactions mechanism is considered. Also, reduced mechanisms recently published by several authors targeted towards the oxidation of n-heptane do not contain sufficient detail regarding the interaction among n-heptane and ethanol to be applicable in this work. It was thus deemed necessary to follow the path of mechanism reduction up to the point where the mechanism has a sufficiently small size to be processed in a reasonable amount of time.

For this purpose, the Necessity Analysis [99] included in the commercially available chemical kinetic solver DARS [100] was used. Further information regarding the method of computing the importance coefficients for each individual species is given in references [99, 101]. This method is similar to other methods

such as DRG [102] and DRG-EP [103]. However, as implemented within the commercially available code, the necessity analysis does not check for interrupted reaction paths that could occur when species are removed from the reaction mechanism. It was thus necessary to verify that mass "sinks" are not formed within the reaction mechanism, where a certain species is provided with a formation path but there are no reactions specified for its consumption.

In the current work, the reference condition chosen was 800K initial temperature, 30bar initial temperature and reactions are taking place in a constant-volume reactor. This condition has been chosen as it is representative for the conditions experienced by the autoigniting mixture within the experimental combustion chamber and it is also close to the optimum reactor characteristics provided by Zeuch *et al.* [101]. The sensitivity analysis, an intermediate step of the necessity analysis, was performed for the hydroxyl radical.

The detailed mechanism containing 563 species and 2652 reactions was reduced to a semi-detailed 244 species, 1285 reactions mechanism. An additional set of reactions for formation and consumption of an electronically excited hydroxyl radical required for replicating OH chemiluminescence [104] for comparison with experimental data has been included as well and the semi-detailed mechanism data provided in Appendix 6.

A comparison between ignition delay data under the same assumptions as described in the previous section is presented in Fig. 4.9 below. A very good

agreement between detailed and semi-detailed mechanism was maintained for various ethanol mole fractions.

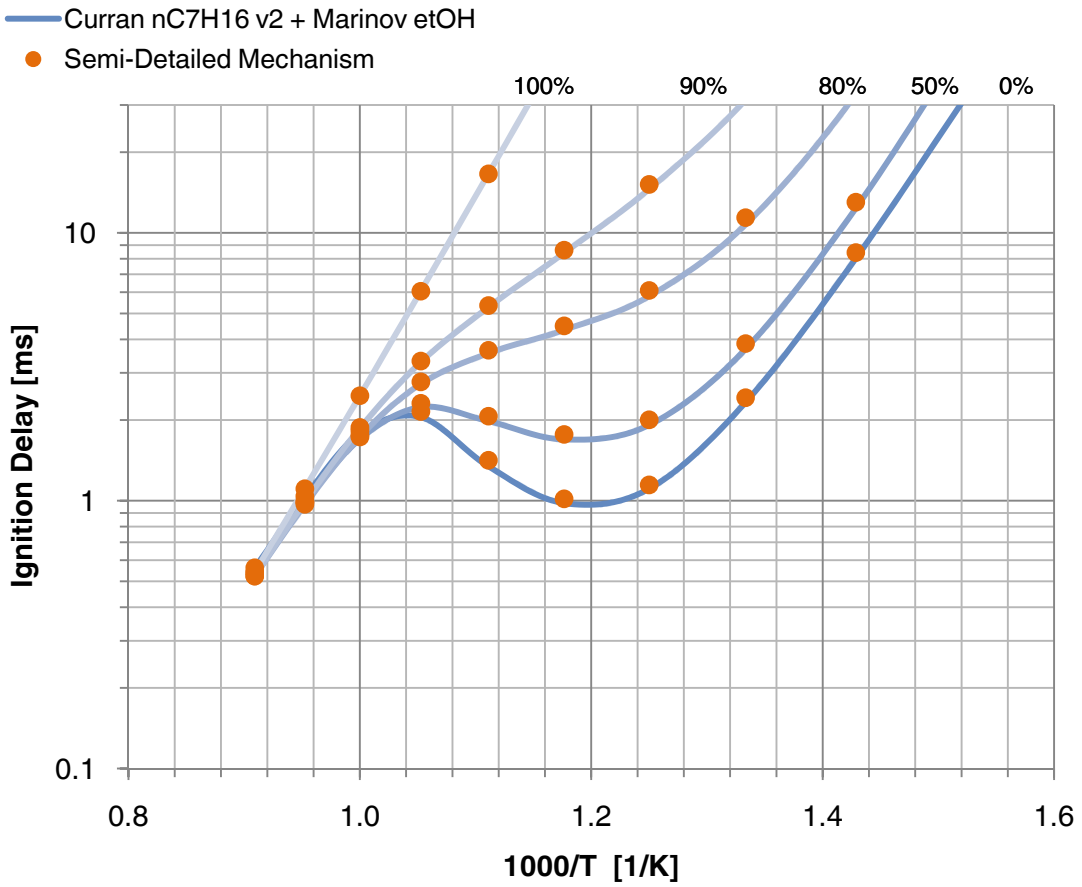

Fig. 4.9. Comparison of ignition delay data for detailed and semi-detailed mechanism. Φ=0.7, T_{ini}=800K, p_{ini}=30bar

4.3 3D CFD Chemical Kinetic Code KIVA4-WSU

For the work currently reported, the open-source FORTRAN based KIVA4 CFD solver was chosen [105, 106]. In order to improve KIVA4 chemical kinetic capabilities, subroutines were written providing KIVA4 with an interface to the chemical kinetic solver CANTERA [107]. The most relevant sections of code have been included in Appendix 2-5 for the reader's reference. Communication between

the CFD solver and the chemical kinetic solver is provided through the MPICH2 MPI implementation [108, 109], thus allowing the parallelization of the chemical kinetic solution. As the chemical kinetic solver is coded using C++, the appropriate compilers were used for the two sets of codes, i.e. Intel FORTRAN *ifort* compiler and GNU *gcc* compiler respectively. The resulting sections of binary code were linked using the Intel FORTRAN compiler. The modified code will be further referenced as KIVA4-WSU and a diagram showing the code structure associated with parallel processing is presented in the figure below.

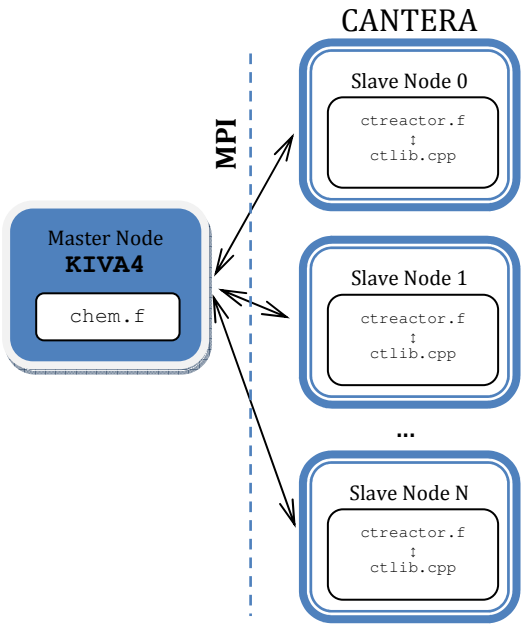

Fig. 4.10. KIVA4-WSU parallel operation diagram

The mass conservation equation solved by KIVA4 is given by:

$$\frac{\partial \rho_m}{\partial t} + \nabla \cdot (\rho_m \boldsymbol{u}) = \nabla \cdot \left[\rho D \nabla \left(\frac{\rho_m}{\rho}\right)\right] + \dot{\rho}_m^c + \dot{\rho}^s \, \delta_{m1}$$

Where $\rho_m$is the density of species m, $\boldsymbol{u}$ is the velocity vector associated with the current location, D is a single diffusion coefficient under the Fick's law

assumption, $\dot{\rho}^s$ is the spray source term which, due to the Dirac delta function δ_{m1}, applies only to the first specie, which is always assumed to be the fuel. In this work the chemical source term $\dot{\rho}_m^c$ for each individual species has been computed using CANTERA. Negative absolute concentrations were not allowed due to solver stability issues.

Further, the energy conservation equation is given by:

$$\frac{\partial(\rho I)}{\partial t} + \nabla \cdot (\rho \boldsymbol{u} I) = -p\nabla \cdot \boldsymbol{u} - \nabla \cdot \left[-K\nabla T - \rho D \sum_m h_m \nabla \left(\frac{\rho_m}{\rho} \right) \right] + \rho\varepsilon + \dot{Q}^c + \dot{Q}^s$$

where I is the specific internal energy, p is the pressure, K is the thermal conductivity term and h_m is the enthalpy associated with each species. Turbulence energy dissipation is taken into account through dissipation rate ε. The enthalpy of evaporation of the spray is considered through the source term $\dot{Q}^s$ while the chemical source term $\dot{Q}^c$ is computed within CANTERA.

As each cell is assumed to be a constant-volume chemical reactor during each timestep, the chemical energy source term will be given by the change in internal energy of the system as:

$$\dot{Q}^c = -\left(I_{P_T} - I_{R_T} \right)$$

where I_{P_T} and I_{R_T} are the internal energies of the system at the temperature associated with the reactants T for the products and reactants respectively.

In this work standard KIVA4 subroutines [110] have been considered, including the wall-film model proposed by O'Rourke [111], the Taylor Analogy Breakup (TAB) [112] model, the O'Rourke collision model and evaporation model

[113] and the Law-of-the-Wall. Fuel was introduced in the combustion chamber with an SMD of 180 μm, which is equal to the injector nozzle diameter.

Due to the relatively large size of the mechanism and considering also a sector mesh containing about 26,000 cells at BDC (shown in the figure below), the computations were run on a small-scale Linux-based cluster containing 72 Xeon cores 2 GHz or higher. This cluster was built and maintained as laboratory infrastructure by the author. An image of the cluster hardware is shown on the next page.

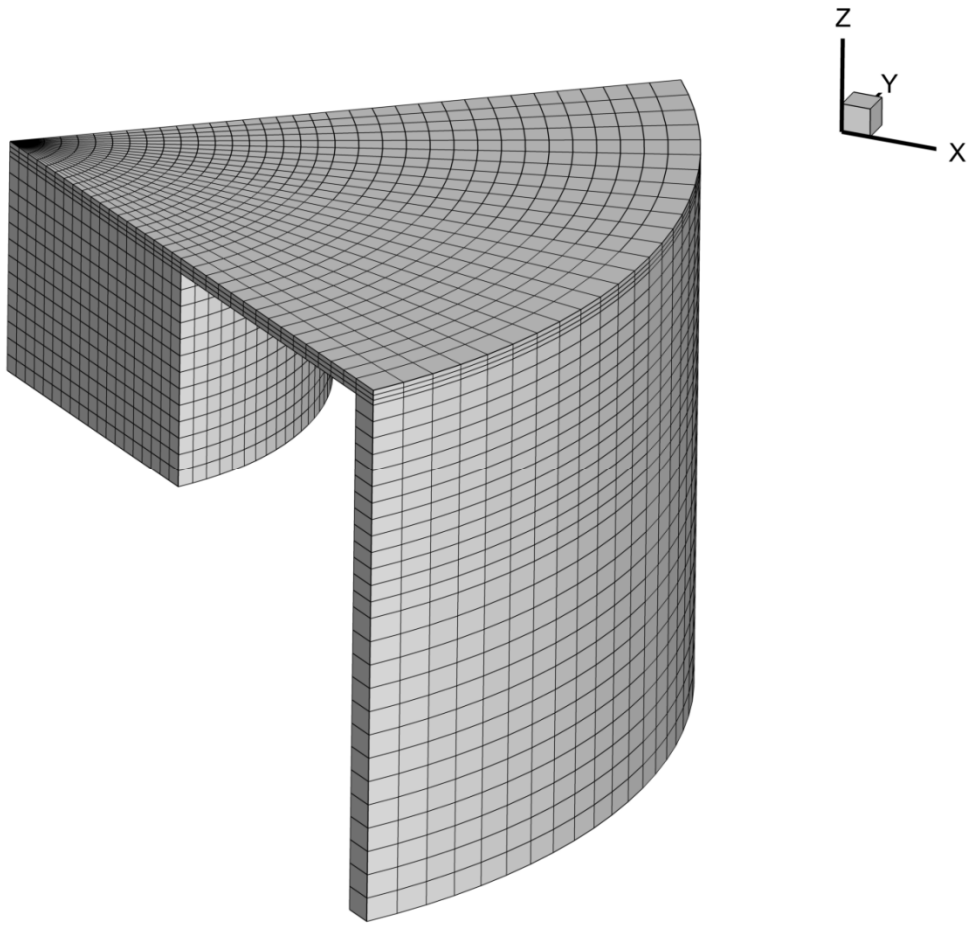

Fig. 4.11 Computational mesh

Fig. 4.12 Computing cluster

4.3.1 The C/O Equivalence Ratio

The C/O atom ratio, which was previously introduced in ref [46], attempts to provide equivalence ratio information throughout the combustion process, even

after the fuels have been decomposed and the traditional definition based on fuel-air ratios no longer holds. The C/O atom ratio is given by:

$$ {}^{C}/_{O}\ \text{atom ratio} = \frac{\sum_i n_i \cdot C_{n_i} H_m O_k}{\sum_i k_i \cdot C_n H_m O_{k_i}} $$

where $C_n H_m O_k$ represents the molar fraction of this specie.

Further, the C/O equivalence ratio is referenced to the stoichiometric C/O atom ratio of n-heptane and is defined as follows:

$$ \phi_{C/O} = {}^{C}/_{O}\ \text{equivalence ratio} = \frac{\left({}^{C}/_{O}\ \text{atom ratio}\right)_{\text{actual}}}{\left({}^{C}/_{O}\ \text{atom ratio}_{\text{Heptane}}\right)_{\text{stoichiometric}}} $$

The equivalence ratio and C/O equivalence ratio are numerically equal if the considered fuel is n-heptane. However, for a blend of fuels, the conversion is not straightforward especially if the fuel ratio is not known. Further details regarding the impact of molecular structure on the C/O ratio are provided in ref [46].

4.3.2 Local Ethanol Energy Fraction

The ethanol fraction (on an energy basis) is assumed to be given by:

$$ etOH_{fraction} = \frac{x_{etOH} \cdot LHV_{etOH}}{x_{etOH} \cdot LHV_{etOH} + x_{Heptane} \cdot LHV_{Heptane}} $$

where *x* represents the mass fraction of the specific fuel.

4.3.3 Measure of Reactivity Stratification

In order to estimate the amount of stratification associated with the reactivity of a heterogeneous mixture, concepts such as standard deviation and coefficient of variation could be employed. However, given the nature of the problem, characterized by unequal total energy release rate, another measure of heterogeneity of a probability density function will be employed. Work performed by sociologist Gini Corrado [114] at the beginning of the 20th century in the area of measures of statistical dispersion for various types of samples but with special interest in income inequality resulted in the development of the Gini index. The Gini index is based on the Lorenz curve [115], a widely used concept in economics and is shown in Fig. 4.13.

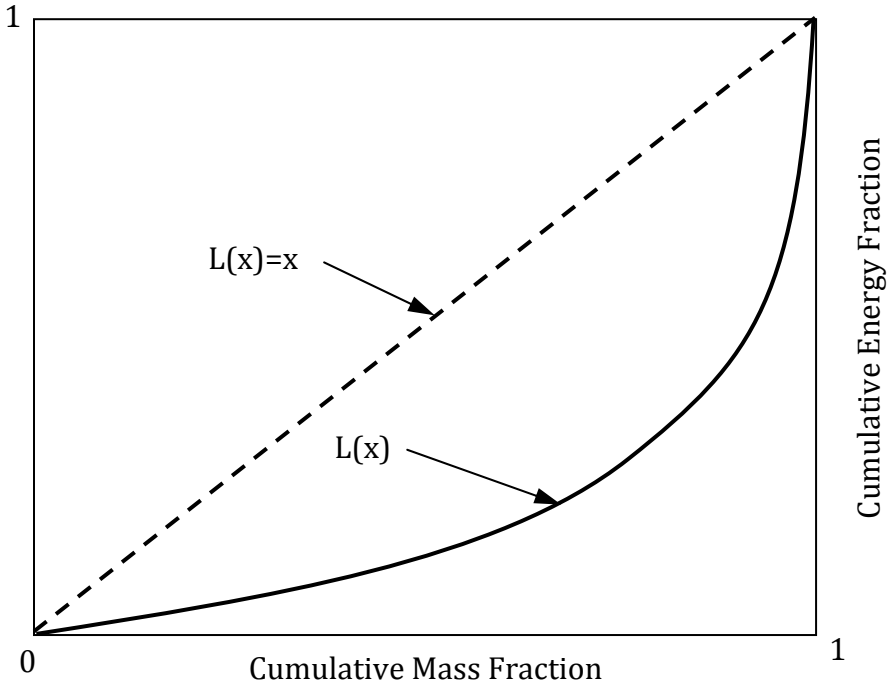

Fig. 4.13 The Lorenz curve

The Gini index is defined as a function of the Lorenz curve introduced above:

$$G = 1 - 2\int_0^1 L(x)dx$$

A Lorenz curve of the type L(x) = x represents a perfectly homogenous mixture and is characterized by a Gini index equal to zero. As the heterogeneity (inequality) increases, the shape of the Lorenz curve deviates from a straight line. A perfect inequality is characterized by a Gini coefficient approaching unity.

Chapter 5. "Experimental Methods and Results"

5.1 Effect of Ethanol on Partially Premixed N-heptane Combustion

5.1.1 Introduction

In order to better understand the underlying physical and chemical phenomena behind ethanol/n-heptane dual-fuel combustion, this combustion mode has been investigated using a set of optical diagnostic techniques, ranging from high-speed imaging to laser induced fluorescence. In the following sections the effect of ethanol on partially premixed combustion of n-heptane will be described. In order to ease data analysis, three operating points have been considered as shown in the table below.

Table 5. Operating Points

Ethanol intake mole fraction ⟶	**0 ppm**	**4200 ppm**	**6600 ppm**
N-heptane injection timing demand [°bTDC]	7.5	10.5	12.5
Solenoid activation time [µs]	450	415	404
N-heptane injection pressure [bar]	800		
Location Peak Premixed Combustion [°aTDC]	7		
Corrected Net IMEP [bar]	2.5		
Intake Temperature [K]	306		
Swirl number	2.0		
Engine speed [rpm]	1200		
Optical diagnostics [y/n]	y	n	y

5.1.2 Ethanol Intake Mole Fraction Measurement

The ethanol intake mole fraction was obtained by using a port fuel injector mounted in the intake system of the naturally aspirated engine. The injector was actuated by the FPGA based cRIO engine controller for durations of 2 and 3 msec respectively. The ethanol was pressurized upstream the injector at a regulated pressure of 2 barg. The intake ethanol mole fraction was evaluated using a FTIR spectrometer (Thermo Nicolete Nexus 670). The resulting spectra are shown in the figure below.

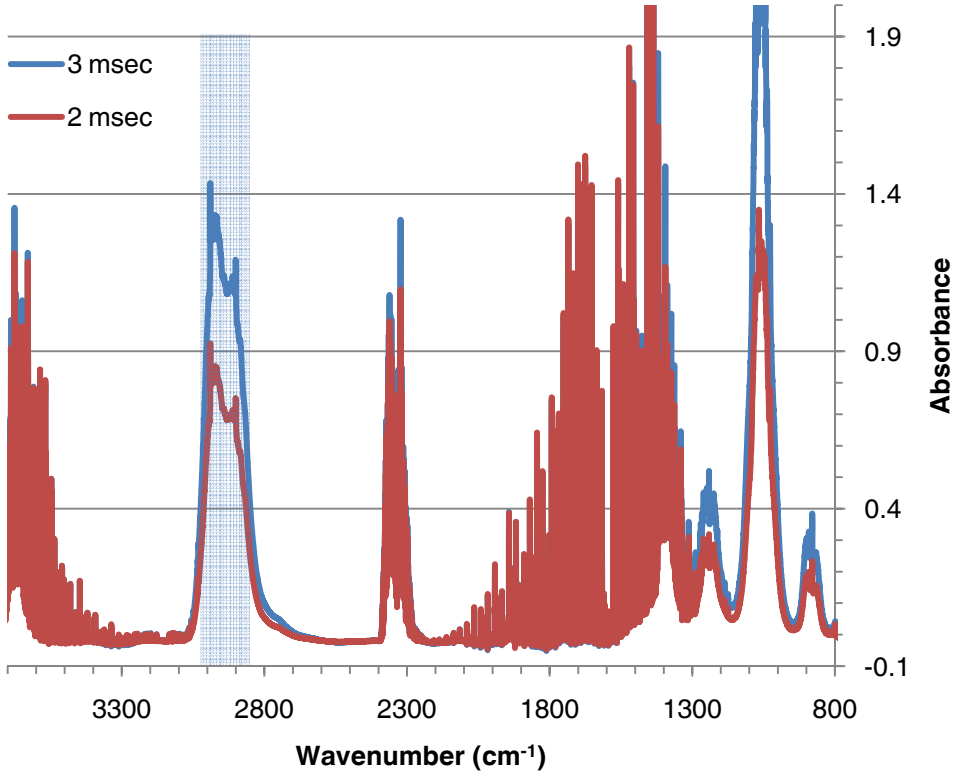

Fig. 5.1. FTIR ethanol spectrum for 2 and 3 msec injector activation time

For this work, the spectral domain highlighted in blue, ranging between 3028 and 2862 cm^{-1} (3.244 to 3.494 µm in air), has been selected for mole fraction

evaluation in order to avoid interference mainly from CO_2 and H_2O as other infrared active species are neither expected nor observed in the intake system of the engine. The intake ethanol mole fraction associated with the operating points considered analyzed according to the procedure described above is shown in Table 5.

5.1.3 Effect of Ethanol on the In-Cylinder Pressure Measurement

The optically accessible engine described in Chapter 3 was operated in skip-firing mode with 3 consecutive firing cycles followed by a variable number of motored cycles. As previously reported [41], this was deemed necessary in order to ensure thermal stability of the Teflon-based composite material used in manufacturing the sealing rings required for dry lubrication of the piston assembly. The number of motored cycles between firing cycles ranged from 7 to 12 and helped in compensating for effects such as ring wear and slight temperature variations.

The in-cylinder pressure was detected by the piezo pressure transducer (AVL GH12D) and the resulting signal was pegged assuming a constant polytropic index of compression as described in section 3.2.3. Based on the in-cylinder pressure measurement, the ARHR was computed for all operating points considered using the heat release analysis method described by Heywood [18]. Fig. 5.2 below shows the in-cylinder pressure ARHR and the uncorrected integrated apparent heat release (AHR) data for the conditions reported in Table 5.

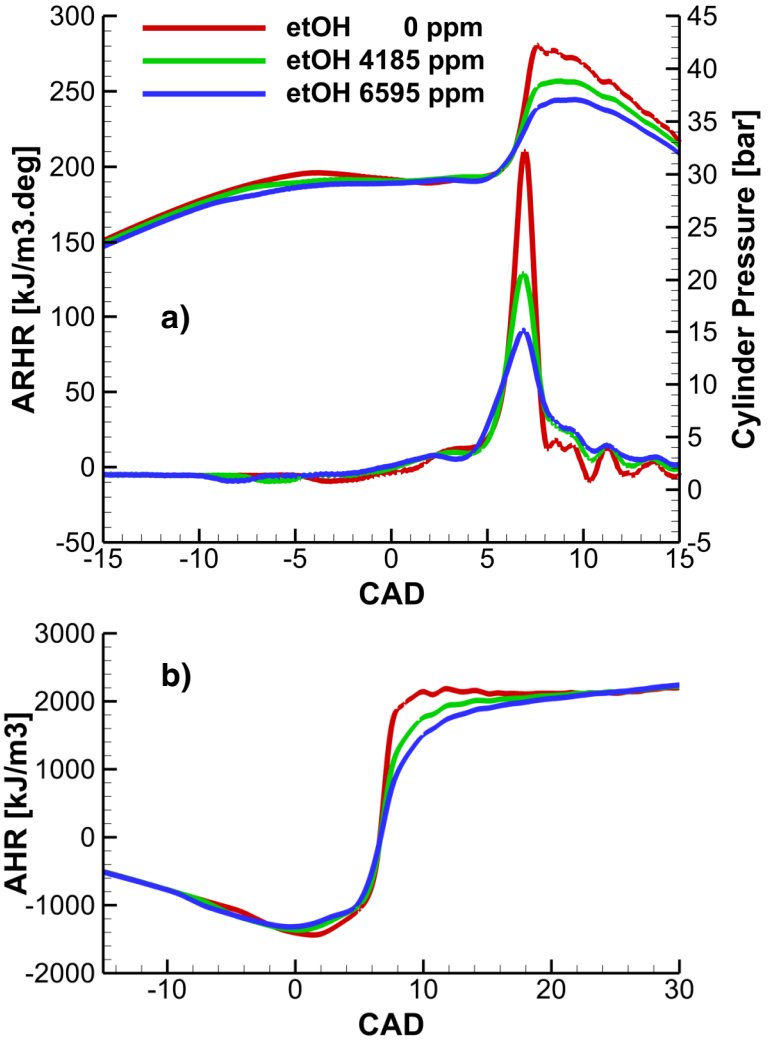

Fig. 5.2. Effect of ethanol addition on n-heptane partially premixed combustion

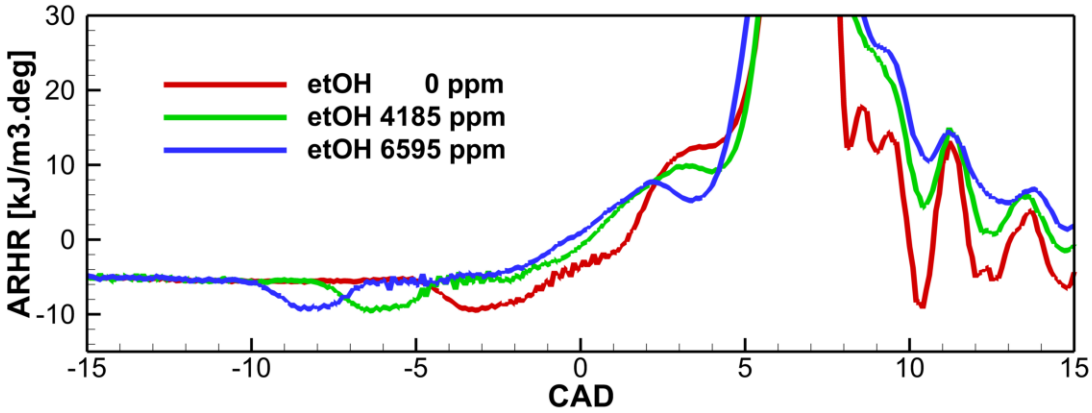

Fig. 5.3. Detail of the Low Temperature Heat Release

As it may be observed in both Fig. 5.2a and Fig. 5.3, the combustion process takes place in mostly premixed mode, with very little indication of any diffusion-controlled combustion typical of high-compression ratio diesel engines. The location of the peak of premixed combustion (LPPC) was maintained at 7°aTDC by adjusting the injection timing as needed. Due to relatively low compression pressure and temperature prior to the injection event, i.e. about 30 bar and 770 K respectively, a low temperature heat release is observed followed by a brief Negative Temperature Coefficient (NTC) period. This behavior is consistent with previous observations [13] related to the two-stage ignition characteristics of n-heptane.

The combustion process is characterized by a fairly long ignition delay compared to typical diesel combustion, mostly due to the decreased compression temperature. Thus, for the conditions chosen, the injection event ends prior to the initiation of significant exothermic reactions.

For the baseline 0 ppm ethanol condition, shown in red, the premixed combustion duration is relatively short and the peak of the premixed combustion is relatively high. During the experimental work the value of this peak was actually limited by a 10 bar/deg target for the rate of pressure rise. Due to this sudden energy release, the pressure trace exhibits typical fluctuations caused by reverberating pressure waves typically identified as “ringing”.

As the amount of intake ethanol is progressively raised to 4200 ppm and 6600 ppm respectively, the peak of premixed combustion decreases, the premixed combustion duration increases and the pressure waves gradually disappear. Thus

ethanol is observed to have the both a delaying effect on combustion as well as resulting in a reduced rate of combustion. It is worth noticing that, while the ARHR associated with n-heptane combustion without ethanol is quite symmetric around its peak, that's no longer the case when ethanol is added. The resulting asymmetric energy release rate would perhaps lead to the conclusion that ethanol results in a decrease of premixed combustion and that diffusion controlled combustion is taking place. However, combustion imaging data that will be presented in a subsequent section does not support this argument. To the contrary, the combustion process remains highly premixed and soot particles typically associated with diffusion controlled combustion are not apparent.

Previous ethanol investigations reported a strong thermal effect of ethanol mainly due to its high enthalpy of evaporation and resulting intake temperature drop. In order to separate the thermal versus chemical effects, the engine was operated with and without intake temperature compensation and the resulting data is presented in Fig. 5.4 below. It may be observed that the thermal effect of ethanol is not as significant as the chemical one, as the impact of intake temperature compensation compared to the impact of ethanol addition is much smaller. This observation is somewhat surprising at a first glance. However, as it will be detailed later in subsequent sections, this observation could be explained by considering the difference in fuel oxidation characteristics (ethanol is a single-stage fuel while n-heptane is a two-stage fuel) as well as the different temperature ranges in which previous versus current research were performed.

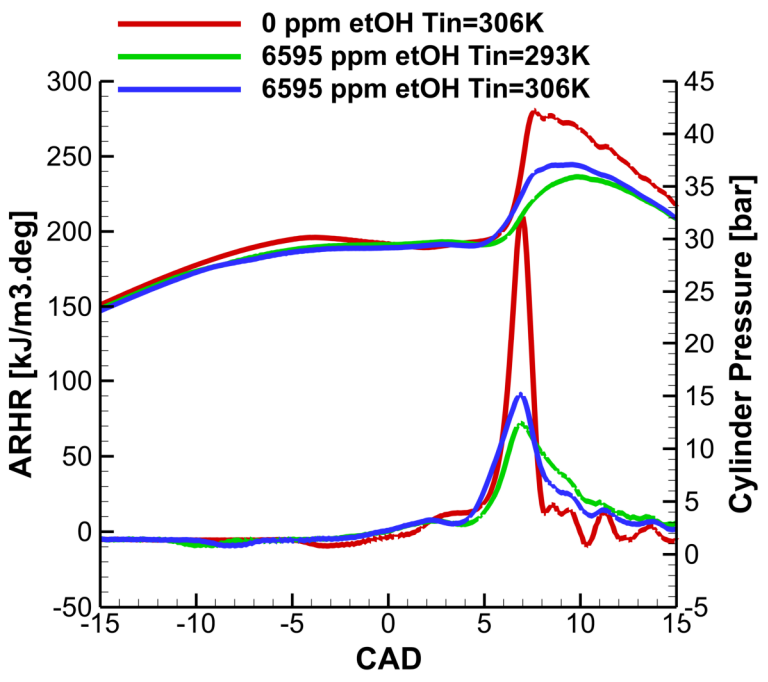

Fig. 5.4. Effect of intake temperature on ethanol/n-heptane dual fuel combustion

Additionally, a small difference in compression pressure prior to the injection event may be observed and this is caused by a slight change in charge density at intake valve close (IVC) as a result of the intake air heating necessary in order to compensate for ethanol evaporation effects. However, the small pressure change is not expected to have a significant impact on the evolution of the combustion process.

5.1.4 High-Speed Spray Imaging

In order to improve the understanding of mixture formation within the combustion mode studied, spray imaging was performed using a high-speed CMOS camera (Vision Research Phantom 7.3) operated at 30,000 frames per second and an exposure of 30 μs. The figure below shows the needle-lift profile measured by a

displacement sensor (MicroEpsilon eddyNCDT 3300). The injector needle is operating within the "ballistic" range without reaching the displacement limit.

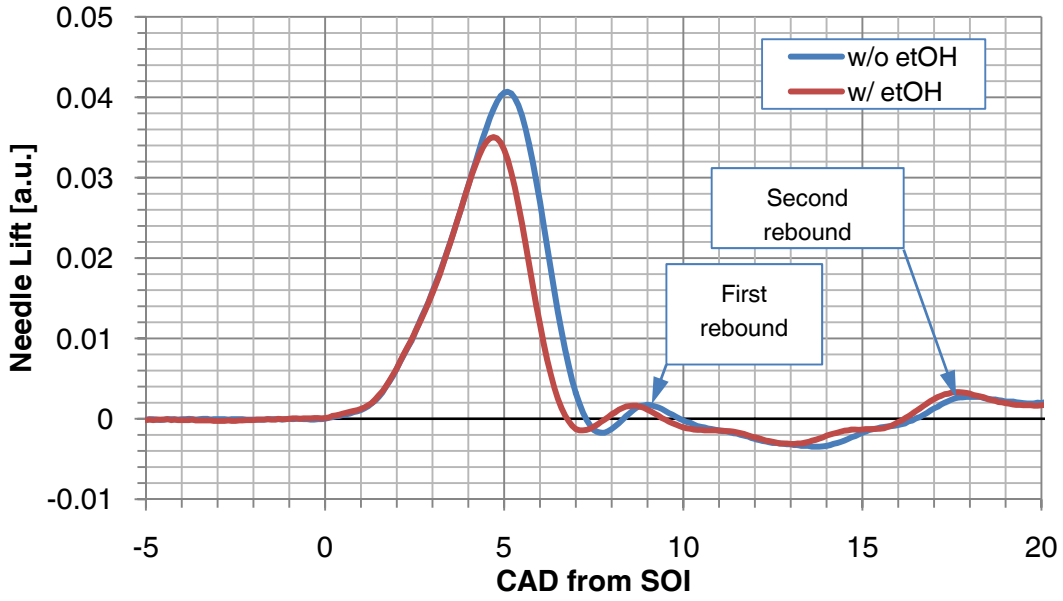

Fig. 5.5. Needle lift profile; the crank angle data is reported with respect to the start of injection.

Due to the decreased activation time associated with the lower amount of n-heptane required to maintain the same load condition when ethanol is added, the injector closes earlier and achieves a lower maximum height compared to the base operating condition. Two additional zones where the needle displacement becomes positive are observed subsequent to the main injection event. This is caused by the elastic deformation of the needle as it closes, which results in a damped vibration.

While the first rebound has been confirmed to result in a post injection event through spray imaging, the timing of the second rebound places it in a high-temperature environment associated with combusting gases and evidence of the rebound resulting in a second post-injection is observed through small amounts of

diffusion-controlled combustion around the injector nozzle in the later stages of combustion. Images associated with these two events will be discussed later and will be shown in Fig. 5.7.

Further, the main injection event is visualized using two relatively simple illumination methods. In Fig. 5.6 shown below, using the first approach, the spray is illuminated through the side windows, installed in the cylinder block as well as in the piston crown, using a high-intensity non-collimated halogen light-source. The signal acquired by the CMOS chip of the high-speed camera is the result of Mie scattering by fuel droplets. As the scattering process is associated with the liquid phase, this illumination method shows neither the location nor the intensity of the vapor phase of the fuel spray. The conditions examined are the same as previously reported for in-cylinder data, where the engine was operated in skip-firing mode. The injector nozzle is visible in the lower part of the image. The imaging targeted the 12 o'clock spray due to the configuration of the available light-source. On the upper part of each image, the edge of the piston side window may be observed. For these investigations a quartz flat window was selected in order to provide the best compromise between in-cylinder flow and impact of window configuration on laser sheet deformation. The laser sheet was used in formaldehyde Planar Laser Induced Fluorescence experiments described later in this chapter.

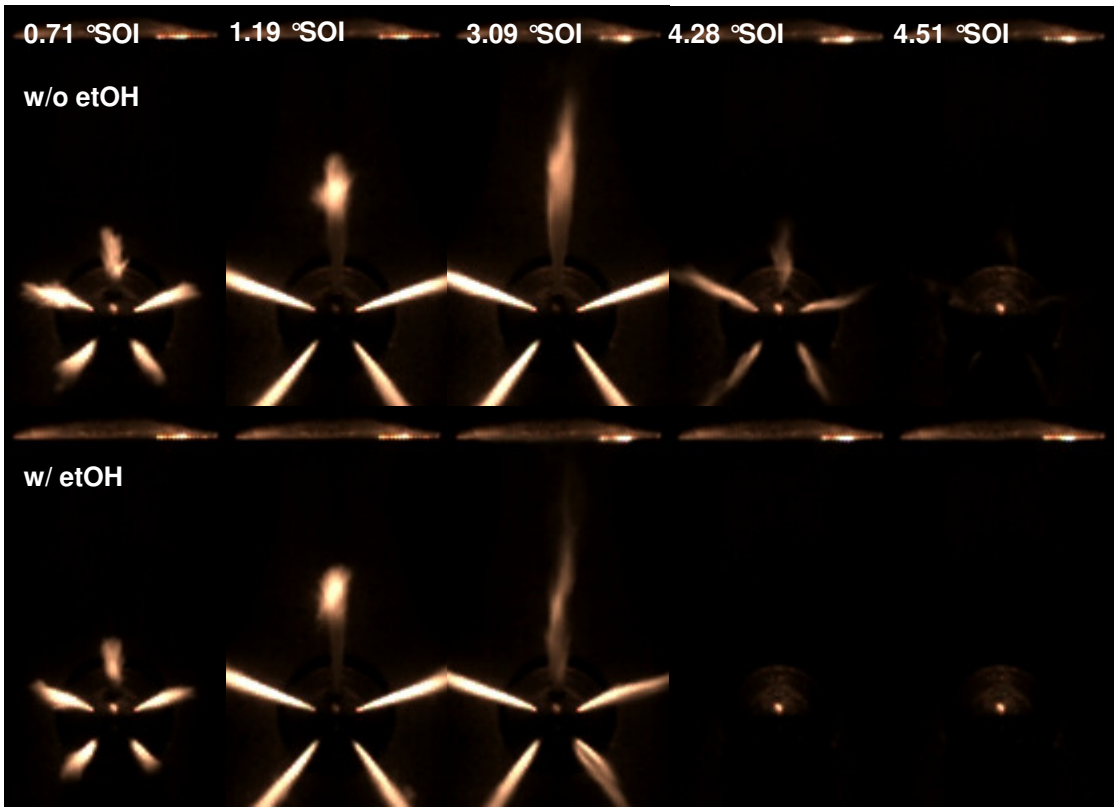

Fig. 5.6. Imaging of injection events for the two conditions studied

As the injection event is initiated, the spray is observed to have a rather non-uniform structure, due to interaction between high-speed and high-momentum liquid droplets and the surrounding gas, which is swirling at a much lower speed. As the spray proceeds to penetrate into the combustion chamber, the jet gradually stabilizes into a narrow cone. However, due to the relatively high volatility of n-heptane, the liquid spray does not appear to impinge on the bowl surface. Rather, it maintains a constant penetration distance (liquid length) for a significant duration of the injection event. As the injection event ends and the needle closes, the light scattered by the spray is observed to disappear. The evidence of secondary injections is shown in the figure below, where a small amount of fuel is observed to

be delivered into the combustion chamber. Evidence for the first post injection is obtained through direct spray imaging for the first rebound and sooty diffusion controlled combustion for the second.

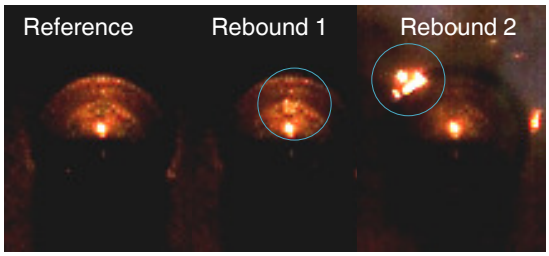

Fig. 5.7. Secondary injections due to needle rebound

Further analysis of the spray imaging data is presented in the next figure, Fig. 5.8, where experimentally acquired images have been post-processed to show a time sequence of the spray event for both injection events according to a procedure previously described in reference [116]. Each individual frame was converted to 1 bit images and the resulting composite image was obtained by displaying only the earliest information, even if the spray is located at certain positions later in the injection event. The first occurrence of a spray location is color-coded based on its crank-angle position referenced with respect to the start of injection (SOI).

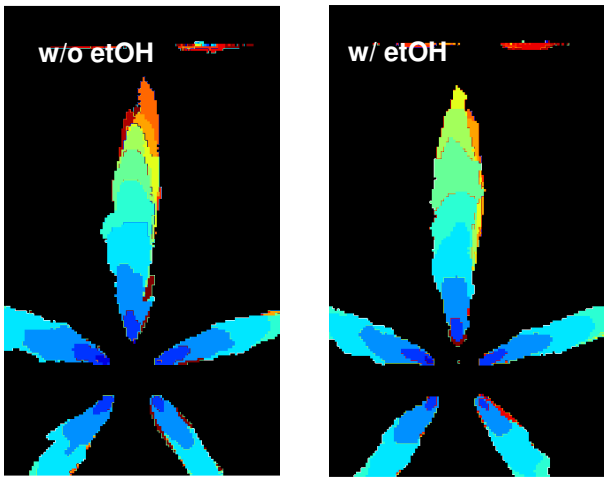

Fig. 5.8. Sequence of spray locations throughout the injection event

It may be observed that the two sprays have a relatively similar evolution, similar cones as well as penetration depths. Neither of them reaches the bowl wall (which appears as a red line in Fig. 5.8). As the first condition will experience higher momentum due to the increased droplet velocity resulting from increased needle-lift, the spray would be expected to have increased penetration. However, the increased droplet momentum is offset by increased droplet break-up and evaporation as the spray interacts with the surrounding low-speed gas.

The second illumination technique involved the back-illumination of the spray in order to obtain a shadowgraph effect capable of identifying the fuel vapor phase. While a better optical access - such as a valve replaced by an optical window - would have been desirable, this type of access was not available at the time when these experiments were conducted.

A sample back-illuminated image is shown in Fig. 5.9a) below. However, by viewing the raw image it is not immediately clear where the vapor phase is located. A relatively simple post-processing method is applied to enhance the features associated with the vapor phase of the flow and is shown in Fig. 5.9b).

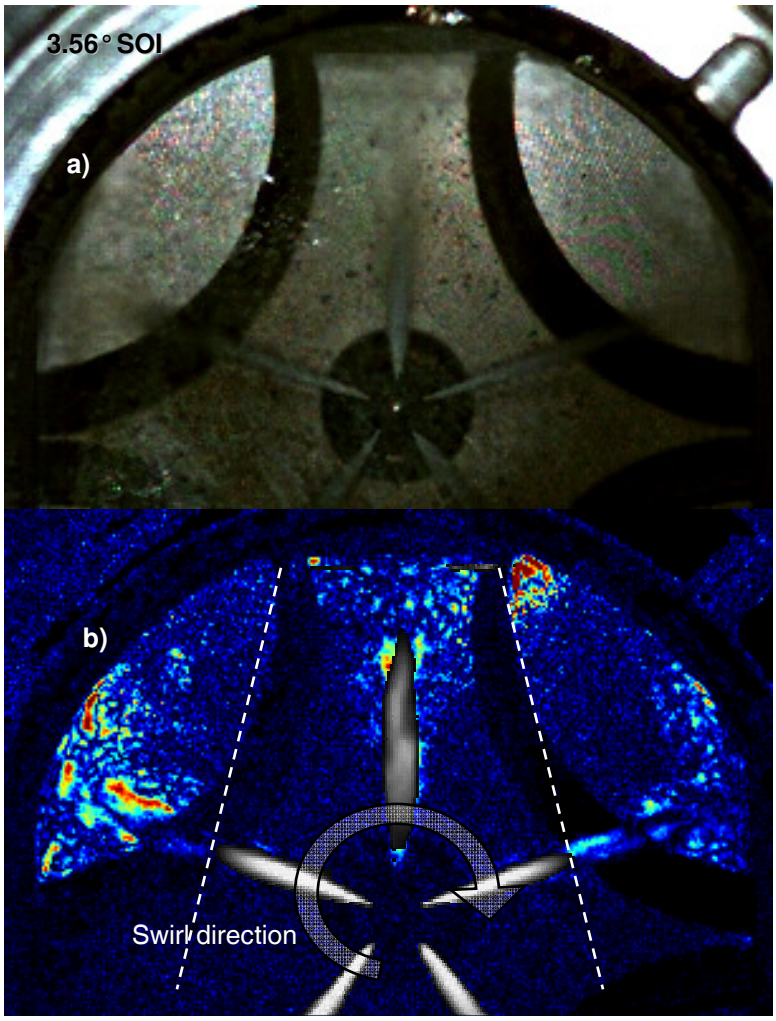

Fig. 5.9. a) Back illuminated spray image
b) composite image showing liquid and vapor phase

Under this method, consecutive images are subtracted from each other upon converting them to a gray-scale (versus the raw image RGB format) and the resulting pixel intensity is given by:

$$I = \left| I_{current} - I_{previous} \right|$$

In Fig. 5.9b) the result of the previous illumination method is superimposed on the image obtained as described above. The reader should be reminded that only the 12 o'clock spray is target by the side illumination and that the other sprays are not fully illuminated due to the physical layout of the optical access (approximate light pattern for the side illumination is shown as dotted lines). Additionally, the shadowgraph effect which actually relies on light reflected from the cylinder head, does not work in the valve seats area, where the angle of incidence of the radiation used for illumination is different from 90°.

From the data shown in Fig. 5.9b), the vapor cloud is observed to actually impinge the bowl wall and it features local recirculation on either side of the spray. The spray is also observed to be affected by the gas swirl motion by the asymmetric features of the vapor phase image.

Based on the information presented above, it is expected that the highest equivalence ratio will be found in the vicinity of the bowl wall and the probability of combustion initiation is highest next to the wall.

5.1.5 High-Speed Visible Range Combustion Imaging

The effect of ethanol on the partially premixed combustion of ethanol has been further investigated using a high-speed visible range camera (Vision Research Phantom 7.3). Under this operation, each frame was individually triggered using a 0.5 CAD signal obtained directly from the crank angle encoder. The TTL level signal was supplied to the FSYNC pin of the high-speed camera and the camera was switched from internal to external triggering. The exposure was limited to 65 μs in order to avoid conflict with frame spacing. Additionally, the camera memory was conserved and a cycle-based time-referencing system was established by operating the camera in memory gate mode. This implies that a triggering signal supplied in this case by the cRIO engine controller determines which acquired frames should be saved in the camera memory and which ones should be discarded.

Crank-angle information regarding each frame as well as current cycle data are determined based on the frame timestamp. Regular images will have timestamp intervals ranging around 71μs for the conditions described, while "boundary" images, located before the end of the memory gate pulse and just after the beginning of the next pulse, will be separated by very large intervals, in the order of magnitude of 100msec. By detecting these large intervals between frame timestamps, crank angle information for each image may be inferred. MATLAB functions used for reading the header information (timestamp) as well as each individual frame from the native CINE format are included in Appendix 1.

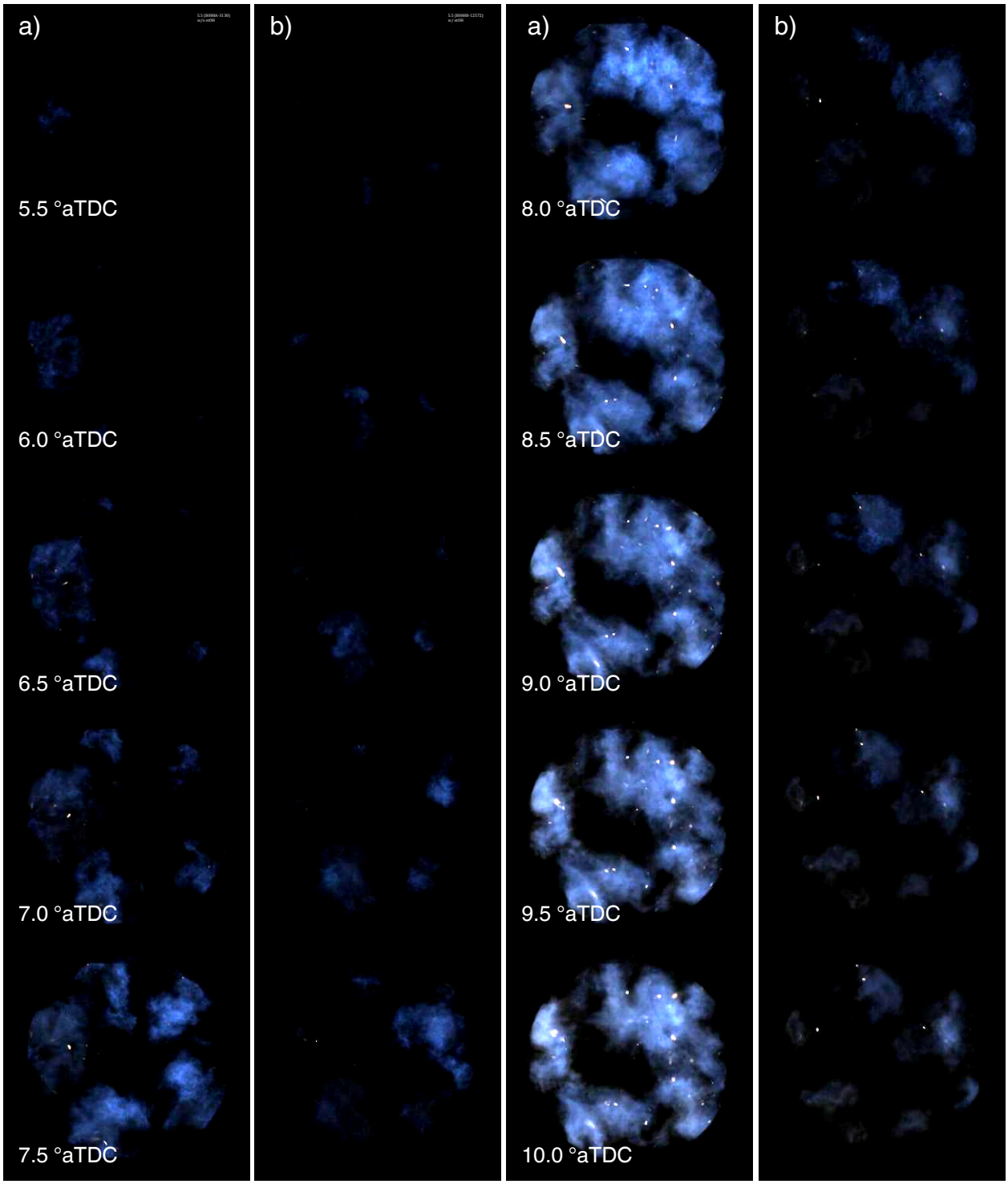

Fig. 5.10 Single-cycle high-speed visible range images a) without ethanol b) with ethanol

Data acquired from a single cycle is available and two representative cycles are shown in Fig. 5.10

a) and b) above. In Fig. 5.10a), an important observation is the lack of soot black-body type luminosity. This behavior is expected, as the fuel considered is a single-molecule straight chain hydrocarbon which was found in previous studies to have low soot production tendency. Small soot spots are still observable though, most probably due to locally rich mixtures. Most of the radiation detected by the high-speed color camera (spectral response shown in Fig. 3.11) resides in the blue spectral range (350-450 nm). As previously described by Gaydon [117], the blue flame associated with this type of hydrocarbon flames should either be caused by CO flame spectral bands or a CO continuum. Spectral measurements of flame chemiluminescence reported in a subsequent section have not shown the presence of any spectral lines associated with the CO flame and thus, the radiation is believed to originate from the CO continuum which previous authors have associated with the single step reaction [117]:

$$CO + O = CO_2 + h\nu$$

Several investigations reported by Gaydon [117] in low-pressure flames show that the light emission intensity is proportional to the forward rate of the reaction shown above. It can be thus concluded that the blue-flame radiation should be proportional to the energy release rate.

Analyzing the results shown in Fig. 5.10b), the same blue flame is observed. However, due to the decrease of the rate of heat release, the blue flame intensity is observed to be dramatically decreased.

While this is an expected finding, it is also somehow surprising with respect to previous findings regarding the effect of formaldehyde on JP-8 combustion [41, 45]. Formaldehyde intake addition was shown to have an inhibiting effect on combustion, as indicated by rate of heat release data, similar to the effect of ethanol. However, combustion imaging data has shown that the soot-free JP-8 combustion, which is quite similar from a light emission stand-point with the n-heptane combustion. It also showed that formaldehyde unexpectedly increased the amount of radiation observed at longer wavelengths, which could either be attributed to increased soot formation or to some unexpected spectral features. The latter is thought to be less likely. The imaging data from the above cited work is included below for completeness.

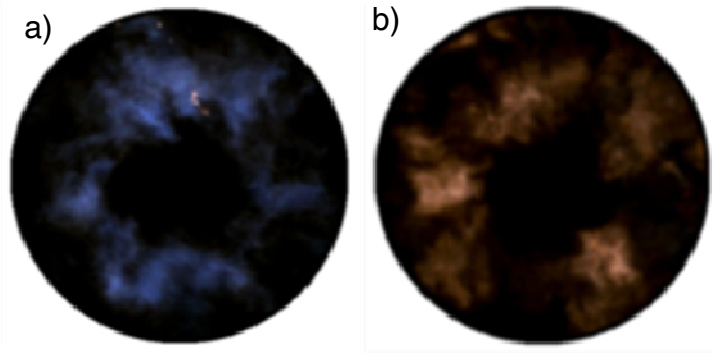

Fig. 5.11a) smokeless JP-8 combustion
b) JP-8 combustion with formaldehyde intake addition

It may be theorized that while the inhibiting pathways associated with formaldehyde and ethanol addition are similar, mainly through OH radical scavenging, formaldehyde probably plays an additional role in reactions which are responsible for the production of soot precursors.

The combustion images have been post-processed in a similar manner as the data presented in Fig. 5.8, and the results are shown in the figure below.

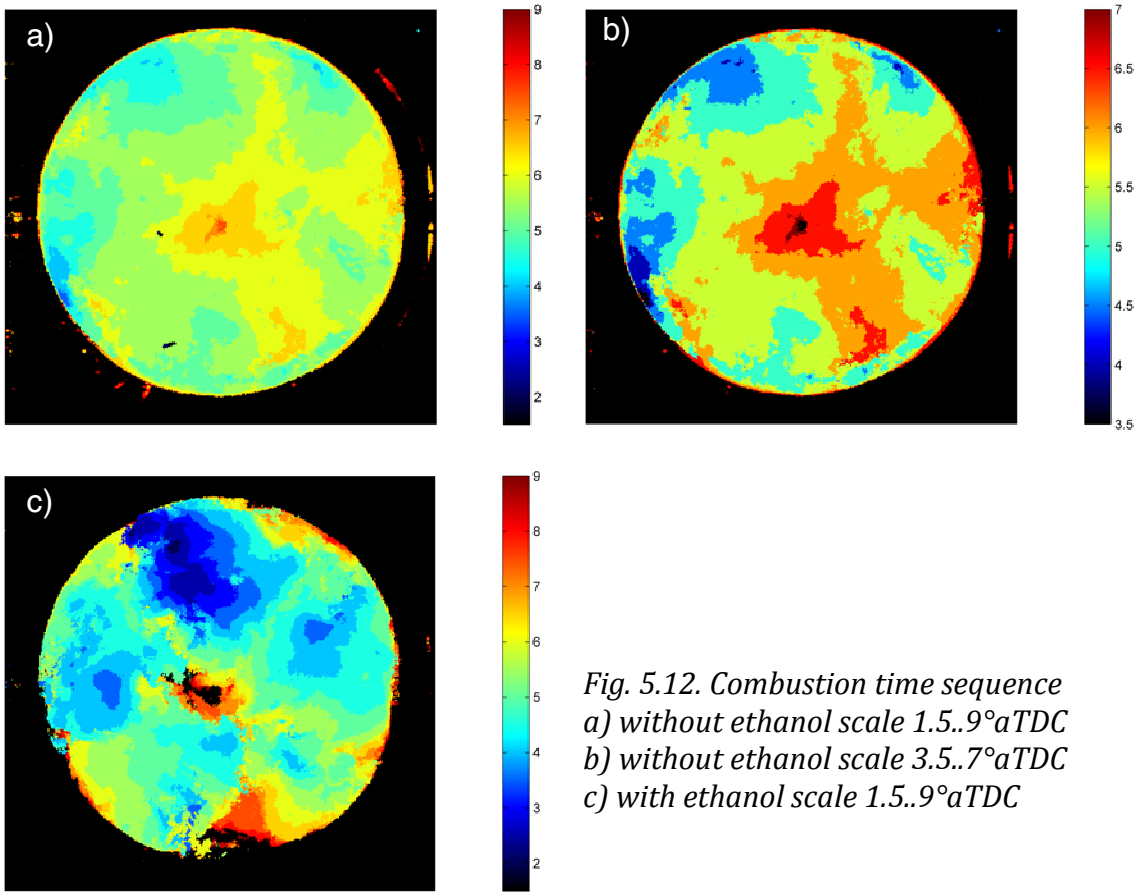

Fig. 5.12. Combustion time sequence
a) without ethanol scale 1.5..9°aTDC
b) without ethanol scale 3.5..7°aTDC
c) with ethanol scale 1.5..9°aTDC

The color-coding change indicates a change in time, events shown in red occurring for the first time later in the cycle, while black areas indicate areas where no detectable activity occurs within the time-frame considered. Fig. 5.12a) and Fig. 5.12c) show the combustion event without and with ethanol addition respectively at

the same timescale. However, due to the fact that under the conditions investigated the combustion event has a longer duration when ethanol is added, data shown in Fig. 5.12a) is shown rescaled in Fig. 5.12b) in order to facilitate comparison. Without ethanol addition, the combustion process starts in close proximity to the wall, which is consistent with the location of highest fuel vapor density as discussed in the previous section. As the reaction zone propagates, it is clearly affected by the charge swirling motion and it eventually reaches the center of the combustion chamber in an inward spiraling pattern. Similar features are maintained by the ethanol / n-heptane dual fuel combustion. However, in this case, the location of first ignition as observed by the high-speed color camera changes slightly towards the center of the combustion. This is most probably due to the increase time available between the injection event and the high temperature heat release.

Further, the blue-flame intensity was integrated across the entire frame and the results of the integration are presented in Fig. 5.13 below for both conditions investigated. For comparison, the rate of heat release data is presented as well. For the purposes of numerical signal integration, high-intensity luminous spots due to soot black-body like emission have been removed prior to integration in order to avoid the resulting bias. This was not significant problem, as the soot spots occur rarely.

One may observe that the blue-flame intensity is considerably higher without ethanol addition, as the blue-flame is suppressed by ethanol. Additionally, the blue flame peak is observed to be slightly delayed with respect to the premixed

combustion heat release peak. This is most probably caused by different chemistry associated with fuel decomposition versus carbon monoxide oxidation. This topic will be further discussed in a following section regarding combustion chemiluminescence spectral measurements. Also, the blue flame is considerably longer than the high-temperature heat release duration as indicated by the rate of heat release diagram.

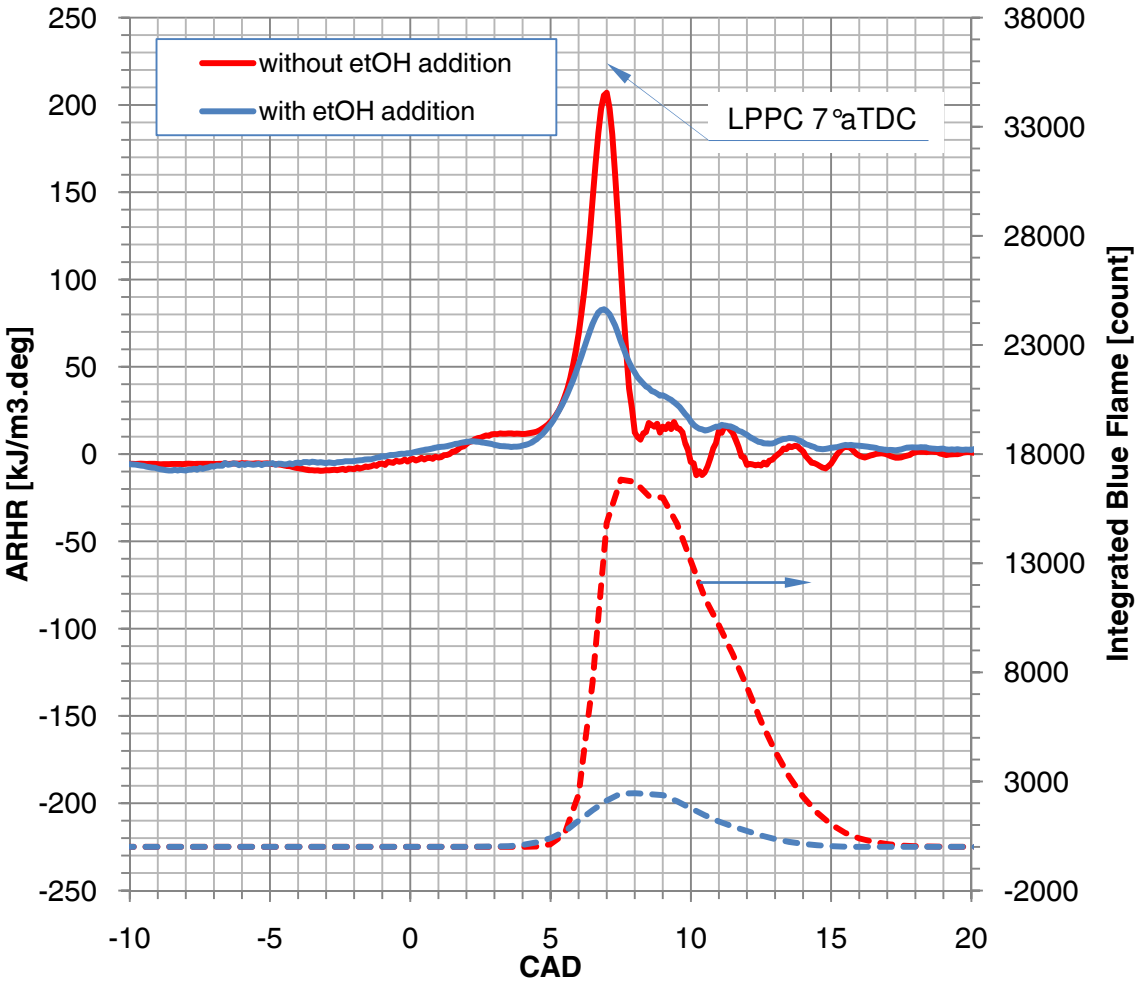

Fig. 5.13. Blue Flame Integral signal evolution (dashed line)

5.1.6 UV filtered Images at 307nm (OH transition)

UV images were acquired using an intensified ICCD camera (Princeton Instruments PIMAX2) equipped with a 78mm UV objective (Electrophysics). The incident radiation was filtered with a 307 nm (targeting the OH radical) with a 10 nm full width half maximum (FWHM). The camera was operated at maximum intensifier gain with an exposure of 80μs. As this particular camera has a limited repetition rate of about 17 Hz, only one image per cycle was available. Thus, the images shown have been sampled in different engine firing cycles and they were selected by the author as being representative of the overall set of images associated with each crank-angle position.

The first set of images shown in Fig. 5.14a) and c) are repeated from Fig. 5.10 in order to provide a complete picture of the combustion process. The location of OH chemiluminescence follows a very similar pattern as the visible range images collected by the high-speed camera and associated with the CO flame, suggesting a close relationship between energy release and OH activity.

Ethanol is observed to reduce the intensity of OH chemiluminescence. As the OH chemiluminescence is the result of spontaneous light emission by electronically excited hydroxyl radicals, along with the fact that the formation of electronically excited OH is directly related to the rate of formation of hydroxyl radicals, the reduced OH chemiluminescence seems to intake an overall reduction in OH production rates.

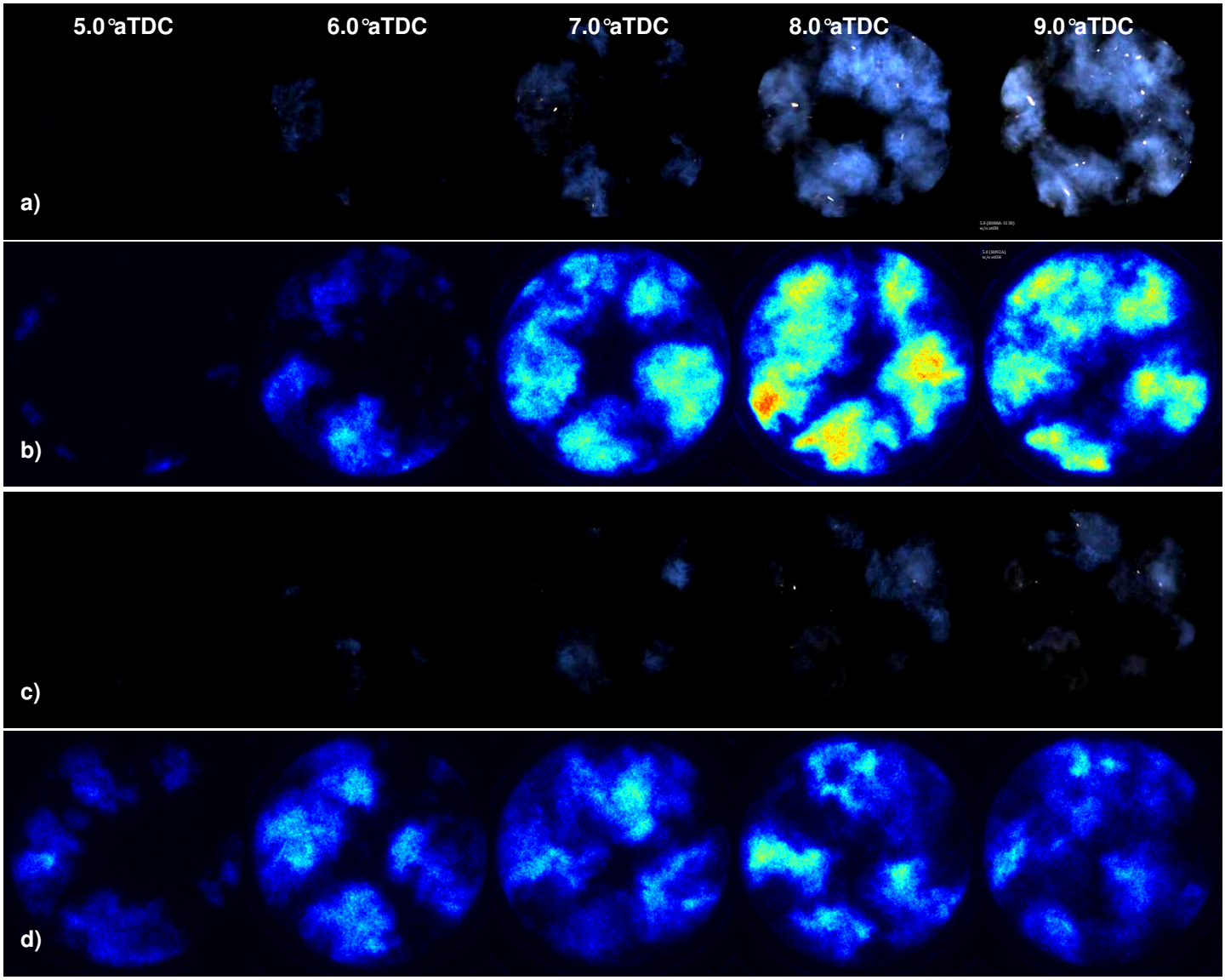

Fig. 5.14. Combustion imaging
a) w/o etOH, Vis b) w/o etOH, 307 nm
c) w/ etOH, Vis d) w/ etOH, 307 nm

5.1.7 Combustion Chemiluminescence Spectral Measurements

Spectral information regarding the natural flame luminosity has been collected using a 150mm diffraction spectrometer (PiActon 2150i). The radiation was collected and focused on the input slit by the 78 mm UV lens (Spectraphysics) and the aperture was maintained at f/4.0 to avoid overfilling the spectrometer optics. For this work a 300 grooves/mm, 300 nm blaze wavelength grating was employed. The ICCD PIMAX2 camera was mounted in the imaging plane of the spectrometer and it was used for data collection. The spectrometer slit was set at 150μm opening as a satisfactory compromise between spectral resolution and signal to noise ratio. During these tests, the spectrometer slit was aligned with the injector tip and the imaging line covered the entire combustion chamber diameter. The signal was integrated along the entire imaging line, resulting in a single spectrum per imaging event characterized by improved signal to noise ratio. The ICCD camera was triggered externally by the engine controller (NI cRIO).

As the engine was operated, spectra were collected at different crank-angles by automatically marching the camera triggering during the experiment. The resulting spectra are presented in Fig. 5.12 below as a 3D surface were information regarding both wavelength and time is available.

Among the most prominent spectral features are clearly the OH peak at 309nm which is actually formed of several strong OH spectral lines which have been "blurred" by Doppler and collision line broadening. Additionally, a fairly strong CH emission is apparent at 431nm.

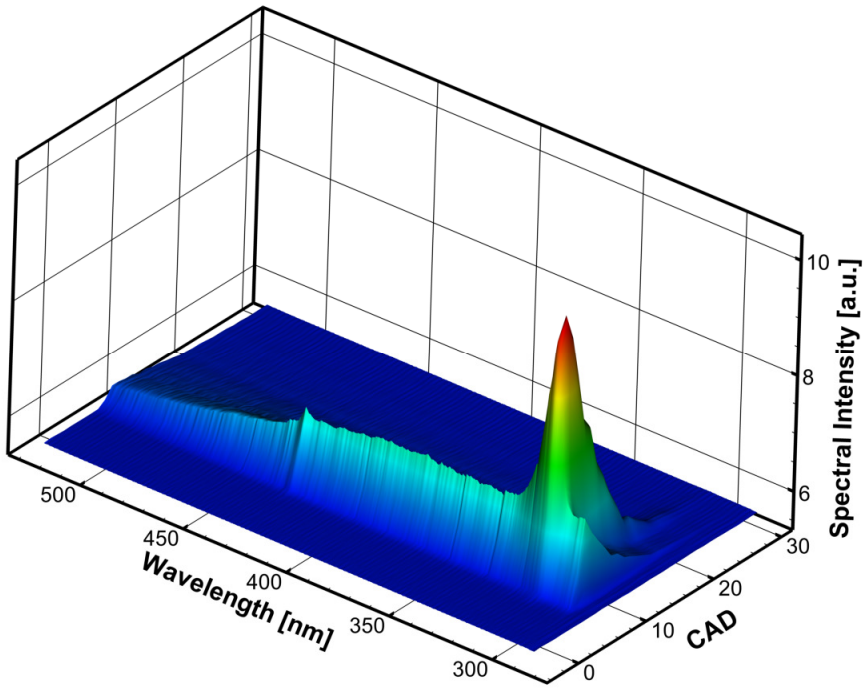

Fig. 5.15. Chemiluminescence spectrum time evolution

The CO flame spectral band is the only significant feature observable in this data. The lack of clearly identifiable spectral lines associated with the CO lines points towards the CO continuum as the potential source of light emission in this part of the visible spectrum.

Next, Fig. 5.16 shows the chemiluminescence spectra at several temporal locations throughout the premixed combustion. The CH chemiluminescent emission is centered around 431 nm and represents the strongest spectral line system associated with this group [117]. This spectral feature is observed to increase its strength as the reactions progress towards the peak of energy release rate located at 7°aTDC. However, after the premixed combustion peak, CH radiation is no longer detectable in the CO continuum. Zero-dimensional modeling of the n-heptane

oxidation process has indicated that CH is indeed formed in significant quantities only during the high-temperature heat release. As electronically excited CH molecules are expected to have a fairly short lifetime compared to the combustion time-scale, CH radiation is expected to mirror the CH formation rates. As the CH mole-fraction peak predicted by kinetic modeling coincides with HTHR peak, the CH production after the peak drops considerably resulting in reduced chemiluminescence.

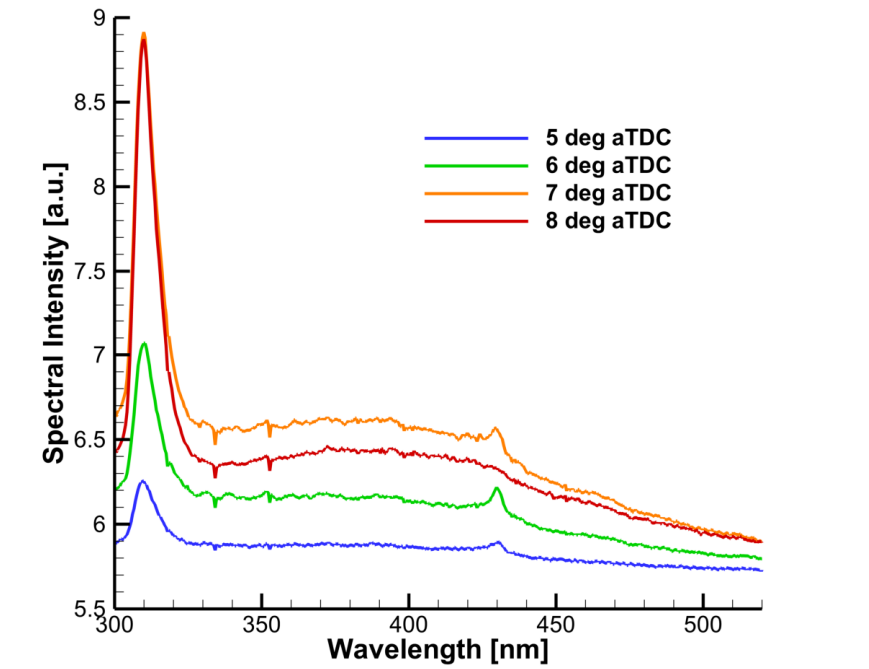

Fig. 5.16. HTHR Chemiluminescence spectra without ethanol addition

Other spectral features observed in the above plot are some weak absorption lines. While the species responsible for these absorption lines have not been positively identified as being associated with a single molecule, several possible

transitions have been identified. First, around 335nm an aldehyde (propinaldehyde) exhibits medium absorptivity [117] while the hydroxyl radical could be responsible for the adsorption line observed at 353nm albeit, this is considered a weak absorption line for OH. Further, two additional absorption lines which are very close to the measurement noise have been identified at 399nm (possibly C_3) and 454nm (NO_2).

The impact of ethanol on chemiluminescence spectra is shown in Fig. 5.17 for two positions, just before and just after the LPPC respectively.

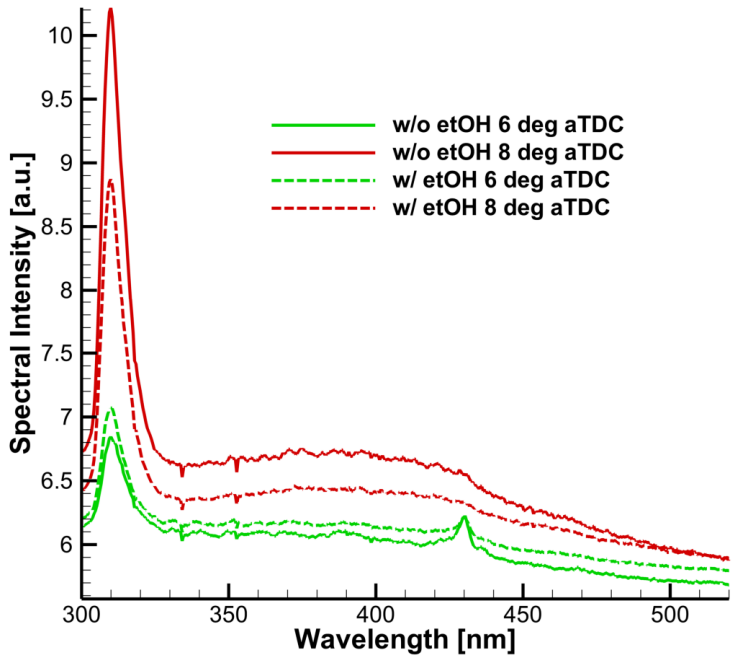

Fig. 5.17. Effect of ethanol on chemiluminescence spectra

Ethanol is observed to have a considerably stronger impact on combustion chemiluminescence after the premixed combustion peak which could be mostly due

to the higher overall signal observed at that particular crank-angle position. The observed spectral features remain largely unchanged with the exception of the OH emission, which is observed to be considerably reduced as ethanol is added subsequent to the peak of heat release. The reduction in OH emission is more pronounced than the overall reduction in CO emission which is caused by the lower-rate of energy release. This is most probably due to the OH scavenging effect of ethanol.

5.1.8 Planar Laser Induced Fluorescence (PLIF) of Formaldehyde

The investigation of formaldehyde distributions within the combustion chamber has been the subject of a recent Society of Automotive Engineers (SAE) draft paper which, at the time of writing this thesis, has been approved for publication. The contents of the draft manuscript are reproduced in this section. Some of the material already introduced within the thesis has been reproduced in the paper for completeness. The figure numbering scheme is different with respect to the rest of the text in order to maintain consistency with the paper manuscript.

SAE 12PFL-0951: Ethanol/N-Heptane Dual-Fuel Partially Premixed Combustion Analysis through Formaldehyde PLIF

ABSTRACT

As a result of recent focus on the control of Low Temperature Combustion (LTC) modes, dual-fuel combustion strategies such as Reactivity Controlled Compression Ignition (RCCI) have been developed. Reactivity stratification of the auto-igniting mixture is thought to be responsible for the increase in allowable engine load compared to other LTC combustion modes such as Homogenous Charge Compression Ignition (HCCI). The current study investigates the effect of ethanol intake fuel injection on in-cylinder formaldehyde formation and stratification within an optically accessible engine operated with n-heptane direct injection using optical measurements and zero-dimensional chemical kinetic models. Images obtained by Planar Laser Induced Fluorescence (PLIF) of formaldehyde using the third harmonic of a pulsed Nd:YAG laser indicate an increase in formaldehyde heterogeneity as measured by the fluorescence signal standard deviation. The experimental observations are complemented by a discussion regarding definitions of "reactivity".

INTRODUCTION

In response to continued demand for improved internal combustion engine efficiency and emissions reduction, previously reported research has focused on Low Temperature Combustion (LTC) modes, such as Homogenous Charge Compression Ignition (HCCI) [67, 68, 69, 70], as potential candidates for future internal combustion engines technologies. While these combustion modes have

been shown to yield high indicated efficiency as well as near-zero engine-out emissions, the lack of a combustion "trigger" results in difficult and often impractical control strategies which limit both the engine load range, engine transient behavior as well as the cold-startability of the engine.

Recently proposed dual-fuel combustion modes, such as Reactivity Controlled Compression Ignition (RCCI) [22, 64, 65, 66], seek to maintain the advantages associated with Low Temperature Combustion while addressing the issues related to combustion phasing control and rate of pressure rise limited engine load.

Furthermore, homogenous mixture combustion modes such as HCCI are characterized by volumetric energy release. While the reduced combustion duration improves the thermodynamic efficiency, it also results in high rates of pressure rise and subsequent engine ringing [71] previously associated with knock in spark-ignition engines. This has an undesirable impact on engine integrity and perceived combustion noise. In order to address these issues along with the need for a method for reliable control of combustion phasing, the internal combustion research community has shown increased interest in kinetically controlled combustion and dual fuel operation. One such combustion mode, the RCCI, is characterized by partially premixed combustion where fuels of different reactivities are used in different ratios in order to obtain a "reactivity" stratification of the combustible mixture. This in turn results in a phase-shift in the ignition delay time experienced by different zones of the combustion chamber and a longer duration of the premixed

phase of combustion. Due to the ample time available between fuel injection and high-temperature heat release, the fuel is highly premixed but not fully homogenous. Thus, the amount of diffusion controlled combustion is minimized, reducing the probability of soot formation.

Work reported by Splitter et.al. [22] investigated the dual-fuel operation of a single-cylinder diesel engine operated with different fuel combinations. The results reported indicate that ethanol, a biofuel and thus renewable energy source, has the most significant impact on the partially premixed combustion mode studied. The authors point towards the inhibiting effect of ethanol, previously reported by Hashimoto [36, 37] which is caused by the scavenging of the hydroxyl radical by the ethanol molecules. Thus, one could hypothesize that ethanol and other chemical species which have a significant impact on the chemical kinetic pathways for fuel decomposition are more suitable for use in reactivity stratification applications compared to other types of fuels. In this work the dual-fuel autoignition process is investigated in an optically accessible diesel engine operated with n-heptane direct injection and anhydrous ethanol (200 proof) intake port injection.

The goal of this research is to investigate the effect of ethanol on formaldehyde formation and formaldehyde heterogeneity. As it has been shown by previous authors [95], formaldehyde plays a significant role throughout the low temperature conditions considered in this work. For this purpose Planar Laser Induced Fluorescence (PLIF) measurements of in-cylinder formaldehyde are reported and analyzed. Further, the experimental observations are supported by

chemical kinetic calculations intended to provide additional insight into the impact of ethanol mole fraction, temperature and equivalence ratio on formaldehyde formation and energy release. Finally, a discussion regarding the experimental observation of reactivity stratification is provided as well.

EXPERIMENTAL SETUP

The experimental setup used in this investigation has been reported in previous publications [41, 42, 43, 44, 45, 46]. Table 9 shows the experimental conditions. The ethanol intake mole fraction was measured using an FTIR spectrometer (Thermo Nicolet Nexus 670).

Table 6. Experimental engine specifications

Optically accessible engine	AVL SCRE5402
Intake system	naturally aspirated
Exhaust gas recirculation	no
Bore x Stroke	85 x 90 mm
Swept Volume	510 cm^3
Compression Ratio	15:1
Engine Speed	1200 rpm
Injection System	Common Rail CP1
Injection Pressure	800 bar
Injector Number of Holes, Type	5 holes, VCO
Hole Diameter	180 µm
Hole Included Angle	142°
Fuel	n-Heptane

Table 7. Operating points

Ethanol intake mole fraction	0 ppm	4200 ppm	6600 ppm
N-heptane injection timing demand [°bTDC]	7.5	10.5	12.5
Common-Rail Injector Solenoid activation time [µs]	450	415	404
N-heptane injection pressure [bar]	800		
Location Peak Premixed Combustion [°aTDC]	7		
Corrected Net IMEP [bar]	2.5		
Intake Temperature [K]	306		
Swirl number	2.0		
Engine speed [rpm]	1200		
Optical diagnostics [y/n]	y	n	y

During the testing reported, the engine was operated in skip-fire operation in order to improve the thermal stability of the optical engine. Under this engine fueling strategy, fuel was injected for 3 consecutive cycles followed by typically 9 motoring cycles.

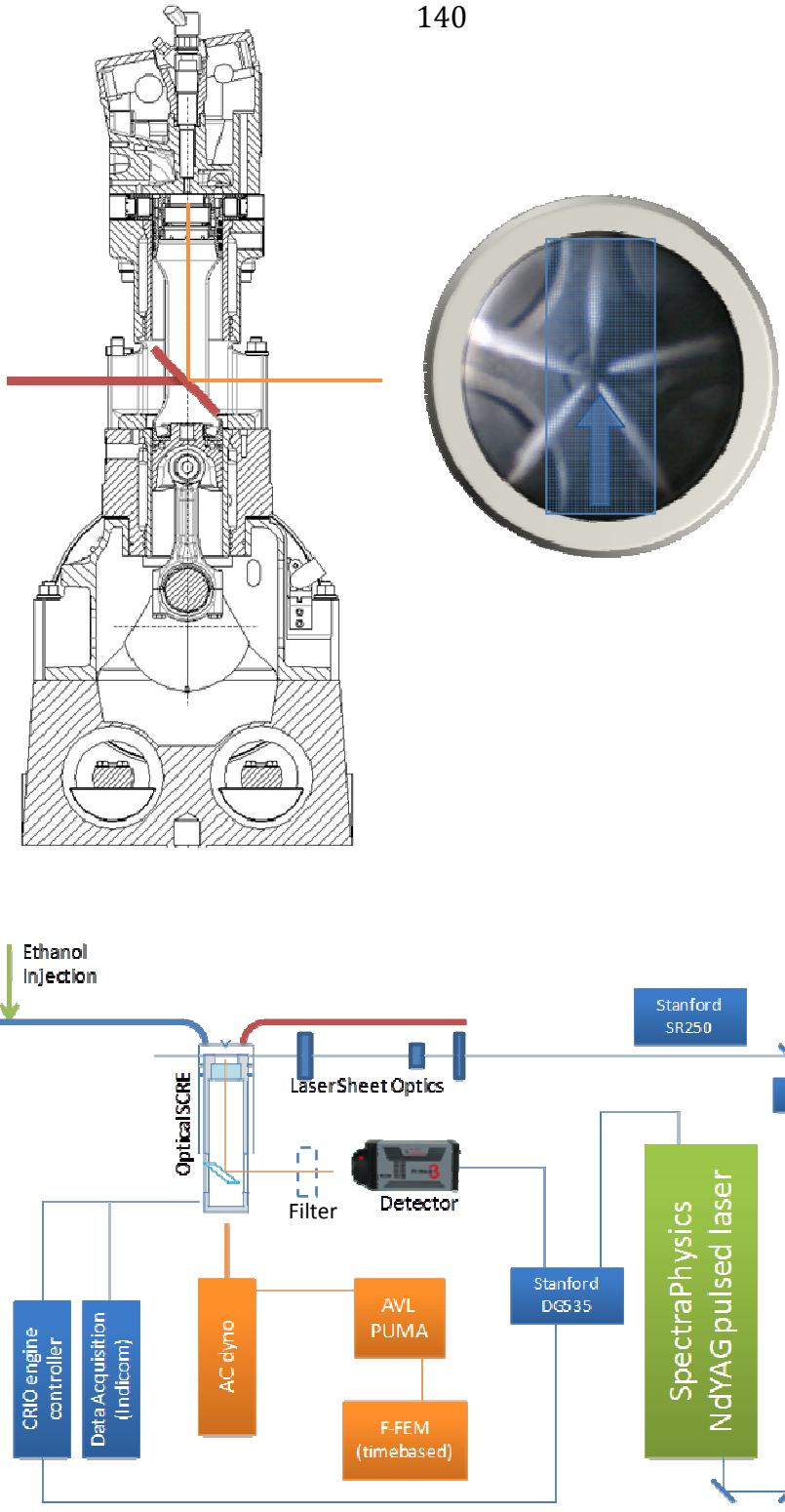

Figure 1. a) cross section through the single cylinder optically accessible engine
b) spray pattern orientation and laser sheet configuration
c) Experimental setup diagram

The single cylinder research engine is provided with full optical access through a 40 mm diameter sapphire window mounted in an elongated piston in order to provide an unobstructed bottom view of the combustion process throughout the entire engine cycle. A cross-section though the engine is shown in Figure 1a) while b) shows the spray orientation and laser sheet positioning. The spray pattern was directed such as to avoid fuel impingement on the laser sheet entrance window. The experimental setup considered in this work is shown in Figure 1c).

The PLIF experiment is carried out using the third harmonic (355 nm) of a Nd:YAG pulsed laser (SpectraPhysics QuantaRay Pro 270), similar to work previously reported in the literature [95, 96, 97]. The engine operating speed was chosen in order to match the nominal frequency of the pulsed laser, i.e. 10 Hz. The laser beam, characterized by a Gaussian profile, has been formed into a laser sheet using a 100 mm focal length cylindrical lens along with a 500 mm focal length plano-concave spherical lens. The laser-sheet is delivered through the combustion chamber of the optically accessible engine via a series of flat fused silica windows mounted in both the adapter plate connecting the cylinder head to the crank-case, and the piston crown respectively. The optical access supplied by these lateral windows is designed to provide laser sheet access for piston positions around the firing TDC of the engine. The laser sheet is aligned parallel to and approximately 4 mm below the fire deck.

In order to account for shot-to-shot laser energy variability, a gated integrator (Stanford Research SR250) is used, resulting in cycle-resolved laser energy measurements. This information is further supplied to the data acquisition system and is used for data processing purposes. The average laser energy is measured using a power meter (Newport 842-PE) connected to the detector head (818P-030-18HP). The experiments reported in this paper used average laser energies of approximately 43 mJ/pulse.

The images were acquired by a PIMAX2 ICCD camera (Princeton Instruments) equipped with a 78 mm UV objective (Electrophysics) with a maximum aperture opening f/3.8. Each frame is synchronized with the engine operation by an FPGA based engine controller (National Instruments cRIO/Drivven Inc.) which in turn triggers a delay generator (Stanford Research DG535). The delay generator is responsible for providing triggers for the laser lamp, Q-switch and ICCD gate with minimum jitter.

Engine data regarding in-cylinder pressure, common-rail pressure and injector needle lift has been acquired by a high-speed data acquisition system (AVL Indimeter 621). The engine crankshaft position signal required by the data acquisition system as well as the FPGA-based real-time engine controller was provided by an optical crank-angle encoder (AVL 365). This encoder is characterized by an optical resolution of 0.5CAD which is further multiplied electronically to gather data at 0.1 CAD resolution.

For these experiments the engine cooling and lubrication systems were conditioned to 60°C for 1 hour prior to initiation of the experiment. The n-heptane fuel was direct-injected into the combustion chamber while the anhydrous ethanol was injected into the intake system of the engine at a distance of approximately 1.5 m upstream of the intake port. This resulted in sufficient mixing and evaporation of the ethanol fuel prior to its delivery into the combustion chamber. Inlet temperature was maintained constant at 306 K by electrical heaters in order to compensate for ethanol evaporation effects. Intake gas was sampled approximately 300 mm upstream of the intake port and the ethanol mole fraction was measured using the FTIR spectrometer.

EFFECT OF ETHANOL MOLE FRACTION, TEMPERATURE AND EQUIVALENCE RATIO ON FORMALDEHYDE

In order to better understand the impact of three of the most significant factors impacting formaldehyde formation, i.e. ethanol fraction, temperature and equivalence ratio, chemical kinetic calculations were performed considering a zero-dimensional constant volume reactor (CHEMKIN PRO - Reaction Design Inc). A mechanism obtained by merging the Curran *et al.* n-heptane mechanism [13] and Marinov high temperature ethanol oxidation mechanism [98] was used to model the interaction between ethanol and n-heptane. This approach is similar to previous work performed by Hashimoto [36, 37]. The resulting mechanism has 563 species and 2652 reactions, compared to 561 and 2539 reactions available in the original

second version of the Curran n-heptane mechanism to account for additional detail regarding ethanol oxidation.

Figure 2 shows a comparison between the ignition delay data obtained using the Curran n-heptane mechanism, the Marinov ethanol mechanism and the merged mechanism for an initial pressure of 30 bar and an equivalence ratio 0.7. The ignition delay data is reported by considering the location of highest OH mole fraction, which is in close proximity to the peak of LTHR. It may be observed that the merged mechanism exhibits excellent agreement with the original mechanisms for the two conditions under which those mechanisms have been validated, i.e. 0% etOH and 100% etOH.

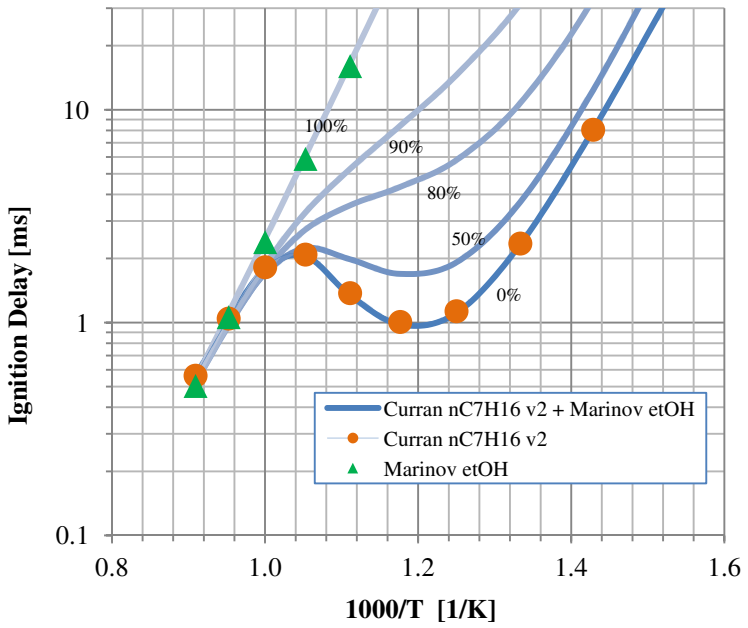

Figure 2. Ignition delay comparison for merged ethanol/n-heptane mechanism with Curran n-heptane oxidation mechanism and Marinov high-temperature ethanol oxidation mechanism; percentages indicate ethanol fraction in fuel mixture

For all analyses performed, the base point was assumed to be characterized by an initial temperature T_{ini}=800 K, initial pressure p_{ini}=30 bar, and an equivalence ratio ϕ=0.7 without ethanol presence in the initial mixture. The oxidizer was assumed to have a composition N_2-3.76:O_2-1. The results obtained from a series of zero-dimensional simulations are discussed further and presented in Figure 3.

The correlation between formaldehyde mole fraction and energy release associated with chemical reactions is investigated. In Figure 3 arrows point towards increased time. As it is evident in Figure 3a), ethanol is observed to have little direct impact on the maximum amount of formaldehyde formed subsequent to fuel low-temperature decomposition (during the NTC phase). However, it significantly reduces the energy release. This could be attributed to the indirect ethanol effect of OH scavenging which impacts the rates of other decomposition reactions. Further, formaldehyde mole fraction as well as maximum low-temperature heat release are observed (Figure 3b) to increase as the initial reactor temperature is decreased. Finally, as the equivalence ratio is changed in Figure 3c), both the maximum formaldehyde and energy release during cool-flame are increasing with an increase in considered equivalence ratio.

These observations will be used further in explaining the results obtained experimentally.

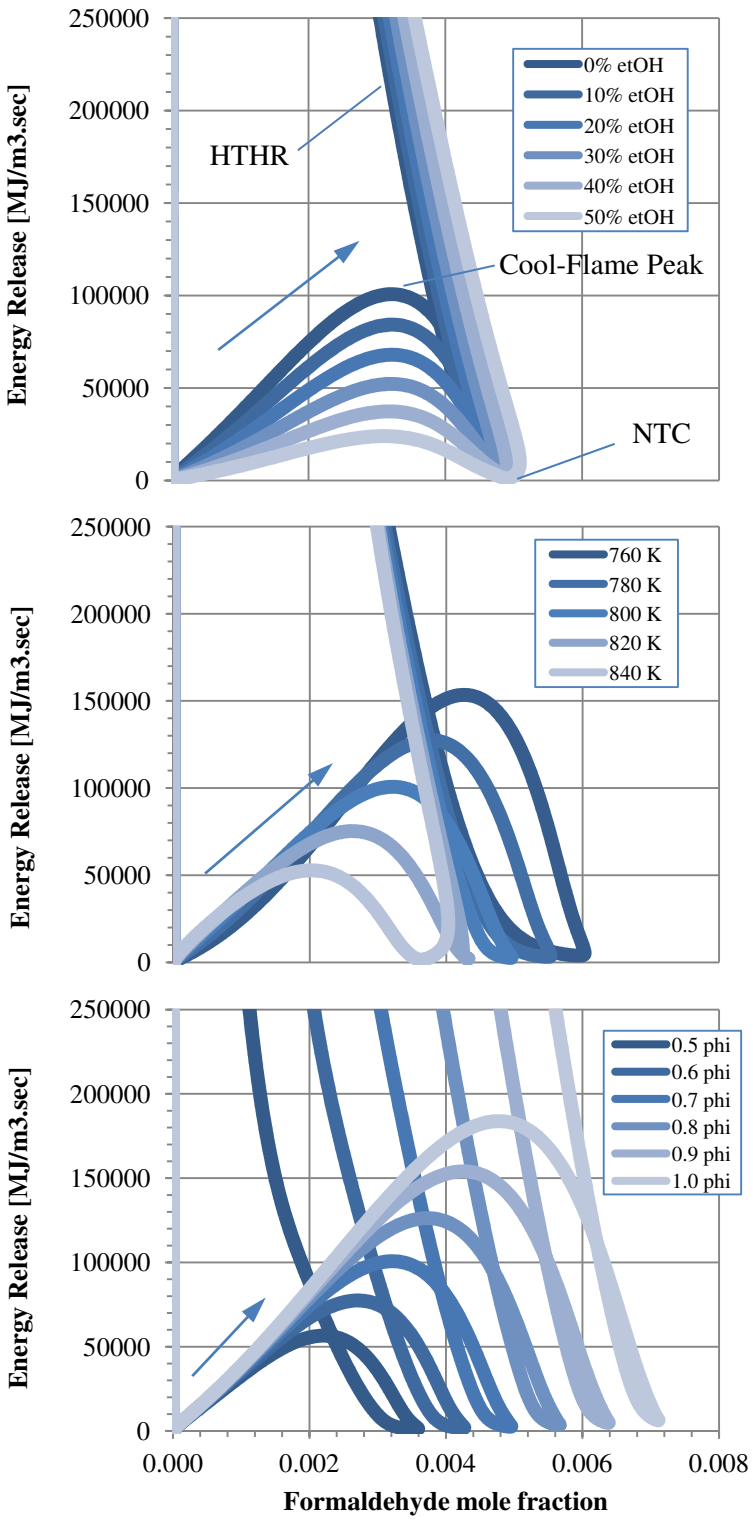

Figure 3. Impact on formaldehyde and heat release of a) ethanol b) temperature c) equivalence ratio

DATA ANALYSIS METHODS

Experimentally acquired PLIF images were analyzed using a set of MATLAB based programs developed specifically for this application. Formaldehyde PLIF images were thus corrected through background subtraction (I_{bg}) as well as laser-sheet non-uniformity (f_{laser}) and pulse-to-pulse laser energy variation ($E_{integrator}$ represents the laser energy measured by the gate integrator while $E_{average}$ represents the average laser energy measured by the Newport power meter). This was deemed necessary as the fluorescence saturation could not be reached with the available laser incident flux density. Thus the corrected pixel intensity becomes:

$$I_{corrected}(i,j) = \left[I_{raw}(i,j) - I_{bg}\right] * f_{laser}(i,j) * \frac{E_{integrator}}{E_{average}} \qquad (1)$$

where the background correction is applied based on a single-valued pixel count. This background correction is applied for each individual frame by considering a set of "virtual" pixels padded to the physical pixels resulting in a total logical frame size of 540x540 pixels compared to the actual CCD detector characterized by a 512x512 pixel array. The appended pixels provide a measurement of the CCD thermally induced counts as well as other potential sources but they are not influenced by radiation incident on the CCD detector. The average value of the appended pixels is considered to be the background correction factor. Additionally, the laser correction factor was characterized by slight two-dimensional heterogeneities due to the Gaussian beam profile used in this experimental work and was taken into account in the value of the f_{laser} correction

factor. As the laser sheet only covers a relatively small fraction of the CCD chip, images were cropped to cover the relevant signal domain prior to image analysis.

Multiple PLIF events were captured at the same engine conditions and cyclic image variability was observed to occur, as expected. Experimental data shown in the next section displays manually selected images deemed as representative of the image sample set available for each operating condition and crank angle position. Each image set consists of 30 PLIF measurements after removing outliers. A set of images intended to show the cycle-to-cycle variability of the LIF signal is shown in Figure 4.

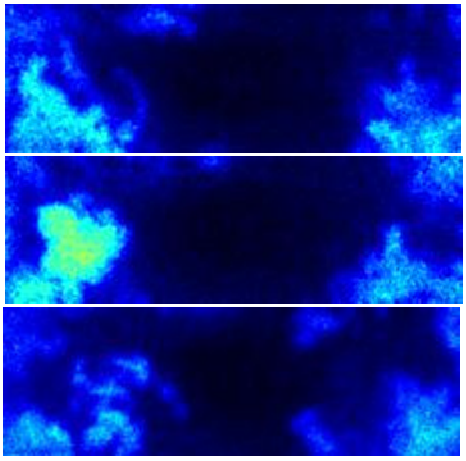

Figure 4 PLIF cyclic variation 5°aTDC w/o ethanol

Further, the standard deviation of image pixel count was considered as a measure of formaldehyde heterogeneity and was computed for each image considered. The average of the set of image standard deviations for each condition is reported within the experimental results section and is given for each condition and crank-angle position considered by:

$$\sigma_{avg} = \overline{\sigma\left(I_{corrected}(\iota, J)\right)}$$

EXPERIMENTAL RESULTS

The effect of ethanol intake injection on the partially premixed low temperature combustion investigated in the current study is shown in Figure 5. The experiments mantained a constant indicated mean effective pressure (IMEP) and location of peak premixed combustion (LPPC) by allowing the n-heptane direct injection timing and activation time to vary as needed. It may be observed that as the amount of ethanol is increased, the n-heptane fuel needs to be injected earlier due to the chemical inhibiting effect of ethanol, while the magnitude of the peak of premixed combustion decreases, allowing for the "stretching" of the energy release. Ringing is noticeable without ethanol addition due to the rapid release of energy and high rate of pressure rise. As the amount of ethanol is increased, the ringing gradually disappears. It can be thus concluded that under low temperature conditions ethanol allows the maximum engine load to be increased for a given allowable rate of pressure rise. The observed impact of ethanol on the engine indicated data is in agreement with previous studies [22, 64, 65, 66].

The addition of ethanol has a strong impact on the cool-flame oxidation chemistry associated with the low-temperature heat release (LTHR). The LTHR is stretched over a longer period of time and the magnitude of its peak decreases as the amount of ethanol increases. This is consistent with the expected inhibiting effect of ethanol.

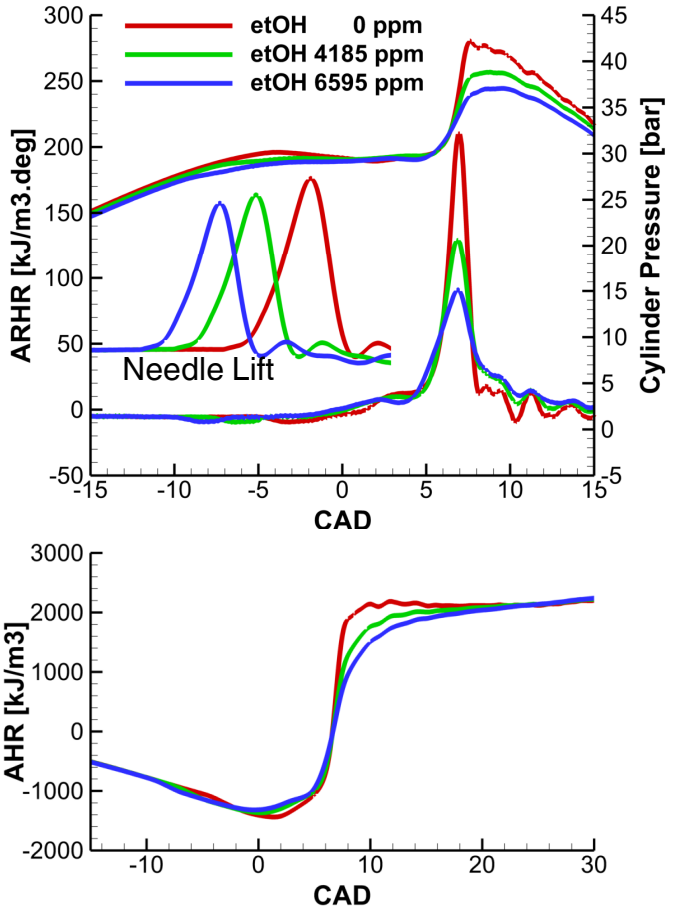

Figure 5 Effect of ethanol on in-cylinder pressure, apparent rate of heat release (ARHR) and cumulative heat release (AHR)

As hypothesized in previously cited publications [22, 64, 65, 66], the dual fuel combustion of ethanol and diesel fuel is characterized by an increased reactivity stratification due to dissimilar chemistry of the two fuels considered, along with competition over combustion radicals responsible for the hydrogen abstraction reaction step [22, 37]. In order to investigate the effect of ethanol on formaldehyde stratification this work used formaldehyde PLIF during the cool-flame, NTC and high-temperature heat release (HTHR) processes.

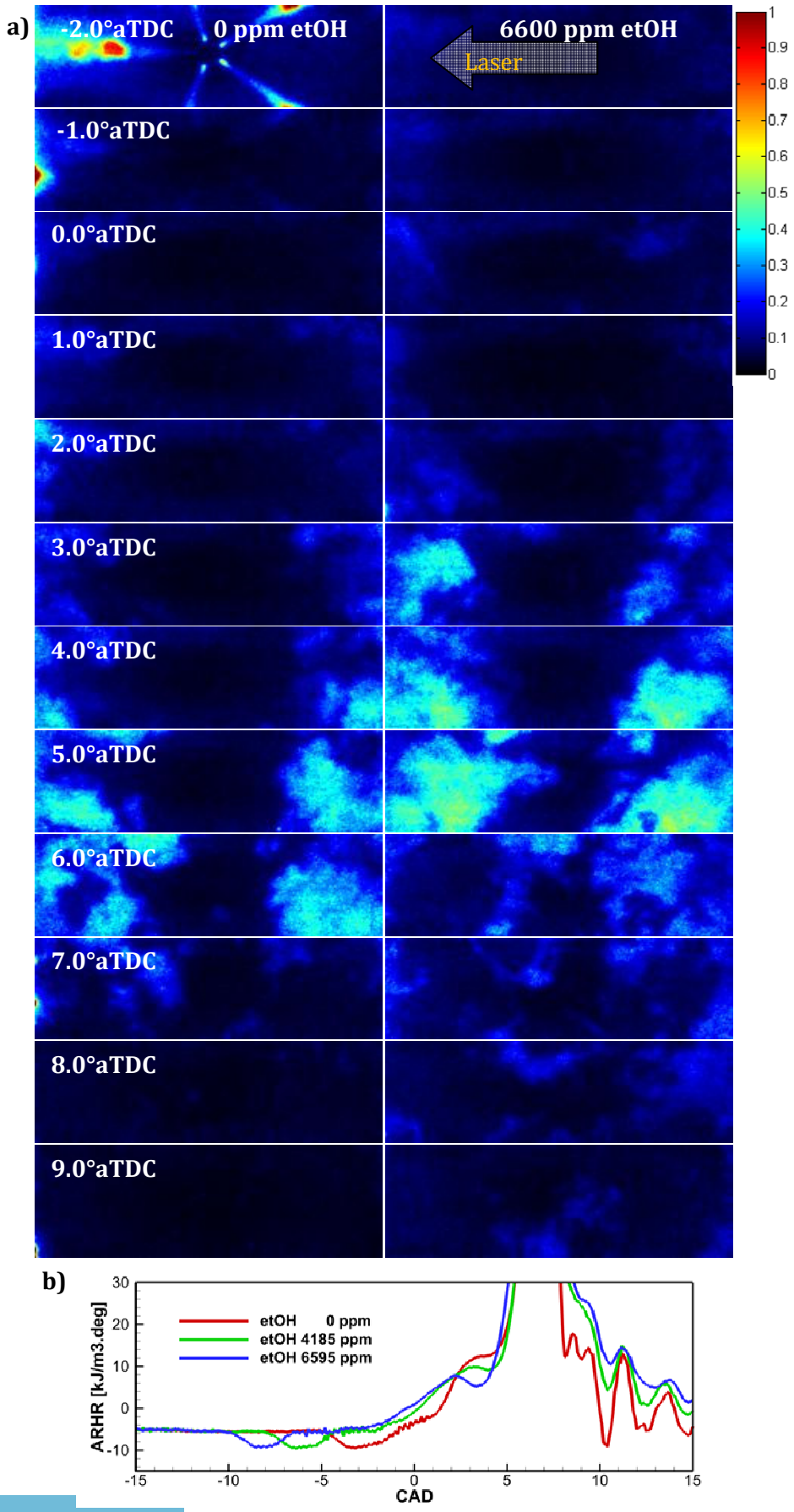

Figure 6 a) PLIF images during the LTHR, NTC and HTHR b) ARHR data with a focus on low temperature energy release

Due to concerns regarding the impact of a complex fuel such as ULSD on the fluorescence signal obtained during engine experiments due to polyaromatic hydrocarbons (PAH), n-heptane was chosen as the "high reactivity" fuel. In order to provide the fuel with the necessary lubricity properties required by the high-pressure injection system, n-heptane was doped with lubricity additive (Infineum R655) resulting in a volume fraction of 500 ppm. The amount of additive was found to provide a satisfactory operation of the experimental setup, and concerns regarding the impact of this additive on the fluorescence signal were previously addressed by Donkerbroek et.al. [118]. Combustion imaging data (not currently reported) collected with a high-speed visible range camera indicated that the combustion both with and without ethanol was basically soot-free, eliminating concerns regarding the influence of the soot blackbody radiation on the measured fluorescence signal.

First, imaging samples of formaldehyde PLIF signal collected between -2°aTDC and 9°aTDC at 1° increments are shown in Figure 6a) above. The evolution of formaldehyde distribution starts from the combustion chamber wall, where fuel impingement occurs and the highest equivalence ratio is expected. Due to the fuel jet orientation, the laser sheet is located slightly above the impinged wall surface. Some interaction between the laser sheet and the spray is visible in the early stages of the 0 ppm etOH condition. This is most probably caused by droplet laser scattering which was not completely rejected by the GG385 filter. As ethanol is added, the injection needs to be advanced in order to maintain the same LPPC and

the injection event ends at about -5°aTDC (Figure 5). Therefore no fuel spray is present at the time the first LIF image is shown.

Next, as time advances, n-heptane evaporates resulting in a stratification of the equivalence ratio distribution within the combustion chamber. When ethanol is used, the n-heptane evaporation occurs in a fairly homogenous mixture of ethanol and air. Thus, for the dual-fuel operation, variable local ethanol fraction as well as equivalence ratio are expected.

Further, formaldehyde quickly proceeds to increase in concentration and move further towards the middle of the combustion chamber. As ethanol is added into the intake system of the engine (right-hand side images in Figure 6a), due to an earlier injection timing required to maintain a constant LPPC, formaldehyde initially covers a larger area of the combustion chamber. However the formaldehyde evolution is observed to be fairly similar, with the dual-fuel operation experiencing a longer period where formaldehyde is present, as expected. These experimentally observed results could be interpreted by considering the previously discussed zero-dimensional chemical kinetic model (Figure 3). It was shown that ethanol has no direct impact on the maximum amount of formaldehyde formed for a given set of operating parameters.

However, ethanol does introduce a phase-shift in formaldehyde formation which should in turn be responsible for increased formaldehyde stratification in the actual heterogeneous combustion system. Additionally, the chemical kinetic model predicts that the formaldehyde amount is increased by decreased temperatures as

well as increased equivalence ratio. This could most probably be caused by the longer residence time of the direct injected n-heptane fuel droplets when ethanol is added due to the increased ignition delay. This in turn results in increased evaporation and, as more liquid n-heptane undergoes evaporation, local temperatures drop and equivalence ratios increase.

Therefore, two competing effects may be identified. The first one is the direct ethanol effect of suppressing the magnitude of low temperature energy release (Figure 3a) while the second is enhanced low temperature energy release caused by dropping temperatures and increased equivalence ratios discussed above (Figure 3b and c). It appears, based on the experimentally determined magnitude of the energy release reported in Figure 6b), that ethanol has a dominant effect, as the magnitude of the low temperature energy release is observed to be reduced by ethanol presence.

Finally, as the combustion process enters the HTHR phase, formaldehyde is depleted by the high-temperature oxidation reactions in favor of hydroxyl radical production as reported previously by Collin et.al. [95].

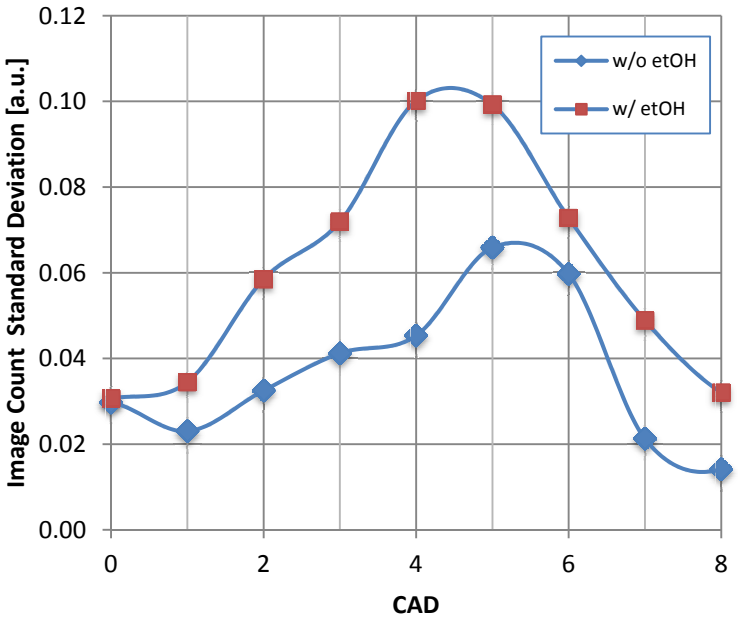

Figure 7 Evolution of average image standard deviation

In order to provide a measurement of the formaldehyde distribution heterogeneity, average image standard deviation computed as previously described in the "Data Analysis Methods" section is presented in Figure 7. Ethanol addition appears to increase the image standard deviation quite significantly while the phase shift in peak standard deviation is consistent with the shift in the occurrence of the low temperature chemistry. The increased standard deviation implies an increase in formaldehyde distribution heterogeneity.

Discussion regarding the experimental observation of reactivity stratification

A core premise for the RCCI dual fuel operation is the concept of reactivity stratification. The correlation between reactivity stratification and formaldehyde appears to be quite complex, nonlinear and perhaps non-monotone, thus an

increase in formaldehyde heterogeneity cannot be attributed directly to increased reactivity stratification at this time.

Additionally, there seems to be a need for a rigorous and generalized definition of "reactivity", which is a fundamental concept behind the dual-fuel partially premixed combustion mode. In the numerical simulation work performed by Splitter et.al. [22], reactivity is defined based on the research octane numbers (RON) associated with the fuels considered. However, this definition holds for as long as fuel decomposition is not significant. As soon as fuel decomposition occurs, reactivity is not longer properly defined according to the aforementioned definition and observation of reactivity becomes a challenge.

Furthermore, while the mixture reactivity and reactivity stratification within the fuel mixing stage could be observed experimentally using techniques such as planar laser induced exciplex fluorescence (PLIEF) [119], as soon as low or high temperature oxidation reactions initiate, this type of experimental observations is no longer applicable.

Probing reactivity and reactivity stratification throughout later stages of combustion requires most probably assigning a species as reactivity marker and following its behavior through either experimental techniques or numerical studies. Such an approach was suggested by Gong [56], assuming CO as the reactivity marker. Within an optically accessible engine the reactivity stratification throughout the high-temperature heat release stage could be investigated using a two-photon CO LIF scheme such as the one proposed by Seitzman *et al.* [120].

SUMMARY/CONCLUSIONS

In the work currently reported, the effect of ethanol on partially premixed low temperature combustion was investigated using Planar Laser Induced Fluorescence (PLIF) in an optically accessible engine.

Towards this purpose, the engine load – IMEP – and combustion phasing – LPPC – were maintained constant across operating conditions by adjusting fueling rate and injection timing. Ethanol was observed to inhibit combustion, increase the premixed combustion duration as well as significantly impact the magnitude and duration of the LTHR associated with the cool-flame oxidation, confirming previously published results.

Further, formaldehyde PLIF images showed that for the partially premixed combustion mode studied, the initial site of formaldehyde formation is in close proximity to the combustion chamber wall, where due to the spray impingement process the highest equivalence ratio is expected. Ethanol is observed to increase the length of the low-temperature combustion stage as suggested by the presence of formaldehyde in the PLIF data. As the peak of HTHR is reached, formaldehyde is observed to be consumed in agreement with previous studies.

Meanwhile, chemical kinetic modelling indicated that ethanol is not expected to have a significant direct impact on the maximum amount of formaldehyde observed throughout the early stages of combustion. Additionally, ethanol is expected to decrease the magnitude of low-temperature heat release. Indirect ethanol effects result in increased local equivalence ratio and decreased local

temperature due to longer ignition delay, which in turn result in increased local formaldehyde formation.

In terms of low-temperature energy release, two competing effects are identified. Ethanol is expected to decrease the low temperature energy release, while temperature and equivalence ratio are expected to increase it. As a net decrease in low temperature energy release is observed experimentally, it was concluded that ethanol plays a dominant role.

Further, average PLIF image standard deviation seems to suggest an increase in formaldehyde heterogeneity as ethanol is added. However, due to the complex relationship between formaldehyde and reactivity, the increased formaldehyde heterogeneity could not be attributed directly to an increased reactivity stratification at this time. Moreover, a discussion supporting the need for a rigurous and general definition of reactivity was presented along with possible experimental techniques that could be employed to measure reactivity and reactivity stratification.

5.2 Effect of ethanol on Partially Premixed ULSD combustion

In order to provide insight into the dual-fuel operation for distillate fuels, a series of experiments was carried out using ethanol and ULSD. While the complex chemical composition of the distillate fuel results in increased analysis uncertainty, it is nonetheless informative to provide a view of its behavior in dual-fuel combusting systems and compare its results with the previously observed n-heptane results.

Additionally, these observations provide validation of the n-heptane results, as n-heptane is not customarily used as a practical fuel for engine operation.

The ULSD fuel properties used in these experiments are reported in Table 8 and Fig. 5.18.

Table 8. ULSD fuel properties

Derived Cetane Number	48.3
Density@15°C [kg/m^3]	842
Lower Heating Value [MJ/kg]	41.2
Kinematic Viscosity @40°C [mm^2/sec]	2.479
Bulk Modulus [GPa]	2.562

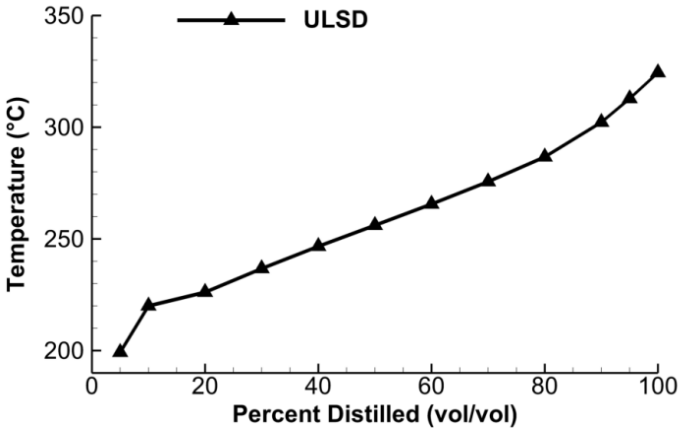

Fig. 5.18. ULSD distillation curve

5.2.1 *Effect of Ethanol on the In-Cylinder Pressure Measurement*

Experiments using ethanol and ULSD followed a similar approach, in order to provide a means of comparison between the two operating modes. To this purpose, comparable energy delivery was maintained while allowing the injection pulses to change accordingly. The same amounts of ethanol were delivered for both cases and an LPPC position around 7°aTDC was maintained in all cases. Table 9 below provides the experimental conditions.

Table 9. Operating points

	0.0 ms* etOH	**2.0 ms* etOH**	**3.0 ms* etOH**
Intake Ethanol mole fraction [ppm]	0	4200	6600
ULSD Injection timing (demand)	9.5	12.0	13.5
Common-Rail Injector Solenoid activation time [ms]	0.48	0.455	0.43
ULSD delivery rate [mm^3/cycle]	13.4	11.7	10.1
Corrected Net IMEP [bar]	2.8	2.8	2.8
LIF experiments [y/n]	y	n	y

* PFI activation duration for 2 barg injection pressure

In-cylinder pressure measurements are reported in Fig. 5.19 below. The results are very similar to the ones obtained using n-heptane and ethanol. Ethanol is observed to have the same heat release "expanding" effect which allows for the increase in maximum engine load allowable.

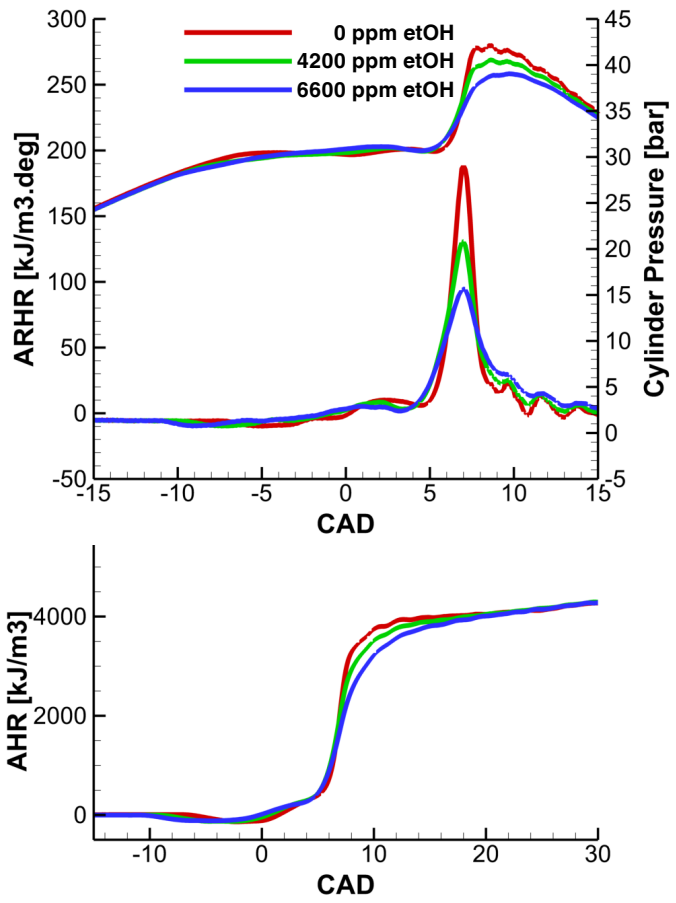

Fig. 5.19. Effect of ethanol on in-cylinder pressure, apparent rate of heat release (ARHR) and cumulative heat release (AHR)

Further, a plot comparing the behavior of n-heptane and ULSD respectively is shown in Fig. 5.20. Besides slight differences in motoring pressure (due to slightly different intake temperatures considered in these two experiments) and the slightly higher total energy release used in the case of ULSD combustion, the two fuels exhibit very similar combustion characteristics and autoignition data obtained using n-heptane should be directly applicable towards the understanding of the interaction between ethanol and the more complex ULSD fuel. In order to maintain

the same LPPC, diesel fuel had to be injected slightly earlier, which is consistent with the lower cetane number associated with ULSD (DCN_{ULSD} = 48 vs $CN_{n\text{-}heptane}$ = 56).

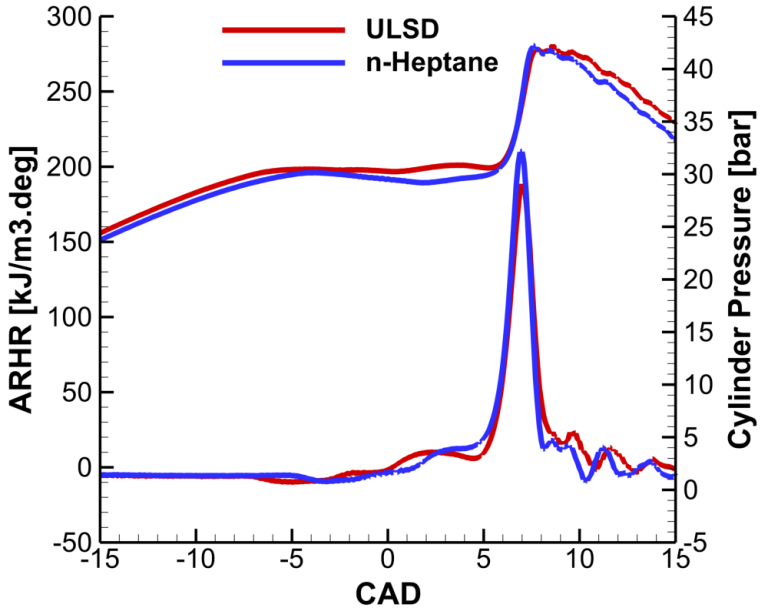

Fig. 5.20. Comparison of in-cylinder pressure and corresponding ARHR between ULSD and n-heptane partially premixed combustion (no ethanol addition)

Next, the results of a series of optical diagnostics are presented. These tests are again similar to the ones performed with n-heptane and are mainly intended to show the difference between the model fuel (n-heptane) and a practical fuel (ULSD).

5.2.2 Visible High-Speed Imaging of Combustion

The high-speed CMOS camera (Phantom v7.3) was used to collect combustion imaging within the visible spectral range. The experimental setup for the ethanol/ULSD investigation was the same as the one used for the ethanol/n-

heptane investigation. The resulting images, which were acquired at 0.5 CAD intervals, are reported in Fig. 5.21 from single combustion events.

While ethanol addition is observed to decrease the blue-flame chemiluminescence as previously noticed for the ethanol/n-heptane combustion (Fig. 5.10), the magnitude of the decrease is significantly smaller than the one identified under ethanol/n-heptane operation. This observation is both interesting and unexpected given the similarity between the two combustion modes studied from a pressure trace and heat release perspective. In the following paragraphs a potential mechanism for the observed behavior is described.

Spectral measurements performed for both ethanol/n-heptane combustion (section 5.1.7) and ULSD combustion (not reported here) did not indicate the presence of CO flame bands. While this could suggest a possible pressure broadening of the CO system due to the relatively high-pressure environment at the time of combustion, it is the author's opinion that this scenario is less likely and the CO radiation is mostly due to the CO continuum. Gaydon [117] reported that in hot flames, such as the blue flame associated with the HTHR, the continuum is dominant. This conclusion is based on the investigation of flat diffusion flames.

Thus, the formation of the CO flame continuum responsible for the blue-flame radiation emission might not be as severely impacted by ethanol presence as in the case of ethanol/n-heptane operation due to the effect of fuel molecular structure associated with the ULSD fuel that changes the rate of the following reaction:

$$CO + O = CO_2 + h\nu$$

Several authors, including Gaydon, favor this reaction as the source of the CO flame continuum compared to a more complex electronically excited radiation formation model.

Further into the high-temperature combustion process, bright, luminous "spots" occur. While the location and intensity if these spots vary from cycle to cycle, they occur each cycle. The intensity and spectral distribution measurements indicate that these "spots" are characterized by a black-body type radiation emission characteristic of high-temperature soot. They are most probably caused by low-momentum droplets left in the combustion chamber as the injection event ends. Due to their low momentum, the droplets are less likely to break-up or evaporate and they act as fuel-rich pockets where diffusion-controlled combustion takes place locally.

As the high-temperature combustion proceeds, pool fires become evident on the piston bowl walls due to liquid fuel impinged and deposited on the lower temperature piston surface.

The lack of soot production associated with n-heptane combustion allowed for a larger number of combustion cycle visualization prior to optical window fouling, which helped the acquisition of experimental data. This is not however the case with ULSD combustion, where the impact of soot as well as other types of deposits on window fouling is significant.

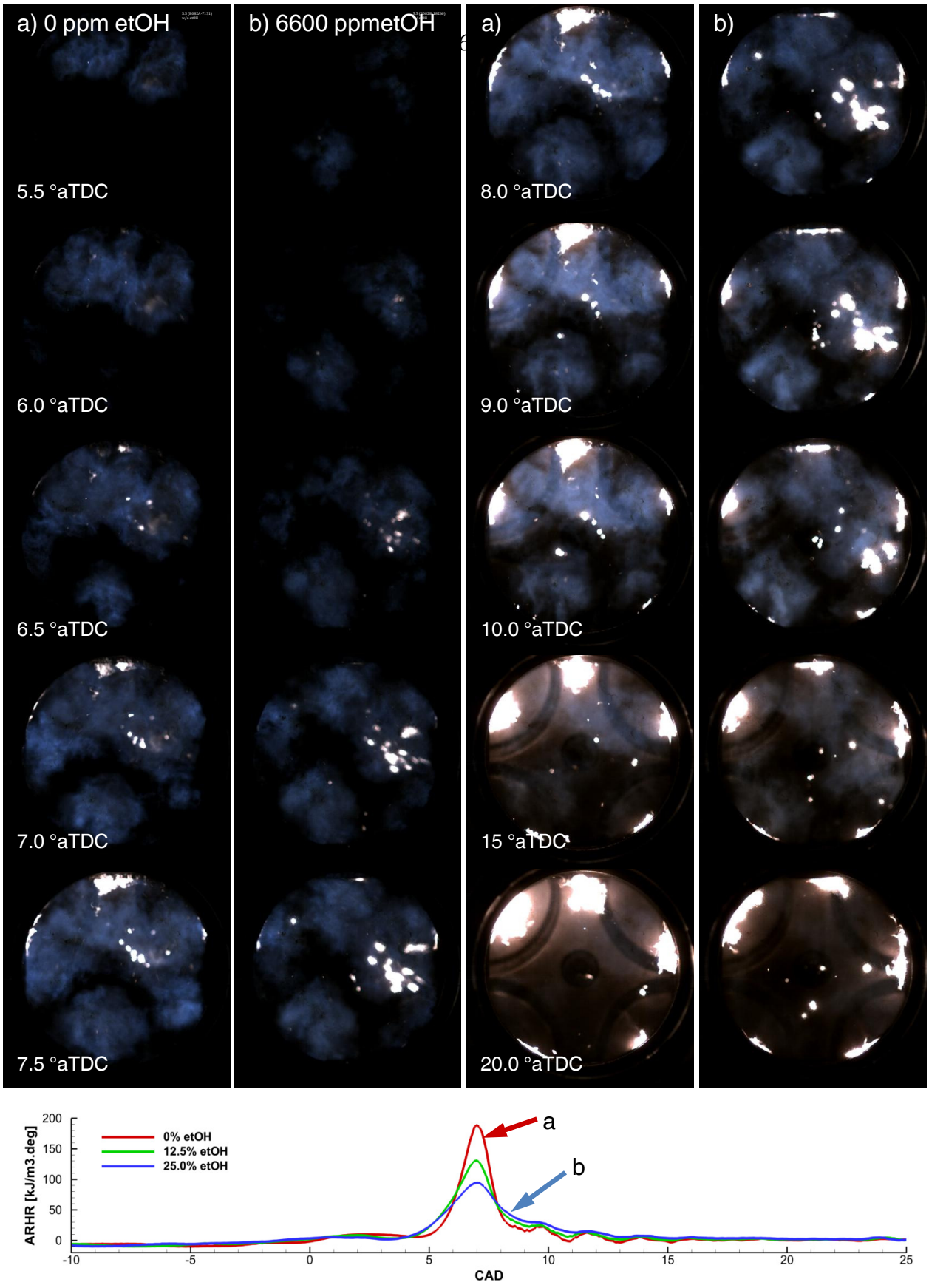

Fig. 5.21. Single-cycle high-speed visible range images ethanol/ULSD combustion a) without ethanol b) with ethanol

Both ULSD and n-heptane combustion exhibit similar trends in terms of the homogeneity of the premixed combustion. The combustion of both fuels exhibit slight spray to spray variability of the observed combustion process. A possible source for this variability is the spray asymmetry caused by the VCO nozzle used in these experiments.

5.2.3 Planar Laser Induced Fluorescence of Formaldehyde

PLIF data was collected for the ethanol/ULSD partially premixed combustion and is reported in the following paragraphs. Throughout this section issues related to the LIF signal interference will be addressed, particularly from poly-aromatic hydrocarbons (PAH). While this is an issue that cannot be easily addressed experimentally, a comparison with the ethanol/n-heptane data is nonetheless informative.

As described in section 5.1.8, a raw LIF signal correction scheme is required in order to compensate for various effects, such as background noise, laser sheet non-uniformity and pulse to pulse energy variation. With respect to the method employed for the ethanol/n-heptane investigation, additional correction parameters were required under ethanol/ULSD operation. These correction methods are described below.

In order to provide sufficient statistical data, fuel was injected for a significant number of cycles, which resulted in a relatively important amount of soot and volatile organic compounds to be deposited on the window of the optically accessible engine. With the aim of accounting for the reduction in window

transmissivity throughout each firing cycle, the window deposits transmissivity was measured at the end of the test. For this measurement, the sapphire window was removed from the engine and the absorption signal of a broadband light-source with both the dirty window as well as a clean window. Each signal was obtained by averaging 1000 image samples acquired with the PIMAX 3 ICCD camera. The signals obtained this way were used to compute the deposits transmissivity. The transmissivity of the image gathering optics as well as the combustion chamber window should not impact the results, as their effect is considered in both measurements. Additionally, the same optical filter pack used for the main experiment was employed in the measurement of the window transmissivity as well.

An example of a window transmissivity distribution is shown in Fig. 5.22. It shows also the combustion chamber area covered by the laser sheet which is of interest for this work.

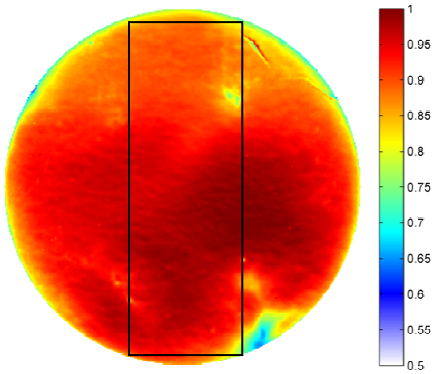

Fig. 5.22. Window deposits transmissivity

So as to provide a window deposits correction factor for each individual cycle, a linear transmissivity decrease is assumed between the beginning of the experiment (clean window) and the end of the experiment (deposit transmissivity measured). If one assumes a constant deposition rate and small values of the deposits transmissivity, the exponential function associated with the Beer-Lambert law may be approximated with a linear function. This in turn allows the linear variation of window transmissivity with time. Thus the corrected pixel intensity becomes:

$$I_{corrected}(i,j) = \left[I_{raw}(i,j) - I_{bg}\right] * f_{laser}(i,j) * \frac{E_{integrator}}{E_{average}} * \frac{1}{\tau_{deposits(i,j)}}$$

where all the components of the corrected intensity have been described in section 5.1.8, except $\tau_{deposits(i,j)}$ which is obtained as described previously.

Due to concerns regarding the impact of a complex fuel such as ULSD on the fluorescence signal obtained during engine experiments, two spectral measurements were carried out. During the first measurement, while the engine was stationary, formaldehyde vapors from an aqueous solution (37% v/v) were delivered in-cylinder and spectral measurements of fluorescence were made. The resulting low-pressure and low-temperature formaldehyde spectrum plotted in Fig. 5.23 shows clearly identifiable peaks centered around the previously reported emission lines associated with the $^1A'' - {}^1A_1$ transition [117].

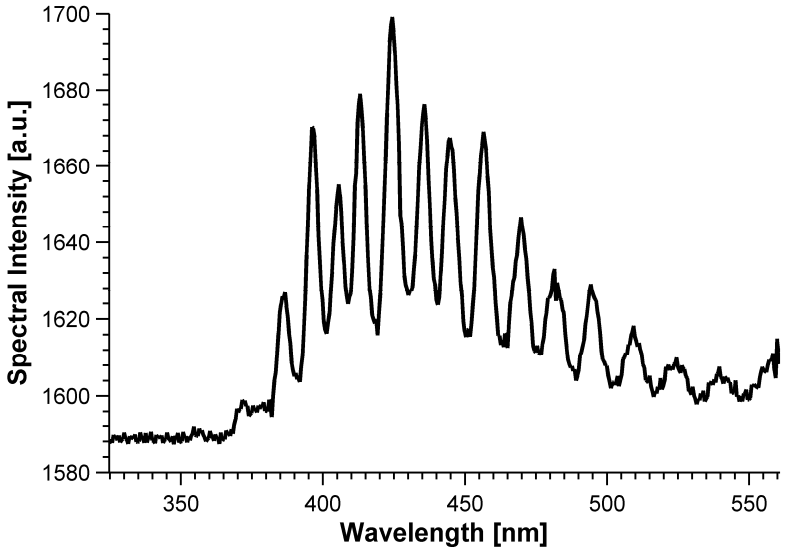

Fig. 5.23. Low pressure, low temperature formaldehyde spectrum (not corrected for optics efficiency)

Similar data was collected at 3 deg aTDC, i.e. the peak of the cool-flame under the conditions studied, and the data is shown in Fig. 5.24 where it is quite obvious that the peaks are less evident due to the increased pressure (around 30 bar) and temperature (around 715K). However, the location of these peaks is consistent with formaldehyde emission lines and no other spectral lines are noticeable. It is also evident that a very small amount of laser radiation escapes the GG385 filter, but its relative intensity is negligible. While additional spectral lines were not identified, a PAH continuum might be present and this spectral measurement cannot confirm or deny the presence of PAH. LIF data discussed later addresses further the issue of PAH interference.

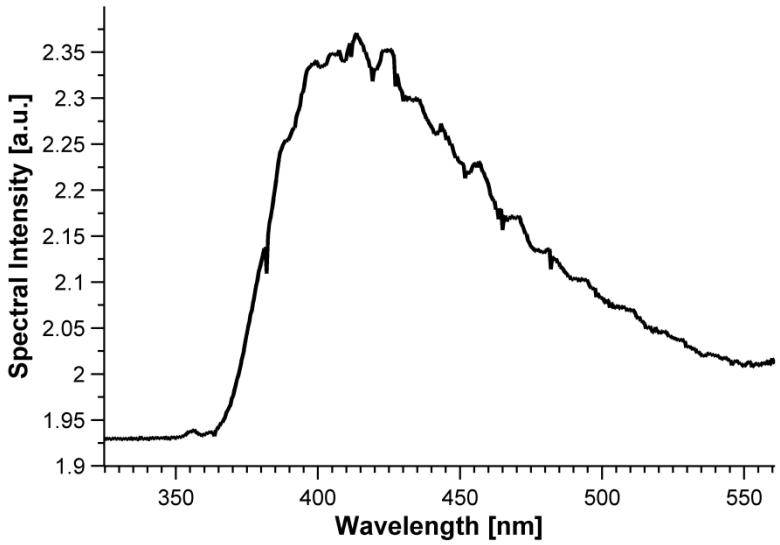

Fig. 5.24. Uncorrected formaldehyde spectrum during cool-flame

Imaging samples of formaldehyde PLIF signal collected between -1°aTDC and 7°aTDC at 1° increments are shown in Fig. 5.25a. In a similar fashion as the data reported for ethanol/n-heptane combustion, the evolution of formaldehyde distribution starts from the combustion chamber wall, where the fuel impinged and the highest equivalence ratio is expected. As time advances, formaldehyde quickly proceeds to increase its concentration as well as move further towards the middle of the combustion chamber. When ethanol is added into the intake system of the engine, as shown in the right-hand side images in Fig. 5.25a, due to an earlier injection timing required to maintain a constant LPPC, formaldehyde covers initially a larger area of the combustion chamber.

Signal intensity cannot be directly compared with Figure 6 in section 5.1.8, as slight experimental setup changes occurred affecting mainly the laser sheet

positioning and thickness. However, the two data-sets can be compared qualitatively.

One of the most significant observations is that while Figure 6 in section 5.1.8 suggests that by the time the combustion process reaches the LPPC, i.e. 7°aTDC, most of the formaldehyde has been already depleted by a strong interaction with the OH radical which now becomes dominant. However, the data in Fig. 5.25a does not show that. Actually, the signal intensity observed is increasing rather than decreasing as expected.

This observation is strong evidence that the LIF signal is indeed affected by PAH interference, which is expected to increase as during the HTHR stage. Thus, at least in the latter images, where PAH interference appears to be significant, the LIF signal is actually indicative of the overall rate of oxidation reactions and activity of the chemical oxidation process rather than formaldehyde concentration.

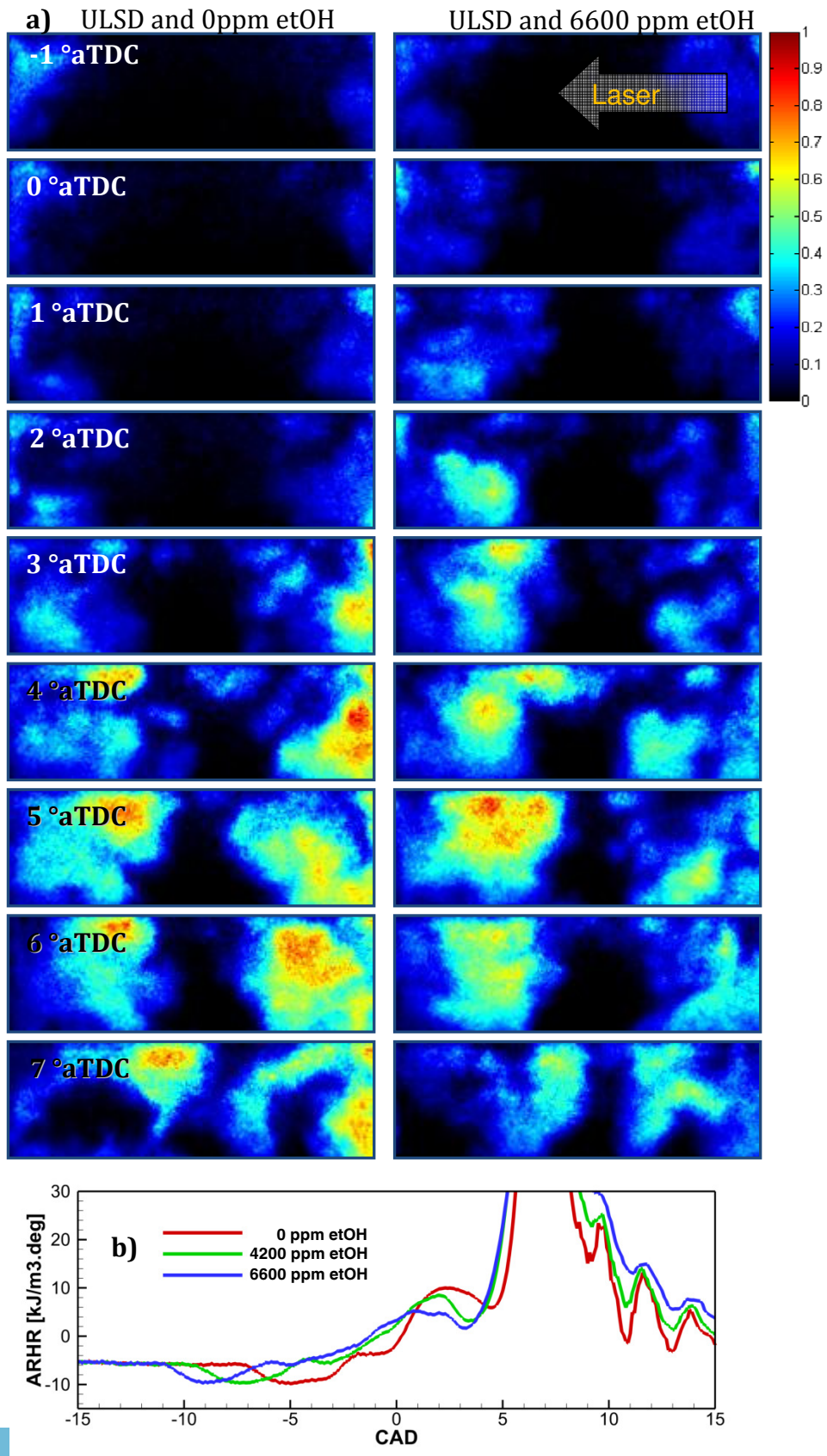

Fig. 5.25. a) PLIF images during the LTHR, NTC and HTHR
b) ARHR data with a focus on low temperature energy release

While the LIF signal cannot be fully attributed to formaldehyde, as in the case of ethanol/n-heptane combustion, a comparison will be attempted, as the formaldehyde component of the signal is expected to be dominant in the early stages of the autoignition process.

Both the results obtained in Fig. 5.25a and the ones from Figure 6a section 5.1.8 indicate a similar activity zone restricted mostly around the combustion chamber wall area. The slight differences can be attributed to the fuel cetane number differences between n-heptane the ULSD, which resulted in different physical ignition delays, as well as the slight change in laser configuration between the two sets of experiments mentioned previously. The results seem to indicate very similar behavior of the two fuels (n-heptane and ULSD) and the results obtained using the model fuel (n-heptane) are directly applicable towards the understanding of dual-fuel combustion of ULSD.

Chapter 6. "Simulation Results"

The previously discussed experimental results have been used to provide modeling boundary conditions for KIVA4-WSU based numerical simulations introduced in section 4.3. The focus of this chapter is to provide supporting data regarding model validation and provide additional insight into the partially premixed dual-fuel operation previously investigated. The simulation work focused on the investigation of n-heptane/ethanol dual fuel operation due to the increased reliability of chemical kinetic data for single molecule fuels as opposed to complex distillates such as ULSD.

6.1 Model Validation

First, in Fig. 6.1 is shown the comparison between the experimentally determined cylinder pressure and apparent rate of heat release and the simulation results. Good agreement is maintained between the model and experiment in terms of combustion phasing, combustion duration as well as low temperature heat release. The CFD model prediction concerning the low-temperature behavior of ethanol-heptane combustion slightly overpredicts the experimentally observed apparent energy release.

Further, Fig. 6.2 and Fig. 6.3 show the comparison between the formaldehyde LIF measurements obtained experimentally and the formaldehyde mass fraction determined through modeling. Again, for the heptane partially premixed combustion, excellent agreement between experimental and modeling data is observed.

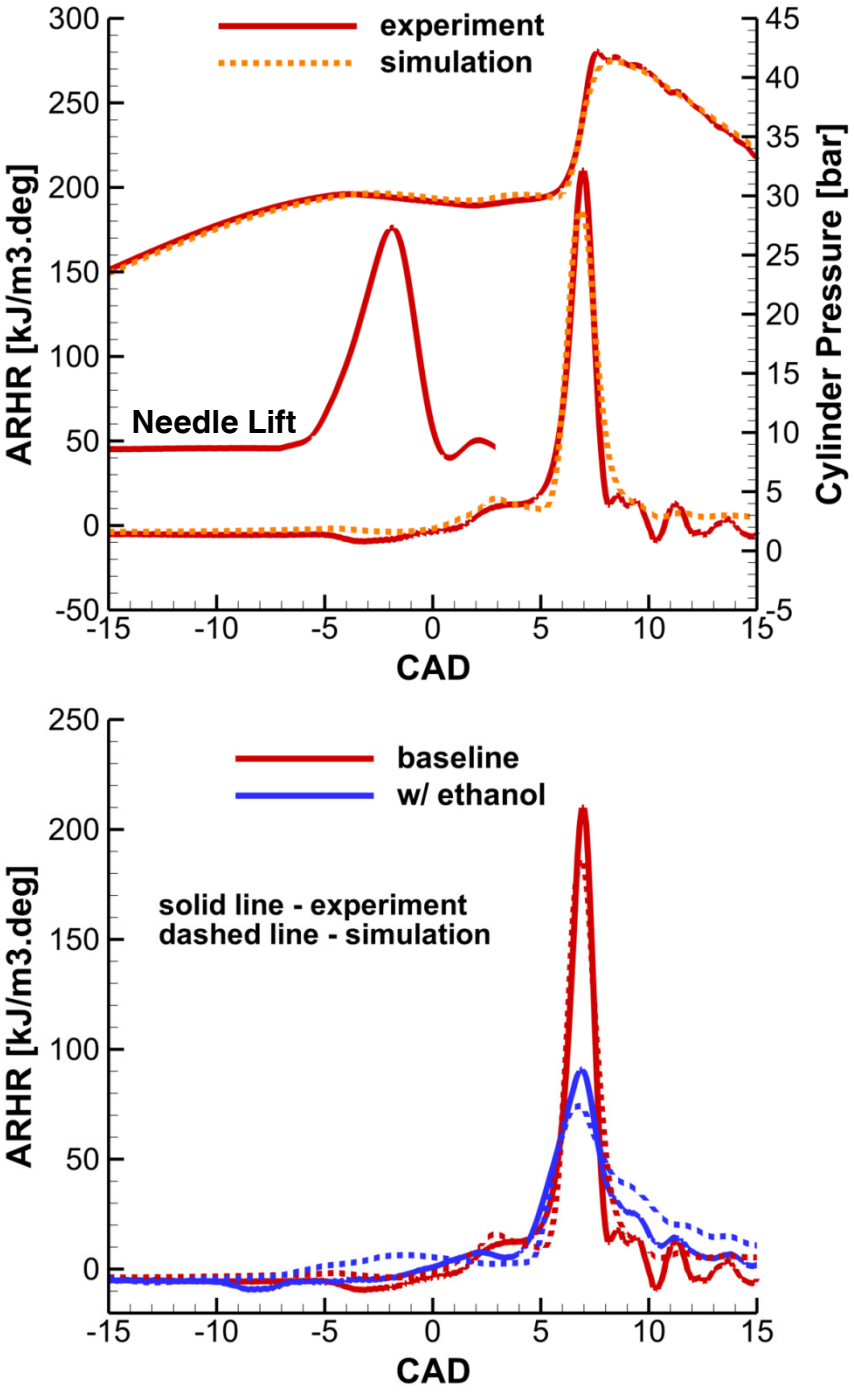

Fig. 6.1 Comparison between experimental and modeling pressure and energy release data

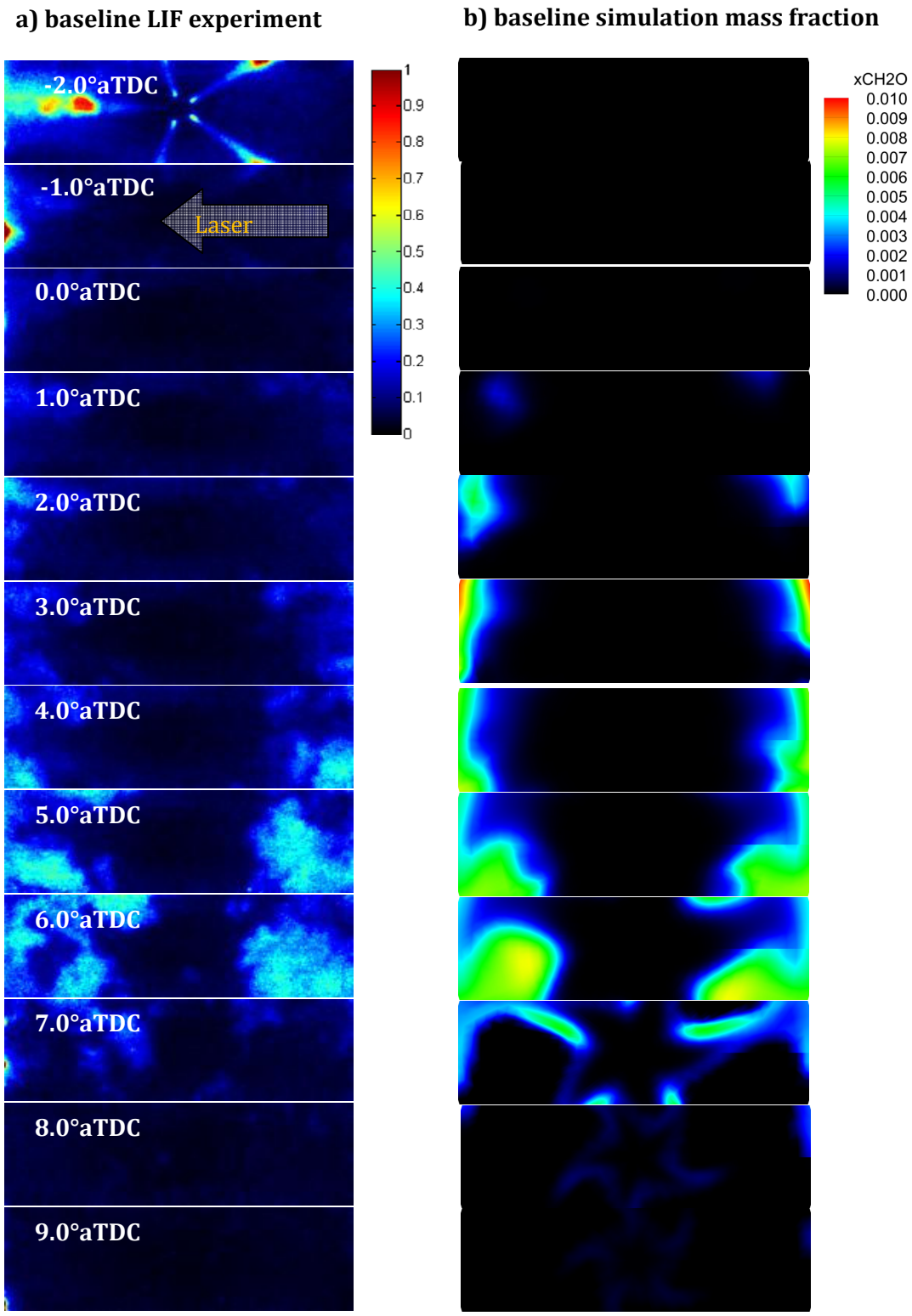

Fig. 6.2 Baseline - comparison between experimental formaldehyde LIF data and modeled formaldehyde mass fraction

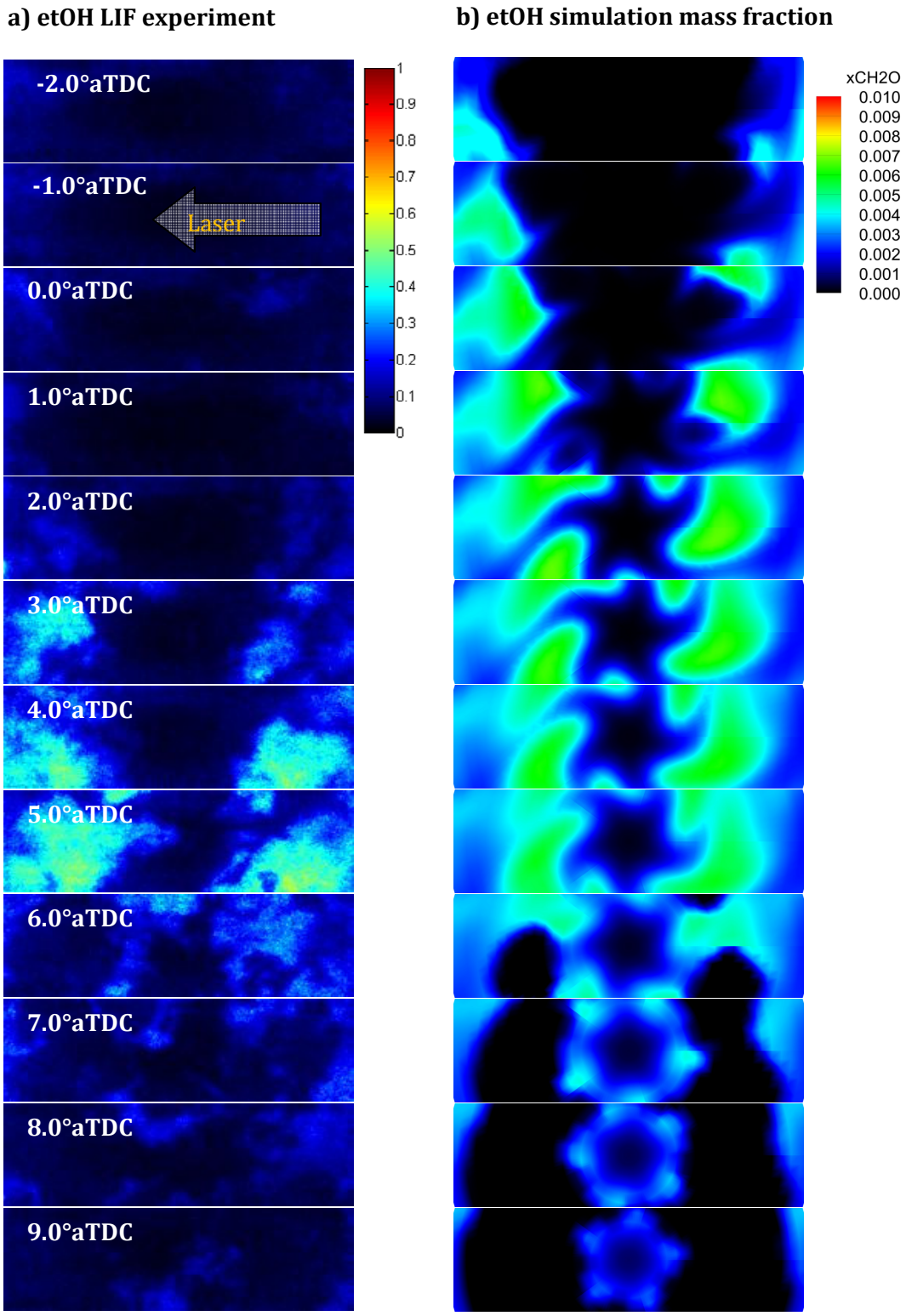

Fig. 6.3 Ethanol/Heptane - comparison between experimental formaldehyde LIF data and modeled formaldehyde mass fraction

The lack of formaldehyde mass fraction during the initial stages of autoignition (-2, -1 CAD aTDC) is expected, as the LIF data is most probably impacted at those early stages by the interaction between the Nd:YAG 355nm laser sheet and the n-heptane spray.

The regions devoid of formaldehyde observed during the latter stages of combustion are associated with the high-temperature energy release and the formation of the hydroxyl radical as previously reported [46].

However, for the ethanol/heptane data shown in Fig. 6.3, while the predicted locations of peak formaldehyde formation as well as formaldehyde consumption follow quite closely the experimentally observations, the model predicts a much earlier formation of formaldehyde. This was partially evident in the ARHR data associated with the heptane-ethanol simulation (Fig. 6.1), that showed significantly longer LTHR compared to the experimental data. In order to improve the low-temperature accuracy of the heptane-ethanol kinetic model, additional low temperature experimental data is needed, such as ignition delay for various blends to ethanol and n-heptane.

Further, the modeling results will be analyzed with a special emphasis on mixture formation and high temperature energy release.

6.2 Modeling Results Discussion

6.2.1 Mixture Formation

The mixture stratification prior to the initiation of the low-temperature reactions is shown in Fig. 6.4. The data is reported at 7.8°bTDC; at this condition the model predicts that all the injected fuel has been fully evaporated (no droplets are present) and no significant fuel decomposition has been yet initiated. By the time the LTHR combustion phase starts this stratification is expected to be reduced to lower levels.

However, as previously discussed in section 5.1.8, determining the amount of fuel distribution stratification is not straightforward when fuel decomposition reactions become significant.

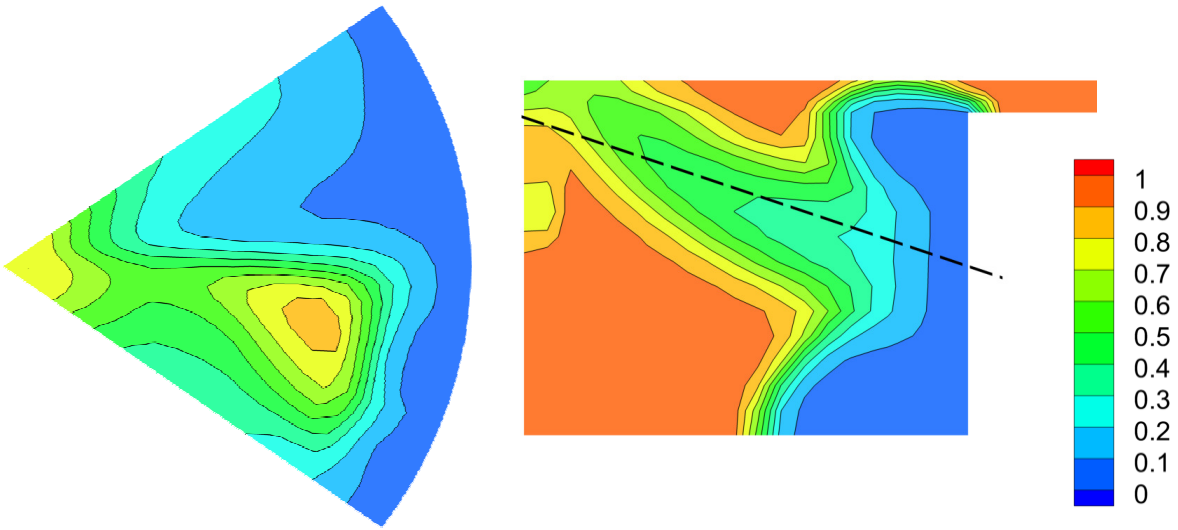

Fig. 6.4 Ethanol energy fraction distribution for ethanol-heptane operation. Left image represents cross-section through the injection plane (shown with dashed line)

6.2.2 Combustion Evolution

Further, Fig. 6.5 illustrates the time evolution for both combustion modes (PCCI and ethanol-heptane dual fuel operation). The color coded data represents the C/O equivalence ratio previously introduced in section 4.3.1.

The rate of energy release is represented also in Fig. 6.5 as numbered contour levels. The energy release levels shown are exponentially spaced.

The direct injection of n-heptane is followed by a mixing process and fuel decomposition. Due to the delaying effect of ethanol and lower n-heptane equivalence ratio, the injection event occurs earlier in the case of dual-fuel operation. This results in increased time available for the flow and diffusion processes to reduce the local equivalence ratio compared to the neat heptane operation. The combustion process is initiated in the fuel rich part of the combustion chamber and a flame front is subsequently formed. Fig. 6.6 shows the development of the ignition kernel downstream the axis of the n-heptane spray (in the direction of the swirl.

A significant observation is related to the position of the ignition kernel. While for the baseline operation the combustion process is initiated in close proximity to the piston bowel surface and on the periphery of the combustion chamber, for the dual-fuel combustion the location of the ignition kernel is shifted upwards, closer to the center of the combustion chamber. Also the ignition kernel is observed to move away from the combustion chamber side wall. This observation is consistent with the experimentally observed behavior shown in Fig. 5.12.

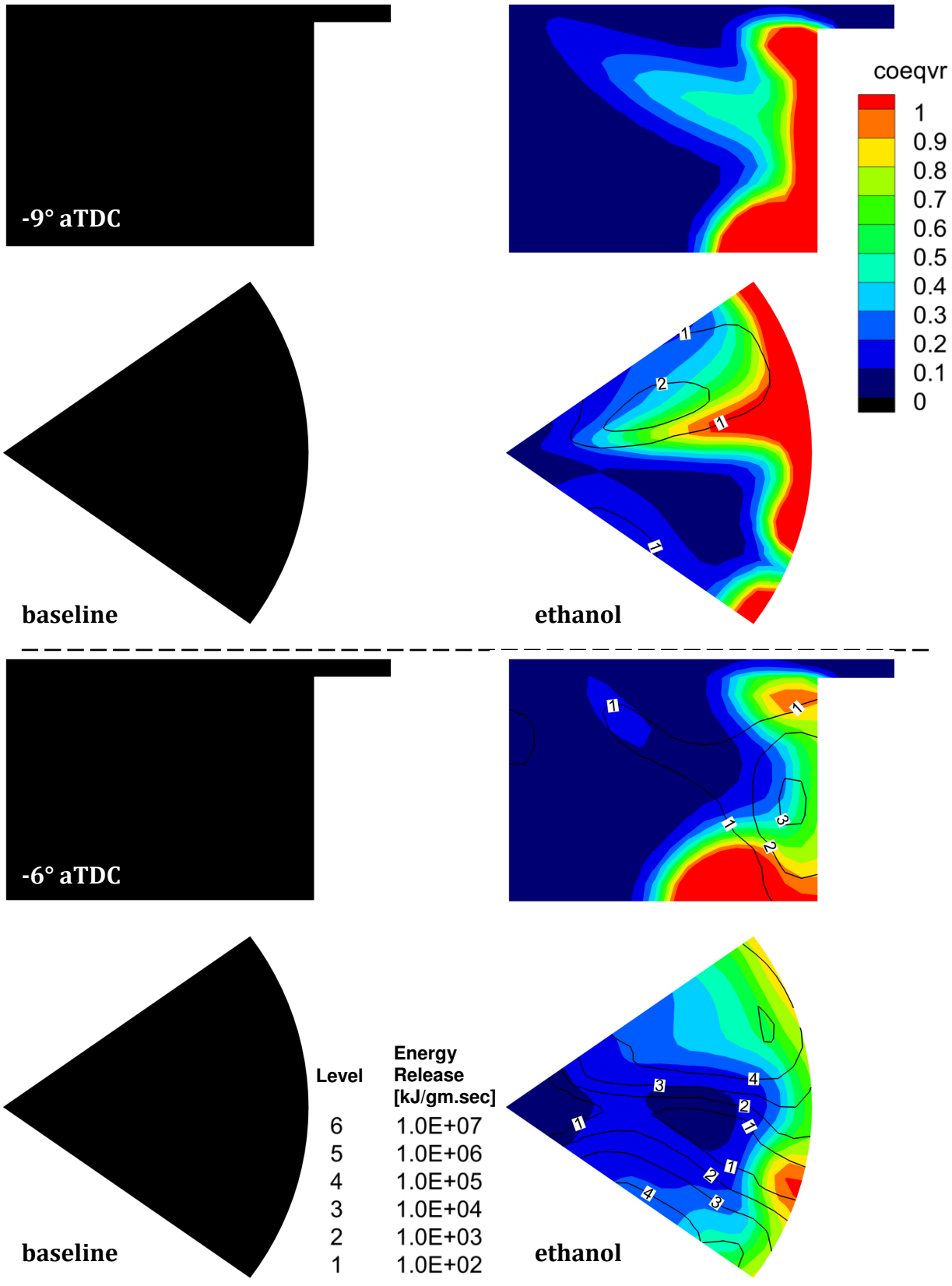

Fig. 6.5 Time evolution of equivalence ratio (color coded) and chemical energy release rate (contour levels)

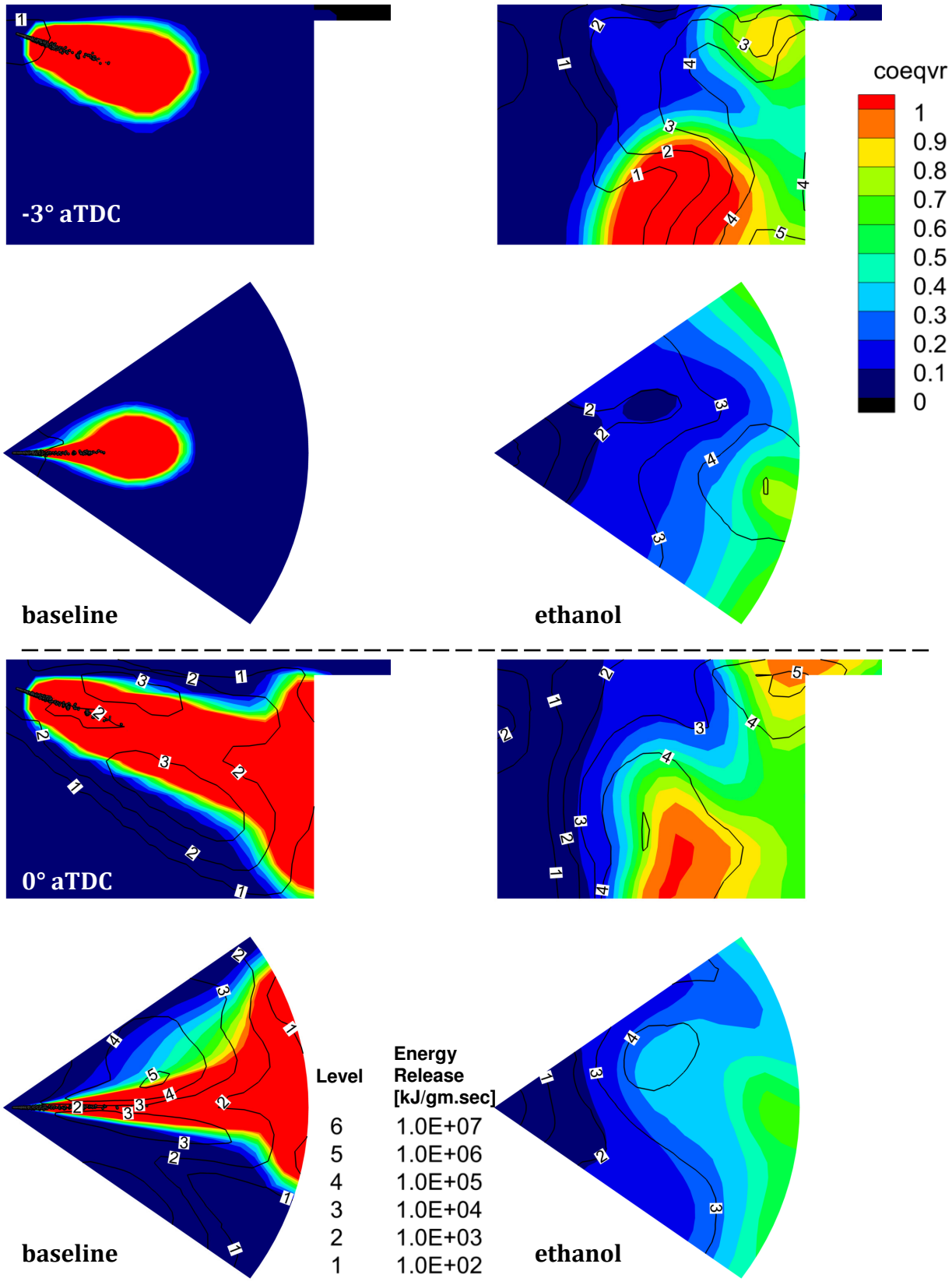

Fig. 6.5 Time evolution of equivalence ratio (color coded) and chemical energy release rate (contour levels) (ctnd)

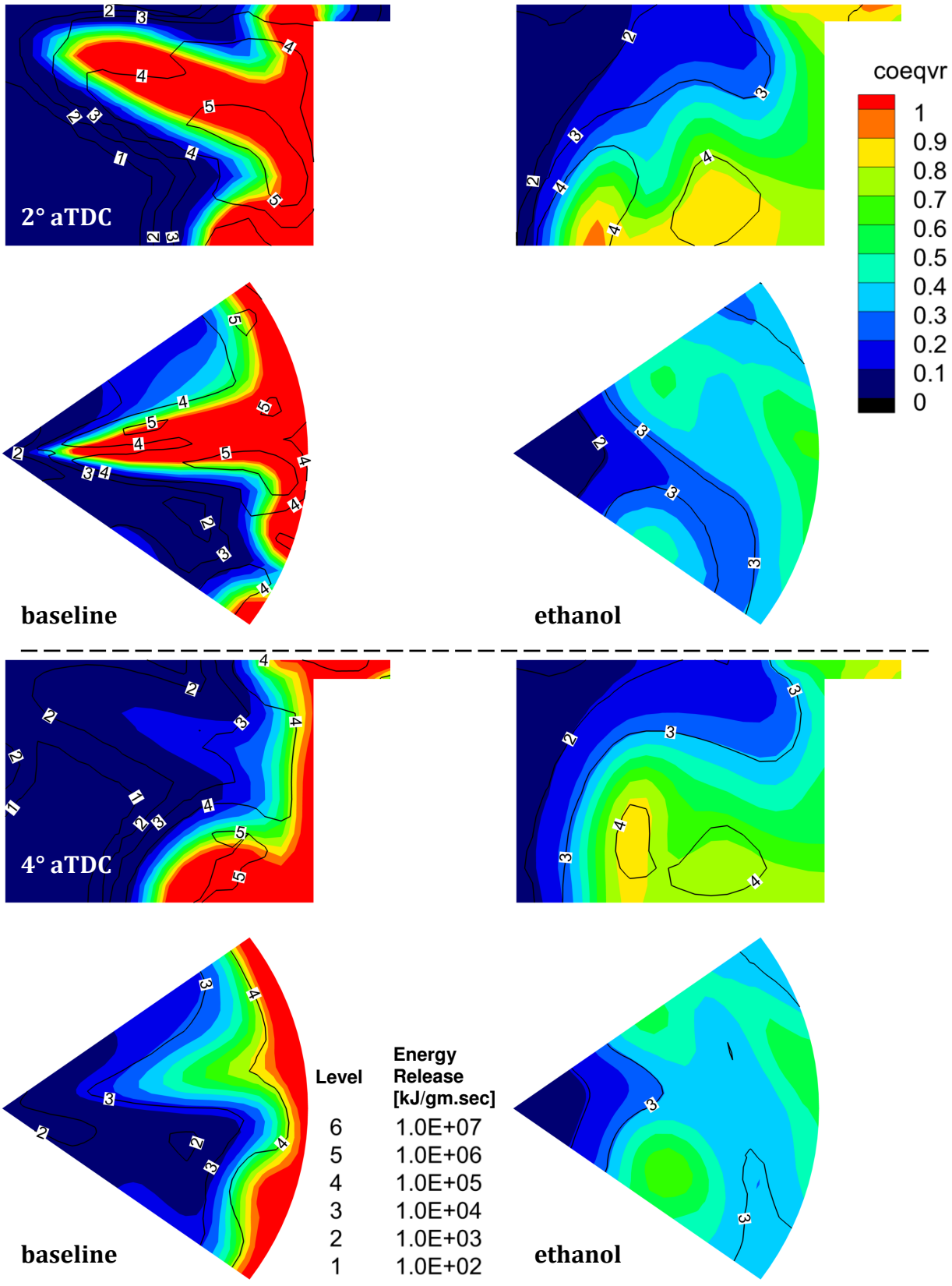

Fig. 6.5 Time evolution of equivalence ratio (color coded) and chemical energy release rate (contour levels) (ctnd)

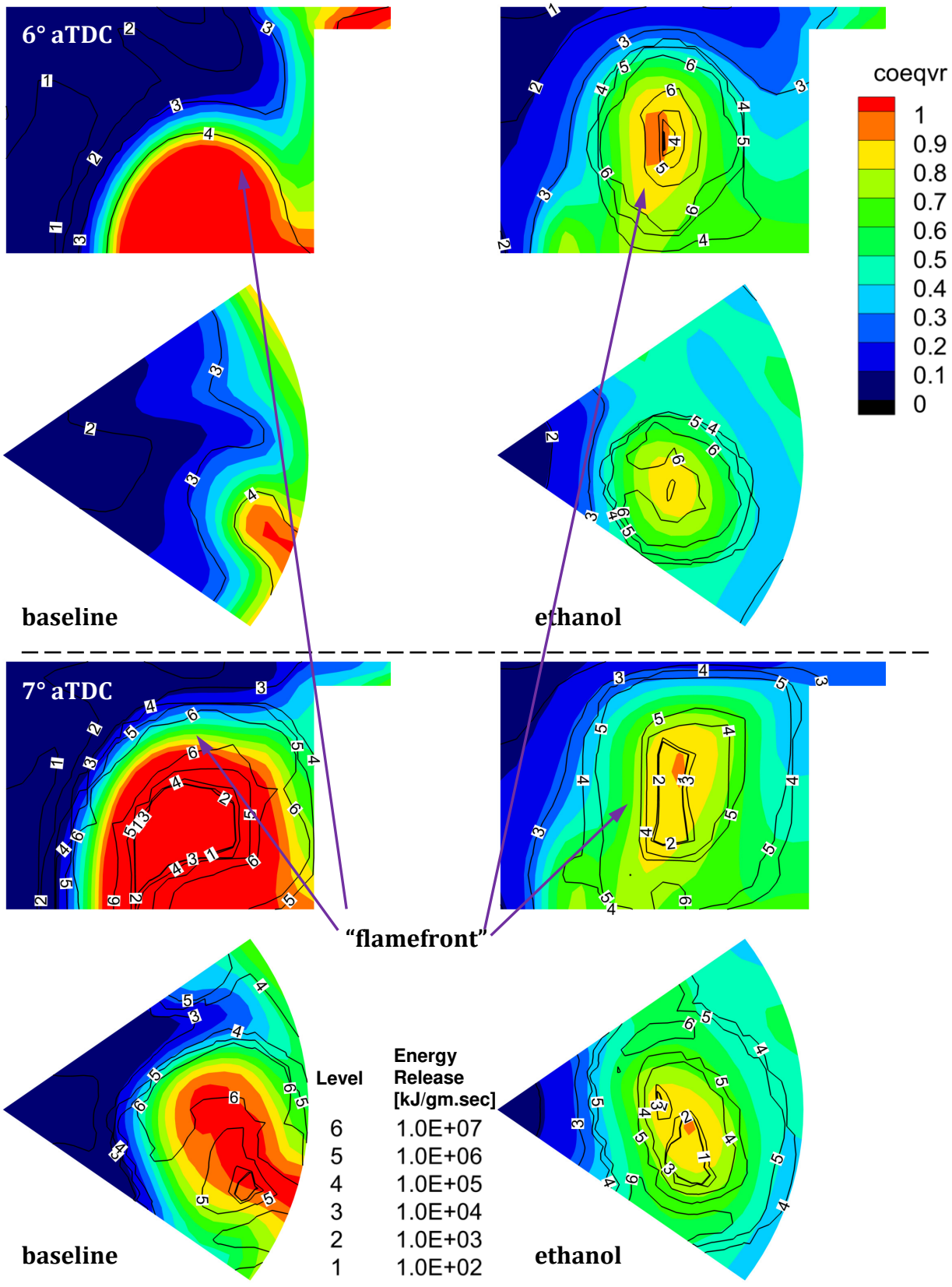

Fig. 6.5 Time evolution of equivalence ratio (color coded) and chemical energy release rate (contour levels) (ctnd)

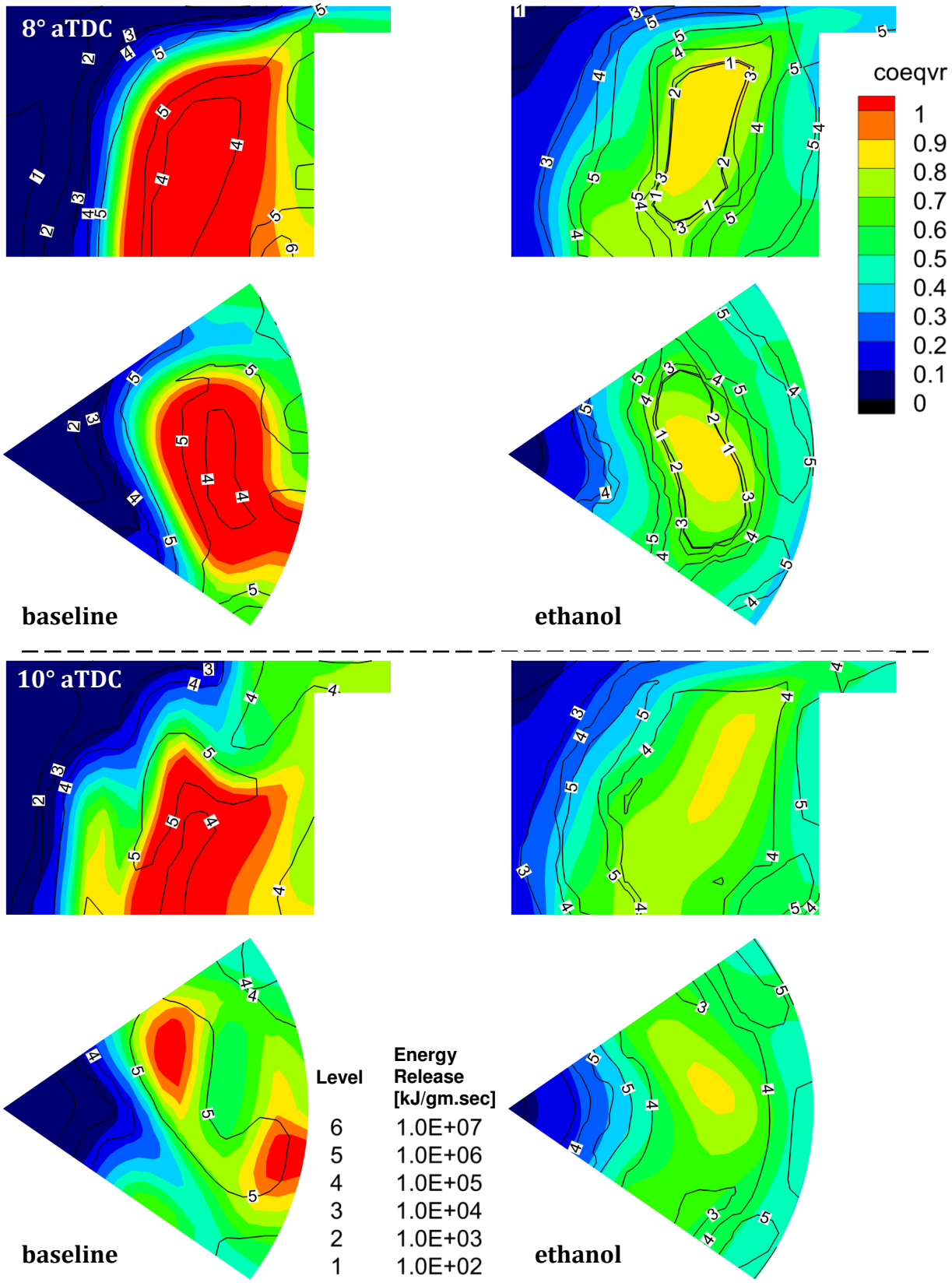

Fig. 6.5 Time evolution of equivalence ratio (color coded) and chemical energy release rate (contour levels) (ctnd)

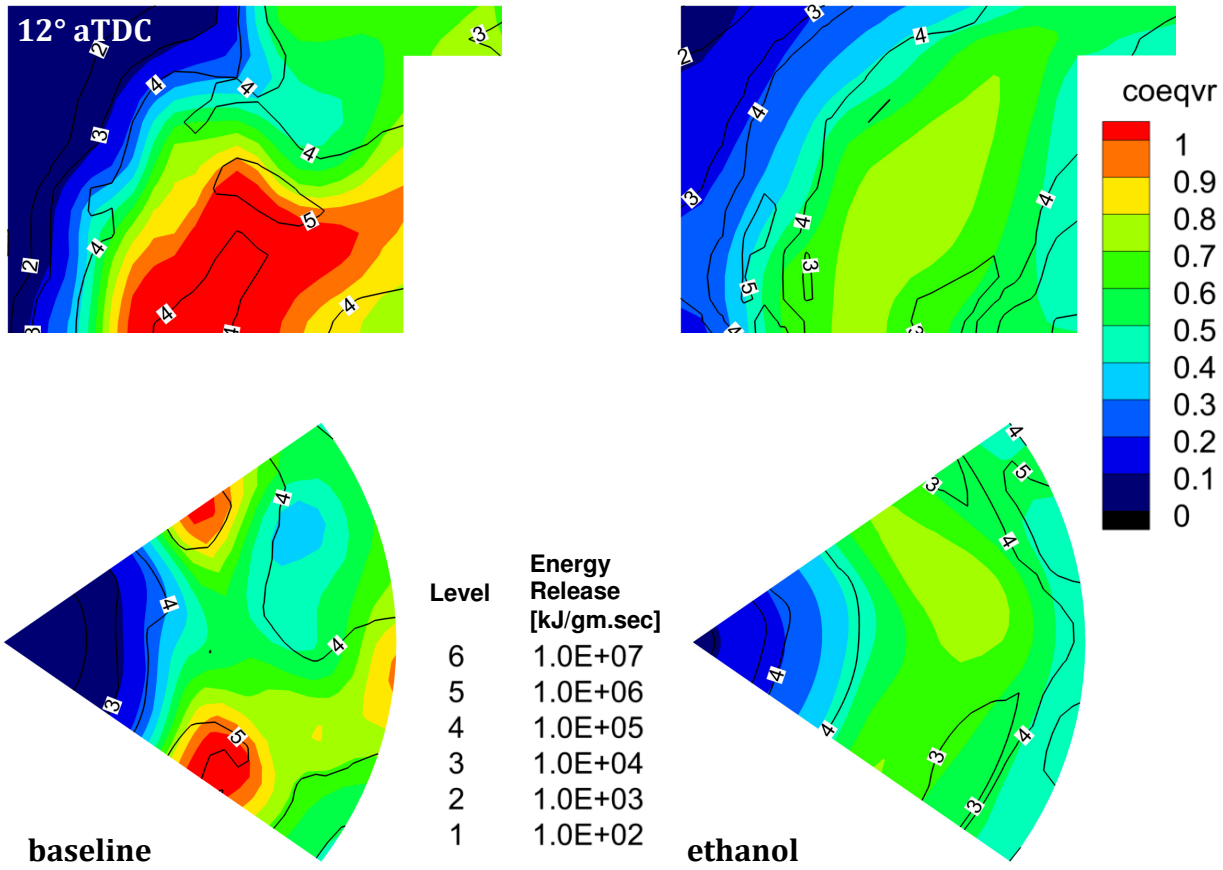

Fig. 6.5 Time evolution of equivalence ratio (color coded) and chemical energy release rate (contour levels)

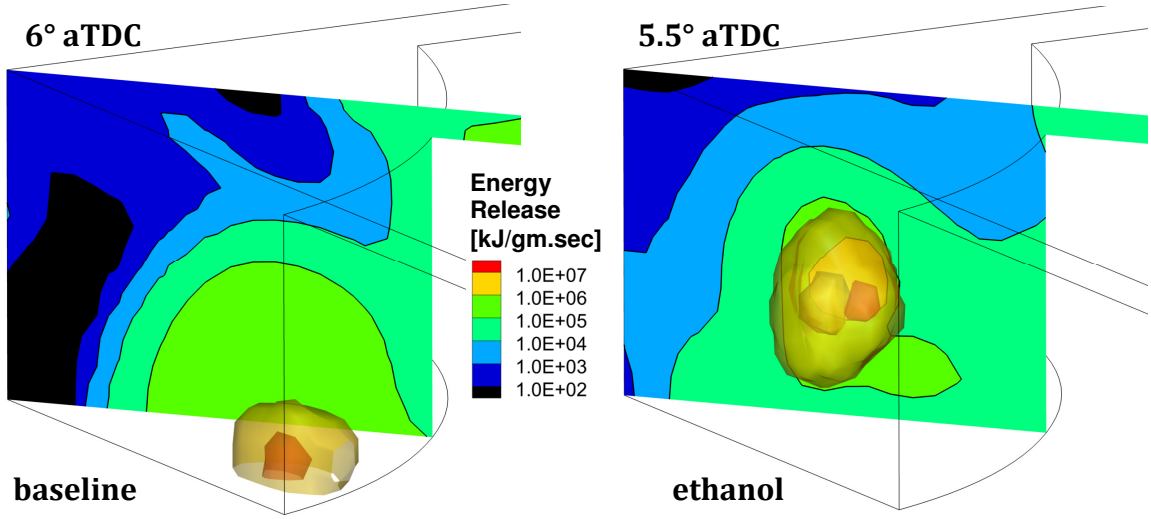

Fig. 6.6 Ignition kernel at 6°aTDC (baseline) and 5.5°aTDC (dual-fuel). Section aligned with spray and energy release isosurfaces.

6.2.3 Reactivity Stratification

As previously discussed in the conclusions subsection of section 5.1.8, one of the fundamental concepts behind dual-fuel strategies such as RCCI is reactivity stratification. In attempting to discuss reactivity stratification in the context of the dual-fuel operation investigated, the chemical energy release provided by the model was chosen as a measure of local reactivity. The data obtained for both baseline and dual-fuel operation is shown in Fig. 6.7. The plots provide histograms of energy release distributions as a function of time.

For the baseline operation with n-heptane, the combustion process starts with a gradually increasing energy release as the system undergoes low temperature oxidation and NTC. As the mixtures enters the HTHR, portion of the mixture will observe large specific energy release.

At the same time, for the dual-fuel operation the process proceeds in a fairly similar fashion with one notable exception. This difference occurring for very low energy release rates is associated with the low temperature decomposition of ethanol. This low temperature energy release has very little impact on the combustion process, as it is roughly ten orders of magnitude smaller than the main combustion event.

Furthermore one may analyze the reactivity stratification by considering the standard deviation and coefficient of variation associated with the instantaneous specific chemical energy release distributions.

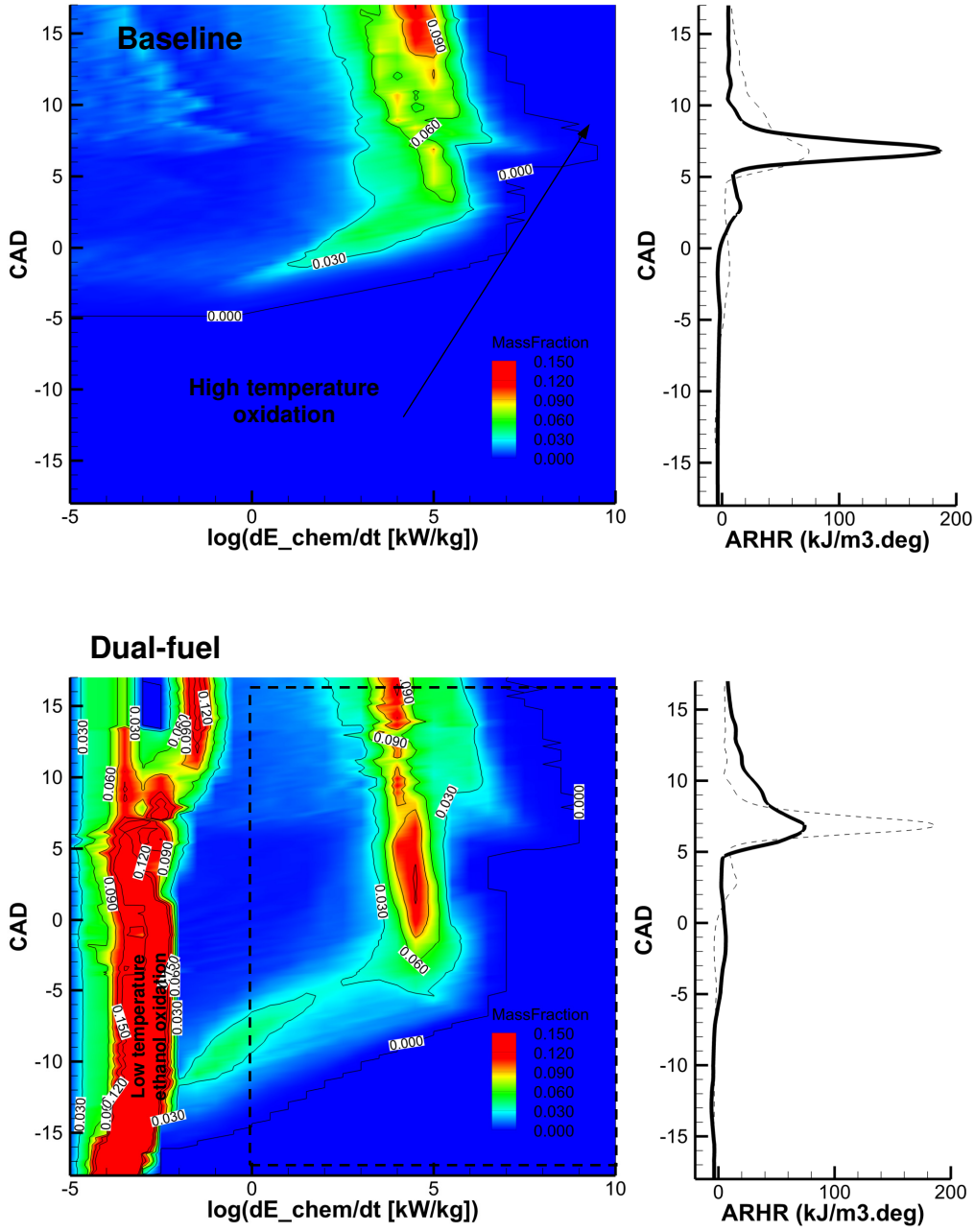

Fig. 6.7. Time dependence of chemical energy release histograms

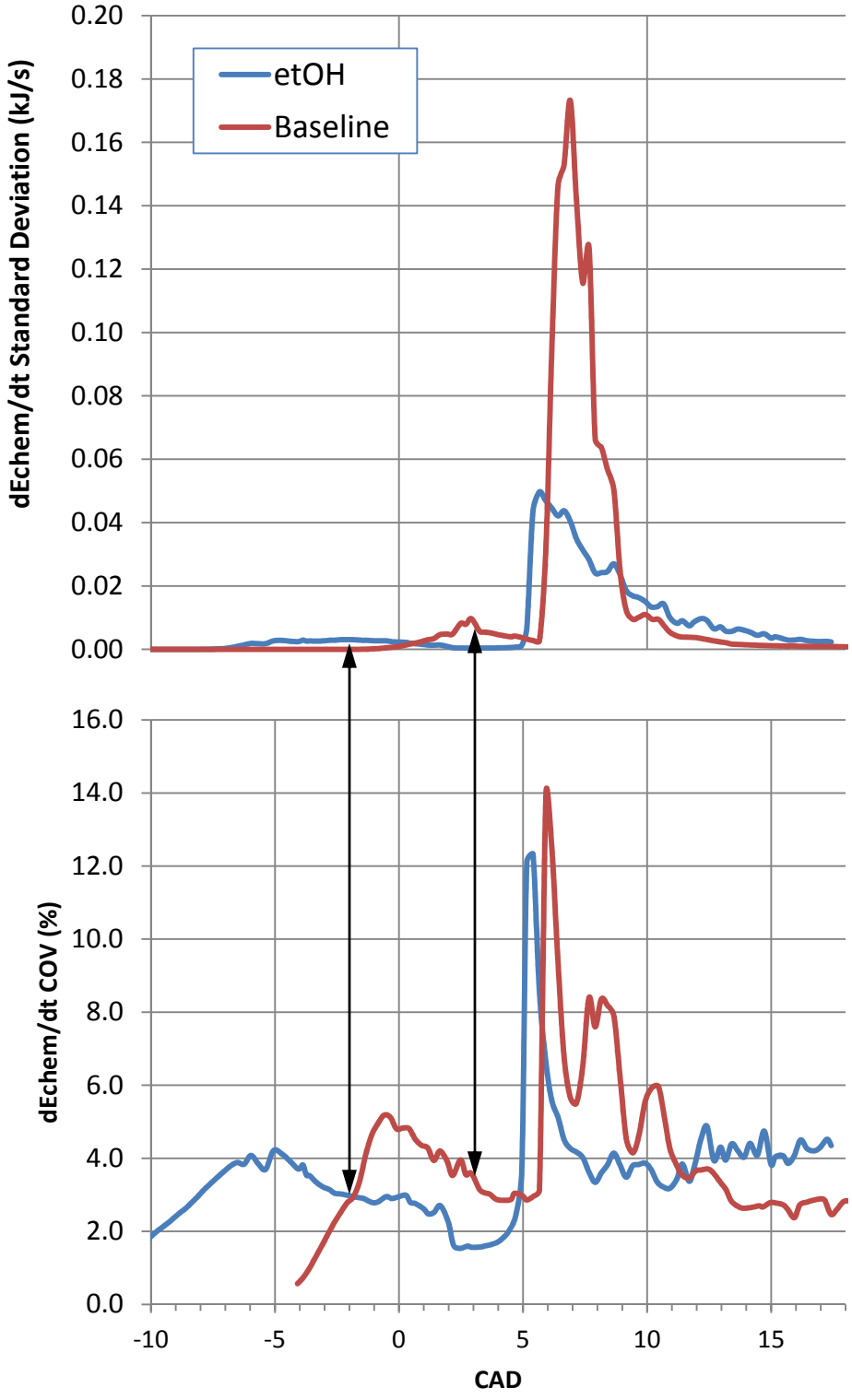

Fig. 6.8 Specific energy release standard deviation (above) and coefficient of variation (below)

The energy release standard deviation and coefficient of variation are shown in Fig. 6.8. Both measures of energy release heterogeneity seem to point towards the baseline condition as the one with higher energy release stratification. However, based on the discussion presented in section 4.3.3, there are strong reasons to believe that these two measures of variability are not able to capture the underlying phenomena. In Fig. 6.9 the energy data is presented in a Lorentz curve plot as described in section 4.3.3. The diagonal line L(x)=x (black line) represents a perfectly homogenous behavior, where each portion of the combustion chamber releases precisely the same amount of energy. Both the baseline and dual-fuel combustion are significantly different from this HCCI-like Lorenz curve. The ethanol addition appears to have a fairly strong impact on the energy release distributions.

The Gini index, introduced in section 4.3.3, represents a measure of distribution stratification. The Gini index is proportional to the area formed between each individual Lorentz curve and the perfectly homogenous distribution L(x)=x. The results associated with the combustion modes studied are shown in Fig. 6.10. It may be observed that while the dual-fuel energy release is significantly more homogenous (lower Gini index values) during the early stages of combustion, the trend is quickly reversed during the HTHR.

However, the magnitude of the difference in energy stratification does not appear to be sufficient to fully explain the observed behavior in terms of increased combustion duration associated with the dual-fuel combustion.

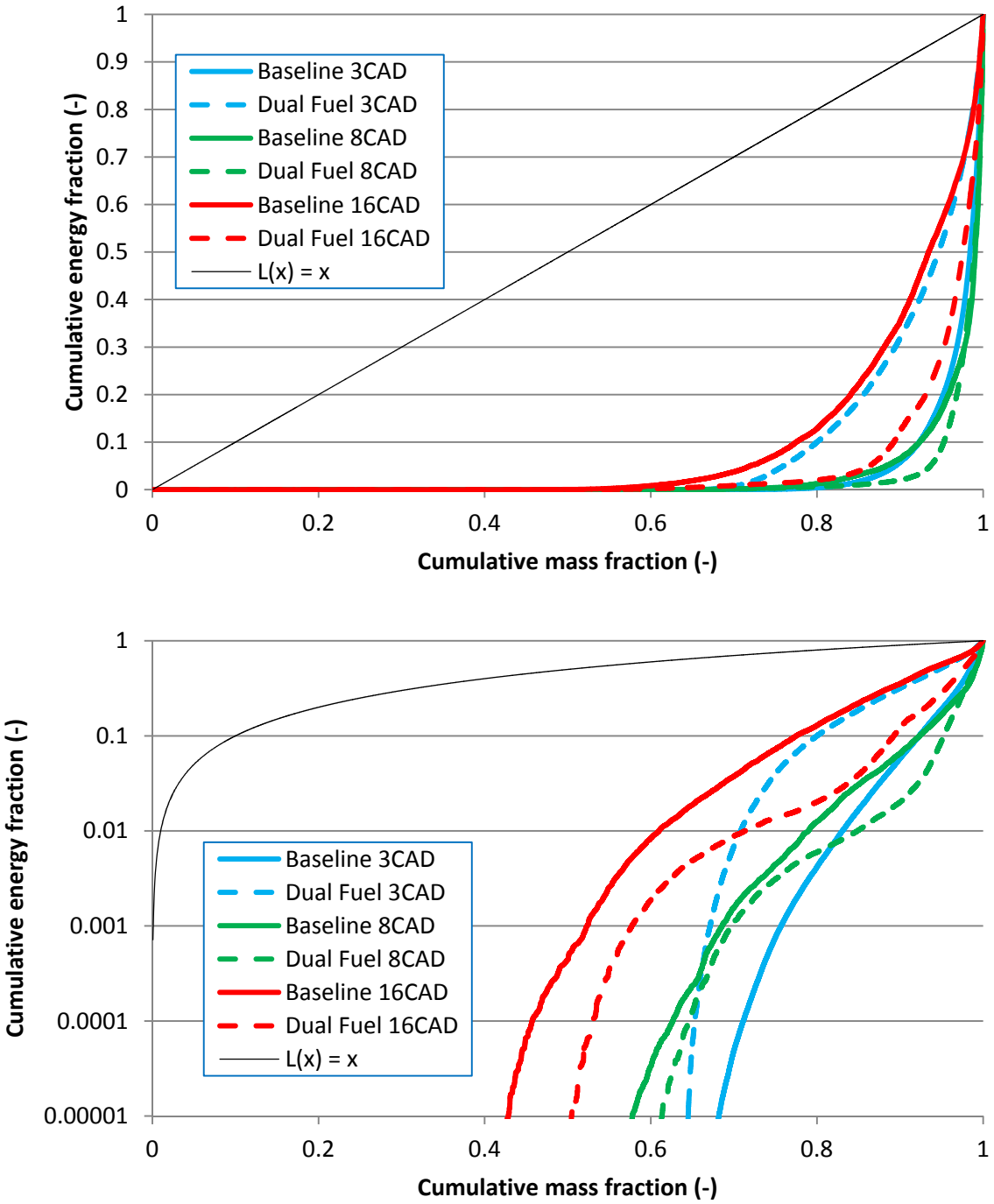

Fig. 6.9 Lorenz curves for baseline and dual-fuel combustion at several crank positions. Linear scale (upper), Logarithmic scale (lower)

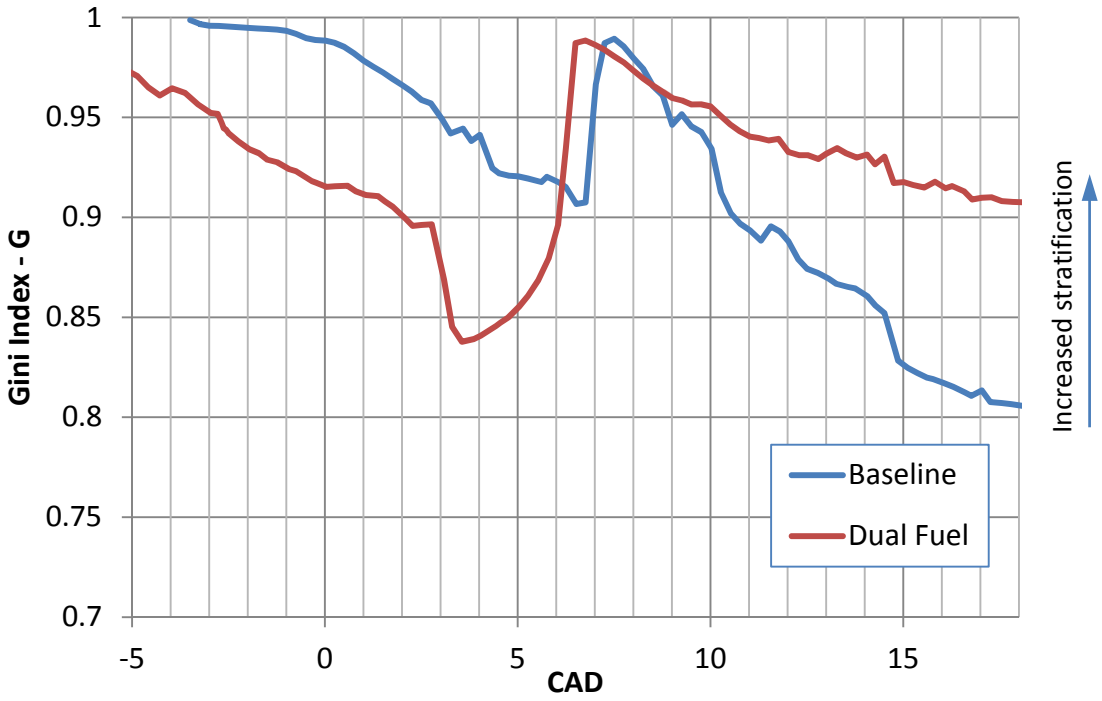

Fig. 6.10 Gini index for baseline and dual-fuel operation

A second possible mechanism for the reduction in energy release rate associated with dual-fuel operation is associated with the flame-front type propagation observed in Fig. 6.5. While the presence of the ignition kernel is almost always guaranteed (there will be at least one for each spray), its location is not as clearly defined. Nonetheless, as the flame-front extends away from the n-heptane rich zone where the combustion process was initiated, it encounters a mixture with a higher fraction of ethanol. The flame-front speed predicted by the numerical simulation is shown in Fig. 6.11. The speed of the flame is observed to be about one order of magnitude higher than the typical laminar burn velocities for those particular fuels [121]. A second relevant observation is related to the dual-fuel flame propagation. Initially both combustion modes are characterized by relatively similar

flame speeds. However, as the flame front reaches the combustion chamber zone with a higher ethanol fraction, the flame speed is observed to decrease to about half of its initial value.

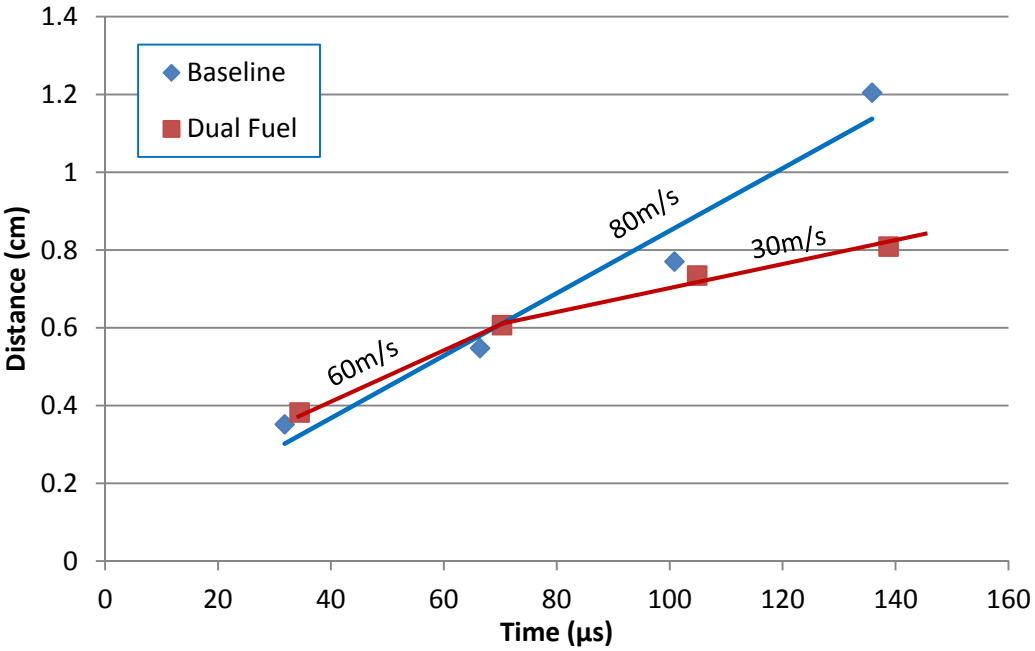

Fig. 6.11 Flame front propagation

This could be attributed to the low-temperature behavior of ethanol, which is a single-stage fuel compared to n-heptane which is a two-stage fuel. Thus ethanol experiences at these ignition temperatures (~800K) very long ignition delay and thus low rate of fuel decomposition and radical formation.

This observation provides an explanation also for the asymmetric shape of the rate of heat release profile. The dual-fuel heat release is characterized by a steeper slope, similar to the baseline combustion. However, as the flame front encounters higher ethanol fractions, the combustion process is prolonged compared to the baseline combustion.

Chapter 7. "Summary and Recommendations"

7.1 Summary

The dual-fuel combustion of n-heptane and ethanol has been investigated in an optically accessible engine representative of a typical light-duty diesel engine configuration. While neither n-heptane nor anhydrous ethanol are practical fuels, they represent a good tradeoff between a fundamental investigation and the real-world fuel complexity.

Dual-fuel combustion has recently regained attention due to increased focus on improved fuel efficiency and regulatory pressure. It has been shown to improve fuel conversion efficiency in laboratory setups through reduced heat transfer and short combustion duration.

Unlike previously published work which concentrated on *what* may be achieved by the dual-fuel combustion, this work attempts to provide insight into *how* combustion occurs during dual-fuel operation.

In order to achieve this goal, several techniques have been employed through both experimental and numerical investigations. First, the mixture formation and combustion process for both the baseline and dual-fuel operation have been characterized using high-speed imaging. Subsequently, UV imaging and spectral measurements provided further detail regarding the chemiluminescent light emission. Following, in-cylinder formaldehyde distribution measurements were performed using planar laser induced fluorescence (PLIF).

These experimental measurements were complemented in chapter 6 with the results of the numerical simulation of in-cylinder chemically reacting fluid flow. The modeling data showed good agreement with the experimental data for both overall behavior in terms of in-cylinder pressure evolution and optical measurements.

In order to quantify the reaction control mechanism, the chemical energy release rate has been chosen as a metric of local reactivity. Additionally, the numerical simulation results predict the formation of a flame front characterized by flame speeds one order of magnitude higher than typical flame-speeds encountered in spark-ignited mixtures. The increased flame speed is attributed to increased low-temperature decomposition associated with n-heptane, which is a two-stage fuel.

The results of the current investigation seem to suggest that the high-temperature heat release seems to be mostly dominated by differences in flame propagation rather than stratification of the energy release. It appears that the reactivity stratification plays thus an indirect role through its impact in flame speed rather than a stratification of the auto-ignition reactions.

The presence of a flame-front in the dual-fuel combustion recently reported by Mark Musculus [122] was not thought to be the dominant combustion rate control mechanism. One of the major differences between the dual-fuel operation used in the previously referenced work and the dual-fuel operation investigated in the current work is related to the ethanol energy fraction, i.e. ~70% versus 25% in the current work.

7.2 Recommendations for Future Work

It is thus apparent that there are two mechanisms controlling the rate of combustion during the dual-fuel operation as previously described. Further work is required in order to determine the relative importance of these two mechanisms under a wider range of operating conditions. A more detailed investigation of the underlying chemical kinetic processes behind the high-speed flame-fronts observed during dual-fuel combustion. Using the experimental and numerical simulation infrastructure developed as a part of this work, the following list of investigations may be performed:

- Numerical simulations of homogenous mixtures of n-heptane and ethanol under various equivalence ratios, relative fractions, initial temperatures and residence times focused towards the investigation of the factors dominating the flame speed under condition relevant for dual-fuel operation.
- Validation of numerical results with experimental determination of flame speed in constant-volume reactors. One of the main barriers towards achieving this goal is the mixture preparation process for the relatively high temperatures (~800K) required for these experiments.
- Expand the dual-fuel operation studies on the optical engine to include data from boosted engine operation. Laboratory-supplied compressed air is sufficient for this type of investigation.

- Expand work to include the impact of EGR on dual-fuel combustion. EGR is required for the higher-load conditions in order to limit the maximum energy release rate.
- Develop method for comparing line-of-sight chemiluminescence optical measurements of CO, OH and CH_2O with numerical results; this provides additional metrics for model validation. KIVA4-WSU has been configured to output the relevant reaction rates required for this type of model validation.
- Apply OH PLIF using the recently commissioned dye laser in order to complement data regarding the flame-front formation as well as allow for the experimental determination of flame-front speeds.
- Apply two-color method and soot LII in order to investigate the impact of dual-fuel operation on the soot formation process and soot radiation. While n-heptane based dual-fuel combustion has been observed to be virtually soot-free, this type of investigation may be carried out using ULSD instead.
- Apply quantitative optical measurements to investigate the mixture formation process.

Below is included the list of publications generated during the PhD program by the author:

- **Journal publications:**

1. Jansons, M., Florea, R., Zha, K., Gingrich, E., "The Effect of HCHO Addition on Combustion in an Optically Accessible Diesel Engine Fueled with JP-8", *Powertrains Fuels & Lubricants Meeting*, October 2010, SAE 2010-01-2136 (selected for SAE Transactions)
2. Jansons, M., Zha, K., Florea, R., Taraza, D., Henein, N., Bryzik, W., "Effect of Swirl Ratio and Wall Temperature on Pre-Injection Chemiluminescence During Starting of an Optical Diesel Engine", *SAE International Journal of Engines*, March 2010 vol. 2 no. 2 173-185
3. Florea, R., Taraza, D., Henein, N., Bryzik, W., "Transient Fluid Flow and Heat Transfer in the EGR Cooler", SAE International Journal of Engines, April 2009 vol. 1 no. 1 558-570
4. Jansons, M., Florea, R., Estefanous, F., Taraza, D., Henein, N., Bryzik, W., "Chemiluminescence imaging of pre-injection reactions during engine starting", *International Journal of Vehicle Design 2009* - Vol. 49, No.1/2/3 pp. 168 – 191

- **Conference Proceedings:**

1. Florea, R., Zha, K.,, Yu, X., Jansons, M., Taraza, D., Henein, N. "Ethanol/N-Heptane Dual-Fuel Partially Premixed Combustion Analysis through Formaldehyde PLIF", SAE Paper 2012-01-0685

2. Zha, K., Yu, X., Florea, R., Jansons, M. "Impact of Biodiesel Blends on In-cylinder Soot Temperature and Concentrations in a Small-Bore Optical Diesel Engine" SAE Paper 2012-01-1311
3. Yu, X., Zha, K., Florea, R., Jansons, M. "Comparison of In-Cylinder Soot Evolution in an Optically Accessible Engine Fueled with JP-8 and ULSD" SAE Paper 2012-01-1315
4. Jansons, M., Florea, R., Zha, K., Florea, E., "The Combined Effect of HCHO and C2H4 Addition on Combustion in an Optically Accessible Diesel Engine Fueled with JP-8", SAE Paper 2011-01-1392.
5. Florea, R., Zha, K., Jansons, M., Taraza, D., Henein, N. "A CFD Study of the Effect of HCHO Addition on Autoignition and Combustion", ASME Fall Technical Conference, Paper number ICEF2011-60212
6. Jansons, M., Florea, R., Zha, K., Estefanous, F., Florea, E., Taraza, D., Bryzik, W., Henein, N., Hoogterp, L., "Optical and Numerical Investigation of Pre-Injection Reactions and Their Effect on the Starting of a Diesel Engine", SAE Paper 2009-01-0648.
7. Jansons, M., Brar, A., Estefanous, F., Florea, R., Taraza, D., Henein, N., Bryzik, W., "Experimental Investigation of Single and Two-Stage Ignition in a Diesel Engine", SAE 2008 World Congress, SAE Paper 2008-01-1071

APPENDIX 1: MATLAB ROUTINE FOR READING PHANTOM CINE FILE HEADER AND FRAME INFORMATION

```
function I=CINEread (filename,frame)
%*********************************************************************
% modified function based on Randy Herold's (ERC Wisc) 2008
% dissertation [116]
%*********************************************************************
fid = fopen (filename, 'r');
if (fread (fid, 1, '*uint16') == 18755)
A = fread (fid, 1, '*uint16'); %Headersize
imcompress = fread (fid, 1, '*uint16'); %Compression
A = fread (fid, 1, '*uint16'); %Version
A = fread (fid, 1, '*int32'); %FirstMovieImage
A = fread (fid, 1, 'uint32'); %TotalImageCount
firstimageno = fread (fid, 1, 'int32'); %FirstImageNo
imcount = fread (fid, 1, 'uint32'); %ImageCount
offimheader = fread (fid, 1, 'uint32'); %OffImageHeader
offsetup = fread (fid, 1, 'uint32'); %OffSetup
offimoffsets = fread (fid, 1, 'uint32'); %OffImageOffsets
trigfrac = fread (fid, 1, 'uint32'); %Trig Timing (fraction)
trigsec = fread (fid, 1, 'uint32'); %Trig Timing (seconds)
fseek (fid, offimheader, 'bof');
junk=fread (fid, 1, '*uint32'); clear junk;
width = fread (fid, 1, 'int32');
height = fread (fid, 1, 'int32');
fseek (fid, offimoffsets, 'bof');
imlocs = fread (fid, double(imcount), 'int64');


fseek (fid, imlocs(frame), 'bof');
AnnotationSize = fread (fid, 1, 'uint32');
Annotation = fread (fid, AnnotationSize/8, 'uint32');
I = zeros(height,width,1);
I = uint16(I);
    for k = 1:1 %each color
        for j=1:height
        I(height-j+1,:,k) = fread (fid, width, '*uint16');
        end %for j
    end %for k
else
input ('hit ctrl - c: there is a problem');
end %if
fclose (fid);
```

```
function [rows,cols,dT]=CINEreadheader (filename)
%*********************************************************************
% modified function based on Randy Herold's (ERC Wisc) 2008
% dissertation [116]
%*********************************************************************
fid = fopen (filename, 'r');
if (fread (fid, 1, '*uint16') == 18755)
A = fread (fid, 1, '*uint16'); %Headersize
A = fread (fid, 1, '*uint16'); %Compression
A = fread (fid, 1, '*uint16'); %Version
A = fread (fid, 1, '*int32'); %FirstMovieImage
A = fread (fid, 1, 'uint32'); %TotalImageCount
firstimageno = fread (fid, 1, 'int32'); %FirstImageNo
imcount = fread (fid, 1, 'uint32'); %ImageCount
offimheader = fread (fid, 1, 'uint32'); %OffImageHeader
offsetup = fread (fid, 1, 'uint32'); %OffSetup
offimoffsets = fread (fid, 1, 'uint32'); %OffImageOffsets
trigfrac = fread (fid, 1, 'uint32'); %Trig Timing (fraction)
trigsec = fread (fid, 1, 'uint32'); %Trig Timing (seconds)
fseek (fid, offimheader, 'bof');
junk=fread (fid, 1, '*uint32'); clear junk;
width = fread (fid, 1, 'int32');
height = fread (fid, 1, 'int32');
fseek (fid, offimoffsets, 'bof');
imlocs = fread (fid, double(imcount), 'int64');
fseek(fid,0,'bof');
for i=1:10000000
if(fread(fid,1,'*uint16') == 1002)
break;
end
end
junk = fread(fid,1,'*uint16'); clear junk;
dT = zeros(imcount,1);
for i=1:imcount
fracstart = fread (fid, 1, 'uint32');
secstart = fread (fid, 1, 'uint32');
dT(i,1) = (secstart-trigsec) + ((fracstart-trigfrac)/(2^32));
end
else
input ('hit ctrl - c: there is a problem');
end %if
rows=height;
cols=width;
fclose (fid);
```

APPENDIX 2: KIVA4-WSU FORTRAN SUBROUTINE FOR TECPLOT 360 CFD OUTPUT

```
*deck plttec
      subroutine plttec
c
c
======================================================================
c
c      writes data to output file for Tecplot 360 (v2010 and 11 tested)
c
c      plttec is called by:  fulout
c
c      plttec calls the following subroutines and functions:  none
c
c
======================================================================
c
c 11/4/2011
c subroutine rewritten by Radu Florea - Wayne State University
c based on previous GMV output
c Output data into Tecplot PLT format - ASCII
      use parametermod, only : zero,nverts,ncells,nspl,npar,nsp
      use kiva1, only : u,v,w,x,y,z,p,temp,ro,tke,eps,spd,afacex,
     &                  afacey,afacez
      use kiva1int, only : numcellsa,numvertsa,iverti,icelli,nodes,
     &                     numfacesa,ifacesi,numfaces,f
      use constants, only : tinynum,one,smallnum1,forthd,pi
      use kiva3, only : ngmv,ncyc,crank,cmueps
      use chemistrydata, only : nrk,fam
      use propertiesdata, only : mw,numoatom,numcatom
      use particledata, only : np,i4mom,i4p,partn,radp,xp,yp,zp,
     &                         up,vp,wp,tp
      use wallfilma, only : hface
      use boundarydata, only : enx,eny,enz,i4bc,ibv
      use char1, only : idsp
      use cantera, only : ct_qf1,ct_qf2
      implicit none
c     Local variables
      integer netcels,netvtxs,i,i4a,i4,ifacecell,n,ii,i4face
      integer imom,ibcflag,i4c,iostatus,isp,vrnum
      double precision epsden,spdi41,dente,den,totmass,parte,sumromw
      double precision sumc,sumo
      character *80 filename
      double precision, allocatable :: work(:),spraywall(:)
      integer, allocatable :: imap(:)

      allocate(imap(nverts))
      imap = 0
c
c
<><><><><><><><><><><><><><><><><><><><><><><><><><><><><><><><><><><><>
c
c +++
```

```
c +++ calculate current filename. here, 48 is the '0' digit in
c +++ standard ASCII, i.e., the 48th character in the collating
c +++ sequence. 'char' converts integer to character:
c +++
      filename='tecplot_'//char(ngmv/100+48)//char(mod(ngmv/10,10)+48)
     &     //char(mod(ngmv,10)+48)//'_fluid.plt'
      write( *,900) filename,ncyc,crank
      write(12,900) filename,ncyc,crank
      open(unit=10,file=filename,iostat=iostatus,
     &     status='unknown',form='formatted')
      write(10,*) 'VARIABLES = '
      write(10,*) '"x" "y" "z" "u" "v" "w"'
      write(10,*) '"pres" "temp" "dens" "tke" "scl" "totm" "coratio"'
      write(10,*) '"coeqvr" "qf1" "qf2"'
      vrnum = 17
c      if (crank.ge.-15) then
      do isp = 1,nsp
         write(10,"(A18)") '"'//idsp(isp)//'"'

         vrnum = vrnum + 1
      end do
c      end if
      write(10,*) 'ZONE T="KIVA4-WSU-fluid"'
      write(10,*) 'STRANDID=1'
      write(10,"('SOLUTIONTIME=',1pe18.10)") crank
      write(10,"('Nodes=',      i18)") numvertsa
      write(10,"('Elements=',   i18)") numcellsa
      write(10,*) 'ZONETYPE=FEBrick'
      write(10,*) 'DATAPACKING=BLOCK'
      write(10,"('VARLOCATION=([7-',I0,']=CELLCENTERED)')") vrnum
      write(10,"('DT=(',A,')')") ('DOUBLE',i=1,vrnum)
c start writing variable values
      write(10,"(1p,5e13.5)") (x(iverti(i)),i=1,numvertsa)
      write(10,"(1p,5e13.5)") (y(iverti(i)),i=1,numvertsa)
      write(10,"(1p,5e13.5)") (z(iverti(i)),i=1,numvertsa)

c +++
      allocate(work(max(nverts,ncells)))
      work = zero

c write velocity "u"
      do 20 i4a=1,numvertsa
         i4 = iverti(i4a)
         work(i4)=u(i4)
      continue
      write(10,"(1p,5e13.5)") (work(iverti(i)),i=1,numvertsa)

c write velocity "v"
      do 30 i4a=1,numvertsa
         i4 = iverti(i4a)
         work(i4)=v(i4)
      continue
      write(10,"(1p,5e13.5)") (work(iverti(i)),i=1,numvertsa)

c write velocity "w"
```

```
      do 40 i4a=1,numvertsa
         i4 = iverti(i4a)
         work(i4)=w(i4)
      continue
      write(10,"(1p,5e13.5)") (work(iverti(i)),i=1,numvertsa)

c write pressure, temperature, density and turbulent kinetic energy
      write(10,"(1p,5e13.5)") (p(icelli(i)),i=1,numcellsa)
      write(10,"(1p,5e13.5)") (temp(icelli(i)),i=1,numcellsa)
      write(10,"(1p,5e13.5)") (ro(icelli(i)),i=1,numcellsa)
      write(10,"(1p,5e13.5)") (tke(icelli(i)),i=1,numcellsa)

c write "scl"
      do 50 i4a=1,numcellsa
         i4c = icelli(i4a)
         epsden=eps(i4c)
         if (eps(i4c).eq.zero) epsden=one
         work(i4c)=cmueps*tke(i4c)*sqrt(tke(i4c))/epsden
      continue
      write(10,"(1p,5e13.5)") (work(icelli(i)),i=1,numcellsa)

c write total mass
      do 69 i4a=1,numcellsa
         i4c = icelli(i4a)
         totmass = zero
         do ii = 1,nspl
            totmass = totmass + spd(i4c,ii)
         end do
         work(i4c)=totmass/ro(i4c)
         if (abs(work(i4c)).lt.tinynum) work(i4c)=zero
      continue

      write(10,"(1p,5e13.5)") (work(icelli(i)),i=1,numcellsa)

c compute c/o atom ratio
      do i4a = 1,numcellsa
        i4c = icelli(i4a)
        sumromw = 0
        sumc = 0
        sumo = 0
        do isp = 1,nsp
           sumromw = sumromw + spd(i4c,isp)/mw(isp)
        end do
        do isp = 1,nsp
           sumc = sumc+ numcatom(isp)*spd(i4c,isp)/mw(isp)/sumromw
           sumo = sumo+ numoatom(isp)*spd(i4c,isp)/mw(isp)/sumromw
        end do
        work(i4c) = sumc/sumo
      end do
      write(10,"(1p,5e13.5)") (work(icelli(i)),i=1,numcellsa)


c co equivalence ratio - c/o ratio actual divided by c/o ratio
stoichiometric
c c/o ratio stoichiometric for n-heptane = 0.318182
```

```
      write(10,"(1p,5e13.5)") (work(icelli(i))/0.318182,i=1,numcellsa)

c write forward reaction rates for reactions 1 and 2 as defined in the
ctlib.cpp file in the cantera folder
      write(10,"(1p,5e13.5)") (ct_qf1(icelli(i)),i=1,numcellsa)
      write(10,"(1p,5e13.5)") (ct_qf2(icelli(i)),i=1,numcellsa)

c write specie density data
      if (crank.ge.-15) then
      do isp = 1,nsp
c     if ( isp.EQ.1 .OR. isp.EQ.2 .OR. isp.EQ.3 .OR. isp.EQ.18 ) then
         write(10,"(1p,10e13.5)") (spd(icelli(i),isp),i=1,numcellsa)
c     end if
      end do
      end if


c write vertex connectivity data

      do i = 1,numvertsa
         imap(iverti(i)) = i
      end do

      do 10 i4a=1,numcellsa
      i4 = icelli(i4a)
      write(10,"(8i7)")                    imap(nodes(4,i4)),
     *                                     imap(nodes(1,i4)),
     1                                     imap(nodes(2,i4)),
     2                                     imap(nodes(3,i4)),
     3                                     imap(nodes(8,i4)),
     4                                     imap(nodes(5,i4)),
     5                                     imap(nodes(6,i4)),
     6                                     imap(nodes(7,i4))

      continue

c finished writing the fluid part of the output file
      close(10)

c droplet particle data

      if(np.eq.0) go to 200

c open new file for particle data
      filename='tecplot_'//char(ngmv/100+48)//char(mod(ngmv/10,10)+48)
     &     //char(mod(ngmv,10)+48)//'_parti.plt'
      open(unit=10,file=filename,iostat=iostatus,
     &     status='unknown',form='formatted')
      write(10,*) 'VARIABLES = '
      write(10,*) '"x" "y" "z" "u" "v" "w" "filmht"'
      write(10,*) '"radius" "temp" "spwall"'
      write(10,*) 'ZONE T="KIVA4-WSU-particle"'
      write(10,*) 'STRANDID=2'
      write(10,"('SOLUTIONTIME=',1pe18.10)") crank
      write(10,"('I=',i18.1,'J=1, K=1 ZONETYPE=Ordered')") np
```

```
      write(10,*) 'DATAPACKING=BLOCK'
      write(10,"('DT=(',A,')')") ('DOUBLE',i=1,10)
c start writing particle data

      write(10,"(1p,5e13.5)") (xp(n),n=1,np)
      write(10,"(1p,5e13.5)") (yp(n),n=1,np)
      write(10,"(1p,5e13.5)") (zp(n),n=1,np)
      write(10,"(1p,5e13.5)") (up(n),n=1,np)
      write(10,"(1p,5e13.5)") (vp(n),n=1,np)
      write(10,"(1p,5e13.5)") (wp(n),n=1,np)
c +++
c +++ calculate film height:
c +++
      do 80 i4a=1,numfacesa
         i4face = ifacesi(i4a)
         hface(i4face)=zero
      continue
      do 90 n=1,np
         imom=i4mom(n)
         if (imom .lt. 999999) go to 90
         ibcflag=imom-1000000
         if (ibcflag .eq. 15) ibcflag = 5
         i4c=i4p(n)
         i4face = numfaces(ibcflag,i4c)
         parte=partn(n)*forthd*pi*radp(n)**3
         hface(i4face) = hface(i4face) +
     &   parte/sqrt(afacex(ibcflag,i4c)**2 + afacey(ibcflag,i4c)**2 +
     &              afacez(ibcflag,i4c)**2)
      continue
      do 100 i4a=1,numcellsa
         i4c = icelli(i4a)
         work(i4c) = -one
         do ifacecell = 1,6
            work(i4c) = max(work(i4c),hface(numfaces(ifacecell,i4c)))
         end do
         if (abs(work(i4c)).lt.tinynum) work(i4c)=zero
      continue
      write(10,"(1p,5e13.5)") (work(icelli(i)),i=1,numcellsa)


c particle temperature
      write(10,"(1p,5e13.5)") (tp(n),n=1,np)
c particle radius
      write(10,"(1p,5e13.5)") (radp(n),n=1,np)

c spwall
      allocate(spraywall(npar))
      do n = 1,np
         if (i4mom(n) .gt. 999999) then
            spraywall(n) = i4mom(n)-1000000
         else
            spraywall(n) = 0.d0
         end if
      end do
      write(10,"(1p,5e13.5)") (spraywall(n),n=1,np)
```

```
      deallocate(spraywall)
      close(10)

      deallocate(imap)
      deallocate(work)
      ngmv=ngmv+1
      return
      format('TEC360 output ',a17,' at cycle',i5, ' crank=',
     &       0pf7.2)
      end
```

APPENDIX 3: KIVA4-WSU FORTRAN MODIFIED SUBROUTINE “CHEM” REPLACING PREVIOUS KIVA4 CHEMISTRY HANDLING WITH A CANTERA INTERFACE (MASTER NODE)

```
*deck chem
      subroutine chem
c =====================================================================
c
c      calculates the change in species densities and internal energy
c      due to kinetic chemical reactions
c
c      chem is called by:  kiva
c
c      chem calls the following subroutines and functions:  pfind
c      chem communicates through MPI to ctreactor.f
c
c =====================================================================
      use emodule,only : toth, vapma
      use parametermod, only : zero,nspl,nsp
      use kiva1, only : temp,spd,tke,eps,ro,vol,sie,p
      use kiva1int, only : npgtzero,numcellsa,icelli,bufflag,f
      use kiva3, only : tcut,tchem,dt,trbchem,capa,cho,ychoi,rdt,
     &                  wchem,facsec,t,t1ign,t2ign,xignl,yignf,
     &                  zignb,i4guess,xignr,yignd,zignt,xignit,
     &                  crank
      use constants, only : one,smallnum3,fourth,third
      use valvedata, only : zpistn
      use chemistrydata, only : nrk,nelem,cm,am,ae,bm,be,cb,zetab,eb,
     &                          cf,zetaf,ef,fbmam,fam,fbm,domega,qr
      use particledata, only : np,npn,xp,yp,zp,i4p,i4mom
      use propertiesdata, only : rmw,mw
      use cantera, only : ctMPIinit, ctmech, ct_numtasks, ct_tag1,
     &                ct_tag2,ct_tag3,ct_tag4,ct_tag5,ct_tag6,ct_tag7,
     &                ct_taskid,proc_time,proc_load,proc_nreact,
     &                ct_qf1,ct_qf2
      implicit none
      integer i4a,i4c,ir,ne,kk,isp,iref
      integer numxignition,numyignition,numzignition
      integer iignition,jignition,kignition,nspark,n
      double precision kf,kb,test
      double precision tijk,rtijk,talog,rp,pp,rom,omeg,rmin
      double precision flam,flbm,ctop,cbot,tkeden,aepsok,adteok
      double precision dtterm,capb,frac1,frac2,ycho,delrho
      double precision frac12,omdot2,omdot3,omdot4,omdmin
      double precision dompr,dtprime,dechem,dechk
      double precision typicallength,spddel,sienew
      double precision dxignition,dyignition,dzignition
      double precision xlocationign,ylocationign,zlocationign
      double precision spdsum


c <><><><><><><><><><><><><><><><><><><><><><><><><><><><><><><><><><>

      include 'mpif.h'
```

```
      DATA capb / 0.5d0 /
      INTEGER   MASTER
      PARAMETER (MASTER = 0)
      INTEGER :: i, status(MPI_STATUS_SIZE), ct_isp_active,
     &           ct_remainder, ct_chunksize, ct_cindx, ct_nreact,
     &           ct_ierr, ct_dest, ct_source
      INTEGER, DIMENSION(numcellsa) :: ct_i4c_active
      DOUBLE PRECISION, DIMENSION(:), ALLOCATABLE :: ctMPI_data,
     &           ctMPI_spd, smf_upd, ct_dechem, ctMPI_qf1, ctMPI_qf2
      INTEGER, DIMENSION(:), ALLOCATABLE :: ctMPI_cells
      DOUBLE PRECISION :: sum1,ct_ro,ck_mc,ck_mf,ct_time,nreact_sum,
     &           proc_load_sum


      IF (ctMPIinit.eq.one) THEN

c %%%%%%%%%%%% MPI Initializations %%%%%%%%%%%%
      call MPI_INIT(ct_ierr)
      call MPI_COMM_SIZE(MPI_COMM_WORLD, ct_numtasks, ct_ierr)
      call MPI_COMM_RANK(MPI_COMM_WORLD, ct_taskid, ct_ierr)

c     initialize time/node array
      do i=1,1000
          proc_time(i) = 0
          proc_load(i) = 0
      end do
c MPI communication tags
      ct_tag1 = 1
      ct_tag2 = 2
      ct_tag3 = 3
      ct_tag4 = 4
      ct_tag5 = 5
      ct_tag6 = 6
      ct_tag7 = 7
c Broadcast cantera mechanism file (canteramech)

      call MPI_BCAST(ctmech, 50, MPI_CHARACTER, MASTER,
     &               MPI_COMM_WORLD, ct_ierr)
      call MPI_BCAST(nsp, 1, MPI_INTEGER, MASTER,
     &               MPI_COMM_WORLD, ct_ierr)
      call MPI_BCAST(mw, nsp, MPI_DOUBLE_PRECISION, MASTER,
     &               MPI_COMM_WORLD, ct_ierr)
!      write(*,*) 'Node', ct_taskid,' - ',ctmech

      ctMPIinit = 0
       IF (ct_taskid .NE. 0) THEN
       WRITE(*,*) 'Warning:: Run Kiva on node',MASTER
       END IF
      END IF

c      write(*,*) 'Node', ct_taskid,' - ',ctmech

      ck_mc = 0
      DO i4a=1,numcellsa
         i4c = icelli(i4a)
```

```
            DO isp = 1,nsp
              ck_mc = ck_mc + spd(i4c,isp)*vol(i4c)
            END DO
         END DO

         IF (np .gt. 0) THEN
            npgtzero = .true.
         ELSE
            npgtzero = .false.
         END IF

         tchem=1.0d-10


ccccccccccccccccccccccccccccccccccccccccccccccccccccccccccccccccccccccccc
c scan for cells which do not meet the criteria to perform chemical
c kinetics calculations
         ct_isp_active = 0

         DO 100 i4a=1,numcellsa
            i4c = icelli(i4a)
            tijk = temp(i4c)
            IF(tijk.lt.tcut) GO TO 100
!            IF(spd(i4c,1).eq.0) GO TO 100
            spdsum = spd(i4c,1)
            DO isp=4,nsp
               spdsum = spdsum+spd(i4c,isp)
            END DO
            IF(spdsum.lt.1d-15) GO TO 100

            ct_isp_active = ct_isp_active+1
            ct_i4c_active(ct_isp_active) = i4c

         CONTINUE


         WRITE(*,*) 'Starting Cantera:: # of chemically active cells',
        &            ct_isp_active,' out of',numcellsa,' CAD =',crank

         IF(ct_isp_active.eq.0) GO TO 160
ccccccccccccccccccccccccccccccccccccccccccccccccccccccccccccccccccccccccc
c calculate the how many reactors are sent to each node. attempt to
c balance the load
         ct_chunksize = INT(FLOOR(DBLE(ct_isp_active / (ct_numtasks-1))))
         ct_remainder = ct_isp_active - ct_chunksize*(ct_numtasks-1)
!         write(*,*) ct_chunksize, ct_remainder
ccccccccccccccccccccccccccccccccccccccccccccccccccccccccccccccccccccccccc
c generate MPI arrays and send MPI data
c ct_indx follows the cells for which the kinetics are to be solved
         ct_cindx = 0

         DO ct_dest=1,ct_numtasks-1
c First KIVA timestep which requires chemical kinetics
         IF (proc_time(ct_dest).eq.0) THEN
            IF (ct_dest.le.ct_remainder) THEN
```

```
            proc_nreact(ct_dest) = ct_chunksize+1
          ELSE
            proc_nreact(ct_dest) = ct_chunksize
          END IF
c Second Kiva-kinetics timestep
       ELSE IF (proc_load(ct_dest).eq.0) THEN
            proc_load(ct_dest) = proc_nreact(ct_dest)/
     &                           proc_time(ct_dest)
       ELSE
            proc_load(ct_dest) = 0.5*proc_load(ct_dest) +
     &      0.5*proc_nreact(ct_dest)/proc_time(ct_dest)
       END IF
       END DO

       proc_load_sum = 0
       DO ct_dest=1,ct_numtasks-1
           proc_load_sum = proc_load_sum + proc_load(ct_dest)
       END DO

       IF (proc_time(1).ne.0) THEN
          nreact_sum = 0
          DO ct_dest=1,ct_numtasks-2
              proc_nreact(ct_dest) = INT(FLOOR(ct_isp_active*
     &        proc_load(ct_dest)/proc_load_sum))
              nreact_sum = nreact_sum + proc_nreact(ct_dest)
          END DO
          proc_nreact(ct_numtasks-1) = ct_isp_active - nreact_sum
       END IF

       write(*,"(1p,1000i6)") ct_dest,
     &           (proc_nreact(i),i=1,ct_numtasks-1)

       ALLOCATE( ctMPI_spd((MAXVAL(proc_nreact))*nsp) )
       ALLOCATE( ctMPI_data((MAXVAL(proc_nreact))*2+1) )
       ALLOCATE( ctMPI_cells(MAXVAL(proc_nreact)) )
       ALLOCATE( ctMPI_qf1(MAXVAL(proc_nreact)) )
       ALLOCATE( ctMPI_qf2(MAXVAL(proc_nreact)) )

       DO 110 ct_dest=1,ct_numtasks-1
c determine how many reactors to sent to each node. If number of
c reactors is not divisible by the number of cantera nodes, distribute
c the remaining tasks to the first nodes
        ct_nreact = proc_nreact(ct_dest)
       ctMPI_data(1) = dt
       DO i = 1,ct_nreact
          ct_cindx = ct_cindx + 1
          i4c = ct_i4c_active(ct_cindx)
          tijk = temp(i4c)
          DO isp = 1,nsp
              ctMPI_spd((i-1)*nsp+isp)=spd(i4c,isp)
          END DO

          ctMPI_cells(i) = i4c
c create data array
c element 1: dt
```

```
c element 2: temperature reactor 1
c element 3: pressure reactor 1
c element 4: temperature reactor 2
c .....
         ctMPI_data((i-1)*2+2) = tijk
c convert pressure data from dynes/cm2 to Pa
         ctMPI_data((i-1)*2+3) = p(i4c)*0.1
       END DO

c Send MPI data to Cantera nodes
       CALL MPI_SEND(ct_nreact, 1, MPI_INTEGER,
      &      ct_dest, ct_tag1, MPI_COMM_WORLD, ct_ierr)
       CALL MPI_SEND(ctMPI_cells(1), ct_nreact, MPI_INTEGER,
      &      ct_dest, ct_tag2, MPI_COMM_WORLD, ct_ierr)
       CALL MPI_SEND(ctMPI_data(1), ct_nreact*2+1,
      1              MPI_DOUBLE_PRECISION, ct_dest, ct_tag3,
      2              MPI_COMM_WORLD, ct_ierr)
       CALL MPI_SEND(ctMPI_spd(1), ct_nreact*nsp,
      1              MPI_DOUBLE_PRECISION, ct_dest, ct_tag4,
      2              MPI_COMM_WORLD, ct_ierr)

       CONTINUE

ccccccccccccccccccccccccccccccccccccccccccccccccccccccccccccccccccccccccccc
c Receive data from CANTERA nodes and present it to KIVA4

       DO 120 ct_source = 1,ct_numtasks-1

       CALL MPI_RECV(ct_nreact, 1, MPI_INTEGER,
      &      ct_source, ct_tag1, MPI_COMM_WORLD, status, ct_ierr)

       ALLOCATE( smf_upd(ct_nreact*nsp) )
       ALLOCATE( ct_dechem(ct_nreact) )

       CALL MPI_RECV(ctMPI_cells(1), ct_nreact, MPI_INTEGER,
      &      ct_source, ct_tag2, MPI_COMM_WORLD, status, ct_ierr)
       CALL MPI_RECV(smf_upd(1), ct_nreact*nsp,
      1              MPI_DOUBLE_PRECISION, ct_source, ct_tag3,
      2              MPI_COMM_WORLD, status, ct_ierr)
       CALL MPI_RECV(ct_dechem(1), ct_nreact,
      1              MPI_DOUBLE_PRECISION, ct_source, ct_tag4,
      2              MPI_COMM_WORLD, status, ct_ierr)
       CALL MPI_RECV(ct_time, 1,
      1              MPI_DOUBLE_PRECISION, ct_source, ct_tag5,
      2              MPI_COMM_WORLD, status, ct_ierr)
c receive forward reaction rate for reaction 1 as defined in the
c ctlib.cpp subroutine
       CALL MPI_RECV(ctMPI_qf1(1), ct_nreact, MPI_DOUBLE_PRECISION,
      &      ct_source, ct_tag6, MPI_COMM_WORLD, status, ct_ierr)
       CALL MPI_RECV(ctMPI_qf2(1), ct_nreact, MPI_DOUBLE_PRECISION,
      &      ct_source, ct_tag7, MPI_COMM_WORLD, status, ct_ierr)
       proc_time(ct_source) = ct_time

       DO i = 1,ct_nreact
```

```
          i4c = ctMPI_cells(i)
          sie(i4c) = sie(i4c) + ct_dechem(i)
          ct_qf1(i4c) = ctMPI_qf1(i)
          ct_qf2(i4c) = ctMPI_qf2(i)
          IF (npgtzero) then
            toth(i4c) = toth(i4c) + ct_dechem(i)*ro(i4c)*vol(i4c)
          END IF
          test = 0
          DO isp = 1,nsp
            spddel = smf_upd((i-1)*nsp+isp)*ro(i4c)
     &               - spd(i4c,isp)
            test = test + spddel
            spd(i4c,isp) = spd(i4c,isp) + spddel
            IF (npgtzero) THEN
                vapma(i4c,isp)=vapma(i4c,isp)+spddel*vol(i4c)
            END IF
          END DO
          if (ABS(test).gt.0.00001) write(*,*) 'Warning mc',test
          wchem=wchem+ct_dechem(i)*ro(i4c)*vol(i4c)*facsec
          dechk=ABS(ct_dechem(i)/sie(i4c))
          tchem=MAX(tchem,dechk)
        END DO
        DEALLOCATE ( smf_upd, ct_dechem )

        CONTINUE

ccccccccccccccccccccccccccccccccccccccccccccccccccccccccccccccccccccccccc
c +++
c +++ KIVA4 ignition -- single point, dual point, or ring
c +++
        if(t.lt.t1ign .or. t.gt.t2ign) return
c this module has been disabled here, as KIVA4-WSU is mainly targeted
c towards auto-ignition studies
        format(' ignition error:  cannot define ignition region'/
     & ' i4=',i6,' iyb=',i6,' izb=',i6,' xp=',1pe12.5,' yp=',
     & e12.5,' zp=',e12.5)
        return
        END
```

APPENDIX 4: KIVA4-WSU FORTRAN PROGRAM OPERATING ON THE "SLAVE" NODES HANDLING CHEMICAL KINETICS THROUGH CANTERA

```
      program main

      include 'mpif.h'
      DATA capb / 0.5d0 /
      INTEGER   MASTER
      PARAMETER (MASTER = 0)
      INTEGER  status(MPI_STATUS_SIZE), ct_ierr, ct_numtasks,
     1         ct_taskid, ct_tag1, ct_tag2, ct_tag3, ct_tag4,
     2         ct_tag5,ct_tag6,ct_tag7,ct_nreact,ct_source,
     3         nsp,j,i
      CHARACTER(LEN=50) :: ctmech
      DOUBLE PRECISION :: dt, ro
      DOUBLE PRECISION, DIMENSION(:), ALLOCATABLE :: ctMPI_data,
     &           ctMPI_spd, tijk, pres, smf, mw, smf_upd, ct_dechem,
     &           qf1,qf2
      INTEGER, DIMENSION(:), ALLOCATABLE :: ctMPI_cells
      DOUBLE PRECISION :: check_smf,ct_time


c %%%%%%%%%%%% MPI Initializations %%%%%%%%%%%%
      CALL MPI_INIT(ct_ierr)
      CALL MPI_COMM_SIZE(MPI_COMM_WORLD, ct_numtasks, ct_ierr)
      CALL MPI_COMM_RANK(MPI_COMM_WORLD, ct_taskid, ct_ierr)

c MPI communication tags
      ct_tag1 = 1
      ct_tag2 = 2
      ct_tag3 = 3
      ct_tag4 = 4
      ct_tag5 = 5
      ct_tag6 = 6
      ct_tag7 = 7

c Broadcast cantera mechanism file (ctmech)
! http://dsrg.mff.cuni.cz/~ceres/sch/mwy/text/ch06s07s05.php
      call MPI_BCAST(ctmech, 50, MPI_CHARACTER, MASTER,
     &               MPI_COMM_WORLD, ct_ierr)
      call MPI_BCAST(nsp, 1, MPI_INTEGER, MASTER,
     &               MPI_COMM_WORLD, ct_ierr)
      ALLOCATE( mw(nsp) )

      call MPI_BCAST(mw, nsp, MPI_DOUBLE_PRECISION, MASTER,
     &               MPI_COMM_WORLD, ct_ierr)

c Receive data from Kiva

      CALL MPI_RECV(ct_nreact, 1, MPI_INTEGER,
     &      MASTER, ct_tag1, MPI_COMM_WORLD, status, ct_ierr)
      ALLOCATE( ctMPI_spd(ct_nreact*nsp) )
      ALLOCATE( ctMPI_data(ct_nreact*2+1) )
      ALLOCATE( ctMPI_cells(ct_nreact) )
```

```
      ALLOCATE( qf1(ct_nreact) )
      ALLOCATE( qf2(ct_nreact) )
      ALLOCATE( smf(ct_nreact*nsp) )
      ALLOCATE( smf_upd(ct_nreact*nsp) )
      ALLOCATE( ct_dechem(ct_nreact) )
      ALLOCATE( tijk(ct_nreact), pres(ct_nreact) )


      CALL MPI_RECV(ctMPI_cells(1), ct_nreact, MPI_INTEGER,
     &      MASTER, ct_tag2, MPI_COMM_WORLD, status, ct_ierr)
      CALL MPI_RECV(ctMPI_data(1), ct_nreact*2+1,
     1              MPI_DOUBLE_PRECISION, MASTER, ct_tag3,
     2              MPI_COMM_WORLD, status, ct_ierr)
c ctMPI_data array structure
c element 1: dt
c element 2: temperature reactor 1
c element 3: pressure reactor 1
c element 4: temperature reactor 2
c .....

      CALL MPI_RECV(ctMPI_spd(1), ct_nreact*nsp,
     1              MPI_DOUBLE_PRECISION, MASTER, ct_tag4,
     2              MPI_COMM_WORLD, status, ct_ierr)

c      IF (ct_taskid.eq.1) THEN
c         WRITE(*,*) 'MPIdata', ctMPI_data(1),ctMPI_data(2)
c         WRITE(*,*) 'MPIspd', ctMPI_spd(1)
c         WRITE(*,*) 'MPIcell', ctMPI_cells(1)
c      END IF


      DO i=1,ct_nreact
         dt = ctMPI_data(1)
         tijk(i) = ctMPI_data((i-1)*2+2)
         pres(i) = ctMPI_data((i-1)*2+3)
         ro = 0
        DO isp = 1,nsp
           j = (i-1)*nsp + isp
           ro = ctMPI_spd(j) + ro
        END DO
        check_smf = 0
        DO isp = 1,nsp
           j = (i-1)*nsp + isp
           smf(j) = ctMPI_spd(j)/ro
           check_smf = check_smf + smf(j)
        END DO

      END DO

      ct_time = MPI_Wtime()

      CALL cantera_reactor(ctmech,smf,tijk,pres,dt,ct_nreact,
     &                     smf_upd, ct_dechem,qf1,qf2)

      ct_time = MPI_Wtime() - ct_time
```

```
      sum1 = 0

ccccccccccccccccccccccccccccccccccccccccccccccccccccccccccccccccccccccccccc
c Send data back to KIVA4

      CALL MPI_SEND(ct_nreact, 1, MPI_INTEGER,
     &      MASTER, ct_tag1, MPI_COMM_WORLD, ct_ierr)
      CALL MPI_SEND(ctMPI_cells(1), ct_nreact, MPI_INTEGER,
     &      MASTER, ct_tag2, MPI_COMM_WORLD, ct_ierr)
      CALL MPI_SEND(smf_upd(1), ct_nreact*nsp,
     1              MPI_DOUBLE_PRECISION, MASTER, ct_tag3,
     2              MPI_COMM_WORLD, ct_ierr)
      CALL MPI_SEND(ct_dechem(1), ct_nreact,
     1              MPI_DOUBLE_PRECISION, MASTER, ct_tag4,
     2              MPI_COMM_WORLD, ct_ierr)
      CALL MPI_SEND(ct_time,1,
     1              MPI_DOUBLE_PRECISION, MASTER, ct_tag5,
     2              MPI_COMM_WORLD, ct_ierr)
      CALL MPI_SEND(qf1(1), ct_nreact,
     1              MPI_DOUBLE_PRECISION, MASTER, ct_tag6,
     2              MPI_COMM_WORLD, ct_ierr)
      CALL MPI_SEND(qf2(1), ct_nreact,
     1              MPI_DOUBLE_PRECISION, MASTER, ct_tag7,
     2              MPI_COMM_WORLD, ct_ierr)


      DEALLOCATE ( ctMPI_spd, ctMPI_data, ctMPI_cells, tijk, pres,
     &             smf, smf_upd, ct_dechem, qf1, qf2)


      GOTO 900
      DEALLOCATE( mw )

      END
```

APPENDIX 5: CANTERA C++ SUBROUTINE FOR CHEMICAL KINETIC SOLVER

```
#include <stdlib.h>
#include <stdio.h>
#include <string.h>
#include <math.h>

//Cantera includes
#include "cantera/Cantera.h"
#include "cantera/zerodim.h"
#include "cantera/IdealGasMix.h"
#include "cantera/kinetics.h"

using namespace CanteraZeroD;

extern "C" {
    void cantera_reactor_(char *, double *, double *, double *, double
*, int *,double *, double *, double *, double *, int);}

void cantera_reactor_(char *ctmech, double *smf, double *tijk, double
*pres, double *dt, int *ct_nreact, double *smf_upd, double *ct_dechem,
double *qf1, double *qf2, int hidden_stringlength){
    int i,j,isp,negsmf;
    for (i = 0; i < *ct_nreact ; i++){
    }

    IdealGasMix gas(ctmech);
    int nsp = gas.nSpecies();
        int nrx = gas.nReactions();
    Reactor combustor;
        double* qf = new double[nrx];
    negsmf = 0;
    for (i = 0; i < *ct_nreact; i++) {
        try {
            vector_fp Yset(nsp, 0.0);
            for ( isp = 0; isp < nsp; isp++ ) {
                j = i*nsp + isp;
                Yset[isp] =  smf[j];
                if (Yset[isp] < 0) {
                    Yset[isp] = 0;
                    negsmf = 1;
                }
            }

            gas.setState_TPY(tijk[i], pres[i],DATA_PTR(Yset));


            combustor.insert(gas);
            ReactorNet sim;
            sim.addReactor(&combustor,false);
            sim.setInitialTime(0);

            double tfinal = *dt;
            double tnow = 0.0;
```

```
            double u1 = combustor.intEnergy_mass();
            while (tnow < tfinal) {
                tnow = sim.step(tfinal);
            }
            double pres_upd = combustor.pressure();
            ThermoPhase& c = combustor.contents();
            for ( isp = 0; isp < nsp; isp++ ) {
                j = i*nsp + isp;

                smf_upd[j] = c.massFraction(isp);
                if (smf_upd[j] < 0){
                    smf_upd[j] = 0;
                    negsmf = 1;
                }
                Yset[isp] = smf_upd[j];
            }

            gas.setState_TPY(tijk[i], pres_upd,DATA_PTR(Yset));
            combustor.insert(gas);
            double u2 = combustor.intEnergy_mass();
// convert from J/kg (cantera unit) to ergs/gm (Kiva unit)
            ct_dechem[i] = -(u2 - u1)*10000;
//extract forward reaction rates for specified reactions for post-
processing
            gas.getFwdRatesOfProgress(qf);
            qf1[i] = qf[26]; //co+o -> co2 (reaction #27)
            qf2[i] = qf[6]; //co+oh-> co2+h (reaction #7)
        }


        catch(const Cantera::CanteraError& e) {
                Cantera::showErrors(std::cerr);
                    cout<< " Cantera complained in cell " << i
                    << " with a Cantera::CanteraError"  << endl;
            }
    }
}
```

APPENDIX 6: SEMI-DETAILED N-HEPTANE ETHANOL OXIDATION MECHANISM

	REACTIONS CONSIDERED			(k = A T**b exp(-E/RT)) A	b	E
1.	CH3+H(+M)=CH4(+M)			2.14E+15	-0.4	0.0
	Low pressure limit:	0.33100E+31	-0.40000E+01	0.21080E+04		
	TROE centering:	0.00000E+00	0.10000E-14	0.10000E-14	0.40000E+02	
	H2	Enhanced by	2.000E+00			
	H2O	Enhanced by	5.000E+00			
	CO	Enhanced by	2.000E+00			
	CO2	Enhanced by	3.000E+00			
2.	CH4+H=CH3+H2			1.73E+04	3.0	8224.0
	Reverse Arrhenius coefficients:			6.61E+02	3.0	7744.0
3.	CH4+OH=CH3+H2O			1.93E+05	2.4	2106.0
	Reverse Arrhenius coefficients:			3.20E+04	2.4	16780.0
4.	CH4+O=CH3+OH			3.15E+12	0.5	10290.0
	Reverse Arrhenius coefficients:			5.30E+10	0.5	7715.0
5.	C2H6+CH3=C2H5+CH4			1.51E-07	6.0	6047.0
	Reverse Arrhenius coefficients:			9.65E-10	6.6	10220.0
6.	HCO+OH=CO+H2O			1.02E+14	0.0	0.0
	Reverse Arrhenius coefficients:			2.90E+15	0.0	105200.0
7.	CO+OH=CO2+H			1.40E+05	1.9	-1347.0
	Reverse Arrhenius coefficients:			1.57E+07	1.9	20990.0
8.	H+O2=O+OH			1.97E+14	0.0	16540.0
	Reverse Arrhenius coefficients:			1.56E+13	0.0	425.0
9.	O+H2=H+OH			5.08E+04	2.7	6292.0
	Reverse Arrhenius coefficients:			2.23E+04	2.7	4197.0
10.	O+H2O=OH+OH			2.97E+06	2.0	13400.0
	Reverse Arrhenius coefficients:			3.01E+05	2.0	-3850.0
11.	OH+H2=H+H2O			2.16E+08	1.5	3430.0
	Reverse Arrhenius coefficients:			9.35E+08	1.5	18580.0
12.	HCO+M=H+CO+M			1.86E+17	-1.0	17000.0
	Reverse Arrhenius coefficients:			6.47E+13	0.0	-442.0
	H2	Enhanced by	2.500E+00			
	H2O	Enhanced by	1.200E+01			
	CO	Enhanced by	1.900E+00			
	CO2	Enhanced by	3.800E+00			
13.	H2O2+OH=H2O+HO2			1.00E+12	0.0	0.0
	Reverse Arrhenius coefficients:			1.68E+11	0.3	31460.0
	Declared duplicate reaction...					
14.	C2H4+O=CH3+HCO			1.02E+07	1.9	179.0
	Reverse Arrhenius coefficients:			2.85E+08	1.1	31770.0
15.	H+C2H4(+M)=C2H5(+M)			1.08E+12	0.5	1822.0
	Low pressure limit:	0.11120E+35	-0.50000E+01	0.44480E+04		
	TROE centering:	0.10000E+01	0.10000E-14	0.95000E+02	0.20000E+03	
	H2	Enhanced by	2.000E+00			
	H2O	Enhanced by	5.000E+00			
	CO	Enhanced by	2.000E+00			
	CO2	Enhanced by	3.000E+00			
16.	CH3OH(+M)=CH3+OH(+M)			1.90E+16	0.0	91730.0
	Low pressure limit:	0.29500E+45	-0.73500E+01	0.95460E+05		
	TROE centering:	0.41400E+00	0.27900E+03	0.54590E+04	0.10000+101	
	H2	Enhanced by	2.000E+00			
	H2O	Enhanced by	1.600E+01			
	CO	Enhanced by	2.000E+00			
	CO2	Enhanced by	3.000E+00			
17.	C2H6+H=C2H5+H2			5.54E+02	3.5	5167.0
	Reverse Arrhenius coefficients:			1.36E-01	4.1	8857.0

```
18. CH3OH+HO2=CH2OH+H2O2                          3.98E+13    0.0    19400.0
    Reverse Arrhenius coefficients:               1.10E+09    1.3    11250.0
19. C2H5+O2=C2H4+HO2                              1.22E+30   -5.8    10100.0
    Reverse Arrhenius coefficients:               1.26E+30   -5.6    22300.0
20. C2H6+OH=C2H5+H2O                              5.80E+07    1.7     1160.0
    Reverse Arrhenius coefficients:               6.14E+04    2.3    20000.0
21. C2H6+O=C2H5+OH                                1.30E+07    2.1     5190.0
    Reverse Arrhenius coefficients:               1.40E+03    2.7     6785.0
22. CH3+HO2=CH3O+OH                               1.10E+13    0.0        0.0
    Reverse Arrhenius coefficients:               4.78E+14   -0.3    24550.0
23. CO+HO2=CO2+OH                                 3.01E+13    0.0    23000.0
    Reverse Arrhenius coefficients:               6.44E+15   -0.3    84610.0
24. CH3+CH3(+M)=C2H6(+M)                          9.21E+16   -1.2      635.8
    Low pressure limit:  0.11350E+37 -0.52460E+01  0.17050E+04
    TROE centering:      0.40500E+00  0.11200E+04  0.69600E+02  0.10000E+16
    H2              Enhanced by    2.000E+00
    H2O             Enhanced by    5.000E+00
    CO              Enhanced by    2.000E+00
    CO2             Enhanced by    3.000E+00
25. H2O+M=H+OH+M                                  1.84E+27   -3.0   122600.0
    Reverse Arrhenius coefficients:               2.25E+22   -2.0        0.0
    H2              Enhanced by    2.500E+00
    H2O             Enhanced by    1.200E+01
    CO              Enhanced by    1.900E+00
    CO2             Enhanced by    3.800E+00
26. H+O2(+M)=HO2(+M)                              1.48E+12    0.6        0.0
    Low pressure limit:  0.35000E+17 -0.41000E+00 -0.11160E+04
    TROE centering:      0.50000E+00  0.10000E-29  0.10000E+31  0.10000+101
    H2              Enhanced by    2.500E+00
    H2O             Enhanced by    1.200E+01
    CO              Enhanced by    1.900E+00
    CO2             Enhanced by    3.800E+00
27. CO+O(+M)=CO2(+M)                              1.80E+10    0.0     2384.0
    Low pressure limit:  0.13500E+25 -0.27880E+01  0.41910E+04
    H2              Enhanced by    2.500E+00
    H2O             Enhanced by    1.200E+01
    CO              Enhanced by    1.900E+00
    CO2             Enhanced by    3.800E+00
28. CO+O2=CO2+O                                   1.62E+13    0.0    47700.0
    Reverse Arrhenius coefficients:               1.43E+14    0.0    53920.0
29. HCO+H=CO+H2                                   7.34E+13    0.0        0.0
    Reverse Arrhenius coefficients:               4.81E+14    0.0    90000.0
30. HCO+O=CO+OH                                   3.02E+13    0.0        0.0
    Reverse Arrhenius coefficients:               8.70E+13    0.0    87900.0
31. CH2O+M=HCO+H+M                                6.28E+29   -3.6    93200.0
    Reverse Arrhenius coefficients:               2.66E+24   -2.6      427.0
32. CH2O+OH=HCO+H2O                               3.43E+09    1.2     -447.0
    Reverse Arrhenius coefficients:               1.19E+09    1.2    29380.0
33. CH2O+H=HCO+H2                                 9.33E+08    1.5     2976.0
    Reverse Arrhenius coefficients:               7.45E+07    1.5    17650.0
34. CH2O+O=HCO+OH                                 4.16E+11    0.6     2762.0
    Reverse Arrhenius coefficients:               1.46E+10    0.6    15340.0
35. CH3+OH=CH2O+H2                                2.25E+13    0.0     4300.0
    Reverse Arrhenius coefficients:               6.76E+14    0.0    76020.0
36. CH3+O=CH2O+H                                  8.00E+13    0.0        0.0
    Reverse Arrhenius coefficients:               1.06E+15    0.0    69630.0
37. CH3+O2=CH3O+O                                 2.00E+18   -1.6    29210.0
    Reverse Arrhenius coefficients:               3.58E+18   -1.6    -1631.0
38. CH2O+CH3=HCO+CH4                              3.64E-06    5.4      998.0
    Reverse Arrhenius coefficients:               7.58E-06    5.4    16150.0
39. HCO+CH3=CH4+CO                                1.21E+14    0.0        0.0
```

```
    Reverse Arrhenius coefficients:                          2.07E+16    0.0    90480.0
40. CH3O(+M)=CH2O+H(+M)                                      5.45E+13    0.0    13500.0
    Low pressure limit:  0.23440E+26 -0.27000E+01  0.30600E+05
41. C2H4(+M)=C2H2+H2(+M)                                     1.80E+13    0.0    76000.0
    Low pressure limit:  0.15000E+16  0.00000E+00  0.55443E+05
42. HO2+O=OH+O2                                              3.25E+13    0.0        0.0
    Reverse Arrhenius coefficients:                          7.86E+14   -0.3    55390.0
43. HCO+HO2=CH2O+O2                                          2.97E+10    0.3    -3861.0
    Reverse Arrhenius coefficients:                          2.05E+13    0.0    38950.0
44. CH3O+O2=CH2O+HO2                                         5.50E+10    0.0     2424.0
    Reverse Arrhenius coefficients:                          1.32E+09    0.3    31390.0
45. CH3+HO2=CH4+O2                                           3.60E+12    0.0        0.0
    Reverse Arrhenius coefficients:                          5.18E+15   -0.3    57960.0
46. HCO+O2=CO+HO2                                            7.58E+12    0.0      410.0
    Reverse Arrhenius coefficients:                          9.03E+11    0.3    32930.0
47. HO2+H=OH+OH                                              7.08E+13    0.0      300.0
    Reverse Arrhenius coefficients:                          1.35E+14   -0.3    39570.0
48. HO2+H=H2+O2                                              1.66E+13    0.0      820.0
    Reverse Arrhenius coefficients:                          9.14E+14   -0.3    58300.0
49. HO2+OH=H2O+O2                                            2.89E+13    0.0     -500.0
    Reverse Arrhenius coefficients:                          6.89E+15   -0.3    72140.0
50. H2O2+O2=HO2+HO2                                          5.94E+17   -0.7    53150.0
    Reverse Arrhenius coefficients:                          4.20E+14    0.0    11980.0
    Declared duplicate reaction...
51. OH+OH(+M)=H2O2(+M)                                       1.24E+14   -0.4        0.0
    Low pressure limit:  0.30410E+31 -0.46300E+01  0.20490E+04
    TROE centering:      0.47000E+00  0.10000E+03  0.20000E+04  0.10000E+16
    H2              Enhanced by    2.500E+00
    H2O             Enhanced by    1.200E+01
    CO              Enhanced by    1.900E+00
    CO2             Enhanced by    3.800E+00
52. H2O2+H=H2O+OH                                            2.41E+13    0.0     3970.0
    Reverse Arrhenius coefficients:                          7.75E+12    0.0    74700.0
53. CH4+HO2=CH3+H2O2                                         3.42E+11    0.0    19290.0
    Reverse Arrhenius coefficients:                          3.36E+11   -0.3     2502.0
54. CH2O+HO2=HCO+H2O2                                        5.82E-03    4.5     6557.0
    Reverse Arrhenius coefficients:                          1.19E-02    4.2     4921.0
55. OH+M=O+H+M                                               3.91E+22   -2.0   105300.0
    Reverse Arrhenius coefficients:                          4.72E+18   -1.0        0.0
    H2              Enhanced by    2.500E+00
    H2O             Enhanced by    1.200E+01
    CO              Enhanced by    1.900E+00
    CO2             Enhanced by    3.800E+00
56. O2+M=O+O+M                                               6.47E+20   -1.5   121500.0
    Reverse Arrhenius coefficients:                          6.17E+15   -0.5        0.0
    H2              Enhanced by    2.500E+00
    H2O             Enhanced by    1.200E+01
    CO              Enhanced by    1.900E+00
    CO2             Enhanced by    3.800E+00
57. H2+M=H+H+M                                               4.57E+19   -1.4   104400.0
    Reverse Arrhenius coefficients:                          2.42E+15   -0.4    -3040.0
    H2              Enhanced by    2.500E+00
    H2O             Enhanced by    1.200E+01
    CO              Enhanced by    1.900E+00
    CO2             Enhanced by    3.800E+00
58. C2H3+H(+M)=C2H4(+M)                                      6.10E+12    0.3      280.0
    Low pressure limit:  0.98000E+30 -0.38600E+01  0.33200E+04
    TROE centering:      0.78200E+00  0.20800E+03  0.26630E+04  0.60950E+04
59. C2H5+C2H3=C2H4+C2H4                                      5.76E+14   -0.6     2490.0
    Reverse Arrhenius coefficients:                          4.82E+14    0.0    71530.0
60. C2H2+H(+M)=C2H3(+M)                                      3.11E+11    0.6     2589.0
```

```
    Low pressure limit:  0.22540E+41 -0.72690E+01  0.65770E+04
    TROE centering:      0.10000E+01  0.10000E-14  0.67500E+03  0.10000E+16
    H2              Enhanced by    2.000E+00
    H2O             Enhanced by    5.000E+00
    CO              Enhanced by    2.000E+00
    CO2             Enhanced by    3.000E+00
61. C2H4+H=C2H3+H2                                  8.42E-03    4.6     2583.0
    Reverse Arrhenius coefficients:                 5.72E-01    3.8     3233.0
62. C2H4+OH=C2H3+H2O                                2.05E+13    0.0     5950.0
    Reverse Arrhenius coefficients:                 6.03E+15   -0.8    21760.0
63. C2H2+M=C2H+H+M                                  4.20E+16    0.0   107000.0
    Reverse Arrhenius coefficients:                 7.13E+07    2.1   -28910.0
64. C2H2+O2=HCCO+OH                                 2.00E+08    1.5    30100.0
    Reverse Arrhenius coefficients:                 2.23E+05    1.5    25400.0
65. CH2+O2=CO+H2O                                   7.28E+19   -2.5     1809.0
    Reverse Arrhenius coefficients:                 8.51E+20   -2.5   179800.0
66. C2H2+OH=C2H+H2O                                 3.37E+07    2.0    14000.0
    Reverse Arrhenius coefficients:                 4.67E+03    3.1      685.0
67. O+C2H2=C2H+OH                                   3.16E+15   -0.6    15000.0
    Reverse Arrhenius coefficients:                 4.44E+10    0.5   -15560.0
68. C2H2+O=CH2+CO                                   6.12E+06    2.0     1900.0
    Reverse Arrhenius coefficients:                 1.15E+06    2.0    52570.0
69. C2H+O2=HCO+CO                                   2.41E+12    0.0        0.0
    Reverse Arrhenius coefficients:                 1.33E+16   -1.1   154100.0
70. C2H+O=CO+CH                                     1.81E+13    0.0        0.0
    Reverse Arrhenius coefficients:                 7.48E+16   -1.1    82130.0
71. CH2+O2=HCO+OH                                   1.29E+20   -3.3      284.0
    Reverse Arrhenius coefficients:                 5.31E+19   -3.3    73170.0
72. CH2+O=CO+H+H                                    5.00E+13    0.0        0.0
    All REV parameters are zero...                  0.000E+00  0.00  0.000E+00
    This reaction is treated as irreversible
73. CH2+H=CH+H2                                     1.00E+18   -1.6        0.0
    Reverse Arrhenius coefficients:                 7.03E+17   -1.6     2990.0
74. CH2+OH=CH+H2O                                   1.13E+07    2.0     3000.0
    Reverse Arrhenius coefficients:                 3.44E+07    2.0    21140.0
75. CH2+O2=CO2+H+H                                  3.29E+21   -3.3     2868.0
    All REV parameters are zero...                  0.000E+00  0.00  0.000E+00
    This reaction is treated as irreversible
76. CH+O2=HCO+O                                     3.30E+13    0.0        0.0
    Reverse Arrhenius coefficients:                 4.40E+13    0.0    71990.0
77. CH3OH+OH=CH2OH+H2O                              7.10E+06    1.8     -596.0
    Reverse Arrhenius coefficients:                 3.29E+01    3.5    22720.0
78. CH3OH+H=CH3O+H2                                 3.60E+12    0.0     6095.0
    Reverse Arrhenius coefficients:                 7.47E+12    0.0     7825.0
79. CH3OH+H=CH2OH+H2                                1.44E+13    0.0     6095.0
    Reverse Arrhenius coefficients:                 1.54E+07    1.7    14250.0
80. CH3OH+CH3=CH2OH+CH4                             3.19E+01    3.2     7172.0
    Reverse Arrhenius coefficients:                 8.93E-04    4.8    15810.0
81. CH3OH+O=CH2OH+OH                                3.88E+05    2.5     3080.0
    Reverse Arrhenius coefficients:                 1.83E-01    4.2     9143.0
82. CH2OH+O2=CH2O+HO2                               6.51E+05    2.3     -770.0
    Reverse Arrhenius coefficients:                 3.02E+10    0.9    21770.0
83. CH2OH(+M)=CH2O+H(+M)                            2.80E+14   -0.7    32820.0
    Low pressure limit:  0.60100E+34 -0.53900E+01  0.36200E+05
    TROE centering:      0.96000E+00  0.67600E+02  0.18550E+04  0.75430E+04
84. C2H3+O2=C2H2+HO2                                2.12E-06    6.0     9484.0
    Reverse Arrhenius coefficients:                 1.11E-07    6.3    17570.0
85. H2O2+O=OH+HO2                                   9.55E+06    2.0     3970.0
    Reverse Arrhenius coefficients:                 1.63E+05    2.3    18180.0
86. C2H2+O=HCCO+H                                   1.43E+07    2.0     1900.0
    Reverse Arrhenius coefficients:                 2.02E+05    2.0    13310.0
```

```
 87. C2H2+OH=CH2CO+H                                   2.19E-04    4.5    -1000.0
     Reverse Arrhenius coefficients:                   2.16E-03    4.5    19660.0
 88. CH2CO+H=CH3+CO                                    1.10E+13    0.0     3400.0
     Reverse Arrhenius coefficients:                   2.40E+12    0.0    40200.0
 89. CH2CO+O=CH2+CO2                                   1.75E+12    0.0     1350.0
     Reverse Arrhenius coefficients:                   3.74E+12    0.0    53690.0
 90. CH2+O2=CH2O+O                                     3.29E+21   -3.3     2868.0
     Reverse Arrhenius coefficients:                   3.86E+22   -3.3    63180.0
 91. CH2CO(+M)=CH2+CO(+M)                              3.00E+14    0.0    70980.0
     Low pressure limit:  0.36000E+16  0.00000E+00  0.59270E+05
 92. CH2CO+O=HCCO+OH                                   1.00E+13    0.0     8000.0
     Reverse Arrhenius coefficients:                   1.43E+10    0.0    -1255.0
 93. CH2CO+OH=HCCO+H2O                                 1.00E+13    0.0     2000.0
     Reverse Arrhenius coefficients:                   1.41E+11    0.0     9995.0
 94. CH2CO+H=HCCO+H2                                   2.00E+14    0.0     8000.0
     Reverse Arrhenius coefficients:                   6.52E+11    0.0      840.0
 95. HCCO+OH=HCO+HCO                                   1.00E+13    0.0        0.0
     Reverse Arrhenius coefficients:                   2.41E+14    0.0    40360.0
 96. HCCO+H=CH2(S)+CO                                  1.10E+14    0.0        0.0
     Reverse Arrhenius coefficients:                   2.05E+12    0.9    27830.0
 97. HCCO+O=H+CO+CO                                    8.00E+13    0.0        0.0
     All REV parameters are zero...                    0.000E+00  0.00  0.000E+00
     This reaction is treated as irreversible
 98. C2H6+O2=C2H5+HO2                                  6.03E+13    0.0    51870.0
     Reverse Arrhenius coefficients:                   2.68E+08    0.9    -1922.0
 99. C2H6+HO2=C2H5+H2O2                                1.32E+13    0.0    20470.0
     Reverse Arrhenius coefficients:                   8.30E+10    0.2     7852.0
100. CH2+O2=CO2+H2                                     1.01E+21   -3.3     1508.0
     Reverse Arrhenius coefficients:                   3.05E+23   -3.3   186700.0
101. CH3+C2H3=CH4+C2H2                                 3.92E+11    0.0        0.0
     Reverse Arrhenius coefficients:                   2.96E+13    0.0    66050.0
102. CH3+C2H5=CH4+C2H4                                 1.95E+13   -0.5        0.0
     Reverse Arrhenius coefficients:                   2.90E+16   -0.7    70170.0
103. CH3OH+CH2O=CH3O+CH3O                              3.84E+13    0.1    84720.0
     Reverse Arrhenius coefficients:                   6.03E+13    0.0        0.0
104. CH2O+CH3O=CH3OH+HCO                               1.02E+11    0.0     2980.0
     Reverse Arrhenius coefficients:                   3.93E+09    0.0    15920.0
105. CH4+CH3O=CH3+CH3OH                                1.57E+11    0.0     8842.0
     Reverse Arrhenius coefficients:                   2.90E+09    0.0     6632.0
106. C2H6+CH3O=C2H5+CH3OH                              2.41E+11    0.0     7090.0
     Reverse Arrhenius coefficients:                   2.84E+07    0.6     9050.0
107. C2H3+H=C2H2+H2                                    2.00E+13    0.0     2500.0
     Reverse Arrhenius coefficients:                   1.33E+13    0.0    68080.0
108. CH3O+CH3OH=CH2OH+CH3OH                            3.00E+11    0.0     4074.0
     Reverse Arrhenius coefficients:                   1.55E+05    1.7    10500.0
109. CH3OH+OH=CH3O+H2O                                 1.00E+06    2.1      496.7
     Reverse Arrhenius coefficients:                   8.98E+06    2.1    17380.0
110. C2H5+H=CH3+CH3                                    3.61E+13    0.0        0.0
     Reverse Arrhenius coefficients:                   5.45E+16   -1.0    16980.0
111. C2H3+O2=CH2O+HCO                                  1.70E+29   -5.3     6500.0
     Reverse Arrhenius coefficients:                   1.66E+29   -5.3    93050.0
112. C2H6=C2H5+H                                       2.78E+21   -1.6   103800.0
     Reverse Arrhenius coefficients:                   3.61E+13    0.0        0.0
113. C2H5OH(+M)=CH2OH+CH3(+M)                          5.71E+23   -1.7    94410.0
     Low pressure limit:  0.31100E+86 -0.18840E+02  0.11310E+06
     TROE centering:      0.50000E+00  0.55000E+03  0.82500E+03  0.61000E+04
     H2              Enhanced by    2.000E+00
     H2O             Enhanced by    5.000E+00
     CO              Enhanced by    2.000E+00
     CO2             Enhanced by    3.000E+00
114. C2H5OH(+M)=C2H5+OH(+M)                            2.40E+23   -1.6    99540.0
```

```
     Low pressure limit:  0.51100E+86 -0.18800E+02  0.11877E+06
     TROE centering:      0.50000E+00  0.65000E+03  0.80000E+03  0.10000E+16
     H2              Enhanced by    2.000E+00
     H2O             Enhanced by    5.000E+00
     CO              Enhanced by    2.000E+00
     CO2             Enhanced by    3.000E+00
115. C2H5OH(+M)=C2H4+H2O(+M)                          2.79E+13    0.1    66140.0
     Low pressure limit:  0.25700E+84 -0.18850E+02  0.86453E+05
     TROE centering:      0.70000E+00  0.35000E+03  0.80000E+03  0.38000E+04
     H2O             Enhanced by    5.000E+00
116. C2H5OH(+M)=CH3CHO+H2(+M)                         7.24E+11    0.1    91010.0
     Low pressure limit:  0.44600E+88 -0.19420E+02  0.11559E+06
     TROE centering:      0.90000E+00  0.90000E+03  0.11000E+04  0.35000E+04
     H2O             Enhanced by    5.000E+00
117. C2H5OH+O2=PC2H4OH+HO2                            2.00E+13    0.0    52800.0
     Reverse Arrhenius coefficients:                  3.47E+08    0.3    -1105.0
118. C2H5OH+O2=SC2H4OH+HO2                            1.50E+13    0.0    50150.0
     Reverse Arrhenius coefficients:                  1.87E+11    0.1     3856.0
119. C2H5OH+OH=PC2H4OH+H2O                            1.74E+11    0.3      600.0
     Reverse Arrhenius coefficients:                  7.20E+08    0.3    19330.0
120. C2H5OH+OH=SC2H4OH+H2O                            4.64E+11    0.1        0.0
     Reverse Arrhenius coefficients:                  1.38E+12   -0.1    26350.0
121. C2H5OH+H=PC2H4OH+H2                              1.23E+07    1.8     5098.0
     Reverse Arrhenius coefficients:                  1.18E+04    1.8     8677.0
122. C2H5OH+H=SC2H4OH+H2                              2.58E+07    1.6     2827.0
     Reverse Arrhenius coefficients:                  1.77E+07    1.4    14020.0
123. C2H5OH+HO2=PC2H4OH+H2O2                          1.23E+04    2.5    15750.0
     Reverse Arrhenius coefficients:                  3.02E+02    2.2     3021.0
124. C2H5OH+HO2=SC2H4OH+H2O2                          8.20E+03    2.5    10750.0
     Reverse Arrhenius coefficients:                  1.45E+05    2.0     5632.0
125. C2H5OH+HO2=C2H5O+H2O2                            2.50E+12    0.0    24000.0
     Reverse Arrhenius coefficients:                  1.51E+14   -1.8    38000.0
126. C2H5OH+O=PC2H4OH+OH                              9.41E+07    1.7     5459.0
     Reverse Arrhenius coefficients:                  3.95E+04    1.7     6943.0
127. C2H5OH+O=SC2H4OH+OH                              1.88E+07    1.9     1824.0
     Reverse Arrhenius coefficients:                  5.66E+06    1.6    10920.0
128. C2H5OH+CH3=PC2H4OH+CH4                           1.33E+02    3.2     9362.0
     Reverse Arrhenius coefficients:                  3.32E+00    3.2    13420.0
129. C2H5OH+CH3=SC2H4OH+CH4                           4.44E+02    2.9     7690.0
     Reverse Arrhenius coefficients:                  7.96E+03    2.7    19360.0
130. C2H5OH+C2H5=PC2H4OH+C2H6                         5.00E+10    0.0    13400.0
     Reverse Arrhenius coefficients:                  1.95E+11   -0.6    13290.0
131. C2H5OH+C2H5=SC2H4OH+C2H6                         5.00E+10    0.0    10400.0
     Reverse Arrhenius coefficients:                  1.40E+14   -0.8    17900.0
132. PC2H4OH=C2H4+OH                                  1.29E+12   -0.4    26850.0
     Reverse Arrhenius coefficients:                  9.93E+11    0.0     -960.0
133. SC2H4OH+M=CH3CHO+H+M                             1.00E+14    0.0    25000.0
     Reverse Arrhenius coefficients:                  4.71E+10    0.9    -3630.0
134. C2H4+CH3=C2H3+CH4                                6.62E+00    3.7     9500.0
     Reverse Arrhenius coefficients:                  1.44E+00    4.0     5472.0
135. CH3CO(+M)=CH3+CO(+M)                             3.00E+12    0.0    16720.0
     Low pressure limit:  0.12000E+16  0.00000E+00  0.12518E+05
136. CH3CHO=CH3+HCO                                   2.61E+15    0.1    80550.0
     Reverse Arrhenius coefficients:                  2.00E+13    0.0        0.0
137. CH3CHO+O2=CH3CO+HO2                              3.01E+13    0.0    39150.0
     Reverse Arrhenius coefficients:                  8.55E+10    0.3    -1940.0
138. CH3CHO+OH=CH3CO+H2O                              2.00E+06    1.8     1300.0
     Reverse Arrhenius coefficients:                  1.35E+06    1.8    32850.0
139. CH3CHO+H=CH3CO+H2                                1.34E+13    0.0     3300.0
     Reverse Arrhenius coefficients:                  2.10E+12    0.0    19690.0
140. CH3CHO+O=CH3CO+OH                                5.94E+12    0.0     1868.0
```

	Reverse Arrhenius coefficients:	4.08E+11	0.0	16170.0
141.	CH3CHO+HO2=CH3CO+H2O2	3.01E+12	0.0	11920.0
	Reverse Arrhenius coefficients:	1.21E+13	-0.3	12010.0
142.	CH3CHO+CH3=CH3CO+CH4	2.61E+06	1.8	5911.0
	Reverse Arrhenius coefficients:	1.07E+07	1.8	22780.0
143.	C3H5-S=C2H2+CH3	9.60E+39	-8.2	42030.0
	Reverse Arrhenius coefficients:	1.61E+40	-8.6	20330.0
144.	C2H2+CH3=C3H4-P+H	1.21E+17	-1.2	16680.0
	Reverse Arrhenius coefficients:	1.00E+14	0.0	4000.0
145.	C3H5-A=C2H2+CH3	2.40E+48	-9.9	82080.0
	Reverse Arrhenius coefficients:	2.61E+46	-9.8	36950.0
146.	C3H6=C2H3+CH3	2.73E+62	-13.3	123200.0
	Reverse Arrhenius coefficients:	4.71E+59	-13.2	29540.0
147.	C2H2+CH3=C3H4-A+H	6.74E+19	-2.1	31590.0
	Reverse Arrhenius coefficients:	1.15E+16	-0.7	15790.0
148.	C3H6=C3H5-A+H	2.01E+61	-13.3	118500.0
	Reverse Arrhenius coefficients:	4.89E+56	-12.2	28080.0
149.	C3H6+O=CH2CO+CH3+H	2.50E+07	1.8	76.0
	Reverse Arrhenius coefficients:	1.00E+00	0.0	0.0
150.	C3H6+O=C2H5+HCO	1.58E+07	1.8	-1216.0
	Reverse Arrhenius coefficients:	1.40E+05	1.9	26510.0
151.	C3H6+O=CH3CHCO+H+H	2.50E+07	1.8	76.0
	All REV parameters are zero...	0.000E+00	0.00	0.000E+00
	This reaction is treated as irreversible			
152.	C3H6=C3H5-S+H	7.71E+69	-16.1	140000.0
	Reverse Arrhenius coefficients:	1.22E+63	-14.6	26160.0
153.	C3H6+HO2=C3H5-A+H2O2	1.50E+11	0.0	14190.0
	Reverse Arrhenius coefficients:	5.87E+05	1.3	9759.0
154.	C3H6+HO2=C3H5-S+H2O2	7.50E+09	0.0	12570.0
	Reverse Arrhenius coefficients:	2.31E+04	1.3	-13420.0
155.	C3H6+HO2=C3H5-T+H2O2	3.00E+09	0.0	9930.0
	Reverse Arrhenius coefficients:	9.23E+03	1.3	-14060.0
156.	C3H6+OH=C3H5-A+H2O	3.12E+06	2.0	-298.0
	Reverse Arrhenius coefficients:	6.19E+06	2.0	31880.0
157.	C3H6+OH=C3H5-S+H2O	2.11E+06	2.0	2778.0
	Reverse Arrhenius coefficients:	2.72E+04	2.5	11530.0
158.	C4H6=C2H3+C2H3	4.03E+19	-1.0	98150.0
	Reverse Arrhenius coefficients:	1.26E+13	0.0	0.0
159.	C4H6+OH=C2H5+CH2CO	1.00E+12	0.0	0.0
	Reverse Arrhenius coefficients:	3.73E+12	0.0	30020.0
160.	C4H6+OH=CH2O+C3H5-A	1.00E+12	0.0	0.0
	Reverse Arrhenius coefficients:	3.50E+06	0.0	71060.0
161.	C4H6+OH=C2H3+CH3CHO	1.00E+12	0.0	0.0
	Reverse Arrhenius coefficients:	5.44E+11	0.0	18550.0
162.	C4H6+O=C2H4+CH2CO	1.00E+12	0.0	0.0
	Reverse Arrhenius coefficients:	6.38E+11	0.0	94340.0
163.	C4H6+O=CH2O+C3H4-A	1.00E+12	0.0	0.0
	Reverse Arrhenius coefficients:	1.08E+12	0.0	79050.0
164.	C2H4+O2=C2H3+HO2	4.00E+13	0.0	58200.0
	Reverse Arrhenius coefficients:	4.94E+13	-0.5	1368.0
165.	CH2O+M=CO+H2+M	1.83E+32	-4.4	87120.0
	Reverse Arrhenius coefficients:	5.07E+27	-3.4	84350.0
166.	NC3H7=CH3+C2H4	2.28E+14	-0.6	28400.0
	Reverse Arrhenius coefficients:	4.10E+11	0.0	7204.0
167.	NC3H7=H+C3H6	2.67E+15	-0.6	36820.0
	Reverse Arrhenius coefficients:	1.00E+13	0.0	2500.0
168.	NC3H7+O2=C3H6+HO2	3.00E+11	0.0	3000.0
	Reverse Arrhenius coefficients:	2.00E+11	0.0	17500.0
169.	C2H4+CH3O=C2H3+CH3OH	1.20E+11	0.0	6750.0
	Reverse Arrhenius coefficients:	1.00E+10	0.0	9000.0
170.	C3H6+OH=C3H5-T+H2O	1.11E+06	2.0	1451.0

	Reverse Arrhenius coefficients:	3.28E+03	2.7	12310.0
171.	C3H6+O=C3H5-A+OH	5.24E+11	0.7	5884.0
	Reverse Arrhenius coefficients:	1.06E+11	0.7	20820.0
172.	C3H6+O=C3H5-S+OH	1.20E+11	0.7	8959.0
	Reverse Arrhenius coefficients:	1.57E+08	1.2	460.0
173.	C3H6+O=C3H5-T+OH	6.03E+10	0.7	7632.0
	Reverse Arrhenius coefficients:	1.80E+07	1.4	1243.0
174.	C3H6+H=C3H5-A+H2	1.73E+05	2.5	2492.0
	Reverse Arrhenius coefficients:	7.93E+04	2.5	19520.0
175.	C3H6+O2=C3H5-S+HO2	2.00E+12	0.0	62900.0
	Reverse Arrhenius coefficients:	1.08E+08	0.8	-984.0
176.	C3H6+H=C2H4+CH3	4.83E+33	-5.8	18500.0
	Reverse Arrhenius coefficients:	2.31E+33	-5.9	31620.0
177.	IC3H7=H+C3H6	8.57E+18	-1.6	40340.0
	Reverse Arrhenius coefficients:	1.30E+13	0.0	1560.0
178.	IC3H7+H=C2H5+CH3	2.00E+13	0.0	0.0
	Reverse Arrhenius coefficients:	4.82E+09	0.7	12090.0
179.	IC3H7+O2=C3H6+HO2	4.50E+11	0.0	5020.0
	Reverse Arrhenius coefficients:	2.00E+11	0.0	17500.0
180.	BC5H10=CH3+C4H7	1.00E+16	0.0	71000.0
	Reverse Arrhenius coefficients:	1.00E+13	0.0	0.0
181.	CC5H10=CH3+C4H7	1.00E+16	0.0	71000.0
	Reverse Arrhenius coefficients:	1.00E+13	0.0	0.0
182.	C5H9=C3H5-A+C2H4	2.50E+13	0.0	45000.0
	All REV parameters are zero...	0.000E+00	0.00	0.000E+00
	This reaction is treated as irreversible			
183.	C5H9=C4H6+CH3	1.34E+15	-0.5	38320.0
	Reverse Arrhenius coefficients:	1.75E+11	0.0	7600.0
184.	C4H7=C4H6+H	1.20E+14	0.0	49300.0
	Reverse Arrhenius coefficients:	4.00E+13	0.0	1300.0
185.	C4H7=C2H4+C2H3	1.00E+11	0.0	37000.0
	Reverse Arrhenius coefficients:	5.00E+10	0.0	7000.0
186.	C4H7+C3H6=C4H8-2+C3H5-A	1.00E+11	0.0	15900.0
	Reverse Arrhenius coefficients:	1.00E+11	0.0	15000.0
187.	C4H8-1+C4H6=C4H7+C4H7	2.35E+12	0.0	46720.0
	Reverse Arrhenius coefficients:	1.60E+12	0.0	0.0
188.	C4H8-2+C4H6=C4H7+C4H7	2.35E+12	0.0	46720.0
	Reverse Arrhenius coefficients:	1.60E+12	0.0	0.0
189.	C4H7+CH3=C4H6+CH4	8.00E+12	0.0	0.0
	Reverse Arrhenius coefficients:	7.05E+13	0.0	57280.0
190.	C3H5-A+C4H7=C3H6+C4H6	6.31E+12	0.0	0.0
	Reverse Arrhenius coefficients:	1.00E+10	0.0	50000.0
191.	C4H7+O2=C4H6+HO2	1.00E+09	0.0	0.0
	Reverse Arrhenius coefficients:	1.00E+11	0.0	17000.0
192.	H+C4H7=C4H6+H2	3.16E+13	0.0	0.0
	Reverse Arrhenius coefficients:	1.07E+13	0.0	56810.0
193.	C2H5+C4H7=C4H6+C2H6	3.98E+12	0.0	0.0
	Reverse Arrhenius coefficients:	3.21E+12	0.0	49840.0
194.	C2H5+C4H7=C2H4+C4H8-1	9.24E+06	1.5	-962.0
	Reverse Arrhenius coefficients:	7.81E+02	2.9	50960.0
195.	C2H5+C4H7=C2H4+C4H8-2	5.00E+11	0.0	0.0
	Reverse Arrhenius coefficients:	8.48E+11	0.0	56330.0
196.	C2H3+C4H7=C2H4+C4H6	3.98E+12	0.0	0.0
	Reverse Arrhenius coefficients:	1.16E+13	0.0	57710.0
197.	C4H8-2=H+C4H7	4.11E+18	-1.0	97350.0
	Reverse Arrhenius coefficients:	5.00E+13	0.0	0.0
198.	C4H8-2+CH3=C4H7+CH4	1.00E+11	0.0	8200.0
	Reverse Arrhenius coefficients:	6.00E+11	0.0	18760.0
199.	C4H8-2+H=C4H7+H2	5.00E+13	0.0	3800.0
	Reverse Arrhenius coefficients:	3.16E+13	0.0	22300.0
200.	C4H8-2+OH=C2H5+CH3CHO	2.60E+13	0.0	0.0

	Reverse Arrhenius coefficients:	2.43E+13	0.0	19930.0
201.	C4H8-2+O=IC3H7+HCO	2.79E+06	2.1	-1775.0
	Reverse Arrhenius coefficients:	1.05E+05	2.1	24040.0
202.	C4H8-2+OH=C4H7+H2O	3.90E+13	0.0	2217.0
	Reverse Arrhenius coefficients:	4.77E+12	0.0	26470.0
203.	C4H8-2+O=C2H4+CH3CHO	4.64E+05	2.1	-1775.0
	Reverse Arrhenius coefficients:	7.40E+04	2.1	82480.0
204.	C4H8-2+HO2=C4H7+H2O2	3.20E+12	0.0	14900.0
	Reverse Arrhenius coefficients:	1.58E+11	0.0	14700.0
205.	C4H8-2+O2=C4H7+HO2	8.00E+13	0.0	35400.0
	Reverse Arrhenius coefficients:	3.00E+11	0.0	0.0
206.	C4H8-1=C3H5-A+CH3	5.00E+15	0.0	71000.0
	Reverse Arrhenius coefficients:	5.00E+12	0.0	0.0
207.	C4H8-1=C2H3+C2H5	1.00E+19	-1.0	96770.0
	Reverse Arrhenius coefficients:	9.00E+12	0.0	0.0
208.	C4H8-1=H+C4H7	4.11E+18	-1.0	97350.0
	Reverse Arrhenius coefficients:	5.00E+13	0.0	0.0
209.	C4H8-1+CH3=C4H7+CH4	1.00E+11	0.0	7300.0
	Reverse Arrhenius coefficients:	6.00E+11	0.0	17860.0
210.	C4H8-1+H=C4H7+H2	5.00E+13	0.0	3900.0
	Reverse Arrhenius coefficients:	4.00E+13	0.0	25200.0
211.	C4H8-1+OH=C4H7+H2O	2.25E+13	0.0	2217.0
	Reverse Arrhenius coefficients:	4.77E+12	0.0	26470.0
212.	C4H8-1+C3H5-A=C4H7+C3H6	7.90E+10	0.0	12400.0
	Reverse Arrhenius coefficients:	1.00E+11	0.0	17500.0
213.	C4H8-1+HO2=C4H7+H2O2	1.40E+12	0.0	14900.0
	Reverse Arrhenius coefficients:	3.16E+11	0.0	13000.0
214.	C4H8-1+O2=C4H7+HO2	2.70E+13	0.0	33200.0
	Reverse Arrhenius coefficients:	3.00E+11	0.0	0.0
215.	SC4H9=C3H6+CH3	7.37E+17	-1.4	30230.0
	Reverse Arrhenius coefficients:	3.30E+11	0.0	7200.0
216.	SC4H9=C4H8-2+H	5.20E+20	-2.4	39720.0
	Reverse Arrhenius coefficients:	1.00E+13	0.0	2900.0
217.	SC4H9=C4H8-1+H	3.59E+20	-2.1	40970.0
	Reverse Arrhenius coefficients:	1.00E+13	0.0	1200.0
218.	SC4H9+O2=C4H8-1+HO2	4.50E-19	0.0	5020.0
	Reverse Arrhenius coefficients:	2.00E-19	0.0	17500.0
219.	SC4H9+O2=C4H8-2+HO2	3.00E-19	0.0	3000.0
	Reverse Arrhenius coefficients:	2.00E-19	0.0	17500.0
220.	PC4H9=C2H5+C2H4	7.50E+17	-1.4	29580.0
	Reverse Arrhenius coefficients:	3.30E+11	0.0	7200.0
221.	PC4H9=C4H8-1+H	1.16E+17	-1.2	38160.0
	Reverse Arrhenius coefficients:	1.00E+13	0.0	2900.0
222.	PC4H9+O2=C4H8-1+HO2	3.00E-19	0.0	3000.0
	Reverse Arrhenius coefficients:	2.00E-19	0.0	17500.0
223.	C4H10=C2H5+C2H5	3.46E+24	-2.3	87750.0
	Reverse Arrhenius coefficients:	4.00E+12	0.0	-596.0
224.	C4H10=NC3H7+CH3	1.37E+21	-1.5	87320.0
	Reverse Arrhenius coefficients:	4.00E+12	0.0	-596.0
225.	C4H10=PC4H9+H	4.56E+21	-1.7	103700.0
	Reverse Arrhenius coefficients:	3.61E+13	0.0	0.0
226.	C4H10=SC4H9+H	1.47E+18	-0.8	99210.0
	Reverse Arrhenius coefficients:	3.61E+13	0.0	0.0
227.	C4H10+O2=PC4H9+HO2	6.00E+13	0.0	52340.0
	Reverse Arrhenius coefficients:	1.63E+08	1.0	-1422.0
228.	C4H10+O2=SC4H9+HO2	4.00E+13	0.0	49800.0
	Reverse Arrhenius coefficients:	3.36E+11	0.1	548.0
229.	C4H10+C3H5-A=PC4H9+C3H6	7.94E+11	0.0	20500.0
	Reverse Arrhenius coefficients:	1.00E+12	0.0	20000.0
230.	C4H10+C3H5-A=SC4H9+C3H6	3.16E+11	0.0	16400.0
	Reverse Arrhenius coefficients:	1.00E+12	0.0	20000.0

231.	C4H10+C2H5=PC4H9+C2H6	1.58E+11	0.0	12300.0
	Reverse Arrhenius coefficients:	3.56E+10	0.0	12920.0
232.	C4H10+C2H5=SC4H9+C2H6	1.00E+11	0.0	10400.0
	Reverse Arrhenius coefficients:	7.12E+10	0.0	9917.0
233.	C4H10+C2H3=PC4H9+C2H4	1.00E+12	0.0	18000.0
	Reverse Arrhenius coefficients:	2.57E+12	0.0	25380.0
234.	C4H10+C2H3=SC4H9+C2H4	8.00E+11	0.0	16800.0
	Reverse Arrhenius coefficients:	2.05E+12	0.0	24180.0
235.	C4H10+CH3=PC4H9+CH4	9.04E-01	3.6	7154.0
	Reverse Arrhenius coefficients:	3.53E-03	4.3	11350.0
236.	C4H10+CH3=SC4H9+CH4	3.02E+00	3.5	5481.0
	Reverse Arrhenius coefficients:	3.65E+01	3.2	14190.0
237.	C4H10+H=PC4H9+H2	1.88E+05	2.8	6280.0
	Reverse Arrhenius coefficients:	2.81E+01	3.4	10000.0
238.	C4H10+H=SC4H9+H2	2.60E+06	2.4	4471.0
	Reverse Arrhenius coefficients:	1.20E+06	2.1	12700.0
239.	C4H10+OH=PC4H9+H2O	1.05E+10	1.0	1586.0
	Reverse Arrhenius coefficients:	6.82E+06	1.7	20460.0
240.	C4H10+OH=SC4H9+H2O	9.34E+07	1.6	-35.0
	Reverse Arrhenius coefficients:	1.87E+08	1.4	23350.0
241.	C4H10+O=PC4H9+OH	1.13E+14	0.0	7850.0
	Reverse Arrhenius coefficients:	1.48E+13	0.0	12240.0
242.	C4H10+O=SC4H9+OH	5.62E+13	0.0	5200.0
	Reverse Arrhenius coefficients:	7.35E+12	0.0	9590.0
243.	C4H10+HO2=PC4H9+H2O2	1.70E+13	0.0	20460.0
	Reverse Arrhenius coefficients:	4.58E+12	0.0	9809.0
244.	C4H10+HO2=SC4H9+H2O2	1.12E+13	0.0	17700.0
	Reverse Arrhenius coefficients:	1.63E+12	0.0	7409.0
245.	C4H10+CH3O=PC4H9+CH3OH	3.00E+11	0.0	7000.0
	Reverse Arrhenius coefficients:	1.22E+10	0.0	50000.0
246.	C4H10+CH3O=SC4H9+CH3OH	6.00E+11	0.0	7000.0
	Reverse Arrhenius coefficients:	2.44E+10	0.0	50000.0
247.	CH3COCH3=CH3CO+CH3	1.22E+23	-2.0	83950.0
	Reverse Arrhenius coefficients:	1.00E+13	0.0	0.0
248.	CH3COCH3+OH=CH3COCH2+H2O	3.38E+07	1.7	830.0
	Reverse Arrhenius coefficients:	7.61E+03	2.6	23260.0
249.	CH3COCH3+H=CH3COCH2+H2	2.30E+05	2.7	6260.0
	Reverse Arrhenius coefficients:	1.20E+01	3.6	13540.0
250.	CH3COCH3+O=CH3COCH2+OH	5.13E+11	0.2	4890.0
	Reverse Arrhenius coefficients:	1.17E+07	1.1	10070.0
251.	CH3COCH3+CH3=CH3COCH2+CH4	3.96E+11	0.0	9784.0
	Reverse Arrhenius coefficients:	5.38E+08	0.9	17540.0
252.	CH3COCH3+CH3O=CH3COCH2+CH3OH	4.34E+11	0.0	6460.0
	Reverse Arrhenius coefficients:	1.09E+07	0.9	12010.0
253.	CH3COCH2=CH2CO+CH3	1.00E+14	0.0	31000.0
	Reverse Arrhenius coefficients:	1.00E+11	0.0	6000.0
254.	CH3COCH3+O2=CH3COCH2+HO2	6.03E+13	0.0	48500.0
	Reverse Arrhenius coefficients:	5.70E+07	1.2	-1706.0
255.	CH3COCH3+HO2=CH3COCH2+H2O2	1.70E+13	0.0	20460.0
	Reverse Arrhenius coefficients:	2.27E+10	0.5	11430.0
256.	C2H5CO=C2H5+CO	1.83E+15	-0.7	12910.0
	Reverse Arrhenius coefficients:	1.51E+11	0.0	4810.0
257.	C2H5CHO+H=C2H5CO+H2	4.00E+13	0.0	4200.0
	Reverse Arrhenius coefficients:	5.85E+12	0.0	20590.0
258.	C2H5CHO+O=C2H5CO+OH	5.00E+12	0.0	1790.0
	Reverse Arrhenius coefficients:	3.21E+11	0.0	16080.0
259.	C2H5CHO+OH=C2H5CO+H2O	2.69E+10	0.8	-340.0
	Reverse Arrhenius coefficients:	1.70E+10	0.8	31200.0
260.	C2H5CHO+CH3=C2H5CO+CH4	2.61E+06	1.8	5911.0
	Reverse Arrhenius coefficients:	9.97E+06	1.8	22780.0
261.	C2H5CHO+HO2=C2H5CO+H2O2	2.80E+12	0.0	13600.0

```
     Reverse Arrhenius coefficients:                1.05E+13   -0.3    13680.0
262. C2H5CHO+CH3O=C2H5CO+CH3OH                      1.00E+12    0.0     3300.0
     Reverse Arrhenius coefficients:                7.06E+10    0.0    17960.0
263. C2H5CHO+C2H5=C2H5CO+C2H6                       1.00E+12    0.0     8000.0
     Reverse Arrhenius coefficients:                5.98E+14   -0.6    20700.0
264. C2H5CHO=C2H5+HCO                               9.85E+18   -0.7    81710.0
     Reverse Arrhenius coefficients:                1.81E+13    0.0        0.0
265. C2H5CHO+O2=C2H5CO+HO2                          1.00E+13    0.0    40700.0
     Reverse Arrhenius coefficients:                2.67E+10    0.3     -396.0
266. C2H5CHO+C2H3=C2H5CO+C2H4                       1.70E+12    0.0     8440.0
     Reverse Arrhenius coefficients:                3.66E+09    0.8    24180.0
267. C2H5CHO+C3H5-A=C2H5CO+C3H6                     1.70E+12    0.0     8440.0
     Reverse Arrhenius coefficients:                1.00E+13    0.0    28000.0
268. C5H10-1=C2H5+C3H5-A                            9.17E+20   -1.6    73990.0
     Reverse Arrhenius coefficients:                4.00E+12    0.0     -596.0
269. C5H10-1+H=C5H9+H2                              2.80E+13    0.0     4000.0
     Reverse Arrhenius coefficients:                1.00E+12    0.0    14000.0
270. C5H10-1+O=C5H9+OH                              2.54E+05    2.6    -1130.0
     Reverse Arrhenius coefficients:                7.00E+11    0.0    29900.0
271. C5H10-1+O=PC4H9+HCO                            1.00E+11    0.0        0.0
     All REV parameters are zero...                 0.000E+00  0.00  0.000E+00
     This reaction is treated as irreversible
272. C5H10-1+O=NC3H7+CH3CO                          1.00E+11    0.0        0.0
     All REV parameters are zero...                 0.000E+00  0.00  0.000E+00
     This reaction is treated as irreversible
273. C5H10-1+OH=C5H9+H2O                            5.12E+06    2.0     -298.0
     Reverse Arrhenius coefficients:                2.06E+07    2.2    34970.0
274. C5H10-1+OH=PC4H9+CH2O                          1.00E+11    0.0        0.0
     All REV parameters are zero...                 0.000E+00  0.00  0.000E+00
     This reaction is treated as irreversible
275. C5H10-1+OH=NC3H7+CH3CHO                        1.00E+11    0.0        0.0
     All REV parameters are zero...                 0.000E+00  0.00  0.000E+00
     This reaction is treated as irreversible
276. C5H10-1+CH3=C5H9+CH4                           1.00E+11    0.0     7300.0
     Reverse Arrhenius coefficients:                6.00E+11    0.0    17900.0
277. H2O2+H=H2+HO2                                  4.82E+13    0.0     7950.0
     Reverse Arrhenius coefficients:                1.88E+12    0.3    24260.0
278. HCO+O=CO2+H                                    3.00E+13    0.0        0.0
     Reverse Arrhenius coefficients:                9.68E+15    0.0   110200.0
279. CH3+M=CH2+H+M                                  1.97E+16    0.0    92520.0
     Reverse Arrhenius coefficients:                2.11E+11    1.0   -19620.0
280. CH3+H=CH2+H2                                   9.00E+13    0.0    15100.0
     Reverse Arrhenius coefficients:                1.82E+13    0.0    10400.0
281. CH3+OH=CH2+H2O                                 3.00E+06    2.0     2500.0
     Reverse Arrhenius coefficients:                2.62E+06    2.0    12960.0
282. CH+CH4=C2H4+H                                  6.00E+13    0.0        0.0
     Reverse Arrhenius coefficients:                3.57E+14    0.0    55480.0
283. CH3OH(+M)=CH2OH+H(+M)                          2.69E+16   -0.1    98940.0
     Low pressure limit:  0.23400E+41 -0.63300E+01  0.10310E+06
     TROE centering:      0.77300E+00  0.69300E+03  0.53330E+04  0.10000+101
284. CH3CO+H=CH2CO+H2                               2.00E+13    0.0        0.0
     Reverse Arrhenius coefficients:                5.63E+17   -1.1    63700.0
285. CH3CO+O=CH2CO+OH                               2.00E+13    0.0        0.0
     Reverse Arrhenius coefficients:                5.95E+18   -1.1   120700.0
286. CH3CO+CH3=CH2CO+CH4                            5.00E+13    0.0        0.0
     Reverse Arrhenius coefficients:                8.20E+17   -0.7    79830.0
287. C2H4+O=CH2CHO+H                                3.39E+06    1.9      179.0
     Reverse Arrhenius coefficients:                9.48E+06    1.8    16050.0
288. C2H5+O=CH3CHO+H                                5.00E+13    0.0        0.0
     Reverse Arrhenius coefficients:                5.50E+14    0.1    74390.0
289. C2H6+CH=C2H5+CH2                               1.10E+14    0.0     -260.0
```

	Reverse Arrhenius coefficients:	3.83E+10	0.6	440.0
290.	CH2OH+CH2O=CH3OH+HCO	1.29E-01	4.6	6596.0
	Reverse Arrhenius coefficients:	9.63E+03	2.9	13110.0
291.	C3H6+O2=C3H5-T+HO2	1.40E+12	0.0	60700.0
	Reverse Arrhenius coefficients:	1.73E+07	1.0	-1074.0
292.	C2H3+C2H4=C4H6+H	5.00E+11	0.0	7300.0
	Reverse Arrhenius coefficients:	1.00E+13	0.0	4700.0
293.	BC5H10+OH=IC5H9+H2O	1.00E+12	0.0	1230.0
	Reverse Arrhenius coefficients:	5.00E+12	0.0	26500.0
294.	CC5H10+OH=IC5H9+H2O	1.00E+12	0.0	1230.0
	Reverse Arrhenius coefficients:	5.00E+12	0.0	26500.0
295.	BC5H10+H=IC5H9+H2	1.00E+12	0.0	3800.0
	Reverse Arrhenius coefficients:	1.00E+12	0.0	25000.0
296.	CC5H10+H=IC5H9+H2	1.00E+12	0.0	3800.0
	Reverse Arrhenius coefficients:	1.00E+12	0.0	25000.0
297.	BC5H10+CH3=IC5H9+CH4	5.00E+11	0.0	7300.0
	Reverse Arrhenius coefficients:	6.00E+11	0.0	25000.0
298.	CC5H10+CH3=IC5H9+CH4	5.00E+11	0.0	7300.0
	Reverse Arrhenius coefficients:	6.00E+11	0.0	25000.0
299.	BC5H10+O=IC5H9+OH	3.70E+05	2.6	-1130.0
	Reverse Arrhenius coefficients:	1.00E+12	0.0	25000.0
300.	CC5H10+O=IC5H9+OH	3.70E+05	2.6	-1130.0
	Reverse Arrhenius coefficients:	1.00E+12	0.0	25000.0
301.	C5H10-2+OH=NC3H7+CH3CHO	2.00E+10	0.0	-4000.0
	Reverse Arrhenius coefficients:	2.00E+13	0.0	20000.0
302.	C5H10-2+O=C3H6+CH3CHO	1.00E+10	0.0	0.0
	Reverse Arrhenius coefficients:	1.00E+12	0.0	81000.0
303.	IC5H9=C3H4-A+C2H5	1.98E+20	-1.6	59240.0
	Reverse Arrhenius coefficients:	2.00E+11	0.0	8300.0
304.	C5H11-1=C2H4+NC3H7	7.97E+17	-1.4	29790.0
	Reverse Arrhenius coefficients:	3.30E+11	0.0	7200.0
305.	C5H11-1=H+C5H10-1	3.48E+15	-0.7	37880.0
	Reverse Arrhenius coefficients:	1.00E+13	0.0	2900.0
306.	C5H11-1+O2=C5H10-1+HO2	3.00E-19	0.0	3000.0
	Reverse Arrhenius coefficients:	2.00E-19	0.0	17500.0
307.	C5H11-1=C5H11-2	3.88E+09	0.3	19760.0
	Reverse Arrhenius coefficients:	1.83E+13	-0.6	24360.0
308.	C5H11-2=C3H6+C2H5	3.03E+21	-2.3	30960.0
	Reverse Arrhenius coefficients:	3.30E+11	0.0	7200.0
309.	C5H11-2=C5H10-1+H	1.64E+19	-1.6	40780.0
	Reverse Arrhenius coefficients:	1.00E+13	0.0	1200.0
310.	C5H11-2=C5H10-2+H	4.73E+20	-2.2	39630.0
	Reverse Arrhenius coefficients:	1.00E+13	0.0	2900.0
311.	C5H11-2+O2=C5H10-1+HO2	4.50E-19	0.0	5020.0
	Reverse Arrhenius coefficients:	2.00E-19	0.0	17500.0
312.	C5H11-2+O2=C5H10-2+HO2	3.00E-19	0.0	3000.0
	Reverse Arrhenius coefficients:	2.00E-19	0.0	17500.0
313.	C5H10-2=CH3+C4H7	1.00E+16	0.0	71000.0
	Reverse Arrhenius coefficients:	1.00E+13	0.0	0.0
314.	C5H10-2+H=C5H9+H2	2.90E+13	0.0	4000.0
	Reverse Arrhenius coefficients:	1.00E+12	0.0	14000.0
315.	C5H10-2+O=C5H9+OH	2.43E+05	2.6	-1130.0
	Reverse Arrhenius coefficients:	7.00E+11	0.0	29900.0
316.	C5H10-2+OH=C5H9+H2O	4.30E+13	0.0	3060.0
	Reverse Arrhenius coefficients:	5.00E+12	0.0	26500.0
317.	C5H10-2+CH3=C5H9+CH4	1.00E+11	0.0	8200.0
	Reverse Arrhenius coefficients:	6.00E+11	0.0	18800.0
318.	BC5H10+OH=IC3H7+CH3CHO	2.00E+10	0.0	-4000.0
	Reverse Arrhenius coefficients:	0.00E+00	0.0	20000.0
319.	C4H10+PC4H9=SC4H9+C4H10	1.00E+11	0.0	10400.0
	Reverse Arrhenius coefficients:	1.50E+11	0.0	12300.0

320.	C2H5O+M=CH3+CH2O+M	1.35E+38	-7.0	23800.0
	Reverse Arrhenius coefficients:	6.44E+36	-7.0	16850.0
321.	C2H5OH+OH=C2H5O+H2O	7.46E+11	0.3	1634.0
	Reverse Arrhenius coefficients:	3.96E+13	-0.1	18520.0
322.	C2H5OH+H=C2H5O+H2	1.50E+07	1.6	3038.0
	Reverse Arrhenius coefficients:	1.84E+08	1.2	4772.0
323.	C2H5OH+O=C2H5O+OH	1.58E+07	2.0	4448.0
	Reverse Arrhenius coefficients:	8.50E+07	1.6	4087.0
324.	C2H5OH+CH3=C2H5O+CH4	1.34E+02	2.9	7452.0
	Reverse Arrhenius coefficients:	4.29E+04	2.5	9666.0
325.	SC2H4OH+O2=CH3CHO+HO2	3.81E+06	2.0	1641.0
	Reverse Arrhenius coefficients:	6.15E+05	2.2	22970.0
326.	C2H5O+O2=CH3CHO+HO2	4.28E+10	0.0	1097.0
	Reverse Arrhenius coefficients:	3.87E+08	0.4	31880.0
327.	H2O2+O2=HO2+HO2	1.84E+14	-0.7	39540.0
	Reverse Arrhenius coefficients:	1.30E+11	0.0	-1629.0
	Declared duplicate reaction...			
328.	C2H3+O2=CH2CHO+O	3.50E+14	-0.6	5260.0
	Reverse Arrhenius coefficients:	2.59E+12	0.1	6459.0
329.	C2H5O2=C2H5+O2	4.93E+50	-11.5	42250.0
	Reverse Arrhenius coefficients:	1.09E+48	-11.5	10220.0
330.	CH3O2+M=CH3+O2+M	4.34E+27	-3.4	30470.0
	Reverse Arrhenius coefficients:	5.44E+25	-3.3	0.0
331.	CH3O2H=CH3O+OH	6.31E+14	0.0	42300.0
	Reverse Arrhenius coefficients:	1.17E+11	0.6	-1771.0
332.	C2H5O2H=C2H5O+OH	6.31E+14	0.0	42300.0
	Reverse Arrhenius coefficients:	8.31E+06	1.7	-3207.0
333.	C3H2+O2=HCCO+CO+H	5.00E+13	0.0	0.0
	All REV parameters are zero...	0.000E+00	0.00	0.000E+00
	This reaction is treated as irreversible			
334.	CH3O2+CH2O=CH3O2H+HCO	1.99E+12	0.0	11660.0
	Reverse Arrhenius coefficients:	8.50E+12	-0.5	7009.0
335.	C2H5O2+CH2O=C2H5O2H+HCO	1.99E+12	0.0	11660.0
	Reverse Arrhenius coefficients:	8.42E+12	-0.5	6605.0
336.	C2H4+CH3O2=C2H3+CH3O2H	2.23E+12	0.0	17190.0
	Reverse Arrhenius coefficients:	8.11E+15	-1.3	-1489.0
337.	C2H4+C2H5O2=C2H3+C2H5O2H	2.23E+12	0.0	17190.0
	Reverse Arrhenius coefficients:	8.03E+15	-1.3	-1893.0
338.	CH4+CH3O2=CH3+CH3O2H	1.81E+11	0.0	18480.0
	Reverse Arrhenius coefficients:	3.71E+11	-0.5	-1327.0
339.	CH4+C2H5O2=CH3+C2H5O2H	1.81E+11	0.0	18480.0
	Reverse Arrhenius coefficients:	3.67E+11	-0.5	-1731.0
340.	CH3OH+CH3O2=CH2OH+CH3O2H	1.81E+12	0.0	13710.0
	Reverse Arrhenius coefficients:	1.04E+08	1.2	2542.0
341.	CH3OH+C2H5O2=CH2OH+C2H5O2H	1.81E+12	0.0	13710.0
	Reverse Arrhenius coefficients:	1.03E+08	1.1	2138.0
342.	C2H5+HO2=C2H5O+OH	3.20E+13	0.0	0.0
	Reverse Arrhenius coefficients:	3.08E+15	-0.3	27490.0
343.	CH3O2+CH3=CH3O+CH3O	7.00E+12	0.0	-1000.0
	Reverse Arrhenius coefficients:	2.97E+16	-0.9	28310.0
344.	CH3O2+C2H5=CH3O+C2H5O	7.00E+12	0.0	-1000.0
	Reverse Arrhenius coefficients:	6.57E+16	-0.9	31260.0
345.	CH3O2+HO2=CH3O2H+O2	1.75E+10	0.0	-3275.0
	Reverse Arrhenius coefficients:	5.16E+13	-0.8	34880.0
346.	H2O2+OH=H2O+HO2	5.80E+14	0.0	9560.0
	Reverse Arrhenius coefficients:	9.77E+13	0.3	41020.0
	Declared duplicate reaction...			
347.	C2H5O2+HO2=C2H5O2H+O2	1.75E+10	0.0	-3275.0
	Reverse Arrhenius coefficients:	5.11E+13	-0.8	34480.0
348.	CH3O2+CH3O2=CH2O+CH3OH+O2	3.11E+14	-1.6	-1051.0
	All REV parameters are zero...	0.000E+00	0.00	0.000E+00

	This reaction is treated as irreversible			
349.	CH3O2+CH3O2=O2+CH3O+CH3O	1.40E+16	-1.6	1860.0
	All REV parameters are zero...	0.000E+00	0.00	0.000E+00
	This reaction is treated as irreversible			
350.	C2H6+CH3O2=C2H5+CH3O2H	1.32E+13	0.0	20470.0
	Reverse Arrhenius coefficients:	1.73E+11	0.1	4832.0
351.	C2H6+C2H5O2=C2H5+C2H5O2H	1.32E+13	0.0	20470.0
	Reverse Arrhenius coefficients:	1.71E+11	0.1	4428.0
352.	O2C2H4OH=PC2H4OH+O2	3.90E+16	-1.0	30000.0
	Reverse Arrhenius coefficients:	1.20E+11	0.0	-1100.0
353.	O2C2H4OH=OH+CH2O+CH2O	1.25E+10	0.0	18900.0
	All REV parameters are zero...	0.000E+00	0.00	0.000E+00
	This reaction is treated as irreversible			
354.	C2H5O2=C2H4O2H	5.64E+47	-11.4	37320.0
	Reverse Arrhenius coefficients:	6.99E+48	-12.2	25850.0
355.	C2H4O2H=C2H4O1-2+OH	4.25E+22	-4.2	22350.0
	All REV parameters are zero...	0.000E+00	0.00	0.000E+00
	This reaction is treated as irreversible			
356.	CH3CO3=CH3CO+O2	4.62E+19	-1.9	39560.0
	Reverse Arrhenius coefficients:	1.20E+11	0.0	-1100.0
357.	CH3CO2+M=CH3+CO2+M	4.40E+15	0.0	10500.0
	Reverse Arrhenius coefficients:	9.65E+12	0.2	21040.0
358.	CH3CO3H=CH3CO2+OH	5.01E+14	0.0	40150.0
	Reverse Arrhenius coefficients:	1.74E+08	1.6	1305.0
359.	CH3CO3+HO2=CH3CO3H+O2	1.75E+10	0.0	-3275.0
	Reverse Arrhenius coefficients:	4.09E+12	-0.3	39040.0
360.	C2H5O+M=CH3CHO+H+M	1.16E+35	-5.9	25270.0
	Reverse Arrhenius coefficients:	3.06E+30	-4.8	6100.0
361.	H2O2+CH3CO3=HO2+CH3CO3H	2.41E+12	0.0	9936.0
	Reverse Arrhenius coefficients:	3.98E+11	0.3	11070.0
362.	CH4+CH3CO3=CH3+CH3CO3H	1.81E+11	0.0	18480.0
	Reverse Arrhenius coefficients:	2.94E+10	0.0	2831.0
363.	C2H4+CH3CO3=C2H3+CH3CO3H	1.13E+13	0.0	30430.0
	Reverse Arrhenius coefficients:	3.26E+15	-0.8	15910.0
364.	C2H6+CH3CO3=C2H5+CH3CO3H	1.70E+13	0.0	20460.0
	Reverse Arrhenius coefficients:	1.77E+10	0.6	8980.0
365.	CH2O+CH3CO3=HCO+CH3CO3H	1.99E+12	0.0	11660.0
	Reverse Arrhenius coefficients:	6.75E+11	0.0	11170.0
366.	C3H6+CH3CO3=C3H5-A+CH3CO3H	3.24E+11	0.0	14900.0
	Reverse Arrhenius coefficients:	2.00E+10	0.0	15000.0
367.	CH3O2+CH3CHO=CH3O2H+CH3CO	3.01E+12	0.0	11920.0
	Reverse Arrhenius coefficients:	2.52E+13	-0.5	8991.0
368.	CH3CHO+CH3CO3=CH3CO+CH3CO3H	3.01E+12	0.0	11920.0
	Reverse Arrhenius coefficients:	2.00E+12	0.0	13150.0
369.	C2H3CO=C2H3+CO	3.04E+14	-0.5	30510.0
	Reverse Arrhenius coefficients:	1.51E+11	0.0	4810.0
370.	C2H3CHO+OH=C2H3CO+H2O	9.24E+06	1.5	-962.0
	Reverse Arrhenius coefficients:	2.15E+07	1.5	35510.0
371.	C2H3CHO+H=C2H3CO+H2	1.34E+13	0.0	3300.0
	Reverse Arrhenius coefficients:	7.19E+12	0.0	24620.0
372.	C2H3CHO+O=C2H3CO+OH	5.94E+12	0.0	1868.0
	Reverse Arrhenius coefficients:	1.40E+12	0.0	21090.0
373.	C2H3CHO+HO2=C2H3CO+H2O2	3.01E+12	0.0	11920.0
	Reverse Arrhenius coefficients:	4.15E+13	-0.3	16940.0
374.	C2H3CHO+CH3=C2H3CO+CH4	2.61E+06	1.8	5911.0
	Reverse Arrhenius coefficients:	3.66E+07	1.8	27710.0
375.	C2H3CHO+CH3O2=C2H3CO+CH3O2H	3.01E+12	0.0	11920.0
	Reverse Arrhenius coefficients:	8.64E+13	-0.5	13920.0
376.	C3H5O=C2H3CHO+H	1.00E+14	0.0	29100.0
	Reverse Arrhenius coefficients:	7.71E+11	0.5	17750.0
377.	C3H5O=C2H3+CH2O	2.03E+12	0.1	23560.0

	Reverse Arrhenius coefficients:	1.50E+11	0.0	10600.0
378.	C3H5O+O2=C2H3CHO+HO2	1.00E+12	0.0	6000.0
	Reverse Arrhenius coefficients:	1.29E+11	0.0	32000.0
379.	C3H5-A+HO2=C3H5O+OH	7.00E+12	0.0	-1000.0
	Reverse Arrhenius coefficients:	2.04E+13	-0.2	12260.0
380.	C3H5-A+CH3O2=C3H5O+CH3O	7.00E+12	0.0	-1000.0
	Reverse Arrhenius coefficients:	1.99E+15	-0.7	17020.0
381.	C3H6+HO2=C3H6O1-2+OH	1.29E+12	0.0	14900.0
	Reverse Arrhenius coefficients:	1.00E-10	0.0	0.0
382.	C3H6+CH3O2=C3H5-A+CH3O2H	3.24E+11	0.0	14900.0
	Reverse Arrhenius coefficients:	2.00E+10	0.0	15000.0
383.	C3H6O1-2=C2H4+CH2O	6.00E+14	0.0	60000.0
	Reverse Arrhenius coefficients:	2.97E+11	0.0	50000.0
384.	C3H6O1-2+OH=CH2O+C2H3+H2O	5.00E+12	0.0	0.0
	All REV parameters are zero...	0.000E+00	0.00	0.000E+00
	This reaction is treated as irreversible			
385.	C3H6O1-2+H=CH2O+C2H3+H2	2.63E+07	2.0	5000.0
	All REV parameters are zero...	0.000E+00	0.00	0.000E+00
	This reaction is treated as irreversible			
386.	C3H6O1-2+O=CH2O+C2H3+OH	8.43E+13	0.0	5200.0
	All REV parameters are zero...	0.000E+00	0.00	0.000E+00
	This reaction is treated as irreversible			
387.	C3H6O1-2+HO2=CH2O+C2H3+H2O2	1.00E+13	0.0	15000.0
	All REV parameters are zero...	0.000E+00	0.00	0.000E+00
	This reaction is treated as irreversible			
388.	C3H6O1-2+CH3O2=CH2O+C2H3+CH3O2H	1.00E+13	0.0	19000.0
	All REV parameters are zero...	0.000E+00	0.00	0.000E+00
	This reaction is treated as irreversible			
389.	C3H6O1-2+CH3=CH2O+C2H3+CH4	2.00E+11	0.0	10000.0
	All REV parameters are zero...	0.000E+00	0.00	0.000E+00
	This reaction is treated as irreversible			
390.	C2H4O2H=C2H4+HO2	9.29E+30	-6.1	19930.0
	Reverse Arrhenius coefficients:	1.91E+27	-5.0	14510.0
391.	C2H4+CH3O2=C2H4O1-2+CH3O	2.82E+12	0.0	17110.0
	All REV parameters are zero...	0.000E+00	0.00	0.000E+00
	This reaction is treated as irreversible			
392.	C2H4+C2H5O2=C2H4O1-2+C2H5O	2.82E+12	0.0	17110.0
	All REV parameters are zero...	0.000E+00	0.00	0.000E+00
	This reaction is treated as irreversible			
393.	C2H4O1-2=CH3+HCO	3.63E+13	0.0	57200.0
	Reverse Arrhenius coefficients:	4.82E+09	0.0	2122.0
394.	C2H4O1-2=CH3CHO	7.41E+12	0.0	53800.0
	Reverse Arrhenius coefficients:	1.28E+11	0.2	79270.0
395.	C2H4O1-2+OH=C2H3O1-2+H2O	1.78E+13	0.0	3610.0
	Reverse Arrhenius coefficients:	1.20E+12	0.2	26950.0
396.	C2H4O1-2+H=C2H3O1-2+H2	8.00E+13	0.0	9680.0
	Reverse Arrhenius coefficients:	1.24E+12	0.2	17860.0
397.	C2H4O1-2+HO2=C2H3O1-2+H2O2	1.13E+13	0.0	30430.0
	Reverse Arrhenius coefficients:	4.50E+12	-0.2	22300.0
398.	C2H4O1-2+CH3O2=C2H3O1-2+CH3O2H	1.13E+13	0.0	30430.0
	Reverse Arrhenius coefficients:	9.38E+12	-0.3	19280.0
399.	C2H4O1-2+C2H5O2=C2H3O1-2+C2H5O2H	1.13E+13	0.0	30430.0
	Reverse Arrhenius coefficients:	9.29E+12	-0.3	18880.0
400.	C2H4O1-2+CH3=C2H3O1-2+CH4	1.07E+12	0.0	11830.0
	Reverse Arrhenius coefficients:	4.33E+11	0.2	20490.0
401.	C2H4O1-2+CH3O=C2H3O1-2+CH3OH	1.20E+11	0.0	6750.0
	Reverse Arrhenius coefficients:	8.97E+08	0.2	13200.0
402.	C3H6OOH1-2=C3H6O1-2+OH	1.25E+15	-1.2	17580.0
	Reverse Arrhenius coefficients:	4.96E+08	1.0	29090.0
403.	C3H6OOH1-3=C3H6O1-3+OH	4.31E+15	-1.3	18240.0
	Reverse Arrhenius coefficients:	1.19E+18	-1.5	33770.0

404.	C3H6OOH2-1=C3H6O1-2+OH	3.46E+16	-1.6	18870.0
	Reverse Arrhenius coefficients:	2.79E+17	-1.5	33090.0
405.	C3H6OOH1-2=C3H6+HO2	5.50E+14	-0.8	15260.0
	Reverse Arrhenius coefficients:	6.47E+10	0.2	8279.0
406.	C3H6OOH2-1=C3H6+HO2	2.44E+19	-2.1	18230.0
	Reverse Arrhenius coefficients:	5.82E+22	-3.2	13960.0
407.	C3H6OOH1-2O2=C3H6OOH1-2+O2	2.39E+25	-2.9	40100.0
	Reverse Arrhenius coefficients:	5.00E+12	0.0	0.0
408.	C3H6OOH1-3=OH+CH2O+C2H4	1.16E+17	-1.1	32570.0
	All REV parameters are zero...	0.000E+00	0.00	0.000E+00
	This reaction is treated as irreversible			
409.	NC3H7O=C2H5+CH2O	1.39E+16	-0.9	19770.0
	Reverse Arrhenius coefficients:	1.00E+11	0.0	11900.0
410.	IC3H7O=CH3+CH3CHO	3.84E+17	-1.2	20490.0
	Reverse Arrhenius coefficients:	1.50E+11	0.0	12900.0
411.	IC3H7O=CH3COCH3+H	2.00E+14	0.0	21500.0
	Reverse Arrhenius coefficients:	7.89E+12	0.2	6810.0
412.	NC3H7O=C2H5CHO+H	2.51E+14	0.0	23400.0
	Reverse Arrhenius coefficients:	4.15E+09	1.1	4470.0
413.	IC3H7O+O2=CH3COCH3+HO2	9.09E+09	0.0	390.0
	Reverse Arrhenius coefficients:	1.00E+11	0.0	32000.0
414.	NC3H7O2H=NC3H7O+OH	1.50E+16	0.0	42500.0
	Reverse Arrhenius coefficients:	1.74E+08	1.7	-3025.0
415.	NC3H7O2+CH2O=NC3H7O2H+HCO	5.60E+12	0.0	13600.0
	Reverse Arrhenius coefficients:	8.00E+11	0.0	10000.0
416.	NC3H7O2+CH3CHO=NC3H7O2H+CH3CO	2.80E+12	0.0	13600.0
	Reverse Arrhenius coefficients:	1.00E+12	0.0	10000.0
417.	NC3H7O2+HO2=NC3H7O2H+O2	1.75E+10	0.0	-3275.0
	Reverse Arrhenius coefficients:	5.10E+13	-0.8	34470.0
418.	C2H4+NC3H7O2=C2H3+NC3H7O2H	1.13E+13	0.0	30430.0
	Reverse Arrhenius coefficients:	3.00E+12	0.0	11500.0
419.	CH3OH+NC3H7O2=CH2OH+NC3H7O2H	6.30E+12	0.0	19360.0
	Reverse Arrhenius coefficients:	1.00E+09	0.0	10000.0
420.	C2H3CHO+NC3H7O2=C2H3CO+NC3H7O2H	2.80E+12	0.0	13600.0
	Reverse Arrhenius coefficients:	1.00E+12	0.0	10000.0
421.	CH4+NC3H7O2=CH3+NC3H7O2H	1.12E+13	0.0	24640.0
	Reverse Arrhenius coefficients:	7.43E+11	0.0	5500.0
422.	CH3+OH=CH2(S)+H2O	2.65E+13	0.0	2186.0
	Reverse Arrhenius coefficients:	3.24E+10	0.9	1211.0
423.	CH3OH+O2=CH2OH+HO2	2.05E+13	0.0	44900.0
	Reverse Arrhenius coefficients:	3.99E+05	2.0	-4424.0
424.	NC3H7O2+CH3O2=NC3H7O+CH3O+O2	1.40E+16	-1.6	1860.0
	All REV parameters are zero...	0.000E+00	0.00	0.000E+00
	This reaction is treated as irreversible			
425.	IC3H7O2+CH3O2=IC3H7O+CH3O+O2	1.40E+16	-1.6	1860.0
	All REV parameters are zero...	0.000E+00	0.00	0.000E+00
	This reaction is treated as irreversible			
426.	H2+NC3H7O2=H+NC3H7O2H	3.01E+13	0.0	26030.0
	Reverse Arrhenius coefficients:	4.80E+13	0.0	7950.0
427.	NC3H7O2=C3H6OOH1-2	2.00E+11	0.0	26850.0
	Reverse Arrhenius coefficients:	1.90E+12	-0.2	17650.0
428.	NC3H7O2=C3H6OOH1-3	3.75E+10	0.0	24400.0
	Reverse Arrhenius coefficients:	5.31E+12	-0.6	11180.0
429.	IC3H7O2=C3H6OOH2-1	6.00E+11	0.0	29400.0
	Reverse Arrhenius coefficients:	3.74E+09	0.1	11810.0
430.	NC3H7O2+C2H6=NC3H7O2H+C2H5	1.70E+13	0.0	20460.0
	Reverse Arrhenius coefficients:	2.20E+11	0.1	4410.0
431.	NC3H7O2+C2H5CHO=NC3H7O2H+C2H5CO	2.00E+11	0.0	9500.0
	Reverse Arrhenius coefficients:	5.00E+09	0.0	10000.0
432.	IC3H7O2+CH3CO3=IC3H7O+CH3CO2+O2	1.40E+16	-1.6	1860.0
	All REV parameters are zero...	0.000E+00	0.00	0.000E+00

	This reaction is treated as irreversible			
433.	NC3H7O2+CH3CO3=NC3H7O+CH3CO2+O2	1.40E+16	-1.6	1860.0
	All REV parameters are zero...	0.000E+00	0.00	0.000E+00
	This reaction is treated as irreversible			
434.	IC3H7O2+C2H5O2=IC3H7O+C2H5O+O2	1.40E+16	-1.6	1860.0
	All REV parameters are zero...	0.000E+00	0.00	0.000E+00
	This reaction is treated as irreversible			
435.	NC3H7O2+C2H5O2=NC3H7O+C2H5O+O2	1.40E+16	-1.6	1860.0
	All REV parameters are zero...	0.000E+00	0.00	0.000E+00
	This reaction is treated as irreversible			
436.	IC3H7O2+IC3H7O2=O2+IC3H7O+IC3H7O	1.40E+16	-1.6	1860.0
	All REV parameters are zero...	0.000E+00	0.00	0.000E+00
	This reaction is treated as irreversible			
437.	NC3H7O2+NC3H7O2=O2+NC3H7O+NC3H7O	1.40E+16	-1.6	1860.0
	All REV parameters are zero...	0.000E+00	0.00	0.000E+00
	This reaction is treated as irreversible			
438.	IC3H7O2+NC3H7O2=IC3H7O+NC3H7O+O2	1.40E+16	-1.6	1860.0
	All REV parameters are zero...	0.000E+00	0.00	0.000E+00
	This reaction is treated as irreversible			
439.	IC3H7O2+CH3=IC3H7O+CH3O	7.00E+12	0.0	-1000.0
	Reverse Arrhenius coefficients:	2.30E+12	0.2	26190.0
440.	IC3H7O2+C2H5=IC3H7O+C2H5O	7.00E+12	0.0	-1000.0
	Reverse Arrhenius coefficients:	5.09E+12	0.2	29130.0
441.	IC3H7O2+IC3H7=IC3H7O+IC3H7O	7.00E+12	0.0	-1000.0
	Reverse Arrhenius coefficients:	8.31E+10	0.7	29640.0
442.	IC3H7O2+NC3H7=IC3H7O+NC3H7O	7.00E+12	0.0	-1000.0
	Reverse Arrhenius coefficients:	1.34E+13	0.1	29620.0
443.	IC3H7O2+PC4H9=IC3H7O+PC4H9O	7.00E+12	0.0	-1000.0
	Reverse Arrhenius coefficients:	2.31E+13	0.0	29360.0
444.	IC3H7O2+SC4H9=IC3H7O+SC4H9O	7.00E+12	0.0	-1000.0
	Reverse Arrhenius coefficients:	5.40E+10	0.7	29320.0
445.	IC3H7O2+C3H5-A=IC3H7O+C3H5O	7.00E+12	0.0	-1000.0
	Reverse Arrhenius coefficients:	1.55E+11	0.3	14900.0
446.	IC3H7O2+C4H7=IC3H7O+C4H7O	7.00E+12	0.0	-1000.0
	Reverse Arrhenius coefficients:	7.63E+08	0.8	19530.0
447.	NC3H7O2+CH3=NC3H7O+CH3O	7.00E+12	0.0	-1000.0
	Reverse Arrhenius coefficients:	1.85E+12	0.2	26450.0
448.	NC3H7O2+C2H5=NC3H7O+C2H5O	7.00E+12	0.0	-1000.0
	Reverse Arrhenius coefficients:	4.09E+12	0.2	29390.0
449.	NC3H7O2+IC3H7=NC3H7O+IC3H7O	7.00E+12	0.0	-1000.0
	Reverse Arrhenius coefficients:	6.68E+10	0.8	29900.0
450.	NC3H7O2+NC3H7=NC3H7O+NC3H7O	7.00E+12	0.0	-1000.0
	Reverse Arrhenius coefficients:	1.08E+13	0.1	29880.0
451.	NC3H7O2+PC4H9=NC3H7O+PC4H9O	7.00E+12	0.0	-1000.0
	Reverse Arrhenius coefficients:	1.85E+13	0.1	29620.0
452.	NC3H7O2+SC4H9=NC3H7O+SC4H9O	7.00E+12	0.0	-1000.0
	Reverse Arrhenius coefficients:	4.34E+10	0.7	29580.0
453.	NC3H7O2+C3H5-A=NC3H7O+C3H5O	7.00E+12	0.0	-1000.0
	Reverse Arrhenius coefficients:	1.24E+11	0.4	15160.0
454.	NC3H7O2+C4H7=NC3H7O+C4H7O	7.00E+12	0.0	-1000.0
	Reverse Arrhenius coefficients:	6.13E+08	0.8	19790.0
455.	C3H6+C2H5O2=C3H5-A+C2H5O2H	3.24E+11	0.0	14900.0
	Reverse Arrhenius coefficients:	2.00E+10	0.0	15000.0
456.	C3H6+NC3H7O2=C3H5-A+NC3H7O2H	3.24E+11	0.0	14900.0
	Reverse Arrhenius coefficients:	2.00E+10	0.0	15000.0
457.	NC3H7O2=NC3H7+O2	3.36E+19	-1.3	35760.0
	Reverse Arrhenius coefficients:	4.52E+12	0.0	0.0
458.	IC3H7O2=IC3H7+O2	2.80E+17	-0.6	36040.0
	Reverse Arrhenius coefficients:	7.54E+12	0.0	0.0
459.	NC3H7+HO2=NC3H7O+OH	7.00E+12	0.0	-1000.0
	Reverse Arrhenius coefficients:	1.77E+15	-0.4	26980.0

460.	IC3H7+HO2=IC3H7O+OH	7.00E+12	0.0	-1000.0
	Reverse Arrhenius coefficients:	1.10E+13	0.2	27000.0
461.	CH3O2+NC3H7=CH3O+NC3H7O	7.00E+12	0.0	-1000.0
	Reverse Arrhenius coefficients:	1.72E+17	-1.0	31740.0
462.	CH3O2+IC3H7=CH3O+IC3H7O	7.00E+12	0.0	-1000.0
	Reverse Arrhenius coefficients:	1.07E+15	-0.3	31760.0
463.	C3H6O1-3=C2H4+CH2O	6.00E+14	0.0	60000.0
	Reverse Arrhenius coefficients:	2.97E+11	0.0	31080.0
464.	C3H6O1-3+OH=CH2O+C2H3+H2O	5.00E+12	0.0	0.0
	All REV parameters are zero...	0.000E+00	0.00	0.000E+00
	This reaction is treated as irreversible			
465.	C3H6O1-3+O=CH2O+C2H3+OH	8.43E+13	0.0	5200.0
	All REV parameters are zero...	0.000E+00	0.00	0.000E+00
	This reaction is treated as irreversible			
466.	C3H6O1-3+H=CH2O+C2H3+H2	2.63E+07	2.0	5000.0
	All REV parameters are zero...	0.000E+00	0.00	0.000E+00
	This reaction is treated as irreversible			
467.	C3H6O1-3+CH3O2=CH2O+C2H3+CH3O2H	1.00E+13	0.0	19000.0
	All REV parameters are zero...	0.000E+00	0.00	0.000E+00
	This reaction is treated as irreversible			
468.	C3H6O1-3+HO2=CH2O+C2H3+H2O2	1.00E+13	0.0	15000.0
	All REV parameters are zero...	0.000E+00	0.00	0.000E+00
	This reaction is treated as irreversible			
469.	C3H6O1-3+CH3=CH2O+C2H3+CH4	2.00E+11	0.0	10000.0
	All REV parameters are zero...	0.000E+00	0.00	0.000E+00
	This reaction is treated as irreversible			
470.	C4H7O=CH3CHO+C2H3	7.94E+14	0.0	19000.0
	Reverse Arrhenius coefficients:	1.00E+10	0.0	20000.0
471.	C4H7O=C2H3CHO+CH3	7.94E+14	0.0	19000.0
	Reverse Arrhenius coefficients:	1.00E+10	0.0	20000.0
472.	C4H7+HO2=C4H7O+OH	7.00E+12	0.0	-1000.0
	Reverse Arrhenius coefficients:	1.01E+11	0.3	16890.0
473.	C4H7+CH3O2=C4H7O+CH3O	7.00E+12	0.0	-1000.0
	Reverse Arrhenius coefficients:	9.84E+12	-0.3	21650.0
474.	C4H7+C2H5O2=C4H7O+C2H5O	7.00E+12	0.0	-1000.0
	Reverse Arrhenius coefficients:	6.95E+08	0.8	19810.0
475.	C4H7+PC4H9O2=C4H7O+PC4H9O	7.00E+12	0.0	-1000.0
	Reverse Arrhenius coefficients:	5.78E+08	0.8	19780.0
476.	C4H7+SC4H9O2=C4H7O+SC4H9O	7.00E+12	0.0	-1000.0
	Reverse Arrhenius coefficients:	6.76E+08	0.8	19510.0
477.	C4H8OH-1O2=C4H8OH-1+O2	1.83E+18	0.1	47470.0
	Reverse Arrhenius coefficients:	2.00E+12	0.0	0.0
478.	C4H8OH-2O2=C4H8OH-2+O2	4.09E+19	-0.2	51980.0
	Reverse Arrhenius coefficients:	2.00E+12	0.0	0.0
479.	C4H8OH-1O2=C2H5CHO+CH2O+OH	1.00E+16	0.0	25000.0
	All REV parameters are zero...	0.000E+00	0.00	0.000E+00
	This reaction is treated as irreversible			
480.	C4H8OH-2O2=OH+CH3CHO+CH3CHO	1.00E+16	0.0	25000.0
	All REV parameters are zero...	0.000E+00	0.00	0.000E+00
	This reaction is treated as irreversible			
481.	C4H8-2+CH3CO3=C4H7+CH3CO3H	1.00E+11	0.0	8000.0
	Reverse Arrhenius coefficients:	2.00E+10	0.0	10000.0
482.	C4H8OH-2=C4H8-2+OH	1.50E+13	0.0	25830.0
	Reverse Arrhenius coefficients:	4.75E+12	0.0	-782.0
483.	C4H8-2+CH3O2=C4H7+CH3O2H	3.20E+12	0.0	14900.0
	Reverse Arrhenius coefficients:	1.58E+11	0.0	14700.0
484.	C4H8-2+C2H5O2=C4H7+C2H5O2H	3.20E+12	0.0	14900.0
	Reverse Arrhenius coefficients:	1.58E+11	0.0	14700.0
485.	C4H8-2+NC3H7O2=C4H7+NC3H7O2H	3.20E+12	0.0	14900.0
	Reverse Arrhenius coefficients:	1.58E+11	0.0	14700.0
486.	C4H8-2+PC4H9O2=C4H7+PC4H9O2H	3.20E+12	0.0	14900.0

```
     Reverse Arrhenius coefficients:                1.58E+11    0.0    14700.0
487. C4H8-1+OH=NC3H7+CH2O                           1.00E+12    0.0        0.0
     Reverse Arrhenius coefficients:                1.62E+12    0.0    13230.0
488. C4H8-1+O=C3H6+CH2O                             7.23E+05    2.3    -1050.0
     Reverse Arrhenius coefficients:                2.00E+05    2.3    80280.0
489. C4H8-1+O=CH3CHO+C2H4                           1.30E+13    0.0      850.0
     Reverse Arrhenius coefficients:                2.07E+12    0.0    85100.0
490. C4H8-1+O=CH3CO+C2H5                            1.30E+13    0.0      850.0
     Reverse Arrhenius coefficients:                2.35E+12    0.0    38150.0
491. C4H8-1+OH=CH3CHO+C2H5                          1.00E+12    0.0        0.0
     Reverse Arrhenius coefficients:                9.33E+12    0.0    19930.0
492. C4H8-1+OH=CH3CO+C2H6                           5.00E+11    0.0        0.0
     Reverse Arrhenius coefficients:                9.83E+12    0.0    32430.0
493. C4H8-1+O=C2H5CHO+CH2                           1.30E+13    0.0      850.0
     Reverse Arrhenius coefficients:                5.71E+09    0.0    11000.0
494. C4H8-1+O=C2H5CO+CH3                            1.30E+13    0.0      850.0
     Reverse Arrhenius coefficients:                4.80E+11    0.0    32550.0
495. C4H8-1+OH=C2H5CHO+CH3                          1.00E+12    0.0        0.0
     Reverse Arrhenius coefficients:                4.95E+10    0.0    16940.0
496. C4H8-1+OH=C2H5CO+CH4                           5.00E+11    0.0        0.0
     Reverse Arrhenius coefficients:                2.20E+13    0.0    34270.0
497. C4H8-1+CH3CO3=C4H7+CH3CO3H                     1.00E+11    0.0     8000.0
     Reverse Arrhenius coefficients:                2.00E+10    0.0    10000.0
498. C4H8OH-1=C4H8-1+OH                             1.50E+13    0.0    25830.0
     Reverse Arrhenius coefficients:                4.75E+12    0.0     -782.0
499. C4H8-1+CH3O2=C4H7+CH3O2H                       1.40E+12    0.0    14900.0
     Reverse Arrhenius coefficients:                3.16E+11    0.0    13000.0
500. C4H8-1+C2H5O2=C4H7+C2H5O2H                     1.40E+12    0.0    14900.0
     Reverse Arrhenius coefficients:                3.16E+11    0.0    13000.0
501. C4H8-1+NC3H7O2=C4H7+NC3H7O2H                   1.40E+12    0.0    14900.0
     Reverse Arrhenius coefficients:                3.16E+11    0.0    13000.0
502. C4H8-1+PC4H9O2=C4H7+PC4H9O2H                   1.40E+12    0.0    14900.0
     Reverse Arrhenius coefficients:                3.16E+11    0.0    13000.0
503. C4H8OOH1-3O2=C4H8OOH1-3+O2                     5.60E+22   -2.2    37960.0
     Reverse Arrhenius coefficients:                7.54E+12    0.0        0.0
504. C4H8OOH1-3O2=NC4KET13+OH                       2.50E+10    0.0    21400.0
     Reverse Arrhenius coefficients:                6.89E+03    1.3    44700.0
505. C4H8OOH1-2=C4H8-1+HO2                          1.61E+17   -1.5    13740.0
     Reverse Arrhenius coefficients:                1.25E+11    0.0     7800.0
506. C4H8OOH1-3=C4H8O1-3+OH                         5.00E+10    0.0    15250.0
     All REV parameters are zero...                 0.000E+00  0.00  0.000E+00
     This reaction is treated as irreversible
507. C4H8OOH1-3=OH+CH2O+C3H6                        6.64E+13   -0.2    29900.0
     All REV parameters are zero...                 0.000E+00  0.00  0.000E+00
     This reaction is treated as irreversible
508. C4H8O1-3+OH=CH2O+C3H5-A+H2O                    5.00E+12    0.0        0.0
     All REV parameters are zero...                 0.000E+00  0.00  0.000E+00
     This reaction is treated as irreversible
509. C4H8O1-3+H=CH2O+C3H5-A+H2                      5.00E+12    0.0        0.0
     All REV parameters are zero...                 0.000E+00  0.00  0.000E+00
     This reaction is treated as irreversible
510. C4H8O1-3+O=CH2O+C3H5-A+OH                      5.00E+12    0.0        0.0
     All REV parameters are zero...                 0.000E+00  0.00  0.000E+00
     This reaction is treated as irreversible
511. C4H8O1-3+HO2=CH2O+C3H5-A+H2O2                  1.00E+13    0.0    15000.0
     All REV parameters are zero...                 0.000E+00  0.00  0.000E+00
     This reaction is treated as irreversible
512. C4H8O1-3+CH3O2=CH2O+C3H5-A+CH3O2H              1.00E+13    0.0    19000.0
     All REV parameters are zero...                 0.000E+00  0.00  0.000E+00
     This reaction is treated as irreversible
513. C4H8O1-3+CH3=CH2O+C3H5-A+CH4                   2.00E+11    0.0    10000.0
```

	All REV parameters are zero...	0.000E+00	0.00	0.000E+00
	This reaction is treated as irreversible			
514.	PC4H9O=NC3H7+CH2O	5.81E+16	-1.0	20260.0
	Reverse Arrhenius coefficients:	1.50E+11	0.0	11900.0
515.	SC4H9O=CH3+C2H5CHO	3.07E+17	-1.3	19240.0
	Reverse Arrhenius coefficients:	1.50E+11	0.0	11900.0
516.	SC4H9O=C2H5+CH3CHO	1.28E+21	-2.1	20400.0
	Reverse Arrhenius coefficients:	1.50E+11	0.0	11900.0
517.	PC4H9O2H=PC4H9O+OH	1.50E+16	0.0	42500.0
	Reverse Arrhenius coefficients:	1.45E+08	1.7	-3055.0
518.	SC4H9O2+SC4H9O2=O2+SC4H9O+SC4H9O	1.40E+16	-1.6	1860.0
	All REV parameters are zero...	0.000E+00	0.00	0.000E+00
	This reaction is treated as irreversible			
519.	SC4H9O2+IC3H7O2=SC4H9O+IC3H7O+O2	1.40E+16	-1.6	1860.0
	All REV parameters are zero...	0.000E+00	0.00	0.000E+00
	This reaction is treated as irreversible			
520.	SC4H9O2+C2H5O2=SC4H9O+C2H5O+O2	1.40E+16	-1.6	1860.0
	All REV parameters are zero...	0.000E+00	0.00	0.000E+00
	This reaction is treated as irreversible			
521.	SC4H9O2+CH3O2=SC4H9O+CH3O+O2	1.40E+16	-1.6	1860.0
	All REV parameters are zero...	0.000E+00	0.00	0.000E+00
	This reaction is treated as irreversible			
522.	SC4H9O2+CH3CO3=SC4H9O+CH3CO2+O2	1.40E+16	-1.6	1860.0
	All REV parameters are zero...	0.000E+00	0.00	0.000E+00
	This reaction is treated as irreversible			
523.	SC4H9O2+HO2=SC4H9O+OH+O2	1.40E-14	-1.6	1860.0
	All REV parameters are zero...	0.000E+00	0.00	0.000E+00
	This reaction is treated as irreversible			
524.	SC4H9O2+CH3=SC4H9O+CH3O	7.00E+12	0.0	-1000.0
	Reverse Arrhenius coefficients:	2.04E+12	0.2	26170.0
525.	SC4H9O2+C2H5=SC4H9O+C2H5O	7.00E+12	0.0	-1000.0
	Reverse Arrhenius coefficients:	4.51E+12	0.2	29110.0
526.	SC4H9O2+IC3H7=SC4H9O+IC3H7O	7.00E+12	0.0	-1000.0
	Reverse Arrhenius coefficients:	7.37E+10	0.8	29620.0
527.	SC4H9O2+NC3H7=SC4H9O+NC3H7O	7.00E+12	0.0	-1000.0
	Reverse Arrhenius coefficients:	1.18E+13	0.1	29600.0
528.	SC4H9O2+PC4H9=SC4H9O+PC4H9O	7.00E+12	0.0	-1000.0
	Reverse Arrhenius coefficients:	2.04E+13	0.0	29340.0
529.	SC4H9O2+SC4H9=SC4H9O+SC4H9O	7.00E+12	0.0	-1000.0
	Reverse Arrhenius coefficients:	4.79E+10	0.7	29300.0
530.	SC4H9O2+C3H5-A=SC4H9O+C3H5O	7.00E+12	0.0	-1000.0
	Reverse Arrhenius coefficients:	1.37E+11	0.4	14880.0
531.	PC4H9O2+CH2O=PC4H9O2H+HCO	5.60E+12	0.0	13600.0
	Reverse Arrhenius coefficients:	8.00E+11	0.0	10000.0
532.	PC4H9O2+CH3CHO=PC4H9O2H+CH3CO	2.80E+12	0.0	13600.0
	Reverse Arrhenius coefficients:	1.00E+12	0.0	10000.0
533.	PC4H9O2+HO2=PC4H9O2H+O2	1.75E+10	0.0	-3275.0
	Reverse Arrhenius coefficients:	5.79E+13	-0.8	34490.0
534.	C3H6+PC4H9O2=C3H5-A+PC4H9O2H	3.24E+11	0.0	14900.0
	Reverse Arrhenius coefficients:	2.00E+10	0.0	15000.0
535.	C2H4+PC4H9O2=C2H3+PC4H9O2H	1.13E+13	0.0	30430.0
	Reverse Arrhenius coefficients:	3.00E+12	0.0	11500.0
536.	CH3OH+PC4H9O2=CH2OH+PC4H9O2H	6.30E+12	0.0	19360.0
	Reverse Arrhenius coefficients:	1.00E+09	0.0	10000.0
537.	C2H3CHO+PC4H9O2=C2H3CO+PC4H9O2H	2.80E+12	0.0	13600.0
	Reverse Arrhenius coefficients:	1.00E+12	0.0	10000.0
538.	CH4+PC4H9O2=CH3+PC4H9O2H	1.12E+13	0.0	24640.0
	Reverse Arrhenius coefficients:	7.43E+11	0.0	5500.0
539.	H2O2+PC4H9O2=HO2+PC4H9O2H	2.40E+12	0.0	10000.0
	Reverse Arrhenius coefficients:	2.40E+12	0.0	10000.0
540.	PC4H9O2+PC4H9O2=O2+PC4H9O+PC4H9O	1.40E+16	-1.6	1860.0

	All REV parameters are zero...	0.000E+00	0.00	0.000E+00
	This reaction is treated as irreversible			
541.	PC4H9O2+SC4H9O2=PC4H9O+SC4H9O+O2	1.40E+16	-1.6	1860.0
	All REV parameters are zero...	0.000E+00	0.00	0.000E+00
	This reaction is treated as irreversible			
542.	PC4H9O2+NC3H7O2=PC4H9O+NC3H7O+O2	1.40E+16	-1.6	1860.0
	All REV parameters are zero...	0.000E+00	0.00	0.000E+00
	This reaction is treated as irreversible			
543.	PC4H9O2+IC3H7O2=PC4H9O+IC3H7O+O2	1.40E+16	-1.6	1860.0
	All REV parameters are zero...	0.000E+00	0.00	0.000E+00
	This reaction is treated as irreversible			
544.	PC4H9O2+C2H5O2=PC4H9O+C2H5O+O2	1.40E+16	-1.6	1860.0
	All REV parameters are zero...	0.000E+00	0.00	0.000E+00
	This reaction is treated as irreversible			
545.	PC4H9O2+CH3O2=PC4H9O+CH3O+O2	1.40E+16	-1.6	1860.0
	All REV parameters are zero...	0.000E+00	0.00	0.000E+00
	This reaction is treated as irreversible			
546.	PC4H9O2+CH3CO3=PC4H9O+CH3CO2+O2	1.40E+16	-1.6	1860.0
	All REV parameters are zero...	0.000E+00	0.00	0.000E+00
	This reaction is treated as irreversible			
547.	PC4H9O2+HO2=PC4H9O+OH+O2	1.40E-14	-1.6	1860.0
	All REV parameters are zero...	0.000E+00	0.00	0.000E+00
	This reaction is treated as irreversible			
548.	H2+PC4H9O2=H+PC4H9O2H	3.01E+13	0.0	26030.0
	Reverse Arrhenius coefficients:	4.80E+13	0.0	7950.0
549.	C2H6+PC4H9O2=C2H5+PC4H9O2H	1.70E+13	0.0	20460.0
	Reverse Arrhenius coefficients:	5.00E+11	0.0	6500.0
550.	PC4H9O2+C2H5CHO=PC4H9O2H+C2H5CO	2.00E+11	0.0	9500.0
	Reverse Arrhenius coefficients:	5.00E+09	0.0	10000.0
551.	PC4H9O2+CH3=PC4H9O+CH3O	7.00E+12	0.0	-1000.0
	Reverse Arrhenius coefficients:	1.74E+12	0.2	26440.0
552.	PC4H9O2+C2H5=PC4H9O+C2H5O	7.00E+12	0.0	-1000.0
	Reverse Arrhenius coefficients:	3.86E+12	0.2	29380.0
553.	PC4H9O2+IC3H7=PC4H9O+IC3H7O	7.00E+12	0.0	-1000.0
	Reverse Arrhenius coefficients:	6.29E+10	0.8	29890.0
554.	PC4H9O2+NC3H7=PC4H9O+NC3H7O	7.00E+12	0.0	-1000.0
	Reverse Arrhenius coefficients:	1.01E+13	0.1	29870.0
555.	PC4H9O2+PC4H9=PC4H9O+PC4H9O	7.00E+12	0.0	-1000.0
	Reverse Arrhenius coefficients:	1.75E+13	0.1	29610.0
556.	PC4H9O2+SC4H9=PC4H9O+SC4H9O	7.00E+12	0.0	-1000.0
	Reverse Arrhenius coefficients:	4.09E+10	0.7	29570.0
557.	PC4H9O2+C3H5-A=PC4H9O+C3H5O	7.00E+12	0.0	-1000.0
	Reverse Arrhenius coefficients:	1.17E+11	0.4	15150.0
558.	PC4H9O2=C4H8OOH1-2	2.00E+11	0.0	26850.0
	Reverse Arrhenius coefficients:	5.60E+08	0.3	11970.0
559.	PC4H9O2=C4H8OOH1-3	2.50E+10	0.0	20850.0
	Reverse Arrhenius coefficients:	3.23E+09	-0.1	7871.0
560.	CH3O2+C4H10=CH3O2H+PC4H9	1.70E+13	0.0	20460.0
	Reverse Arrhenius coefficients:	5.00E+11	0.0	6500.0
561.	CH3O2+C4H10=CH3O2H+SC4H9	1.12E+13	0.0	17700.0
	Reverse Arrhenius coefficients:	5.00E+11	0.0	6500.0
562.	C2H5O2+C4H10=C2H5O2H+PC4H9	1.70E+13	0.0	20460.0
	Reverse Arrhenius coefficients:	5.00E+11	0.0	6500.0
563.	C2H5O2+C4H10=C2H5O2H+SC4H9	1.12E+13	0.0	17700.0
	Reverse Arrhenius coefficients:	5.00E+11	0.0	6500.0
564.	NC3H7O2+C4H10=NC3H7O2H+PC4H9	1.70E+13	0.0	20460.0
	Reverse Arrhenius coefficients:	5.00E+11	0.0	6500.0
565.	NC3H7O2+C4H10=NC3H7O2H+SC4H9	1.12E+13	0.0	17700.0
	Reverse Arrhenius coefficients:	5.00E+11	0.0	6500.0
566.	PC4H9O2+C4H10=PC4H9O2H+PC4H9	1.70E+13	0.0	20460.0
	Reverse Arrhenius coefficients:	5.00E+11	0.0	6500.0

567.	PC4H9O2+C4H10=PC4H9O2H+SC4H9	1.12E+13	0.0	17700.0
	Reverse Arrhenius coefficients:	5.00E+11	0.0	6500.0
568.	C4H10+CH3CO3=PC4H9+CH3CO3H	1.70E+13	0.0	20460.0
	Reverse Arrhenius coefficients:	5.00E+11	0.0	6500.0
569.	C4H10+CH3CO3=SC4H9+CH3CO3H	1.12E+13	0.0	17700.0
	Reverse Arrhenius coefficients:	5.00E+11	0.0	6500.0
570.	C4H10+C2H5O=PC4H9+C2H5OH	3.00E+11	0.0	7000.0
	Reverse Arrhenius coefficients:	1.00E+10	0.0	9000.0
571.	C4H10+C2H5O=SC4H9+C2H5OH	6.00E+11	0.0	7000.0
	Reverse Arrhenius coefficients:	1.00E+10	0.0	9000.0
572.	CH3COCH2O2=CH3COCH2+O2	8.09E+15	-1.1	27450.0
	Reverse Arrhenius coefficients:	1.20E+11	0.0	-1100.0
573.	CH3COCH3+CH3COCH2O2=CH3COCH2+CH3COCH2O2H	1.00E+11	0.0	5000.0
	Reverse Arrhenius coefficients:	2.00E+10	0.0	10000.0
574.	CH2O+CH3COCH2O2=HCO+CH3COCH2O2H	1.29E+11	0.0	9000.0
	Reverse Arrhenius coefficients:	2.51E+10	0.0	10100.0
575.	HO2+CH3COCH2O2=CH3COCH2O2H+O2	1.00E+12	0.0	0.0
	All REV parameters are zero...	0.000E+00	0.00	0.000E+00
	This reaction is treated as irreversible			
576.	CH3COCH2O2H=CH3COCH2O+OH	1.00E+16	0.0	43000.0
	Reverse Arrhenius coefficients:	2.04E+09	1.6	-4375.0
577.	CH3COCH2O=CH3CO+CH2O	8.71E+16	-1.2	13760.0
	Reverse Arrhenius coefficients:	1.00E+11	0.0	11900.0
578.	C2H5CHO+CH3O2=C2H5CO+CH3O2H	3.01E+12	0.0	11920.0
	Reverse Arrhenius coefficients:	2.36E+13	-0.5	8983.0
579.	C2H5CHO+C2H5O=C2H5CO+C2H5OH	6.03E+11	0.0	3300.0
	Reverse Arrhenius coefficients:	3.02E+11	0.0	18160.0
580.	C2H5CHO+C2H5O2=C2H5CO+C2H5O2H	3.01E+12	0.0	11920.0
	Reverse Arrhenius coefficients:	2.34E+13	-0.5	8579.0
581.	C2H5CHO+CH3CO3=C2H5CO+CH3CO3H	3.01E+12	0.0	11920.0
	Reverse Arrhenius coefficients:	1.87E+12	0.0	13140.0
582.	C2H5CHO+PC4H9=C2H5CO+C4H10	1.70E+12	0.0	8440.0
	Reverse Arrhenius coefficients:	9.70E+13	0.0	18820.0
583.	C2H5CHO+SC4H9=C2H5CO+C4H10	1.70E+12	0.0	8440.0
	Reverse Arrhenius coefficients:	9.70E+13	0.0	18820.0
584.	C2H5CHO+C4H7=C2H5CO+C4H8-1	1.70E+12	0.0	8440.0
	Reverse Arrhenius coefficients:	1.00E+13	0.0	28000.0
585.	C2H5CHO+C4H7=C2H5CO+C4H8-2	1.70E+12	0.0	8440.0
	Reverse Arrhenius coefficients:	1.00E+13	0.0	28000.0
586.	C2H5O2=C2H4+HO2	3.37E+55	-13.4	44670.0
	Reverse Arrhenius coefficients:	1.39E+49	-12.1	21620.0
587.	C2H4O2H=C2H5+O2	2.15E+37	-8.2	28020.0
	Reverse Arrhenius coefficients:	2.42E+35	-8.0	8312.0
588.	C3H4-A+HO2=C2H4+CO+OH	1.00E+12	0.0	14000.0
	Reverse Arrhenius coefficients:	1.00E+00	0.0	0.0
589.	C3H4-A+HO2=C3H3+H2O2	3.00E+13	0.0	14000.0
	Reverse Arrhenius coefficients:	1.55E+16	-1.4	44000.0
590.	CH3CHO+OH=CH3+HOCHO	3.00E+15	-1.1	0.0
	Reverse Arrhenius coefficients:	5.35E+19	-1.7	119800.0
591.	C3H5-T+O2=C3H4-A+HO2	1.89E+30	-5.6	15540.0
	Reverse Arrhenius coefficients:	1.57E+31	-5.8	26610.0
592.	C5H11O2-1=C5H11-1+O2	1.96E+20	-1.5	35810.0
	Reverse Arrhenius coefficients:	4.52E+12	0.0	0.0
593.	C5H11-1+C5H11O2-1=C5H11O-1+C5H11O-1	7.00E+12	0.0	-1000.0
	Reverse Arrhenius coefficients:	3.87E+13	0.0	29890.0
594.	C5H11O2-2=C5H11-2+O2	5.19E+17	-0.8	35970.0
	Reverse Arrhenius coefficients:	7.54E+12	0.0	0.0
595.	C5H11O2-1=C5H10OOH1-2	2.00E+11	0.0	26850.0
	Reverse Arrhenius coefficients:	2.08E+10	-0.1	13850.0
596.	C5H11O2-1=C5H10OOH1-3	2.50E+10	0.0	20850.0
	Reverse Arrhenius coefficients:	2.60E+09	-0.1	7850.0

597.	C5H11O2-1=C5H10OOH1-4	3.12E+09	0.0	19050.0
	Reverse Arrhenius coefficients:	3.26E+08	-0.1	6050.0
598.	C5H11O2-1+CH3O2=O2+C5H11O-1+CH3O	1.40E+16	-1.6	1860.0
	All REV parameters are zero...	0.000E+00	0.00	0.000E+00
	This reaction is treated as irreversible			
599.	C5H11O2-1+C5H11O2-1=O2+C5H11O-1+C5H11O-1	1.40E+16	-1.6	1860.0
	All REV parameters are zero...	0.000E+00	0.00	0.000E+00
	This reaction is treated as irreversible			
600.	H2O2+C5H11O2-1=HO2+C5H11O2H-1	2.40E+12	0.0	10000.0
	Reverse Arrhenius coefficients:	2.40E+12	0.0	10000.0
601.	C5H11O2-1+HO2=C5H11O2H-1+O2	1.75E+10	0.0	-3275.0
	Reverse Arrhenius coefficients:	4.98E+13	-0.8	34480.0
602.	C5H11O2H-1=C5H11O-1+OH	1.50E+16	0.0	42500.0
	Reverse Arrhenius coefficients:	1.41E+08	1.8	-3055.0
603.	C5H11O-1=CH2O+PC4H9	4.24E+16	-1.0	20010.0
	Reverse Arrhenius coefficients:	6.25E+10	0.0	11900.0
604.	C5H10OOH1-3=C5H10O1-3+OH	5.00E+10	0.0	15250.0
	All REV parameters are zero...	0.000E+00	0.00	0.000E+00
	This reaction is treated as irreversible			
605.	C5H10OOH1-4=C5H10O1-4+OH	6.25E+09	0.0	6000.0
	All REV parameters are zero...	0.000E+00	0.00	0.000E+00
	This reaction is treated as irreversible			
606.	C5H10OOH1-2=C5H10-1+HO2	5.73E+17	-1.6	15900.0
	Reverse Arrhenius coefficients:	1.25E+11	0.0	8070.0
607.	C5H10OOH1-3=OH+CH2O+C4H8-1	8.28E+13	-0.2	30090.0
	All REV parameters are zero...	0.000E+00	0.00	0.000E+00
	This reaction is treated as irreversible			
608.	C5H10OOH1-3O2=C5H10OOH1-3+O2	8.04E+22	-2.3	37970.0
	Reverse Arrhenius coefficients:	7.54E+12	0.0	0.0
609.	C5H10OOH1-4O2=C5H10OOH1-4+O2	8.04E+22	-2.3	37970.0
	Reverse Arrhenius coefficients:	7.54E+12	0.0	0.0
610.	C5H10OOH1-3O2=NC5KET13+OH	2.50E+10	0.0	21400.0
	Reverse Arrhenius coefficients:	5.33E+03	1.4	44700.0
611.	C5H10OOH1-4O2=NC5KET14+OH	3.12E+09	0.0	19350.0
	Reverse Arrhenius coefficients:	6.66E+02	1.4	42650.0
612.	C5H10O1-3+OH=C2H4+C2H5CO+H2O	2.50E+12	0.0	0.0
	All REV parameters are zero...	0.000E+00	0.00	0.000E+00
	This reaction is treated as irreversible			
613.	C5H10O1-4+OH=CH3COCH2+C2H4+H2O	2.50E+12	0.0	0.0
	All REV parameters are zero...	0.000E+00	0.00	0.000E+00
	This reaction is treated as irreversible			
614.	C5H10O1-3+OH=HCO+C4H8-1+H2O	2.50E+12	0.0	0.0
	All REV parameters are zero...	0.000E+00	0.00	0.000E+00
	This reaction is treated as irreversible			
615.	C5H10O1-4+OH=CH2CHO+C3H6+H2O	2.50E+12	0.0	0.0
	All REV parameters are zero...	0.000E+00	0.00	0.000E+00
	This reaction is treated as irreversible			
616.	C5H10O1-3+HO2=C2H4+C2H5CO+H2O2	5.00E+12	0.0	17700.0
	All REV parameters are zero...	0.000E+00	0.00	0.000E+00
	This reaction is treated as irreversible			
617.	C5H10O1-4+HO2=CH3COCH2+C2H4+H2O2	5.00E+12	0.0	17700.0
	All REV parameters are zero...	0.000E+00	0.00	0.000E+00
	This reaction is treated as irreversible			
618.	C5H10O1-3+HO2=HCO+C4H8-1+H2O2	5.00E+12	0.0	17700.0
	All REV parameters are zero...	0.000E+00	0.00	0.000E+00
	This reaction is treated as irreversible			
619.	C5H10O1-4+HO2=CH2CHO+C3H6+H2O2	5.00E+12	0.0	17700.0
	All REV parameters are zero...	0.000E+00	0.00	0.000E+00
	This reaction is treated as irreversible			
620.	C3H6+O2=C3H5-A+HO2	4.00E+12	0.0	39900.0
	Reverse Arrhenius coefficients:	3.33E+10	0.3	-556.0

621.	C3H6+CH3=C3H5-A+CH4	2.21E+00	3.5	5675.0
	Reverse Arrhenius coefficients:	2.65E+01	3.5	23180.0
622.	C3H6+CH3=C3H5-S+CH4	1.35E+00	3.5	12850.0
	Reverse Arrhenius coefficients:	1.05E-01	4.0	6925.0
623.	C3H6+CH3=C3H5-T+CH4	8.40E-01	3.5	11660.0
	Reverse Arrhenius coefficients:	1.50E-02	4.2	7842.0
624.	C3H6+C2H5=C3H5-A+C2H6	1.00E+11	0.0	9800.0
	Reverse Arrhenius coefficients:	5.37E+05	1.3	16440.0
625.	C3H5-T=C2H2+CH3	2.16E+10	-8.3	45110.0
	Reverse Arrhenius coefficients:	1.61E+10	-8.6	20330.0
626.	C3H5-A+HO2=C2H3+CH2O+OH	1.00E-18	0.0	0.0
	Reverse Arrhenius coefficients:	1.00E-30	0.0	0.0
627.	C3H5-A+H=C3H4-A+H2	1.81E+13	0.0	0.0
	Reverse Arrhenius coefficients:	1.23E+13	0.1	47230.0
628.	C3H5-A+CH3=C3H4-A+CH4	1.00E+11	0.0	0.0
	Reverse Arrhenius coefficients:	4.92E+12	0.1	47780.0
629.	C3H5-A+C2H5=C2H6+C3H4-A	4.00E+11	0.0	0.0
	Reverse Arrhenius coefficients:	1.80E+12	0.1	40330.0
630.	C3H5-A+C2H5=C2H4+C3H6	4.00E+11	0.0	0.0
	Reverse Arrhenius coefficients:	6.94E+16	-1.3	52800.0
631.	C3H5-A+C2H3=C2H4+C3H4-A	1.00E+12	0.0	0.0
	Reverse Arrhenius coefficients:	1.62E+13	0.1	48190.0
632.	C3H4-A+C3H6=C3H5-A+C3H5-A	8.39E+17	-1.3	33690.0
	Reverse Arrhenius coefficients:	1.00E+12	0.0	0.0
633.	C3H5-A+O2=C2H3CHO+OH	2.47E+13	-0.4	23020.0
	Reverse Arrhenius coefficients:	1.90E+14	-0.8	74880.0
634.	C3H5-S+O2=CH3CHO+HCO	4.34E+12	0.0	0.0
	Reverse Arrhenius coefficients:	1.61E+17	-1.3	96530.0
635.	C3H5-S+H=C3H4-A+H2	3.33E+12	0.0	0.0
	Reverse Arrhenius coefficients:	7.98E+12	0.1	68860.0
636.	C3H5-S+CH3=C3H4-A+CH4	1.00E+11	0.0	0.0
	Reverse Arrhenius coefficients:	6.25E+12	0.1	69340.0
637.	C3H5-T+O2=CH3COCH2+O	3.81E+17	-1.4	5580.0
	Reverse Arrhenius coefficients:	2.00E+11	0.0	17500.0
638.	C3H5-T+H=C3H4-P+H2	3.33E+12	0.0	0.0
	Reverse Arrhenius coefficients:	2.14E+16	-0.9	71050.0
639.	C3H5-T+CH3=C3H4-P+CH4	1.00E+11	0.0	0.0
	Reverse Arrhenius coefficients:	1.68E+16	-0.9	71530.0
640.	C3H4-A+M=C3H3+H+M	1.14E+17	0.0	70000.0
	Reverse Arrhenius coefficients:	1.80E+15	-0.4	10610.0
641.	C3H4-A=C3H4-P	1.20E+15	0.0	92400.0
	Reverse Arrhenius coefficients:	3.22E+18	-1.0	96590.0
642.	C3H4-A+O2=C3H3+HO2	4.00E+13	0.0	39160.0
	Reverse Arrhenius coefficients:	1.18E+11	0.3	38.0
643.	C3H4-A+HO2=CH2CO+CH2+OH	4.00E+12	0.0	19000.0
	Reverse Arrhenius coefficients:	1.00E+00	0.0	0.0
644.	C3H3+H=C3H2+H2	5.00E+13	0.0	0.0
	Reverse Arrhenius coefficients:	3.85E+10	0.4	4600.0
645.	C3H4-A+OH=C3H3+H2O	1.00E+07	2.0	1000.0
	Reverse Arrhenius coefficients:	7.00E+06	2.0	34520.0
646.	C3H4-A+O=C2H4+CO	7.80E+12	0.0	1600.0
	Reverse Arrhenius coefficients:	8.28E+13	-0.2	124800.0
647.	C3H2+OH=C2H2+HCO	5.00E+13	0.0	0.0
	Reverse Arrhenius coefficients:	2.91E+20	-1.4	78520.0
648.	C3H5-A=C3H4-A+H	6.66E+15	-0.4	63220.0
	Reverse Arrhenius coefficients:	2.40E+11	0.7	3007.0
649.	C3H5-T=C3H4-A+H	3.51E+14	-0.4	40890.0
	Reverse Arrhenius coefficients:	8.50E+12	0.0	2000.0
650.	C3H4-A+H=C3H3+H2	2.00E+07	2.0	5000.0
	Reverse Arrhenius coefficients:	3.24E+06	2.0	23360.0
651.	C3H4-A+CH3=C3H3+CH4	3.67E-02	4.0	6830.0

	Reverse Arrhenius coefficients:	1.55E-01	4.0	25670.0
652.	C3H4-A+C3H5-A=C3H3+C3H6	2.00E+11	0.0	7700.0
	Reverse Arrhenius coefficients:	2.64E+19	-2.7	42140.0
653.	C3H4-A+C2H=C3H3+C2H2	1.00E+13	0.0	0.0
	Reverse Arrhenius coefficients:	1.42E+16	-1.4	53820.0
654.	C3H4-P+M=C3H3+H+M	1.14E+17	0.0	70000.0
	Reverse Arrhenius coefficients:	6.71E+11	0.6	6420.0
655.	C3H4-P=C2H+CH3	4.20E+16	0.0	100000.0
	Reverse Arrhenius coefficients:	1.02E+12	0.6	-1600.0
656.	C3H4-P+O2=C3H3+HO2	2.00E+13	0.0	41600.0
	Reverse Arrhenius coefficients:	2.35E+11	0.1	78.0
657.	C3H4-P+HO2=C2H4+CO+OH	3.00E+12	0.0	19000.0
	Reverse Arrhenius coefficients:	1.00E+00	0.0	0.0
658.	C3H4-P+OH=C3H3+H2O	1.00E+07	2.0	1000.0
	Reverse Arrhenius coefficients:	2.80E+07	1.8	32120.0
659.	C3H4-P+O=C3H3+OH	7.65E+08	1.5	8600.0
	Reverse Arrhenius coefficients:	2.18E+08	1.3	22460.0
660.	C3H4-P+O=C2H3+HCO	3.20E+12	0.0	2010.0
	Reverse Arrhenius coefficients:	2.55E+12	-0.4	32350.0
661.	C3H4-P+O=HCCO+CH3	9.60E+08	1.0	0.0
	Reverse Arrhenius coefficients:	1.64E+10	-0.2	24090.0
662.	C3H5-T=C3H4-P+H	1.08E+15	-0.6	38490.0
	Reverse Arrhenius coefficients:	6.50E+12	0.0	2000.0
663.	C3H5-S=C3H4-P+H	4.19E+15	-0.8	37480.0
	Reverse Arrhenius coefficients:	5.80E+12	0.0	3100.0
664.	C3H4-P+H=C3H3+H2	2.00E+07	2.0	5000.0
	Reverse Arrhenius coefficients:	1.30E+07	1.8	20960.0
665.	C3H4-P+CH3=C3H3+CH4	1.50E+00	3.5	5600.0
	Reverse Arrhenius coefficients:	2.54E+01	3.3	22040.0
666.	C3H4-P+C2H=C3H3+C2H2	1.00E+12	0.0	0.0
	Reverse Arrhenius coefficients:	5.30E+11	-0.4	49630.0
667.	C3H4-P+C2H3=C3H3+C2H4	1.00E+12	0.0	7700.0
	Reverse Arrhenius coefficients:	9.54E+11	-0.4	52450.0
668.	C3H4-P+C3H5-A=C3H3+C3H6	1.00E+12	0.0	7700.0
	Reverse Arrhenius coefficients:	4.93E+16	-1.7	37950.0
669.	C3H3+O=CH2O+C2H	1.00E+13	0.0	0.0
	Reverse Arrhenius coefficients:	5.45E+14	0.0	31610.0
670.	C3H3+OH=C3H2+H2O	1.00E+13	0.0	0.0
	Reverse Arrhenius coefficients:	1.34E+15	0.0	15680.0
671.	C3H3+O2=CH2CO+HCO	3.01E+10	0.0	2870.0
	Reverse Arrhenius coefficients:	4.88E+11	0.0	59470.0
672.	C3H3+CH3=C2H5+C2H	4.56E+17	-1.1	48730.0
	Reverse Arrhenius coefficients:	1.81E+13	0.0	0.0
673.	SC4H9O2=SC4H9+O2	2.06E+17	-0.7	35740.0
	Reverse Arrhenius coefficients:	7.54E+12	0.0	0.0
674.	SC4H9+HO2=SC4H9O+OH	7.00E+12	0.0	-1000.0
	Reverse Arrhenius coefficients:	7.14E+12	0.2	26680.0
675.	CH3O2+SC4H9=CH3O+SC4H9O	7.00E+12	0.0	-1000.0
	Reverse Arrhenius coefficients:	6.97E+14	-0.4	31440.0
676.	PC4H9O2=PC4H9+O2	6.16E+19	-1.4	35510.0
	Reverse Arrhenius coefficients:	4.52E+12	0.0	0.0
677.	PC4H9+HO2=PC4H9O+OH	7.00E+12	0.0	-1000.0
	Reverse Arrhenius coefficients:	3.05E+15	-0.5	26720.0
678.	CH3O2+PC4H9=CH3O+PC4H9O	7.00E+12	0.0	-1000.0
	Reverse Arrhenius coefficients:	2.98E+17	-1.1	31480.0
679.	C2H3O1-2=CH3CO	8.50E+14	0.0	14000.0
	Reverse Arrhenius coefficients:	1.49E+14	0.0	47680.0
680.	C2H3O1-2=CH2CHO	1.00E+14	0.0	14000.0
	Reverse Arrhenius coefficients:	1.62E+15	-0.4	42460.0
681.	CH2CHO=CH2CO+H	3.09E+15	-0.3	50820.0
	Reverse Arrhenius coefficients:	5.00E+13	0.0	12300.0

682.	CH2CHO+O2=CH2O+CO+OH	2.00E+13	0.0	4200.0
	All REV parameters are zero...	0.000E+00	0.00	0.000E+00
	This reaction is treated as irreversible			
683.	NC4KET13=CH3CHO+CH2CHO+OH	1.05E+16	0.0	41600.0
	All REV parameters are zero...	0.000E+00	0.00	0.000E+00
	This reaction is treated as irreversible			
684.	NC5KET13=C2H5CHO+CH2CHO+OH	1.05E+16	0.0	41600.0
	All REV parameters are zero...	0.000E+00	0.00	0.000E+00
	This reaction is treated as irreversible			
685.	NC5KET14=CH3CHO+CH2CH2CHO+OH	1.05E+16	0.0	41600.0
	All REV parameters are zero...	0.000E+00	0.00	0.000E+00
	This reaction is treated as irreversible			
686.	O2CHO=HCO+O2	7.77E+26	-4.0	44230.0
	Reverse Arrhenius coefficients:	1.20E+11	0.0	-1100.0
687.	C3H5-A+O2=C3H4-A+HO2	2.18E+21	-2.9	30760.0
	Reverse Arrhenius coefficients:	2.69E+19	-2.4	20500.0
688.	C3H5-A+O2=CH2CHO+CH2O	7.14E+15	-1.2	21050.0
	Reverse Arrhenius coefficients:	4.94E+16	-1.4	88620.0
689.	C3H5-A+O2=C2H2+CH2O+OH	9.72E+29	-5.7	21450.0
	All REV parameters are zero...	0.000E+00	0.00	0.000E+00
	This reaction is treated as irreversible			
690.	HCCO+O2=CO2+HCO	2.40E+11	0.0	-854.0
	Reverse Arrhenius coefficients:	1.47E+14	0.0	133600.0
691.	C3H6+H=C3H5-S+H2	8.04E+05	2.5	12280.0
	Reverse Arrhenius coefficients:	2.39E+03	3.0	5876.0
692.	CH2CO+OH=CH2OH+CO	3.73E+12	0.0	-1013.0
	Reverse Arrhenius coefficients:	9.43E+06	1.7	27490.0
693.	CH3+O2=CH2O+OH	7.47E+11	0.0	14250.0
	Reverse Arrhenius coefficients:	7.78E+11	0.0	67770.0
694.	C2H4+H2=CH3+CH3	3.77E+12	0.8	84710.0
	Reverse Arrhenius coefficients:	1.00E+14	0.0	32000.0
695.	C3H5-T+O2=CH2O+CH3CO	3.71E+25	-4.0	7043.0
	Reverse Arrhenius coefficients:	1.87E+27	-4.4	101200.0
696.	IC3H7+OH=C3H6+H2O	2.41E+13	0.0	0.0
	Reverse Arrhenius coefficients:	2.98E+12	0.6	83820.0
697.	IC3H7+O=CH3COCH3+H	4.82E+13	0.0	0.0
	Reverse Arrhenius coefficients:	1.29E+16	-0.2	79380.0
698.	IC3H7+O=CH3CHO+CH3	4.82E+13	0.0	0.0
	Reverse Arrhenius coefficients:	1.28E+11	0.8	86480.0
699.	C3H6+H=C3H5-T+H2	4.05E+05	2.5	9794.0
	Reverse Arrhenius coefficients:	2.76E+02	3.2	5500.0
700.	C3H6=C3H5-T+H	5.62E+71	-16.6	139300.0
	Reverse Arrhenius coefficients:	2.03E+64	-14.9	27550.0
701.	CH2CCH2OH+O2=CH2OH+CO+CH2O	4.34E+12	0.0	0.0
	All REV parameters are zero...	0.000E+00	0.00	0.000E+00
	This reaction is treated as irreversible			
702.	CH2CCH2OH=C2H2+CH2OH	2.16E+40	-8.3	45110.0
	Reverse Arrhenius coefficients:	1.61E+40	-8.6	20330.0
703.	CH2CCH2OH=C3H4-A+OH	6.70E+16	-1.1	42580.0
	Reverse Arrhenius coefficients:	8.50E+12	0.0	2000.0
704.	C2H4+HO2=C2H4O1-2+OH	2.23E+12	0.0	17190.0
	Reverse Arrhenius coefficients:	1.08E+14	-0.2	37790.0
705.	NC3H7CHO+O2=NC3H7CO+HO2	2.00E+13	0.5	42200.0
	Reverse Arrhenius coefficients:	1.00E+07	0.5	4000.0
706.	NC3H7CHO+OH=NC3H7CO+H2O	2.69E+10	0.8	-340.0
	Reverse Arrhenius coefficients:	1.85E+10	0.8	31220.0
707.	NC3H7CHO+H=NC3H7CO+H2	4.00E+13	0.0	4200.0
	Reverse Arrhenius coefficients:	1.80E+13	0.0	24000.0
708.	NC3H7CHO+O=NC3H7CO+OH	5.00E+12	0.0	1790.0
	Reverse Arrhenius coefficients:	1.00E+12	0.0	19000.0
709.	NC3H7CHO+HO2=NC3H7CO+H2O2	2.80E+12	0.0	13600.0

	Reverse Arrhenius coefficients:	1.00E+12	0.0	10000.0
710.	NC3H7CHO+CH3=NC3H7CO+CH4	1.70E+12	0.0	8440.0
	Reverse Arrhenius coefficients:	1.50E+13	0.0	28000.0
711.	NC3H7CHO+CH3O=NC3H7CO+CH3OH	1.15E+11	0.0	1280.0
	Reverse Arrhenius coefficients:	3.00E+11	0.0	18000.0
712.	NC3H7CHO+CH3O2=NC3H7CO+CH3O2H	1.00E+12	0.0	9500.0
	Reverse Arrhenius coefficients:	2.50E+10	0.0	10000.0
713.	NC3H7CHO+OH=C3H6CHO-1+H2O	5.27E+09	1.0	1586.0
	Reverse Arrhenius coefficients:	1.09E+09	1.0	21020.0
714.	NC3H7CHO+OH=C3H6CHO-2+H2O	4.67E+07	1.6	-35.0
	Reverse Arrhenius coefficients:	8.06E+05	1.9	21940.0
715.	NC3H7CHO+OH=C3H6CHO-3+H2O	2.70E+09	1.0	-149.0
	Reverse Arrhenius coefficients:	6.19E+10	0.8	28740.0
716.	NC3H7CHO+HO2=C3H6CHO-1+H2O2	9.03E-01	3.6	7153.0
	Reverse Arrhenius coefficients:	1.11E+00	3.3	-4874.0
717.	NC3H7CHO+HO2=C3H6CHO-2+H2O2	1.48E+04	2.6	13910.0
	Reverse Arrhenius coefficients:	1.51E+03	2.6	4424.0
718.	NC3H7CHO+HO2=C3H6CHO-3+H2O2	3.61E+03	2.5	10530.0
	Reverse Arrhenius coefficients:	4.92E+05	2.0	7954.0
719.	NC3H7CHO+CH3O2=C3H6CHO-1+CH3O2H	6.03E+12	0.0	19380.0
	Reverse Arrhenius coefficients:	3.04E+13	-0.5	6628.0
720.	NC3H7CHO+CH3O2=C3H6CHO-2+CH3O2H	9.63E+03	2.6	13910.0
	Reverse Arrhenius coefficients:	4.05E+03	2.4	3704.0
721.	NC3H7CHO+CH3O2=C3H6CHO-3+CH3O2H	9.63E+03	2.6	11510.0
	Reverse Arrhenius coefficients:	5.39E+06	1.8	8212.0
722.	NC3H7CO=NC3H7+CO	5.32E+15	-0.9	13400.0
	Reverse Arrhenius coefficients:	1.50E+11	0.0	4800.0
723.	C2H5COCH3+OH=CH2CH2COCH3+H2O	7.55E+09	1.0	1586.0
	Reverse Arrhenius coefficients:	1.53E+09	1.0	21020.0
724.	C2H5COCH3+OH=CH3CHCOCH3+H2O	8.45E+11	0.0	-228.0
	Reverse Arrhenius coefficients:	1.59E+13	-0.2	28620.0
725.	C2H5COCH3+OH=C2H5COCH2+H2O	5.10E+11	0.0	1192.0
	Reverse Arrhenius coefficients:	6.63E+13	-0.7	27670.0
726.	C2H5COCH3+HO2=CH2CH2COCH3+H2O2	2.38E+04	2.5	16490.0
	Reverse Arrhenius coefficients:	2.86E+04	2.2	4459.0
727.	C2H5COCH3+HO2=CH3CHCOCH3+H2O2	2.00E+11	0.0	8698.0
	Reverse Arrhenius coefficients:	2.23E+13	-0.6	6080.0
728.	C2H5COCH3+HO2=C2H5COCH2+H2O2	2.38E+04	2.5	14690.0
	Reverse Arrhenius coefficients:	1.84E+07	1.5	9702.0
729.	C2H5COCH3+O=CH2CH2COCH3+OH	2.25E+13	0.0	7700.0
	Reverse Arrhenius coefficients:	4.62E+11	0.0	9882.0
730.	C2H5COCH3+O=CH3CHCOCH3+OH	3.07E+13	0.0	3400.0
	Reverse Arrhenius coefficients:	5.85E+13	-0.2	15000.0
731.	C2H5COCH3+O=C2H5COCH2+OH	5.00E+12	0.0	5962.0
	Reverse Arrhenius coefficients:	6.59E+13	-0.7	15190.0
732.	C2H5COCH3+H=CH2CH2COCH3+H2	9.16E+06	2.0	7700.0
	Reverse Arrhenius coefficients:	4.28E+05	2.0	11980.0
733.	C2H5COCH3+H=CH3CHCOCH3+H2	4.46E+06	2.0	3200.0
	Reverse Arrhenius coefficients:	1.93E+07	1.8	16890.0
734.	C2H5COCH3+H=C2H5COCH2+H2	9.30E+12	0.0	6357.0
	Reverse Arrhenius coefficients:	2.79E+14	-0.7	17680.0
735.	C2H5COCH3+O2=CH2CH2COCH3+HO2	2.05E+13	0.0	51310.0
	Reverse Arrhenius coefficients:	1.74E+10	0.3	-1895.0
736.	C2H5COCH3+O2=CH3CHCOCH3+HO2	1.55E+13	0.0	41970.0
	Reverse Arrhenius coefficients:	1.22E+12	0.1	-1822.0
737.	C2H5COCH3+O2=C2H5COCH2+HO2	2.05E+13	0.0	49150.0
	Reverse Arrhenius coefficients:	1.12E+13	-0.4	2988.0
738.	C2H5COCH3+CH3=CH2CH2COCH3+CH4	3.19E+01	3.2	7172.0
	Reverse Arrhenius coefficients:	3.89E+01	3.2	11930.0
739.	C2H5COCH3+CH3=CH3CHCOCH3+CH4	1.74E+00	3.5	3680.0
	Reverse Arrhenius coefficients:	1.97E+02	3.2	17850.0

740. C2H5COCH3+CH3=C2H5COCH2+CH4	1.62E+11	0.0	9630.0
Reverse Arrhenius coefficients:	1.27E+14	-0.7	21430.0
741. C2H5COCH3+CH3O=CH2CH2COCH3+CH3OH	2.17E+11	0.0	6460.0
Reverse Arrhenius coefficients:	4.89E+09	0.0	9007.0
742. C2H5COCH3+CH3O=CH3CHCOCH3+CH3OH	1.45E+11	0.0	2771.0
Reverse Arrhenius coefficients:	3.03E+11	-0.2	14730.0
743. C2H5COCH3+CH3O=C2H5COCH2+CH3OH	2.17E+11	0.0	4660.0
Reverse Arrhenius coefficients:	3.14E+12	-0.7	14250.0
744. C2H5COCH3+CH3O2=CH2CH2COCH3+CH3O2H	3.01E+12	0.0	19380.0
Reverse Arrhenius coefficients:	7.52E+12	-0.5	4329.0
745. C2H5COCH3+CH3O2=CH3CHCOCH3+CH3O2H	2.00E+12	0.0	15250.0
Reverse Arrhenius coefficients:	4.64E+14	-0.7	9612.0
746. C2H5COCH3+CH3O2=C2H5COCH2+CH3O2H	3.01E+12	0.0	17580.0
Reverse Arrhenius coefficients:	4.84E+15	-1.2	9572.0
747. C2H5COCH3+C2H3=CH2CH2COCH3+C2H4	5.00E+11	0.0	10400.0
Reverse Arrhenius coefficients:	3.44E+08	0.8	14030.0
748. C2H5COCH3+C2H3=CH3CHCOCH3+C2H4	3.00E+11	0.0	3400.0
Reverse Arrhenius coefficients:	1.91E+10	0.6	16440.0
749. C2H5COCH3+C2H3=C2H5COCH2+C2H4	6.15E+10	0.0	4278.0
Reverse Arrhenius coefficients:	2.72E+10	0.1	14950.0
750. C2H5COCH3+C2H5=CH2CH2COCH3+C2H6	5.00E+10	0.0	13400.0
Reverse Arrhenius coefficients:	9.55E+12	-0.6	13990.0
751. C2H5COCH3+C2H5=CH3CHCOCH3+C2H6	3.00E+10	0.0	8600.0
Reverse Arrhenius coefficients:	5.32E+14	-0.8	18600.0
752. C2H5COCH3+C2H5=C2H5COCH2+C2H6	5.00E+10	0.0	11600.0
Reverse Arrhenius coefficients:	6.14E+15	-1.3	19230.0
753. CH3CHCO+OH=C2H5+CO2	1.73E+12	0.0	-1010.0
All REV parameters are zero...	0.000E+00	0.00	0.000E+00
This reaction is treated as irreversible			
754. CH3CHCO+OH=SC2H4OH+CO	2.00E+12	0.0	-1010.0
All REV parameters are zero...	0.000E+00	0.00	0.000E+00
This reaction is treated as irreversible			
755. CH3CHCO+H=C2H5+CO	4.40E+12	0.0	1459.0
All REV parameters are zero...	0.000E+00	0.00	0.000E+00
This reaction is treated as irreversible			
756. CH3CHCO+O=CH3CHO+CO	3.20E+12	0.0	-437.0
All REV parameters are zero...	0.000E+00	0.00	0.000E+00
This reaction is treated as irreversible			
757. CH2CH2CHO=C2H4+HCO	3.13E+13	-0.5	24590.0
Reverse Arrhenius coefficients:	1.50E+11	0.0	8300.0
758. CH2CH2COCH3=C2H4+CH3CO	5.97E+12	0.0	20730.0
Reverse Arrhenius coefficients:	2.11E+11	0.0	7350.0
759. C2H5COCH2=CH2CO+C2H5	1.57E+13	0.0	30000.0
Reverse Arrhenius coefficients:	2.11E+11	0.0	7350.0
760. CH3CHCHO+HO2=C2H5CHO+O2	7.35E+12	0.0	1310.0
Reverse Arrhenius coefficients:	8.07E+13	-0.1	45070.0
761. CH3CHCHO+HO2=CH3CHOCHO+OH	9.64E+12	0.0	0.0
Reverse Arrhenius coefficients:	1.55E+16	-1.0	21740.0
762. CH3CHOCHO=CH3CHO+HCO	3.98E+13	0.0	9700.0
Reverse Arrhenius coefficients:	4.34E+05	1.7	8282.0
763. CH3CHCHO=C2H3CHO+H	3.52E+15	-0.5	41060.0
Reverse Arrhenius coefficients:	6.50E+12	0.0	2900.0
764. CH3CHCHO=CH3CHCO+H	1.14E+16	-0.7	40310.0
Reverse Arrhenius coefficients:	5.00E+12	0.0	1200.0
765. CH3CHCHO+H2=C2H5CHO+H	2.16E+05	2.4	18990.0
Reverse Arrhenius coefficients:	4.31E+04	2.6	5265.0
766. C2H5CHO+HO2=CH3CHCHO+H2O2	8.00E+10	0.0	11920.0
Reverse Arrhenius coefficients:	1.03E+13	-0.6	9337.0
767. CH3CHCHO+O2=CH3CHCO+HO2	1.81E+11	0.0	1840.0
Reverse Arrhenius coefficients:	2.73E+10	0.0	12690.0
768. CH3CHCHO+O2=C2H3CHO+HO2	2.72E+11	0.0	7240.0

	Reverse Arrhenius coefficients:	1.73E+11	-0.2	19040.0
769.	CH3CHCHO+O2=CH3CHO+CO+OH	3.62E+10	0.0	0.0
	All REV parameters are zero...	0.000E+00	0.00	0.000E+00
	This reaction is treated as irreversible			
770.	CH3CHCOCH3=C2H3COCH3+H	3.42E+16	-0.8	41770.0
	Reverse Arrhenius coefficients:	5.00E+12	0.0	1200.0
771.	CH3CHCOCH3=CH3CHCO+CH3	1.41E+15	-0.4	38340.0
	Reverse Arrhenius coefficients:	1.23E+11	0.0	7800.0
772.	C3H6CHO-3=C2H3CHO+CH3	3.17E+14	-0.4	29900.0
	Reverse Arrhenius coefficients:	1.23E+11	0.0	7800.0
773.	C3H6CHO-2=C3H6+HCO	8.25E+12	-0.2	21900.0
	Reverse Arrhenius coefficients:	1.00E+11	0.0	6000.0
774.	C3H6CHO-1=C2H4+CH2CHO	7.40E+11	0.0	21970.0
	Reverse Arrhenius coefficients:	2.11E+11	0.0	7350.0
775.	C2H5COC2H5+OH=C2H5COC2H4P+H2O	1.05E+10	1.0	1586.0
	Reverse Arrhenius coefficients:	1.19E+09	0.9	21030.0
776.	C2H5COC2H5+HO2=C2H5COC2H4P+H2O2	4.76E+04	2.5	16490.0
	Reverse Arrhenius coefficients:	3.20E+04	2.2	4472.0
777.	C2H5COC2H5+O2=C2H5COC2H4P+HO2	4.10E+13	0.0	51310.0
	Reverse Arrhenius coefficients:	1.95E+10	0.3	-1882.0
778.	C2H5COC2H5+H=C2H5COC2H4P+H2	1.83E+07	2.0	7700.0
	Reverse Arrhenius coefficients:	4.79E+05	2.0	11990.0
779.	C2H5COC2H5+C2H3=C2H5COC2H4P+C2H4	1.00E+12	0.0	10400.0
	Reverse Arrhenius coefficients:	3.85E+08	0.8	14040.0
780.	C2H5COC2H5+C2H5=C2H5COC2H4P+C2H6	1.00E+11	0.0	13400.0
	Reverse Arrhenius coefficients:	1.07E+13	-0.6	14000.0
781.	C2H5COC2H5+CH3O=C2H5COC2H4P+CH3OH	4.34E+11	0.0	6460.0
	Reverse Arrhenius coefficients:	5.48E+09	0.0	9020.0
782.	C2H5COC2H5+CH3O2=C2H5COC2H4P+CH3O2H	6.02E+12	0.0	19380.0
	Reverse Arrhenius coefficients:	1.66E+13	-0.5	6642.0
783.	C2H5COC2H4P=C2H5CO+C2H4	1.55E+17	-1.5	27840.0
	Reverse Arrhenius coefficients:	7.00E+10	0.0	9600.0
784.	NC3H7COCH3+OH=C3H6COCH3-1+H2O	2.06E+07	1.7	753.0
	Reverse Arrhenius coefficients:	3.60E+06	1.8	20170.0
785.	NC3H7COCH3+OH=C3H6COCH3-2+H2O	3.62E+07	1.6	-247.0
	Reverse Arrhenius coefficients:	3.67E+05	2.0	21660.0
786.	NC3H7COCH3+OH=C3H6COCH3-3+H2O	8.45E+11	0.0	-228.0
	Reverse Arrhenius coefficients:	2.37E+13	-0.3	28700.0
787.	NC3H7COCH3+OH=NC3H7COCH2+H2O	5.10E+11	0.0	1192.0
	Reverse Arrhenius coefficients:	9.29E+13	-0.7	27730.0
788.	NC3H7COCH3+HO2=C3H6COCH3-1+H2O2	2.38E+04	2.5	16490.0
	Reverse Arrhenius coefficients:	2.46E+04	2.2	4442.0
789.	NC3H7COCH3+HO2=C3H6COCH3-2+H2O2	5.60E+12	0.0	17700.0
	Reverse Arrhenius coefficients:	3.37E+11	0.1	8142.0
790.	NC3H7COCH3+HO2=C3H6COCH3-3+H2O2	2.00E+11	0.0	8698.0
	Reverse Arrhenius coefficients:	3.33E+13	-0.6	6160.0
791.	NC3H7COCH3+HO2=NC3H7COCH2+H2O2	2.38E+04	2.5	14690.0
	Reverse Arrhenius coefficients:	2.57E+07	1.5	9762.0
792.	NC3H7COCH3+CH3O2=C3H6COCH3-1+CH3O2H	3.01E+12	0.0	19380.0
	Reverse Arrhenius coefficients:	1.28E+13	-0.5	6607.0
793.	NC3H7COCH3+CH3O2=C3H6COCH3-2+CH3O2H	1.99E+12	0.0	17050.0
	Reverse Arrhenius coefficients:	4.93E+11	-0.1	6774.0
794.	NC3H7COCH3+CH3O2=C3H6COCH3-3+CH3O2H	2.00E+12	0.0	15250.0
	Reverse Arrhenius coefficients:	1.37E+15	-0.8	11990.0
795.	NC3H7COCH3+CH3O2=NC3H7COCH2+CH3O2H	3.01E+12	0.0	17580.0
	Reverse Arrhenius coefficients:	1.34E+16	-1.2	11930.0
796.	C3H6COCH3-1=C2H4+CH3COCH2	2.90E+16	-1.2	27000.0
	Reverse Arrhenius coefficients:	1.00E+11	0.0	8600.0
797.	C3H6COCH3-2=C3H6+CH3CO	2.72E+16	-1.1	25590.0
	Reverse Arrhenius coefficients:	1.00E+11	0.0	7800.0
798.	C3H6COCH3-3=C2H3COCH3+CH3	9.62E+15	-0.8	32390.0

	Reverse Arrhenius coefficients:	1.00E+11	0.0	7800.0
799.	NC3H7COCH2=NC3H7+CH2CO	1.23E+18	-1.4	43450.0
	Reverse Arrhenius coefficients:	1.00E+11	0.0	11600.0
800.	NC3H7COC2H4P=NC3H7CO+C2H4	5.40E+17	-1.4	26040.0
	Reverse Arrhenius coefficients:	2.50E+11	0.0	7800.0
801.	NC4H9CHO+O2=NC4H9CO+HO2	2.00E+13	0.5	42200.0
	Reverse Arrhenius coefficients:	1.00E+07	0.0	40000.0
802.	NC4H9CHO+OH=NC4H9CO+H2O	2.69E+10	0.8	-340.0
	Reverse Arrhenius coefficients:	2.14E+10	0.7	31240.0
803.	NC4H9CHO+H=NC4H9CO+H2	4.00E+13	0.0	4200.0
	Reverse Arrhenius coefficients:	1.80E+13	0.0	24000.0
804.	NC4H9CHO+O=NC4H9CO+OH	5.00E+12	0.0	1790.0
	Reverse Arrhenius coefficients:	1.00E+12	0.0	19000.0
805.	NC4H9CHO+HO2=NC4H9CO+H2O2	2.80E+12	0.0	13600.0
	Reverse Arrhenius coefficients:	1.00E+12	0.0	10000.0
806.	NC4H9CHO+CH3=NC4H9CO+CH4	1.70E+12	0.0	8440.0
	Reverse Arrhenius coefficients:	1.50E+13	0.0	28000.0
807.	NC4H9CHO+CH3O=NC4H9CO+CH3OH	1.15E+11	0.0	1280.0
	Reverse Arrhenius coefficients:	3.00E+11	0.0	18000.0
808.	NC4H9CHO+CH3O2=NC4H9CO+CH3O2H	1.00E+12	0.0	9500.0
	Reverse Arrhenius coefficients:	2.50E+10	0.0	10000.0
809.	NC4H9CHO+OH=C4H8CHO-1+H2O	5.27E+09	1.0	1586.0
	Reverse Arrhenius coefficients:	1.23E+09	0.9	21040.0
810.	NC4H9CHO+OH=C4H8CHO-2+H2O	4.67E+07	1.6	-35.0
	Reverse Arrhenius coefficients:	6.84E+05	1.9	21920.0
811.	NC4H9CHO+OH=C4H8CHO-3+H2O	4.67E+07	1.6	-35.0
	Reverse Arrhenius coefficients:	6.84E+05	1.9	21920.0
812.	NC4H9CHO+OH=C4H8CHO-4+H2O	4.67E+07	1.6	-35.0
	Reverse Arrhenius coefficients:	1.20E+09	1.3	28870.0
813.	NC4H9CHO+HO2=C4H8CHO-1+H2O2	2.76E+04	2.5	16480.0
	Reverse Arrhenius coefficients:	3.83E+04	2.2	4471.0
814.	NC4H9CHO+HO2=C4H8CHO-2+H2O2	1.48E+04	2.6	13910.0
	Reverse Arrhenius coefficients:	1.28E+03	2.6	4399.0
815.	NC4H9CHO+HO2=C4H8CHO-3+H2O2	1.48E+04	2.6	13910.0
	Reverse Arrhenius coefficients:	1.28E+03	2.6	4399.0
816.	NC4H9CHO+HO2=C4H8CHO-4+H2O2	2.95E+04	2.6	13910.0
	Reverse Arrhenius coefficients:	4.51E+06	2.0	11350.0
817.	NC4H9CHO+CH3O2=C4H8CHO-1+CH3O2H	6.03E+12	0.0	19380.0
	Reverse Arrhenius coefficients:	3.44E+13	-0.5	6646.0
818.	NC4H9CHO+CH3O2=C4H8CHO-2+CH3O2H	1.99E+12	0.0	17050.0
	Reverse Arrhenius coefficients:	7.11E+11	-0.2	6821.0
819.	NC4H9CHO+CH3O2=C4H8CHO-3+CH3O2H	1.99E+12	0.0	17050.0
	Reverse Arrhenius coefficients:	7.11E+11	-0.2	6821.0
820.	NC4H9CHO+CH3O2=C4H8CHO-4+CH3O2H	3.98E+12	0.0	17050.0
	Reverse Arrhenius coefficients:	2.50E+15	-0.8	13770.0
821.	C4H8CHO-1=C2H4+CH2CH2CHO	5.98E+18	-1.6	30430.0
	Reverse Arrhenius coefficients:	2.50E+11	0.0	7800.0
822.	C4H8CHO-2=C3H6+CH2CHO	2.98E+14	-0.8	23320.0
	Reverse Arrhenius coefficients:	1.00E+11	0.0	7800.0
823.	C4H8CHO-3=C4H8-1+HCO	4.80E+14	-0.7	24350.0
	Reverse Arrhenius coefficients:	1.00E+11	0.0	7800.0
824.	C4H8CHO-4=C2H3CHO+C2H5	1.86E+18	-1.3	30830.0
	Reverse Arrhenius coefficients:	1.00E+11	0.0	7800.0
825.	NC4H9CO=PC4H9+CO	1.00E+11	0.0	9600.0
	Reverse Arrhenius coefficients:	1.00E+11	0.0	0.0
826.	AC3H5CO=C3H5-A+CO	6.20E+15	-1.1	-330.0
	Reverse Arrhenius coefficients:	1.50E+11	0.0	4810.0
827.	C3H6OH=C3H6+OH	9.36E+12	0.0	27120.0
	Reverse Arrhenius coefficients:	9.93E+11	0.0	-960.0
828.	HOC3H6O2=C3H6OH+O2	2.87E+19	-1.9	34290.0
	Reverse Arrhenius coefficients:	1.20E+11	0.0	-1100.0

829.	HOC3H6O2=CH3CHO+CH2O+OH	1.25E+10	0.0	18900.0
	All REV parameters are zero...	0.000E+00	0.00	0.000E+00
	This reaction is treated as irreversible			
830.	C5H11-1+HO2=C5H11O-1+OH	7.00E+12	0.0	-1000.0
	Reverse Arrhenius coefficients:	8.08E+15	-0.6	27010.0
831.	C5H11-1+CH3O2=C5H11O-1+CH3O	7.00E+12	0.0	-1000.0
	Reverse Arrhenius coefficients:	7.89E+17	-1.2	31770.0
832.	HOCH2O=CH2O+OH	1.64E+14	-0.1	21890.0
	Reverse Arrhenius coefficients:	2.60E+12	0.0	-614.0
833.	HOCH2O=HOCHO+H	1.00E+14	0.0	14900.0
	Reverse Arrhenius coefficients:	3.08E+11	0.6	7944.0
834.	HOCHO+M=CO+H2O+M	2.30E+13	0.0	50000.0
	Reverse Arrhenius coefficients:	1.42E+10	0.5	46840.0
835.	HOCHO+M=CO2+H2+M	1.50E+16	0.0	57000.0
	Reverse Arrhenius coefficients:	2.40E+14	0.5	61020.0
836.	HOCHO=HCO+OH	4.59E+18	-0.5	108300.0
	Reverse Arrhenius coefficients:	1.00E+14	0.0	0.0
837.	HOCHO+OH=H2O+CO2+H	2.62E+06	2.1	916.0
	All REV parameters are zero...	0.000E+00	0.00	0.000E+00
	This reaction is treated as irreversible			
838.	HOCHO+OH=H2O+CO+OH	1.85E+07	1.5	-962.0
	All REV parameters are zero...	0.000E+00	0.00	0.000E+00
	This reaction is treated as irreversible			
839.	HOCHO+H=H2+CO2+H	4.24E+06	2.1	4868.0
	All REV parameters are zero...	0.000E+00	0.00	0.000E+00
	This reaction is treated as irreversible			
840.	HOCHO+H=H2+CO+OH	6.03E+13	-0.3	2988.0
	All REV parameters are zero...	0.000E+00	0.00	0.000E+00
	This reaction is treated as irreversible			
841.	HOCHO+CH3=CH4+CO+OH	3.90E-07	5.8	2200.0
	All REV parameters are zero...	0.000E+00	0.00	0.000E+00
	This reaction is treated as irreversible			
842.	HOCHO+HO2=H2O2+CO+OH	1.00E+12	0.0	11920.0
	All REV parameters are zero...	0.000E+00	0.00	0.000E+00
	This reaction is treated as irreversible			
843.	HOCHO+O=CO+OH+OH	1.77E+18	-1.9	2975.0
	All REV parameters are zero...	0.000E+00	0.00	0.000E+00
	This reaction is treated as irreversible			
844.	CH2(S)+M=CH2+M	1.00E+13	0.0	0.0
	Reverse Arrhenius coefficients:	7.16E+15	-0.9	11430.0
845.	CH2(S)+CH4=CH3+CH3	4.00E+13	0.0	0.0
	Reverse Arrhenius coefficients:	5.43E+15	-0.9	15650.0
846.	CH2(S)+C2H6=CH3+C2H5	1.20E+14	0.0	0.0
	Reverse Arrhenius coefficients:	1.04E+14	-0.3	19820.0
847.	CH2(S)+O2=CO+OH+H	7.00E+13	0.0	0.0
	All REV parameters are zero...	0.000E+00	0.00	0.000E+00
	This reaction is treated as irreversible			
848.	CH2(S)+H2=CH3+H	7.00E+13	0.0	0.0
	Reverse Arrhenius coefficients:	2.48E+17	-0.9	16130.0
849.	CH2(S)+H=CH+H2	3.00E+13	0.0	0.0
	Reverse Arrhenius coefficients:	1.51E+16	-0.9	14420.0
850.	CH2(S)+O=CO+H+H	3.00E+13	0.0	0.0
	All REV parameters are zero...	0.000E+00	0.00	0.000E+00
	This reaction is treated as irreversible			
851.	CH2(S)+OH=CH2O+H	3.00E+13	0.0	0.0
	Reverse Arrhenius coefficients:	3.19E+18	-0.9	87860.0
852.	CH2(S)+CO2=CH2O+CO	3.00E+12	0.0	0.0
	Reverse Arrhenius coefficients:	2.85E+15	-0.9	65520.0
853.	CH2(S)+CH3=C2H4+H	2.00E+13	0.0	0.0
	Reverse Arrhenius coefficients:	2.67E+15	-0.1	68840.0
854.	CH2(S)+CH2CO=C2H4+CO	1.60E+14	0.0	0.0

	Reverse Arrhenius coefficients:	4.60E+15	-0.1	105600.0
855.	C6H13-1+O2=C6H12-1+HO2	3.00E-19	0.0	3000.0
	Reverse Arrhenius coefficients:	2.00E-19	0.0	17500.0
856.	C6H13-3+O2=C6H12-2+HO2	3.00E-19	0.0	3000.0
	Reverse Arrhenius coefficients:	2.00E-19	0.0	17500.0
857.	C6H13-1=C2H4+PC4H9	5.45E+17	-1.3	29580.0
	Reverse Arrhenius coefficients:	3.30E+11	0.0	7200.0
858.	C6H13-1=C6H12-1+H	2.09E+16	-0.9	37940.0
	Reverse Arrhenius coefficients:	1.00E+13	0.0	2900.0
859.	C6H13-3=C4H8-1+C2H5	5.61E+17	-1.3	29600.0
	Reverse Arrhenius coefficients:	1.50E+11	0.0	7200.0
860.	C6H13-3=C5H10-1+CH3	6.27E+12	0.0	28680.0
	Reverse Arrhenius coefficients:	1.50E+11	0.0	7200.0
861.	C6H13-3=C6H12-2+H	2.76E+15	-0.7	37590.0
	Reverse Arrhenius coefficients:	1.00E+13	0.0	2900.0
862.	C6H13-1=C6H13-3	1.50E+09	1.0	33760.0
	Reverse Arrhenius coefficients:	9.71E+07	1.3	36270.0
863.	C6H12-1+OH=C6H11+H2O	3.00E+13	0.0	1230.0
	Reverse Arrhenius coefficients:	9.76E+14	-0.1	39260.0
864.	C6H12-2+OH=C6H11+H2O	3.00E+13	0.0	1230.0
	Reverse Arrhenius coefficients:	1.99E+15	-0.3	36380.0
865.	C6H12-1+H=C6H11+H2	3.70E+13	0.0	3900.0
	Reverse Arrhenius coefficients:	2.78E+14	-0.1	26770.0
866.	C6H12-2+H=C6H11+H2	3.70E+13	0.0	3900.0
	Reverse Arrhenius coefficients:	5.66E+14	-0.3	23900.0
867.	C6H12-1+CH3=C6H11+CH4	1.00E+12	0.0	7300.0
	Reverse Arrhenius coefficients:	1.96E+14	-0.1	30650.0
868.	C6H12-2+CH3=C6H11+CH4	1.00E+12	0.0	7300.0
	Reverse Arrhenius coefficients:	3.99E+14	-0.3	27780.0
869.	C6H12-1+O=C6H11+OH	2.12E+11	0.1	9125.0
	Reverse Arrhenius coefficients:	7.00E+11	0.0	29900.0
870.	C6H12-2+O=C6H11+OH	1.04E+11	0.3	12000.0
	Reverse Arrhenius coefficients:	7.00E+11	0.0	29900.0
871.	C6H12-1+OH=C5H11-1+CH2O	1.00E+11	0.0	-4000.0
	All REV parameters are zero...	0.000E+00	0.00	0.000E+00
	This reaction is treated as irreversible			
872.	C6H12-2+OH=PC4H9+CH3CHO	1.00E+11	0.0	-4000.0
	All REV parameters are zero...	0.000E+00	0.00	0.000E+00
	This reaction is treated as irreversible			
873.	C6H12-1+O=C5H11-1+HCO	1.00E+11	0.0	-1050.0
	All REV parameters are zero...	0.000E+00	0.00	0.000E+00
	This reaction is treated as irreversible			
874.	C6H12-2+O=PC4H9+CH3CO	1.00E+11	0.0	-1050.0
	All REV parameters are zero...	0.000E+00	0.00	0.000E+00
	This reaction is treated as irreversible			
875.	C6H11=C3H6+C3H5-A	2.50E+13	0.0	45000.0
	Reverse Arrhenius coefficients:	1.00E+10	0.0	17000.0
876.	C6H11=C4H8-1+C2H3	2.50E-17	0.0	45000.0
	Reverse Arrhenius coefficients:	1.50E-20	0.0	7400.0
877.	C6H11=C4H7+C2H4	2.50E-17	0.0	45000.0
	Reverse Arrhenius coefficients:	1.50E-20	0.0	7400.0
878.	C6H12-1=NC3H7+C3H5-A	1.00E+16	0.0	71000.0
	Reverse Arrhenius coefficients:	1.00E+13	0.0	0.0
879.	C6H12-2=C2H5+C4H7	1.00E+16	0.0	71000.0
	Reverse Arrhenius coefficients:	1.00E+13	0.0	0.0
880.	C6H13O2-1=C6H13-1+O2	5.15E+20	-1.7	35780.0
	Reverse Arrhenius coefficients:	4.52E+12	0.0	0.0
881.	C6H13-1+C6H13O2-1=C6H13O-1+C6H13O-1	7.00E+12	0.0	-1000.0
	Reverse Arrhenius coefficients:	9.78E+13	-0.2	29840.0
882.	C6H13O2-1=C6H12OOH1-3	2.50E+10	0.0	20850.0
	Reverse Arrhenius coefficients:	3.00E+09	-0.1	7860.0

883.	C6H13O2-1=C6H12OOH1-4	3.12E+09	0.0	19050.0
	Reverse Arrhenius coefficients:	3.75E+08	-0.1	6060.0
884.	C6H13O2-1+CH3O2=C6H13O-1+CH3O+O2	1.40E+16	-1.6	1860.0
	All REV parameters are zero...	0.000E+00	0.00	0.000E+00
	This reaction is treated as irreversible			
885.	C6H13O2-1+C6H13O2-1=O2+C6H13O-1+C6H13O-1	1.40E+16	-1.6	1860.0
	All REV parameters are zero...	0.000E+00	0.00	0.000E+00
	This reaction is treated as irreversible			
886.	C6H13O-1=C5H11-1+CH2O	1.81E+17	-1.1	20300.0
	Reverse Arrhenius coefficients:	1.00E+11	0.0	11900.0
887.	C6H12OOH1-3=C6H12O1-3+OH	7.50E+10	0.0	15250.0
	All REV parameters are zero...	0.000E+00	0.00	0.000E+00
	This reaction is treated as irreversible			
888.	C6H12OOH1-4=C6H12O1-4+OH	9.38E+09	0.0	7000.0
	All REV parameters are zero...	0.000E+00	0.00	0.000E+00
	This reaction is treated as irreversible			
889.	C6H12OOH1-3=OH+CH2O+C5H10-1	7.70E+13	-0.2	30090.0
	All REV parameters are zero...	0.000E+00	0.00	0.000E+00
	This reaction is treated as irreversible			
890.	C6H12OOH1-3O2=C6H12OOH1-3+O2	8.87E+22	-2.3	37980.0
	Reverse Arrhenius coefficients:	7.54E+12	0.0	0.0
891.	C6H12OOH1-4O2=C6H12OOH1-4+O2	8.87E+22	-2.3	37980.0
	Reverse Arrhenius coefficients:	7.54E+12	0.0	0.0
892.	C6H12OOH1-3O2=NC6KET13+OH	2.50E+10	0.0	21400.0
	Reverse Arrhenius coefficients:	4.24E+03	1.4	44670.0
893.	NC6KET13=NC3H7CHO+CH2CHO+OH	1.05E+16	0.0	41600.0
	All REV parameters are zero...	0.000E+00	0.00	0.000E+00
	This reaction is treated as irreversible			
894.	C6H12O1-3+OH=C5H10-1+HCO+H2O	2.50E+12	0.0	0.0
	All REV parameters are zero...	0.000E+00	0.00	0.000E+00
	This reaction is treated as irreversible			
895.	C6H12O1-4+OH=C4H8-1+CH2CHO+H2O	2.50E+12	0.0	0.0
	All REV parameters are zero...	0.000E+00	0.00	0.000E+00
	This reaction is treated as irreversible			
896.	C6H12O1-3+OH=C2H4+NC3H7CO+H2O	2.50E+12	0.0	0.0
	All REV parameters are zero...	0.000E+00	0.00	0.000E+00
	This reaction is treated as irreversible			
897.	C6H12O1-4+OH=C2H4+C2H5COCH2+H2O	2.50E+12	0.0	0.0
	All REV parameters are zero...	0.000E+00	0.00	0.000E+00
	This reaction is treated as irreversible			
898.	C6H12O1-3+HO2=C5H10-1+HCO+H2O2	5.00E+12	0.0	17700.0
	All REV parameters are zero...	0.000E+00	0.00	0.000E+00
	This reaction is treated as irreversible			
899.	C6H12O1-4+HO2=C4H8-1+CH2CHO+H2O2	5.00E+12	0.0	17700.0
	All REV parameters are zero...	0.000E+00	0.00	0.000E+00
	This reaction is treated as irreversible			
900.	C6H12O1-3+HO2=C2H4+NC3H7CO+H2O2	5.00E+12	0.0	17700.0
	All REV parameters are zero...	0.000E+00	0.00	0.000E+00
	This reaction is treated as irreversible			
901.	C6H12O1-4+HO2=C2H4+C2H5COCH2+H2O2	5.00E+12	0.0	17700.0
	All REV parameters are zero...	0.000E+00	0.00	0.000E+00
	This reaction is treated as irreversible			
902.	C6H13-1+HO2=C6H13O-1+OH	7.00E+12	0.0	-1000.0
	Reverse Arrhenius coefficients:	2.08E+16	-0.8	26970.0
903.	C6H13-1+CH3O2=C6H13O-1+CH3O	7.00E+12	0.0	-1000.0
	Reverse Arrhenius coefficients:	2.04E+18	-1.4	31740.0
904.	NC7H16=H+C7H15-1	1.34E+88	-21.2	142800.0
	Reverse Arrhenius coefficients:	3.37E+82	-20.2	39610.0
905.	NC7H16=H+C7H15-2	6.50E+87	-21.0	139500.0
	Reverse Arrhenius coefficients:	5.21E+80	-19.7	38890.0
906.	NC7H16=H+C7H15-3	6.50E+87	-21.0	139500.0

	Reverse Arrhenius coefficients:	5.21E+80	-19.7	38890.0
907.	NC7H16=H+C7H15-4	3.25E+87	-21.0	139500.0
	Reverse Arrhenius coefficients:	5.19E+80	-19.7	38890.0
908.	NC7H16=C6H13-1+CH3	2.93E+73	-16.6	118900.0
	Reverse Arrhenius coefficients:	8.35E+66	-15.8	31830.0
909.	NC7H16=C5H11-1+C2H5	8.10E+77	-17.6	120400.0
	Reverse Arrhenius coefficients:	8.30E+67	-16.1	32350.0
910.	NC7H16=PC4H9+NC3H7	1.42E+78	-17.7	120700.0
	Reverse Arrhenius coefficients:	1.36E+68	-16.1	32460.0
911.	NC7H16+H=C7H15-1+H2	1.88E+05	2.8	6280.0
	Reverse Arrhenius coefficients:	8.93E+03	2.7	10550.0
912.	NC7H16+H=C7H15-2+H2	2.60E+06	2.4	4471.0
	Reverse Arrhenius coefficients:	3.93E+03	2.7	11260.0
913.	NC7H16+H=C7H15-3+H2	2.60E+06	2.4	4471.0
	Reverse Arrhenius coefficients:	3.93E+03	2.7	11260.0
914.	NC7H16+H=C7H15-4+H2	1.30E+06	2.4	4471.0
	Reverse Arrhenius coefficients:	3.91E+03	2.7	11260.0
915.	NC7H16+O=C7H15-1+OH	1.93E+05	2.7	3716.0
	Reverse Arrhenius coefficients:	4.02E+03	2.6	5893.0
916.	NC7H16+O=C7H15-2+OH	9.54E+04	2.7	2106.0
	Reverse Arrhenius coefficients:	6.33E+01	3.0	6798.0
917.	NC7H16+O=C7H15-3+OH	9.54E+04	2.7	2106.0
	Reverse Arrhenius coefficients:	6.33E+01	3.0	6798.0
918.	NC7H16+O=C7H15-4+OH	4.77E+04	2.7	2106.0
	Reverse Arrhenius coefficients:	6.31E+01	3.0	6798.0
919.	NC7H16+OH=C7H15-1+H2O	1.05E+10	1.0	1590.0
	Reverse Arrhenius coefficients:	1.50E+10	1.1	23330.0
920.	NC7H16+OH=C7H15-2+H2O	9.40E+07	1.6	-35.0
	Reverse Arrhenius coefficients:	6.15E+05	1.9	21910.0
921.	NC7H16+OH=C7H15-3+H2O	9.40E+07	1.6	-35.0
	Reverse Arrhenius coefficients:	6.15E+05	1.9	21910.0
922.	NC7H16+OH=C7H15-4+H2O	4.70E+07	1.6	-35.0
	Reverse Arrhenius coefficients:	6.12E+05	1.9	21910.0
923.	NC7H16+HO2=C7H15-1+H2O2	1.68E+13	0.0	20440.0
	Reverse Arrhenius coefficients:	2.05E+13	-0.4	8399.0
924.	NC7H16+HO2=C7H15-2+H2O2	1.12E+13	0.0	17690.0
	Reverse Arrhenius coefficients:	4.35E+11	0.0	8165.0
925.	NC7H16+HO2=C7H15-3+H2O2	1.12E+13	0.0	17690.0
	Reverse Arrhenius coefficients:	4.35E+11	0.0	8165.0
926.	NC7H16+HO2=C7H15-4+H2O2	5.60E+12	0.0	17690.0
	Reverse Arrhenius coefficients:	4.33E+11	0.0	8165.0
927.	NC7H16+CH3=C7H15-1+CH4	9.04E-01	3.6	7154.0
	Reverse Arrhenius coefficients:	1.12E+00	3.6	11910.0
928.	NC7H16+CH3=C7H15-2+CH4	5.41E+04	2.3	7287.0
	Reverse Arrhenius coefficients:	2.14E+03	2.6	14550.0
929.	NC7H16+CH3=C7H15-3+CH4	5.41E+04	2.3	7287.0
	Reverse Arrhenius coefficients:	2.14E+03	2.6	14550.0
930.	NC7H16+CH3=C7H15-4+CH4	2.70E+04	2.3	7287.0
	Reverse Arrhenius coefficients:	2.13E+03	2.6	14550.0
931.	NC7H16+O2=C7H15-1+HO2	6.00E+13	0.0	52800.0
	Reverse Arrhenius coefficients:	5.18E+10	0.3	-406.0
932.	NC7H16+O2=C7H15-2+HO2	4.00E+13	0.0	50150.0
	Reverse Arrhenius coefficients:	1.10E+09	0.7	-541.0
933.	NC7H16+O2=C7H15-3+HO2	4.00E+13	0.0	50150.0
	Reverse Arrhenius coefficients:	1.10E+09	0.7	-541.0
934.	NC7H16+O2=C7H15-4+HO2	2.00E+13	0.0	50150.0
	Reverse Arrhenius coefficients:	1.09E+09	0.7	-541.0
935.	NC7H16+C2H5=C7H15-1+C2H6	1.00E+11	0.0	13400.0
	Reverse Arrhenius coefficients:	3.20E+11	0.0	12300.0
936.	NC7H16+C2H5=C7H15-2+C2H6	1.00E+11	0.0	10400.0
	Reverse Arrhenius coefficients:	1.00E+11	0.0	12900.0

937. NC7H16+C2H5=C7H15-3+C2H6	1.00E+11	0.0	10400.0
Reverse Arrhenius coefficients:	1.00E+11	0.0	12900.0
938. NC7H16+C2H5=C7H15-4+C2H6	5.00E+10	0.0	10400.0
Reverse Arrhenius coefficients:	1.00E+11	0.0	12900.0
939. NC7H16+CH3O=C7H15-1+CH3OH	3.16E+11	0.0	7000.0
Reverse Arrhenius coefficients:	1.20E+10	0.0	9200.0
940. NC7H16+CH3O=C7H15-2+CH3OH	2.19E+11	0.0	5000.0
Reverse Arrhenius coefficients:	8.90E+09	0.0	7200.0
941. NC7H16+CH3O=C7H15-3+CH3OH	2.19E+11	0.0	5000.0
Reverse Arrhenius coefficients:	8.90E+09	0.0	7200.0
942. NC7H16+CH3O=C7H15-4+CH3OH	1.10E+11	0.0	5000.0
Reverse Arrhenius coefficients:	8.90E+09	0.0	7200.0
943. NC7H16+C2H3=C7H15-1+C2H4	1.00E+12	0.0	18000.0
Reverse Arrhenius coefficients:	2.57E+12	0.0	25400.0
944. NC7H16+C2H3=C7H15-2+C2H4	8.00E+11	0.0	16800.0
Reverse Arrhenius coefficients:	2.00E+12	0.0	24200.0
945. NC7H16+C2H3=C7H15-3+C2H4	8.00E+11	0.0	16800.0
Reverse Arrhenius coefficients:	2.00E+12	0.0	24200.0
946. NC7H16+C2H3=C7H15-4+C2H4	4.00E+11	0.0	16800.0
Reverse Arrhenius coefficients:	2.00E+12	0.0	24200.0
947. NC7H16+CH3O2=C7H15-1+CH3O2H	1.21E+13	0.0	20430.0
Reverse Arrhenius coefficients:	3.60E+12	0.0	9800.0
948. NC7H16+CH3O2=C7H15-2+CH3O2H	8.06E+12	0.0	17700.0
Reverse Arrhenius coefficients:	2.38E+11	0.0	3700.0
949. NC7H16+CH3O2=C7H15-3+CH3O2H	8.06E+12	0.0	17700.0
Reverse Arrhenius coefficients:	2.38E+11	0.0	3700.0
950. NC7H16+CH3O2=C7H15-4+CH3O2H	4.03E+12	0.0	17700.0
Reverse Arrhenius coefficients:	2.38E+11	0.0	3700.0
951. NC7H16+C7H15O2-1=C7H15-1+C7H15O2H-1	1.21E+13	0.0	20430.0
Reverse Arrhenius coefficients:	1.44E+10	0.0	15000.0
952. NC7H16+C7H15O2-2=C7H15-1+C7H15O2H-2	1.21E+13	0.0	20430.0
Reverse Arrhenius coefficients:	1.44E+10	0.0	15000.0
953. NC7H16+C7H15O2-3=C7H15-1+C7H15O2H-3	1.21E+13	0.0	20430.0
Reverse Arrhenius coefficients:	1.44E+10	0.0	15000.0
954. NC7H16+C7H15O2-4=C7H15-1+C7H15O2H-4	1.21E+13	0.0	20430.0
Reverse Arrhenius coefficients:	1.44E+10	0.0	15000.0
955. NC7H16+C7H15O2-1=C7H15-2+C7H15O2H-1	8.06E+12	0.0	17700.0
Reverse Arrhenius coefficients:	1.44E+10	0.0	15000.0
956. NC7H16+C7H15O2-2=C7H15-2+C7H15O2H-2	8.06E+12	0.0	17700.0
Reverse Arrhenius coefficients:	1.44E+10	0.0	15000.0
957. NC7H16+C7H15O2-3=C7H15-2+C7H15O2H-3	8.06E+12	0.0	17700.0
Reverse Arrhenius coefficients:	1.44E+10	0.0	15000.0
958. NC7H16+C7H15O2-4=C7H15-2+C7H15O2H-4	8.06E+12	0.0	17700.0
Reverse Arrhenius coefficients:	1.44E+10	0.0	15000.0
959. NC7H16+C7H15O2-1=C7H15-3+C7H15O2H-1	8.06E+12	0.0	17700.0
Reverse Arrhenius coefficients:	1.44E+10	0.0	15000.0
960. NC7H16+C7H15O2-2=C7H15-3+C7H15O2H-2	8.06E+12	0.0	17700.0
Reverse Arrhenius coefficients:	1.44E+10	0.0	15000.0
961. NC7H16+C7H15O2-3=C7H15-3+C7H15O2H-3	8.06E+12	0.0	17700.0
Reverse Arrhenius coefficients:	1.44E+10	0.0	15000.0
962. NC7H16+C7H15O2-4=C7H15-3+C7H15O2H-4	8.06E+12	0.0	17700.0
Reverse Arrhenius coefficients:	1.44E+10	0.0	15000.0
963. NC7H16+C7H15O2-1=C7H15-4+C7H15O2H-1	4.03E+12	0.0	17700.0
Reverse Arrhenius coefficients:	1.44E+10	0.0	15000.0
964. NC7H16+C7H15O2-2=C7H15-4+C7H15O2H-2	4.03E+12	0.0	17700.0
Reverse Arrhenius coefficients:	1.44E+10	0.0	15000.0
965. NC7H16+C7H15O2-3=C7H15-4+C7H15O2H-3	4.03E+12	0.0	17700.0
Reverse Arrhenius coefficients:	1.44E+10	0.0	15000.0
966. NC7H16+C7H15O2-4=C7H15-4+C7H15O2H-4	4.03E+12	0.0	17700.0
Reverse Arrhenius coefficients:	1.44E+10	0.0	15000.0
967. NC7H16+C7H15-1=C7H15-2+NC7H16	1.00E+11	0.0	10400.0

	Reverse Arrhenius coefficients:	1.50E+11	0.0	12300.0
968.	NC7H16+C7H15-1=C7H15-3+NC7H16	1.00E+11	0.0	10400.0
	Reverse Arrhenius coefficients:	1.50E+11	0.0	12300.0
969.	NC7H16+C7H15-1=C7H15-4+NC7H16	5.00E+10	0.0	10400.0
	Reverse Arrhenius coefficients:	1.50E+11	0.0	12300.0
970.	NC7H16+C7H15-2=C7H15-3+NC7H16	1.00E+11	0.0	10400.0
	Reverse Arrhenius coefficients:	1.00E+11	0.0	10400.0
971.	NC7H16+C7H15-2=C7H15-4+NC7H16	5.00E+10	0.0	10400.0
	Reverse Arrhenius coefficients:	1.00E+11	0.0	10400.0
972.	NC7H16+C7H15-3=C7H15-4+NC7H16	5.00E+10	0.0	10400.0
	Reverse Arrhenius coefficients:	1.00E+11	0.0	10400.0
973.	C7H15-1=C5H11-1+C2H4	8.16E+17	-1.4	30840.0
	Reverse Arrhenius coefficients:	1.00E+11	0.0	8200.0
974.	C7H15-1=C7H14-1+H	4.20E+16	-0.9	37940.0
	Reverse Arrhenius coefficients:	1.00E+13	0.0	2900.0
975.	C7H15-2=PC4H9+C3H6	2.22E+16	-0.9	30130.0
	Reverse Arrhenius coefficients:	1.00E+11	0.0	8200.0
976.	C7H15-2=C7H14-1+H	1.34E+15	-0.6	38760.0
	Reverse Arrhenius coefficients:	1.00E+13	0.0	1200.0
977.	C7H15-2=C7H14-2+H	2.71E+15	-0.7	37590.0
	Reverse Arrhenius coefficients:	1.00E+13	0.0	2900.0
978.	C7H15-3=C4H8-1+NC3H7	9.63E+17	-1.4	30580.0
	Reverse Arrhenius coefficients:	1.00E+11	0.0	7700.0
979.	C7H15-3=C6H12-1+CH3	1.03E+14	-0.4	28690.0
	Reverse Arrhenius coefficients:	1.75E+11	0.0	7200.0
980.	C7H15-3=C7H14-2+H	2.71E+15	-0.7	37590.0
	Reverse Arrhenius coefficients:	1.00E+13	0.0	2900.0
981.	C7H15-3=C7H14-3+H	2.02E+15	-0.7	37680.0
	Reverse Arrhenius coefficients:	1.00E+13	0.0	2900.0
982.	C7H15-4=C2H5+C5H10-1	5.43E+16	-0.9	30590.0
	Reverse Arrhenius coefficients:	1.00E+11	0.0	8200.0
983.	C7H15-4=C7H14-3+H	4.02E+15	-0.7	37680.0
	Reverse Arrhenius coefficients:	1.00E+13	0.0	2900.0
984.	C7H15-1+O2=C7H14-1+HO2	3.00E-09	0.0	3000.0
	Reverse Arrhenius coefficients:	2.44E-10	0.3	17920.0
985.	C7H15-2+O2=C7H14-1+HO2	4.50E-09	0.0	5020.0
	Reverse Arrhenius coefficients:	1.15E-08	-0.1	17420.0
986.	C7H15-2+O2=C7H14-2+HO2	3.00E-09	0.0	3000.0
	Reverse Arrhenius coefficients:	3.79E-09	0.1	18270.0
987.	C7H15-3+O2=C7H14-2+HO2	3.00E-09	0.0	3000.0
	Reverse Arrhenius coefficients:	3.79E-09	0.1	18270.0
988.	C7H15-3+O2=C7H14-3+HO2	3.00E-09	0.0	3000.0
	Reverse Arrhenius coefficients:	5.09E-09	0.0	18180.0
989.	C7H15-4+O2=C7H14-3+HO2	6.00E-09	0.0	3000.0
	Reverse Arrhenius coefficients:	5.11E-09	0.0	18180.0
990.	C7H15-1=C7H15-3	1.39E+09	1.0	33760.0
	Reverse Arrhenius coefficients:	4.41E+07	1.4	36280.0
991.	C7H15-1=C7H15-4	2.54E+09	0.3	19760.0
	Reverse Arrhenius coefficients:	1.61E+08	0.7	22280.0
992.	C7H15-2=C7H15-3	9.59E+08	1.4	39700.0
	Reverse Arrhenius coefficients:	9.59E+08	1.4	39700.0
993.	C7H15-1=C7H15-2	5.48E+08	1.6	38760.0
	Reverse Arrhenius coefficients:	1.74E+07	2.0	41280.0
994.	C7H14-1+OH=C7H13+H2O	3.00E+13	0.0	1230.0
	Reverse Arrhenius coefficients:	7.92E+14	-0.5	36480.0
995.	C7H14-2+OH=C7H13+H2O	3.00E+13	0.0	1230.0
	Reverse Arrhenius coefficients:	1.60E+15	-0.6	33600.0
996.	C7H14-3+OH=C7H13+H2O	3.00E+13	0.0	1230.0
	Reverse Arrhenius coefficients:	1.19E+15	-0.6	33700.0
997.	C7H14-1+H=C7H13+H2	3.70E+13	0.0	3900.0
	Reverse Arrhenius coefficients:	2.26E+14	-0.5	23990.0

```
 998. C7H14-2+H=C7H13+H2                          3.70E+13    0.0     3900.0
      Reverse Arrhenius coefficients:             4.57E+14   -0.6    21120.0
 999. C7H14-3+H=C7H13+H2                          3.70E+13    0.0     3900.0
      Reverse Arrhenius coefficients:             3.40E+14   -0.6    21210.0
1000. C7H14-1+CH3=C7H13+CH4                       1.00E+12    0.0     7300.0
      Reverse Arrhenius coefficients:             1.59E+14   -0.5    27870.0
1001. C7H14-2+CH3=C7H13+CH4                       1.00E+12    0.0     7300.0
      Reverse Arrhenius coefficients:             3.23E+14   -0.6    25000.0
1002. C7H14-3+CH3=C7H13+CH4                       1.00E+12    0.0     7300.0
      Reverse Arrhenius coefficients:             2.40E+14   -0.6    25090.0
1003. C7H14-1+O=C7H13+OH                          2.62E+11    0.5    11900.0
      Reverse Arrhenius coefficients:             7.00E+11    0.0    29900.0
1004. C7H14-2+O=C7H13+OH                          1.29E+11    0.6    14780.0
      Reverse Arrhenius coefficients:             7.00E+11    0.0    29900.0
1005. C7H14-3+O=C7H13+OH                          1.73E+11    0.6    14680.0
      Reverse Arrhenius coefficients:             7.00E+11    0.0    29900.0
1006. C7H14-1+OH=CH2O+C6H13-1                     1.00E+11    0.0    -4000.0
      All REV parameters are zero...              0.000E+00   0.00   0.000E+00
      This reaction is treated as irreversible
1007. C7H14-1+OH=CH3CHO+C5H11-1                   1.00E+11    0.0    -4000.0
      All REV parameters are zero...              0.000E+00   0.00   0.000E+00
      This reaction is treated as irreversible
1008. C7H14-2+OH=CH3CHO+C5H11-1                   1.00E+11    0.0    -4000.0
      All REV parameters are zero...              0.000E+00   0.00   0.000E+00
      This reaction is treated as irreversible
1009. C7H14-2+OH=C2H5CHO+PC4H9                    1.00E+11    0.0    -4000.0
      All REV parameters are zero...              0.000E+00   0.00   0.000E+00
      This reaction is treated as irreversible
1010. C7H14-3+OH=C2H5CHO+PC4H9                    1.00E+11    0.0    -4000.0
      All REV parameters are zero...              0.000E+00   0.00   0.000E+00
      This reaction is treated as irreversible
1011. C7H14-1+O=CH2CHO+C5H11-1                    1.00E+11    0.0    -1050.0
      All REV parameters are zero...              0.000E+00   0.00   0.000E+00
      This reaction is treated as irreversible
1012. C7H14-2+O=CH3CHO+C5H10-1                    1.00E+11    0.0    -1050.0
      All REV parameters are zero...              0.000E+00   0.00   0.000E+00
      This reaction is treated as irreversible
1013. C7H14-3+O=CH3CHO+C5H10-1                    1.00E+11    0.0    -1050.0
      All REV parameters are zero...              0.000E+00   0.00   0.000E+00
      This reaction is treated as irreversible
1014. C7H13=C3H5-A+C4H8-1                         2.50E+13    0.0    45000.0
      Reverse Arrhenius coefficients:             1.00E+13    0.0     9600.0
1015. C7H13=C4H7+C3H6                             2.50E+13    0.0    45000.0
      Reverse Arrhenius coefficients:             1.00E+13    0.0     9600.0
1016. C7H14-1=PC4H9+C3H5-A                        1.00E+16    0.0    71000.0
      Reverse Arrhenius coefficients:             1.00E+13    0.0        0.0
1017. C7H14-2=C4H7+NC3H7                          1.00E+16    0.0    71000.0
      Reverse Arrhenius coefficients:             1.00E+13    0.0        0.0
1018. C7H14-3=C4H7+NC3H7                          1.00E+16    0.0    71000.0
      Reverse Arrhenius coefficients:             1.00E+13    0.0        0.0
1019. C7H15O2-1=C7H15-1+O2                        2.66E+20   -1.7    35400.0
      Reverse Arrhenius coefficients:             4.52E+12    0.0        0.0
1020. C7H15O2-2=C7H15-2+O2                        1.36E+23   -2.4    37670.0
      Reverse Arrhenius coefficients:             7.54E+12    0.0        0.0
1021. C7H15O2-3=C7H15-3+O2                        9.88E+21   -2.0    37860.0
      Reverse Arrhenius coefficients:             7.54E+12    0.0        0.0
1022. C7H15O2-4=C7H15-4+O2                        1.36E+23   -2.4    37670.0
      Reverse Arrhenius coefficients:             7.54E+12    0.0        0.0
1023. C7H15-1+C7H15O2-1=C7H15O-1+C7H15O-1         7.00E+12    0.0    -1000.0
      Reverse Arrhenius coefficients:             5.56E+13   -0.2    30260.0
1024. C7H15-1+C7H15O2-2=C7H15O-1+C7H15O-2         7.00E+12    0.0    -1000.0
```

	Reverse Arrhenius coefficients:	3.16E+13	-0.1	29890.0
1025.	C7H15-1+C7H15O2-3=C7H15O-1+C7H15O-3	7.00E+12	0.0	-1000.0
	Reverse Arrhenius coefficients:	4.35E+14	-0.5	29700.0
1026.	C7H15-1+C7H15O2-4=C7H15O-1+C7H15O-4	7.00E+12	0.0	-1000.0
	Reverse Arrhenius coefficients:	3.16E+13	-0.1	29890.0
1027.	C7H15-2+C7H15O2-1=C7H15O-2+C7H15O-1	7.00E+12	0.0	-1000.0
	Reverse Arrhenius coefficients:	9.69E+15	-0.8	32160.0
1028.	C7H15-2+C7H15O2-2=C7H15O-2+C7H15O-2	7.00E+12	0.0	-1000.0
	Reverse Arrhenius coefficients:	5.51E+15	-0.7	31790.0
1029.	C7H15-2+C7H15O2-3=C7H15O-2+C7H15O-3	7.00E+12	0.0	-1000.0
	Reverse Arrhenius coefficients:	7.57E+16	-1.1	31600.0
1030.	C7H15-2+C7H15O2-4=C7H15O-2+C7H15O-4	7.00E+12	0.0	-1000.0
	Reverse Arrhenius coefficients:	5.51E+15	-0.7	31790.0
1031.	C7H15-3+C7H15O2-1=C7H15O-3+C7H15O-1	7.00E+12	0.0	-1000.0
	Reverse Arrhenius coefficients:	9.69E+15	-0.8	32160.0
1032.	C7H15-3+C7H15O2-2=C7H15O-3+C7H15O-2	7.00E+12	0.0	-1000.0
	Reverse Arrhenius coefficients:	5.51E+15	-0.7	31790.0
1033.	C7H15-3+C7H15O2-3=C7H15O-3+C7H15O-3	7.00E+12	0.0	-1000.0
	Reverse Arrhenius coefficients:	7.57E+16	-1.1	31600.0
1034.	C7H15-3+C7H15O2-4=C7H15O-3+C7H15O-4	7.00E+12	0.0	-1000.0
	Reverse Arrhenius coefficients:	5.51E+15	-0.7	31790.0
1035.	C7H15-4+C7H15O2-1=C7H15O-4+C7H15O-1	7.00E+12	0.0	-1000.0
	Reverse Arrhenius coefficients:	9.69E+15	-0.8	32160.0
1036.	C7H15-4+C7H15O2-2=C7H15O-4+C7H15O-2	7.00E+12	0.0	-1000.0
	Reverse Arrhenius coefficients:	5.51E+15	-0.7	31790.0
1037.	C7H15-4+C7H15O2-3=C7H15O-4+C7H15O-3	7.00E+12	0.0	-1000.0
	Reverse Arrhenius coefficients:	7.57E+16	-1.1	31600.0
1038.	C7H15-4+C7H15O2-4=C7H15O-4+C7H15O-4	7.00E+12	0.0	-1000.0
	Reverse Arrhenius coefficients:	5.51E+15	-0.7	31790.0
1039.	C7H15O2-1=C7H14OOH1-2	2.00E+11	0.0	26850.0
	Reverse Arrhenius coefficients:	2.12E+10	-0.1	14240.0
1040.	C7H15O2-1=C7H14OOH1-3	2.50E+10	0.0	20850.0
	Reverse Arrhenius coefficients:	2.65E+09	-0.1	8240.0
1041.	C7H15O2-1=C7H14OOH1-4	3.12E+09	0.0	19050.0
	Reverse Arrhenius coefficients:	3.32E+08	-0.1	6440.0
1042.	C7H15O2-2=C7H14OOH2-1	3.00E+11	0.0	29400.0
	Reverse Arrhenius coefficients:	8.06E+11	-0.5	14360.0
1043.	C7H15O2-2=C7H14OOH2-3	2.00E+11	0.0	26850.0
	Reverse Arrhenius coefficients:	2.26E+10	-0.1	14270.0
1044.	C7H15O2-2=C7H14OOH2-4	2.50E+10	0.0	20850.0
	Reverse Arrhenius coefficients:	2.83E+09	-0.1	8270.0
1045.	C7H15O2-2=C7H14OOH2-5	3.12E+09	0.0	19050.0
	Reverse Arrhenius coefficients:	3.53E+08	-0.1	6470.0
1046.	C7H15O2-3=C7H14OOH3-1	3.75E+10	0.0	24400.0
	Reverse Arrhenius coefficients:	1.38E+12	-0.9	9170.0
1047.	C7H15O2-3=C7H14OOH3-2	2.00E+11	0.0	26850.0
	Reverse Arrhenius coefficients:	3.11E+11	-0.5	14080.0
1048.	C7H15O2-3=C7H14OOH3-4	2.00E+11	0.0	26850.0
	Reverse Arrhenius coefficients:	3.11E+11	-0.5	14080.0
1049.	C7H15O2-3=C7H14OOH3-5	2.50E+10	0.0	20850.0
	Reverse Arrhenius coefficients:	3.88E+10	-0.5	8080.0
1050.	C7H15O2-3=C7H14OOH3-6	3.12E+09	0.0	19050.0
	Reverse Arrhenius coefficients:	4.86E+09	-0.5	6280.0
1051.	C7H15O2-4=C7H14OOH4-1	9.38E+09	0.0	22350.0
	Reverse Arrhenius coefficients:	2.52E+10	-0.5	7310.0
1052.	C7H15O2-4=C7H14OOH4-2	5.00E+10	0.0	20850.0
	Reverse Arrhenius coefficients:	5.66E+09	-0.1	8270.0
1053.	C7H15O2-4=C7H14OOH4-3	4.00E+11	0.0	26850.0
	Reverse Arrhenius coefficients:	4.52E+10	-0.1	14270.0
1054.	C7H15O2-1+HO2=C7H15O2H-1+O2	1.75E+10	0.0	-3275.0
	Reverse Arrhenius coefficients:	5.02E+13	-0.8	34870.0

1055.	C7H15O2-2+HO2=C7H15O2H-2+O2	1.75E+10	0.0	-3275.0
	Reverse Arrhenius coefficients:	5.97E+13	-0.8	34900.0
1056.	C7H15O2-3+HO2=C7H15O2H-3+O2	1.75E+10	0.0	-3275.0
	Reverse Arrhenius coefficients:	4.93E+13	-0.8	34880.0
1057.	C7H15O2-4+HO2=C7H15O2H-4+O2	1.75E+10	0.0	-3275.0
	Reverse Arrhenius coefficients:	5.98E+13	-0.8	34900.0
1058.	H2O2+C7H15O2-1=HO2+C7H15O2H-1	2.40E+12	0.0	10000.0
	Reverse Arrhenius coefficients:	2.40E+12	0.0	10000.0
1059.	H2O2+C7H15O2-2=HO2+C7H15O2H-2	2.40E+12	0.0	10000.0
	Reverse Arrhenius coefficients:	2.40E+12	0.0	10000.0
1060.	H2O2+C7H15O2-3=HO2+C7H15O2H-3	2.40E+12	0.0	10000.0
	Reverse Arrhenius coefficients:	2.40E+12	0.0	10000.0
1061.	H2O2+C7H15O2-4=HO2+C7H15O2H-4	2.40E+12	0.0	10000.0
	Reverse Arrhenius coefficients:	2.40E+12	0.0	10000.0
1062.	C7H15O2-1+CH3O2=C7H15O-1+CH3O+O2	1.40E+16	-1.6	1860.0
	All REV parameters are zero...	0.000E+00	0.00	0.000E+00
	This reaction is treated as irreversible			
1063.	C7H15O2-2+CH3O2=C7H15O-2+CH3O+O2	1.40E+16	-1.6	1860.0
	All REV parameters are zero...	0.000E+00	0.00	0.000E+00
	This reaction is treated as irreversible			
1064.	C7H15O2-3+CH3O2=C7H15O-3+CH3O+O2	1.40E+16	-1.6	1860.0
	All REV parameters are zero...	0.000E+00	0.00	0.000E+00
	This reaction is treated as irreversible			
1065.	C7H15O2-4+CH3O2=C7H15O-4+CH3O+O2	1.40E+16	-1.6	1860.0
	All REV parameters are zero...	0.000E+00	0.00	0.000E+00
	This reaction is treated as irreversible			
1066.	C7H15O2-1+C7H15O2-1=O2+C7H15O-1+C7H15O-1	1.40E+16	-1.6	1860.0
	All REV parameters are zero...	0.000E+00	0.00	0.000E+00
	This reaction is treated as irreversible			
1067.	C7H15O2-1+C7H15O2-2=C7H15O-1+C7H15O-2+O2	1.40E+16	-1.6	1860.0
	All REV parameters are zero...	0.000E+00	0.00	0.000E+00
	This reaction is treated as irreversible			
1068.	C7H15O2-1+C7H15O2-3=C7H15O-1+C7H15O-3+O2	1.40E+16	-1.6	1860.0
	All REV parameters are zero...	0.000E+00	0.00	0.000E+00
	This reaction is treated as irreversible			
1069.	C7H15O2-1+C7H15O2-4=C7H15O-1+C7H15O-4+O2	1.40E+16	-1.6	1860.0
	All REV parameters are zero...	0.000E+00	0.00	0.000E+00
	This reaction is treated as irreversible			
1070.	C7H15O2-2+C7H15O2-2=O2+C7H15O-2+C7H15O-2	1.40E+16	-1.6	1860.0
	All REV parameters are zero...	0.000E+00	0.00	0.000E+00
	This reaction is treated as irreversible			
1071.	C7H15O2-2+C7H15O2-3=C7H15O-2+C7H15O-3+O2	1.40E+16	-1.6	1860.0
	All REV parameters are zero...	0.000E+00	0.00	0.000E+00
	This reaction is treated as irreversible			
1072.	C7H15O2-2+C7H15O2-4=C7H15O-2+C7H15O-4+O2	1.40E+16	-1.6	1860.0
	All REV parameters are zero...	0.000E+00	0.00	0.000E+00
	This reaction is treated as irreversible			
1073.	C7H15O2-3+C7H15O2-3=O2+C7H15O-3+C7H15O-3	1.40E+16	-1.6	1860.0
	All REV parameters are zero...	0.000E+00	0.00	0.000E+00
	This reaction is treated as irreversible			
1074.	C7H15O2-3+C7H15O2-4=C7H15O-3+C7H15O-4+O2	1.40E+16	-1.6	1860.0
	All REV parameters are zero...	0.000E+00	0.00	0.000E+00
	This reaction is treated as irreversible			
1075.	C7H15O2-4+C7H15O2-4=O2+C7H15O-4+C7H15O-4	1.40E+16	-1.6	1860.0
	All REV parameters are zero...	0.000E+00	0.00	0.000E+00
	This reaction is treated as irreversible			
1076.	C7H15O2H-1=C7H15O-1+OH	1.50E+16	0.0	42500.0
	Reverse Arrhenius coefficients:	1.43E+08	1.7	-3055.0
1077.	C7H15O2H-2=C7H15O-2+OH	1.25E+16	0.0	41600.0
	Reverse Arrhenius coefficients:	5.72E+07	1.8	-4355.0
1078.	C7H15O2H-3=C7H15O-3+OH	1.25E+16	0.0	41600.0

	Reverse Arrhenius coefficients:	9.51E+08	1.4	-4525.0
1079.	C7H15O2H-4=C7H15O-4+OH	1.25E+16	0.0	41600.0
	Reverse Arrhenius coefficients:	5.72E+07	1.8	-4355.0
1080.	C7H15O-1=CH2O+C6H13-1	4.68E+17	-1.3	20260.0
	Reverse Arrhenius coefficients:	1.00E+11	0.0	11900.0
1081.	C7H15O-2=CH3CHO+C5H11-1	8.66E+21	-2.4	21880.0
	Reverse Arrhenius coefficients:	1.00E+11	0.0	12900.0
1082.	C7H15O-3=C2H5CHO+PC4H9	5.60E+21	-2.3	21360.0
	Reverse Arrhenius coefficients:	1.00E+11	0.0	12900.0
1083.	C7H15O-4=NC3H7CHO+NC3H7	6.68E+21	-2.3	21620.0
	Reverse Arrhenius coefficients:	1.00E+11	0.0	12900.0
1084.	C7H14OOH1-2=C7H14-1+HO2	7.66E+18	-2.0	18400.0
	Reverse Arrhenius coefficients:	1.00E+11	0.0	10530.0
1085.	C7H14OOH2-1=C7H14-1+HO2	1.89E+21	-2.8	20760.0
	Reverse Arrhenius coefficients:	1.00E+11	0.0	10530.0
1086.	C7H14OOH2-3=C7H14-2+HO2	1.61E+20	-2.5	21350.0
	Reverse Arrhenius coefficients:	1.00E+11	0.0	11530.0
1087.	C7H14OOH3-2=C7H14-2+HO2	1.61E+20	-2.5	21350.0
	Reverse Arrhenius coefficients:	1.00E+11	0.0	11530.0
1088.	C7H14OOH3-4=C7H14-3+HO2	1.20E+20	-2.5	20440.0
	Reverse Arrhenius coefficients:	1.00E+11	0.0	10530.0
1089.	C7H14OOH4-3=C7H14-3+HO2	2.39E+20	-2.5	20440.0
	Reverse Arrhenius coefficients:	1.00E+11	0.0	10530.0
1090.	C7H14OOH1-3=C7H14O1-3+OH	7.50E+10	0.0	15250.0
	All REV parameters are zero...	0.000E+00	0.00	0.000E+00
	This reaction is treated as irreversible			
1091.	C7H14OOH1-4=C7H14O1-4+OH	9.38E+09	0.0	7000.0
	All REV parameters are zero...	0.000E+00	0.00	0.000E+00
	This reaction is treated as irreversible			
1092.	C7H14OOH2-4=C7H14O2-4+OH	7.50E+10	0.0	15250.0
	All REV parameters are zero...	0.000E+00	0.00	0.000E+00
	This reaction is treated as irreversible			
1093.	C7H14OOH2-5=C7H14O2-5+OH	9.38E+09	0.0	7000.0
	All REV parameters are zero...	0.000E+00	0.00	0.000E+00
	This reaction is treated as irreversible			
1094.	C7H14OOH3-1=C7H14O1-3+OH	7.50E+10	0.0	15250.0
	All REV parameters are zero...	0.000E+00	0.00	0.000E+00
	This reaction is treated as irreversible			
1095.	C7H14OOH3-5=C7H14O3-5+OH	7.50E+10	0.0	15250.0
	All REV parameters are zero...	0.000E+00	0.00	0.000E+00
	This reaction is treated as irreversible			
1096.	C7H14OOH3-6=C7H14O2-5+OH	9.38E+09	0.0	7000.0
	All REV parameters are zero...	0.000E+00	0.00	0.000E+00
	This reaction is treated as irreversible			
1097.	C7H14OOH4-1=C7H14O1-4+OH	9.38E+09	0.0	7000.0
	All REV parameters are zero...	0.000E+00	0.00	0.000E+00
	This reaction is treated as irreversible			
1098.	C7H14OOH4-2=C7H14O2-4+OH	7.50E+10	0.0	15250.0
	All REV parameters are zero...	0.000E+00	0.00	0.000E+00
	This reaction is treated as irreversible			
1099.	C7H14OOH1-3=OH+CH2O+C6H12-1	8.12E+13	-0.1	31090.0
	All REV parameters are zero...	0.000E+00	0.00	0.000E+00
	This reaction is treated as irreversible			
1100.	C7H14OOH2-4=OH+CH3CHO+C5H10-1	5.36E+17	-1.4	26750.0
	All REV parameters are zero...	0.000E+00	0.00	0.000E+00
	This reaction is treated as irreversible			
1101.	C7H14OOH3-1=OH+NC4H9CHO+C2H4	2.21E+19	-1.7	26980.0
	All REV parameters are zero...	0.000E+00	0.00	0.000E+00
	This reaction is treated as irreversible			
1102.	C7H14OOH3-5=OH+C2H5CHO+C4H8-1	2.47E+18	-1.6	27020.0
	All REV parameters are zero...	0.000E+00	0.00	0.000E+00

```
      This reaction is treated as irreversible
1103. C7H14OOH4-2=OH+NC3H7CHO+C3H6                1.30E+18   -1.5    26800.0
      All REV parameters are zero...              0.000E+00  0.00  0.000E+00
      This reaction is treated as irreversible
1104. C7H14OOH1-2O2=C7H14OOH1-2+O2                1.37E+23   -2.4    37640.0
      Reverse Arrhenius coefficients:             7.54E+12    0.0       0.0
1105. C7H14OOH1-3O2=C7H14OOH1-3+O2                1.37E+23   -2.4    37640.0
      Reverse Arrhenius coefficients:             7.54E+12    0.0       0.0
1106. C7H14OOH1-4O2=C7H14OOH1-4+O2                1.37E+23   -2.4    37640.0
      Reverse Arrhenius coefficients:             7.54E+12    0.0       0.0
1107. C7H14OOH2-1O2=C7H14OOH2-1+O2                3.32E+20   -1.6    35280.0
      Reverse Arrhenius coefficients:             4.52E+12    0.0       0.0
1108. C7H14OOH2-3O2=C7H14OOH2-3+O2                1.39E+23   -2.4    37600.0
      Reverse Arrhenius coefficients:             7.54E+12    0.0       0.0
1109. C7H14OOH2-4O2=C7H14OOH2-4+O2                1.39E+23   -2.4    37600.0
      Reverse Arrhenius coefficients:             7.54E+12    0.0       0.0
1110. C7H14OOH2-5O2=C7H14OOH2-5+O2                1.39E+23   -2.4    37600.0
      Reverse Arrhenius coefficients:             7.54E+12    0.0       0.0
1111. C7H14OOH3-1O2=C7H14OOH3-1+O2                3.32E+20   -1.6    35280.0
      Reverse Arrhenius coefficients:             4.52E+12    0.0       0.0
1112. C7H14OOH3-2O2=C7H14OOH3-2+O2                1.39E+23   -2.4    37600.0
      Reverse Arrhenius coefficients:             7.54E+12    0.0       0.0
1113. C7H14OOH3-4O2=C7H14OOH3-4+O2                1.39E+23   -2.4    37600.0
      Reverse Arrhenius coefficients:             7.54E+12    0.0       0.0
1114. C7H14OOH3-5O2=C7H14OOH3-5+O2                1.39E+23   -2.4    37600.0
      Reverse Arrhenius coefficients:             7.54E+12    0.0       0.0
1115. C7H14OOH3-6O2=C7H14OOH3-6+O2                1.39E+23   -2.4    37600.0
      Reverse Arrhenius coefficients:             7.54E+12    0.0       0.0
1116. C7H14OOH4-1O2=C7H14OOH4-1+O2                1.67E+20   -1.6    35280.0
      Reverse Arrhenius coefficients:             4.52E+12    0.0       0.0
1117. C7H14OOH4-2O2=C7H14OOH4-2+O2                6.97E+22   -2.4    37600.0
      Reverse Arrhenius coefficients:             7.54E+12    0.0       0.0
1118. C7H14OOH4-3O2=C7H14OOH4-3+O2                6.97E+22   -2.4    37600.0
      Reverse Arrhenius coefficients:             7.54E+12    0.0       0.0
1119. C7H14OOH1-3O2=NC7KET13+OH                   2.50E+10    0.0    21400.0
      Reverse Arrhenius coefficients:             3.30E+03    1.4    45040.0
1120. C7H14OOH1-4O2=NC7KET14+OH                   3.12E+09    0.0    19350.0
      Reverse Arrhenius coefficients:             4.13E+02    1.4    42990.0
1121. C7H14OOH2-3O2=NC7KET23+OH                   1.00E+11    0.0    23850.0
      Reverse Arrhenius coefficients:             8.64E+03    1.6    47000.0
1122. C7H14OOH2-4O2=NC7KET24+OH                   1.25E+10    0.0    17850.0
      Reverse Arrhenius coefficients:             1.62E+02    1.8    44200.0
1123. C7H14OOH2-5O2=NC7KET25+OH                   1.56E+09    0.0    16050.0
      Reverse Arrhenius coefficients:             2.02E+01    1.8    42400.0
1124. C7H14OOH3-2O2=NC7KET32+OH                   1.00E+11    0.0    23850.0
      Reverse Arrhenius coefficients:             5.86E+03    1.6    47260.0
1125. C7H14OOH3-4O2=NC7KET34+OH                   1.00E+11    0.0    23850.0
      Reverse Arrhenius coefficients:             5.86E+03    1.6    47260.0
1126. C7H14OOH3-5O2=NC7KET35+OH                   1.25E+10    0.0    17850.0
      Reverse Arrhenius coefficients:             1.62E+02    1.8    44200.0
1127. C7H14OOH3-6O2=NC7KET36+OH                   1.56E+09    0.0    16050.0
      Reverse Arrhenius coefficients:             2.02E+01    1.8    42400.0
1128. C7H14OOH4-1O2=NC7KET41+OH                   1.56E+09    0.0    16050.0
      Reverse Arrhenius coefficients:             2.55E+01    1.8    42720.0
1129. C7H14OOH4-2O2=NC7KET42+OH                   1.25E+10    0.0    17850.0
      Reverse Arrhenius coefficients:             1.62E+02    1.8    44200.0
1130. C7H14OOH4-3O2=NC7KET43+OH                   1.00E+11    0.0    23850.0
      Reverse Arrhenius coefficients:             5.86E+03    1.6    47260.0
1131. NC7KET13=NC4H9CHO+CH2CHO+OH                 1.05E+16    0.0    41600.0
      All REV parameters are zero...              0.000E+00  0.00  0.000E+00
      This reaction is treated as irreversible
```

```
1132. NC7KET14=NC3H7CHO+CH2CH2CHO+OH                1.05E+16    0.0    41600.0
      All REV parameters are zero...                0.000E+00  0.00  0.000E+00
      This reaction is treated as irreversible
1133. NC7KET23=NC4H9CHO+CH3CO+OH                    1.05E+16    0.0    41600.0
      All REV parameters are zero...                0.000E+00  0.00  0.000E+00
      This reaction is treated as irreversible
1134. NC7KET24=NC3H7CHO+CH3COCH2+OH                 1.05E+16    0.0    41600.0
      All REV parameters are zero...                0.000E+00  0.00  0.000E+00
      This reaction is treated as irreversible
1135. NC7KET25=C2H5CHO+CH2CH2COCH3+OH               1.05E+16    0.0    41600.0
      All REV parameters are zero...                0.000E+00  0.00  0.000E+00
      This reaction is treated as irreversible
1136. NC7KET32=CH3CHO+NC4H9CO+OH                    1.05E+16    0.0    41600.0
      All REV parameters are zero...                0.000E+00  0.00  0.000E+00
      This reaction is treated as irreversible
1137. NC7KET34=NC3H7CHO+C2H5CO+OH                   1.05E+16    0.0    41600.0
      All REV parameters are zero...                0.000E+00  0.00  0.000E+00
      This reaction is treated as irreversible
1138. NC7KET35=C2H5CHO+C2H5COCH2+OH                 1.05E+16    0.0    41600.0
      All REV parameters are zero...                0.000E+00  0.00  0.000E+00
      This reaction is treated as irreversible
1139. NC7KET36=CH3CHO+C2H5COC2H4P+OH                1.05E+16    0.0    41600.0
      All REV parameters are zero...                0.000E+00  0.00  0.000E+00
      This reaction is treated as irreversible
1140. NC7KET41=CH2O+NC3H7COC2H4P+OH                 1.50E+16    0.0    42000.0
      All REV parameters are zero...                0.000E+00  0.00  0.000E+00
      This reaction is treated as irreversible
1141. NC7KET42=CH3CHO+NC3H7COCH2+OH                 1.05E+16    0.0    41600.0
      All REV parameters are zero...                0.000E+00  0.00  0.000E+00
      This reaction is treated as irreversible
1142. NC7KET43=C2H5CHO+NC3H7CO+OH                   1.05E+16    0.0    41600.0
      All REV parameters are zero...                0.000E+00  0.00  0.000E+00
      This reaction is treated as irreversible
1143. C7H14O1-3+OH=C6H12-1+HCO+H2O                  2.50E+12    0.0        0.0
      All REV parameters are zero...                0.000E+00  0.00  0.000E+00
      This reaction is treated as irreversible
1144. C7H14O1-4+OH=C5H10-1+CH2CHO+H2O               2.50E+12    0.0        0.0
      All REV parameters are zero...                0.000E+00  0.00  0.000E+00
      This reaction is treated as irreversible
1145. C7H14O2-4+OH=CH3CO+C5H10-1+H2O                2.50E+12    0.0        0.0
      All REV parameters are zero...                0.000E+00  0.00  0.000E+00
      This reaction is treated as irreversible
1146. C7H14O2-5+OH=CH3COCH2+C4H8-1+H2O              2.50E+12    0.0        0.0
      All REV parameters are zero...                0.000E+00  0.00  0.000E+00
      This reaction is treated as irreversible
1147. C7H14O3-5+OH=C2H5CO+C4H8-1+H2O                2.50E+12    0.0        0.0
      All REV parameters are zero...                0.000E+00  0.00  0.000E+00
      This reaction is treated as irreversible
1148. C7H14O1-3+OH=C2H4+NC4H9CO+H2O                 2.50E+12    0.0        0.0
      All REV parameters are zero...                0.000E+00  0.00  0.000E+00
      This reaction is treated as irreversible
1149. C7H14O1-4+OH=C2H4+NC3H7COCH2+H2O              2.50E+12    0.0        0.0
      All REV parameters are zero...                0.000E+00  0.00  0.000E+00
      This reaction is treated as irreversible
1150. C7H14O2-4+OH=C3H6+NC3H7CO+H2O                 2.50E+12    0.0        0.0
      All REV parameters are zero...                0.000E+00  0.00  0.000E+00
      This reaction is treated as irreversible
1151. C7H14O2-5+OH=C3H6+C2H5COCH2+H2O               2.50E+12    0.0        0.0
      All REV parameters are zero...                0.000E+00  0.00  0.000E+00
      This reaction is treated as irreversible
1152. C7H14O3-5+OH=C2H5CHO+C4H7+H2O                 2.50E+12    0.0        0.0
```

```
      All REV parameters are zero...                0.000E+00  0.00  0.000E+00
      This reaction is treated as irreversible
1153. C7H14O1-3+HO2=C6H12-1+HCO+H2O2                5.00E+12    0.0    17700.0
      All REV parameters are zero...                0.000E+00  0.00  0.000E+00
      This reaction is treated as irreversible
1154. C7H14O1-4+HO2=C5H10-1+CH2CHO+H2O2             5.00E+12    0.0    17700.0
      All REV parameters are zero...                0.000E+00  0.00  0.000E+00
      This reaction is treated as irreversible
1155. C7H14O2-4+HO2=CH3CO+C5H10-1+H2O2              5.00E+12    0.0    17700.0
      All REV parameters are zero...                0.000E+00  0.00  0.000E+00
      This reaction is treated as irreversible
1156. C7H14O2-5+HO2=CH3COCH2+C4H8-1+H2O2            5.00E+12    0.0    17700.0
      All REV parameters are zero...                0.000E+00  0.00  0.000E+00
      This reaction is treated as irreversible
1157. C7H14O3-5+HO2=C2H5CO+C4H8-1+H2O2              5.00E+12    0.0    17700.0
      All REV parameters are zero...                0.000E+00  0.00  0.000E+00
      This reaction is treated as irreversible
1158. C7H14O1-3+HO2=C2H4+NC4H9CO+H2O2               5.00E+12    0.0    17700.0
      All REV parameters are zero...                0.000E+00  0.00  0.000E+00
      This reaction is treated as irreversible
1159. C7H14O1-4+HO2=C2H4+NC3H7COCH2+H2O2            5.00E+12    0.0    17700.0
      All REV parameters are zero...                0.000E+00  0.00  0.000E+00
      This reaction is treated as irreversible
1160. C7H14O2-4+HO2=C3H6+NC3H7CO+H2O2               5.00E+12    0.0    17700.0
      All REV parameters are zero...                0.000E+00  0.00  0.000E+00
      This reaction is treated as irreversible
1161. C7H14O2-5+HO2=C3H6+C2H5COCH2+H2O2             5.00E+12    0.0    17700.0
      All REV parameters are zero...                0.000E+00  0.00  0.000E+00
      This reaction is treated as irreversible
1162. C7H14O3-5+HO2=C2H5CHO+C4H7+H2O2               5.00E+12    0.0    17700.0
      All REV parameters are zero...                0.000E+00  0.00  0.000E+00
      This reaction is treated as irreversible
1163. C4H7CO1-4=C4H7+CO                             2.79E+09    0.5     -160.0
      Reverse Arrhenius coefficients:               1.50E+11    0.0     4810.0
1164. C7H14OOH1-4=C5H10-1+C2H4+HO2                  2.44E+16   -1.1    29450.0
      All REV parameters are zero...                0.000E+00  0.00  0.000E+00
      This reaction is treated as irreversible
1165. C7H14OOH2-4=C5H9OOH1-4+C2H5                   1.67E+18   -1.8    27670.0
      Reverse Arrhenius coefficients:               9.25E+10    0.0     7800.0
1166. C7H14OOH2-5=C4H8-1+C3H6OOH2-1                 2.13E+16   -1.0    28800.0
      Reverse Arrhenius coefficients:               8.50E+10    0.0     7800.0
1167. C7H14OOH3-5=C6H11OOH1-4+CH3                   5.28E+12    0.2    30280.0
      Reverse Arrhenius coefficients:               1.00E+11    0.0     7800.0
1168. C7H15-1+HO2=C7H15O-1+OH                       7.00E+12    0.0    -1000.0
      Reverse Arrhenius coefficients:               1.13E+16   -0.8    26980.0
1169. C7H15-2+HO2=C7H15O-2+OH                       7.00E+12    0.0    -1000.0
      Reverse Arrhenius coefficients:               1.97E+18   -1.4    28890.0
1170. C7H15-3+HO2=C7H15O-3+OH                       7.00E+12    0.0    -1000.0
      Reverse Arrhenius coefficients:               1.97E+18   -1.4    28890.0
1171. C7H15-4+HO2=C7H15O-4+OH                       7.00E+12    0.0    -1000.0
      Reverse Arrhenius coefficients:               1.97E+18   -1.4    28890.0
1172. C7H15-1+CH3O2=C7H15O-1+CH3O                   7.00E+12    0.0    -1000.0
      Reverse Arrhenius coefficients:               1.10E+18   -1.3    31750.0
1173. C7H15-2+CH3O2=C7H15O-2+CH3O                   7.00E+12    0.0    -1000.0
      Reverse Arrhenius coefficients:               1.92E+20   -1.9    33660.0
1174. C7H15-3+CH3O2=C7H15O-3+CH3O                   7.00E+12    0.0    -1000.0
      Reverse Arrhenius coefficients:               1.92E+20   -1.9    33660.0
1175. C7H15-4+CH3O2=C7H15O-4+CH3O                   7.00E+12    0.0    -1000.0
      Reverse Arrhenius coefficients:               1.92E+20   -1.9    33660.0
1176. C5H9OOH1-4=C5H9O1-4+OH                        1.18E+20   -1.4    46050.0
      Reverse Arrhenius coefficients:               2.00E+13    0.0        0.0
```

```
1177. C6H11OOH1-4=C6H11O1-4+OH                          1.23E+20   -1.4    46050.0
      Reverse Arrhenius coefficients:                   2.00E+13    0.0        0.0
1178. C5H9O1-4=CH3CHO+C3H5-A                            7.72E+20   -2.4     5890.0
      Reverse Arrhenius coefficients:                   5.00E+10    0.0     9600.0
1179. C6H11O1-4=C2H5CHO+C3H5-A                          1.21E+21   -2.5     5641.0
      Reverse Arrhenius coefficients:                   5.00E+10    0.0     9600.0
1180. H+HO2=O+H2O                                       3.01E+13    0.0     1721.0
1181. CH3O+H=CH3+OH                                     1.00E+13    0.0        0.0
1182. CH2OH+H=CH3+OH                                    1.00E+13    0.0        0.0
1183. CH3+M=CH+H2+M                                     6.90E+14    0.0    82469.0
1184. CH3OH(+M)=CH2(S)+H2O(+M)                          2.84E+10    1.0    83871.0
      Low pressure limit:  0.17800E+50 -0.88100E+01  0.93369E+05
      TROE centering:      0.90000E+00  0.74000E+03  0.98000E+03  0.51000E+04
      H2O              Enhanced by    1.000E+01
      H2               Enhanced by    2.000E+00
      CO2              Enhanced by    3.000E+00
      CO               Enhanced by    2.000E+00
1185. CH3OH(+M)=CH2O+H2(+M)                             2.03E+09    1.0    91443.0
      Low pressure limit:  0.97840E+48 -0.84000E+01  0.10176E+06
      TROE centering:      0.90000E+00  0.82500E+03  0.11250E+04  0.57000E+04
      H2O              Enhanced by    1.000E+01
      H2               Enhanced by    2.000E+00
      CO2              Enhanced by    3.000E+00
      CO               Enhanced by    2.000E+00
1186. CH3O+CH3=CH2O+CH4                                 1.20E+13    0.0        0.0
1187. CH3O+H=CH2O+H2                                    2.00E+13    0.0        0.0
1188. CH2OH+H=CH2O+H2                                   2.00E+13    0.0        0.0
1189. CH3O+OH=CH2O+H2O                                  1.00E+13    0.0        0.0
1190. CH2OH+OH=CH2O+H2O                                 1.00E+13    0.0        0.0
1191. CH3O+O=CH2O+OH                                    1.00E+13    0.0        0.0
1192. CH2OH+O=CH2O+OH                                   1.00E+13    0.0        0.0
1193. CH3O+CO=CH3+CO2                                   4.68E+02    3.2     5380.0
1194. CH2+OH=CH2O+H                                     2.50E+13    0.0        0.0
1195. CH2+CO2=CH2O+CO                                   1.10E+11    0.0     1000.0
1196. CH2+O=CO+H2                                       3.00E+13    0.0        0.0
1197. CH2+CH2=C2H2+H+H                                  4.00E+13    0.0        0.0
1198. CH2+HCCO=C2H3+CO                                  3.00E+13    0.0        0.0
1199. CH2+C2H2=C3H3+H                                   1.20E+13    0.0     6600.0
1200. CH2(S)+C2H2=C3H3+H                                1.50E+14    0.0        0.0
1201. CH2(S)+C2H4=C3H5-A+H                              1.30E+14    0.0        0.0
1202. CH+O=CO+H                                         5.70E+13    0.0        0.0
1203. CH+OH=HCO+H                                       3.00E+13    0.0        0.0
1204. CH+CO2=HCO+CO                                     3.40E+12    0.0      690.0
1205. CH+H2O=CH2O+H                                     1.17E+15   -0.8        0.0
1206. CH+CH2O=CH2CO+H                                   9.46E+13    0.0     -515.0
1207. CH+C2H2=C3H2+H                                    1.00E+14    0.0        0.0
1208. CH+CH2=C2H2+H                                     4.00E+13    0.0        0.0
1209. CH+CH3=C2H3+H                                     3.00E+13    0.0        0.0
1210. SC2H4OH+M=CH3+CH2O+M                              1.35E+38   -7.0    23800.0
1211. PC2H4OH+CO=C2H5+CO2                               4.68E+02    3.2     5380.0
1212. PC2H4OH+H=CH3+CH2OH                               3.00E+13    0.0        0.0
1213. PC2H4OH+H=C2H4+H2O                                3.00E+13    0.0        0.0
1214. PC2H4OH+OH=CH3CHO+H2O                             1.00E+13    0.0        0.0
1215. SC2H4OH+CH3=C3H6+H2O                              1.00E+13    0.0        0.0
1216. SC2H4OH+O=CH3CHO+OH                               1.00E+14    0.0        0.0
1217. SC2H4OH+H=C2H4+H2O                                3.00E+13    0.0        0.0
1218. SC2H4OH+H=CH3+CH2OH                               3.00E+13    0.0        0.0
1219. SC2H4OH+HO2=CH3CHO+OH+OH                          4.00E+13    0.0        0.0
1220. SC2H4OH+OH=CH3CHO+H2O                             5.00E+12    0.0        0.0
1221. CH3CHO+OH=CH2CHO+H2O                              1.72E+05    2.4      815.0
1222. CH3CHO+O=CH2CHO+OH                                3.72E+13   -0.2     3556.0
```

```
1223. CH3CHO+H=CH2CHO+H2                              1.85E+12    0.4     5359.0
1224. CH3CHO+CH3=CH2CHO+CH4                           2.45E+01    3.1     5727.0
1225. CH3CHO+HO2=CH2CHO+H2O2                          2.32E+11    0.4    14864.0
1226. C2H5+H=C2H4+H2                                  1.25E+14    0.0     8000.0
1227. C2H5+OH=C2H4+H2O                                4.00E+13    0.0        0.0
1228. C2H5+O=CH3+CH2O                                 1.00E+14    0.0        0.0
1229. C2H5+O2=CH3CHO+OH                               4.90E+11   -0.5     8357.0
1230. C2H3+O=CH2CO+H                                  3.00E+13    0.0        0.0
1231. C2H3+OH=C2H2+H2O                                2.00E+13    0.0        0.0
1232. C2H3+C2H=C2H2+C2H2                              3.00E+13    0.0        0.0
1233. C2H3+CH=CH2+C2H2                                5.00E+13    0.0        0.0
1234. C2H3+CH3=C3H5-A+H                               4.73E+02    3.7     5677.0
1235. C2H2+OH=CH3+CO                                  4.83E-04    4.0    -2000.0
1236. C2H2+CH3=C2H+CH4                                1.81E+11    0.0    17289.0
1237. CH2CHO+H=CH3+HCO                                5.00E+13    0.0        0.0
1238. CH2CHO+H=CH2CO+H2                               2.00E+13    0.0        0.0
1239. CH2CHO+O=CH2O+HCO                               1.00E+14    0.0        0.0
1240. CH2CHO+OH=CH2CO+H2O                             3.00E+13    0.0        0.0
1241. CH2CHO+CH3=C2H5+CO+H                            4.90E+14   -0.5        0.0
1242. CH2CHO+HO2=CH2O+HCO+OH                          7.00E+12    0.0        0.0
1243. CH2CHO+HO2=CH3CHO+O2                            3.00E+12    0.0        0.0
1244. CH2CHO=CH3+CO                                   1.17E+43   -9.8    43756.0
1245. C2H+H2=C2H2+H                                   4.09E+05    2.4      864.3
1246. C2H+OH=HCCO+H                                   2.00E+13    0.0        0.0
1247. C2H+O2=CO+CO+H                                  9.04E+12    0.0     -457.0
1248. HCCO+C2H2=C3H3+CO                               1.00E+11    0.0     3000.0
1249. HCCO+O=CH+CO2                                   2.95E+13    0.0     1113.0
1250. HCCO+O2=HCO+CO+O                                2.50E+08    1.0        0.0
1251. HCCO+CH=C2H2+CO                                 5.00E+13    0.0        0.0
1252. HCCO+HCCO=C2H2+CO+CO                            1.00E+13    0.0        0.0
1253. HCCO+OH=C2O+H2O                                 3.00E+13    0.0        0.0
1254. C2O+H=CH+CO                                     1.00E+13    0.0        0.0
1255. C2O+O=CO+CO                                     5.00E+13    0.0        0.0
1256. C2O+OH=CO+CO+H                                  2.00E+13    0.0        0.0
1257. C2O+O2=CO+CO+O                                  2.00E+13    0.0        0.0
1258. NC3H7(+M)=C2H4+CH3(+M)                          1.23E+13   -0.1    30202.0
      Low pressure limit:  0.54850E+50 -0.10000E+02  0.35766E+05
      TROE centering:      0.21700E+01  0.10000E-14  0.25100E+03  0.11850E+04
      H2O             Enhanced by    5.000E+00
      H2              Enhanced by    2.000E+00
      CO2             Enhanced by    3.000E+00
      CO              Enhanced by    2.000E+00
1259. C3H6+H(+M)=IC3H7(+M)                            5.70E+09    1.2      874.0
      Low pressure limit:  0.16400E+55 -0.11100E+02  0.93640E+04
      TROE centering:      0.10000E+01  0.10000E-14  0.26000E+03  0.30000E+04
      H2O             Enhanced by    5.000E+00
      H2              Enhanced by    2.000E+00
      CO2             Enhanced by    3.000E+00
      CO              Enhanced by    2.000E+00
1260. NC3H7+H=C2H5+CH3                                1.00E+14    0.0        0.0
1261. C3H6=C2H2+CH4                                   2.50E+12    0.0    70000.0
1262. C3H6=C3H4-A+H2                                  3.00E+13    0.0    80000.0
1263. C3H6+HCO=C3H5-A+CH2O                            1.08E+07    1.9    17010.0
1264. CH3CHCO+OH=C2H3CO+H2O                           4.00E+06    2.0        0.0
1265. CH3CHCO+O=C2H3CO+OH                             7.60E+08    1.5     8500.0
1266. CH3CHCO+H=C2H3CO+H2                             2.00E+05    2.5     2500.0
1267. CH3CHCO+O=CH3+HCO+CO                            3.00E+07    2.0        0.0
1268. C2H3CHO+O=CH2CO+HCO+H                           5.01E+07    1.8       76.0
1269. C2H3CHO+H=C2H4+HCO                              2.00E+13    0.0     3500.0
1270. C2H3CHO+O2=C2H3CO+HO2                           3.00E+13    0.0    36000.0
1271. C2H3CO+O=C2H3+CO2                               1.00E+14    0.0        0.0
```

```
1272. C3H5O+CO=C3H5-A+CO2                               4.68E+02    3.2     5380.0
1273. C2H3CHO+H(+M)=C3H5O(+M)                           5.40E+11    0.5     2600.0
      Low pressure limit:  0.15000E+31 -0.48000E+01  0.55600E+04
      TROE centering:      0.78000E+00  0.94000E+02  0.15550E+04  0.42000E+04
      H2O             Enhanced by    5.000E+00
1274. C3H5-A+OH=C3H4-A+H2O                              1.00E+13    0.0        0.0
1275. C3H5-A+O=C2H3CHO+H                                1.81E+14    0.0        0.0
1276. C3H5-S+O2=CH3CHCO+H+O                             1.60E+15   -0.8     3135.0
1277. C3H5-S+O=CH3CHCO+H                                1.00E+14    0.0        0.0
1278. C3H5-S+OH=C3H4-A+H2O                              1.00E+13    0.0        0.0
1279. C3H5-S+H=C3H5-A+H                                 1.00E+14    0.0        0.0
1280. C3H5-T+H=C3H5-A+H                                 1.00E+14    0.0        0.0
1281. C3H5-T+O=CH2CO+CH3                                1.00E+14    0.0        0.0
1282. C3H5-T+H=C3H4-A+H2                                4.00E+13    0.0        0.0
1283. C3H5-T+OH=C3H4-A+H2O                              2.00E+13    0.0        0.0
1284. C3H3+CH3=C3H2+CH4                                 2.00E+13    0.0        0.0
1285. C3H2+O=C2H2+CO                                    1.00E+14    0.0        0.0
1286. H+O+M=>OHs+M                                      6.00E+14    0.0     6940.0
1287. CH+O2=>OHs+CO                                     3.24E+14   -0.4     4150.0
1288. OHs+H2O=>OH+H2O                                   5.92E+12    0.5     -861.0
1289. OHs+CO2=>OH+CO2                                   2.75E+12    0.5     -968.0
1290. OHs+CO=>OH+CO                                     3.23E+12    0.5     -787.0
1291. OHs+H2=>OH+H2                                     2.95E+12    0.5     -444.0
1292. OHs+O2=>OH+O2                                     2.10E+12    0.5     -482.0
1293. OHs+OH=>OH+OH                                     1.50E+12    0.5        0.0
1294. OHs+H=>OH+H                                       1.50E+12    0.5        0.0
1295. OHs+O=>OH+O                                       1.50E+12    0.5        0.0
1296. OHs+N2=>OH+N2                                     1.08E+11    0.5    -1238.0
1297. OHs+CH4=>OH+CH4                                   3.36E+12    0.5     -635.0

 UNITS for the preceding reactions (unless otherwise noted):
       A units mole-cm-sec-K, E units cal/mole
```

REFERENCES

[1] Somerscales, E.F.C. and Zagotta, A.A., *"History of the Internal Combustion Engine"*. 1989: American Society of Mechanical Engineers. Internal Combustion Engine Division. ISBN: 0791803759

[2] *"U.S. Energy Information Administration"*. 2011; Available from: http://tonto.eia.gov

[3] *"U.S. Bureau of Labor Statistics Consumer Price Index"*. http://www.fintrend.com 2011;

[4] *"U.S. Census Bureau"*. 2011; Available from: http://www.census.gov

[5] Keller, C.F., *"Global Warming: The Balance of Evidence and Its Policy Implications"*. TheScientificWorldJOURNAL 2003: p. 357-411

[6] Keller, C.F., *"Global Warming 2007. An Update to Global Warming: The Balance of Evidence and Its Policy Implications"*. TheScientificWorldJOURNAL, 2007: p. 381-399

[7] *"Climate Change 2007. Fourth Assessment"*. 2007, United Nations Energy Programme Intergovernamental Panel on Climate Change.

[8] *"Germany - Oilseeds and Products Biodiesel in Germany - an overview 2002"*. 2002, US Embassy Berlin.

[9] Alexander, C. and Hurt, C., *"Biofuels and Their impact on Food Prices"*. 2007, Department of Agricultural Economics, Purdue University.

[10] Larminie, J. and Lowry, J., *"Electric Vehicle Technology Explained"*. 2003: John Wiley & Sons. ISBN: 0-470-85163-5

[11] Kirubakaran, A., Jain, S. and Nema, R.K., *"A review on fuel cell technologies and power electronic interface".* Renewable and Sustainable Energy Reviews, 2009. **13**(9): p. 2430-2440

[12] Vining, C.B., *"An inconvenient truth about thermoelectrics".* Nat Mater, 2009. **8**(2): p. 83-85

[13] Curran, H.J., Gaffuri, P., Pitz, W.J. and Westbrook, C.K., *"A Comprehensive Modeling Study of n-Heptane Oxidation".* Combustion and Flame, 1998. **114**(1-2): p. 149-177

[14] Battin-Leclerc, F., *"Detailed chemical kinetic models for the low-temperature combustion of hydrocarbons with application to gasoline and diesel fuel surrogates".* Progress in Energy and Combustion Science, 2008. **34**(4): p. 440-498

[15] Dec, J.E. *"A conceptual model of DI diesel combustion based on laser-sheet imaging"*. Paper SAE 970873

[16] Johnson, T.V., *"Review of diesel emissions and control".* SAE International Journal of Fuels and Lubricants, 2010. **3**(Compendex): p. 16-29

[17] Johnson, T.V. *"Diesel Emissions in Review"*. Paper 2011-01-0304

[18] Heywood, J.B., *"Internal Combustion Engine Fundamentals"*. 1988: McGraw-Hill. ISBN: 007028637X

[19] Ryan, T.W., Callahan, T.J. and Mehta, D. *"HCCI in a Variable Compression Ratio Engine-Effects of Engine Variables"*. Paper SAE 2004-01-1971

[20] Kokjohn, S.L. and Reitz, R.D., *"Investigation of charge preparation strategies for controlled premixed charge compression ignition combustion using a variable pressure injection system".* International Journal of Engine Research, 2010. **11**(Compendex): p. 257-282

[21] Lee, T. and Reitz, R.D., *"The effect of intake boost pressure on MK (Modulated Kinetics) combustion".* JSME International Journal, Series B: Fluids and Thermal Engineering, 2003. **46**(Compendex): p. 451-459

[22] Splitter, D., Hanson, R., Kokjohn, S. and Reitz, R. *"Reactivity Controlled Compression Ignition (RCCI) Heavy-Duty Engine Operation at Mid-and High-Loads with Conventional and Alternative Fuels"*. Paper SAE 2011-01-0363

[23] Sjöberg, M. and Dec, J.E. *"Ethanol Autoignition Characteristics and HCCI Performance for Wide Ranges of Engine Speed, Load and Boost"*. Paper 2010-01-0338

[24] Cracknell, R.F., Head, R.A., McAllister, L.J. and Andrae, J.C.G. *"Octane Sensitivity in Gasoline Fuels Containing Nitro-Alkanes: A Possible Means of Controlling Combustion Phasing for HCCI"*. Paper 2009-01-0301

[25] Cracknell, R., Ariztegui, J., Barnes, K., Bessonette, P., Cannella, W., Douce, F., Kelecom, B., Kraft, H., Lampreia, I., Rickeard, D.J., Savarese, M.C., Williams, J. and Rose, K.D., *"Advanced combustion for low emissions and high efficiency: a literature review of HCCI combustion concepts"*. 2008, concawe.org report 04/08.

[26] *"Low-temperature Combustion and Autoignition, Volume 35 (Comprehensive Chemical Kinetics)"*, ed. M.J. Pilling. 1997: Elsevier. ISBN: 0 444 82485 5

[27] Gray, B.F., Kalliadasis, S., Lazarovici, A., Macaskill, C., Merkin, J.H. and Scott, S.K., *"The suppression of an exothermic branched-chain flame through endothermic reaction and radical scavenging".* Proc. R. Soc. Lond. A 2002(458): p. 2119-2138

[28] Lazarovici, A., Kalliadasis, S., Merkin, J.H., Scott, S.K. and Simon, P.L., *"The propagation and inhibition of an exothermic branched-chain flame with an endothermic reaction and radical scavenging".* Journal of Engineering Mathematics, 2004(49): p. 41-55

[29] Eng, J.A., Leppard, W.R. and Sloane, T.M. *"The effect of POx on the Autoignition Chemistry of n-heptane and Isooctane in an HCCI Engine"*. Paper SAE 2002-01-2861

[30] Shudo, T. and Takahashi, T. *"Influence of Reformed Gas Composition on HCCI Combustion of Onboard Methanol-Reformed Gases"*. Paper 2004-01-1908

[31] Shudo, T. and Yamada, H., *"Hydrogen as an ignition-controlling agent for HCCI combustion engine by suppressing the low-temperature oxidation".* International Journal of Hydrogen Energy, 2007. **32**: p. 3066-3072

[32] Shudo, T., Kitahara, S. and Ogawa, H. *"Influence of Carbon Dioxide on Combustion in an HCCI Engine with the Ignition-Control by Hydrogen"*. Paper 2006-01-3248

[33] Sjöberg, M., Dec, J.E. and Hwang, W. *"Thermodynamic and Chemical Effects of EGR and its constituents on HCCI Autoignition"*. Paper 2007-01-0207

[34] Kongsereeparp, P. and Checkel, M.D. *"Study of Reformer Gas Effects on n-Heptane HCCI Combustion Using a Chemical Kinetic Mechanism Optimized by Genetic Algorithm"*. Paper SAE 2008-01-0039

[35] Xingcai, L., Libin, J. and Zhen, H. *"Numerical simulation and experimental study on the n-heptane HCCI combustion with port injection of reaction additive"*. Paper SAE 2007-01-1875

[36] Hashimoto, K. *"Effect of Ethanol on the HCCI Combustion"*. Paper SAE 2007-01-2038

[37] Hashimoto, K. *"Inhibition Effect of Ethanol on Homogeneous Charge Compression Ignition of Heptane"*. Paper SAE 2008-01-2504

[38] Yamada, H., Ohtomo, M., Yoshii, M. and Tezaki, M., *"Controlling mechanism of ignition enhancing and suppressing additives in premixed compression ignition".* Int. J. Engine Res., 2005. **6**: p. 331-340

[39] Yamada, H., Yoshii, M. and Tezaki, A., *"Chemical mechanistic analysis of additive effects in homogeneous charge compression ignition of dimethyl ether".* Proceedings of the Combustion Institute, 2005. **30**: p. 2773–2780

[40] Kuwahara, K., Ando, H., Furutani, M. and Ohta, Y., *"Impact of formaldehyde addition on auto-ignition in internal-combustion engines".* JSME International Journal, Series B: Fluids and Thermal Engineering, 2006. **48**(4): p. 708-716

[41] Jansons, M., Florea, R., Zha, K. and Gingrich, E., *"The Effect of HCHO Addition on Combustion in an Optically Accessible Diesel Engine Fueled with JP-8".* SAE International Journal of Fuels and Lubricants, 2010. **3**(2): p. 671-690

[42] Jansons, M., Zha, K., Florea, R., Taraza, D., Henein, N. and Bryzik, W., *"Effect of Swirl Ratio and Wall Temperature on Pre-Injection Chemiluminescence During Starting of an Optical Diesel Engine".* SAE International Journal of Engines, 2010. **2**(2): p. 173-185

[43] Jansons, M., Florea, R., Estefanous, F., Taraza, D., Henein, N.A. and Bryzik, W., *"Chemiluminescence imaging of pre-injection reactions during engine starting".* International Journal of Vehicle Design (IJVD), 2009. **49**(1/2/3): p. 168-191

[44] Jansons, M., Florea, R., Zha, K., Estefanous, F., Florea, E., Taraza, D., Bryzik, W., Henein, N. and Hoogterp, L. *"Optical and Numerical Investigation of Pre-Injection Reactions and Their Effect on the Starting of a Diesel Engine"*. Paper SAE Paper 2009-01-0648

[45] Jansons, M., Florea, R., Zha, K. and Florea, E., *"The Combined Effect of HCHO and C2H4 Addition on Combustion in an Optically Accessible Diesel Engine Fueled with JP-8".* SAE Int. J. Engines, 2011. **4**(1): p. 2048-2064

[46] Florea, R., Zha, K., Jansons, M., Taraza, D. and Henein, N. *"A CFD Study of the Effect of HCHO Addition on Autoignition and Combustion"*. Paper ASME Paper: ICEF2011-60212

[47] Babushok, V., Tsang, W., Linteris, G.T. and Reinelt, D., *"Chemical limits to flame inhibition".* Combustion and Flame, 1998. **115**(4): p. 551-560

[48] Rumminger, M.D., Reinelt, D., Babushok, V. and Linteris, G.T., *"Numerical study of the inhibition of premixed and diffusion flames by iron pentacarbonyl".* Combustion and Flame, 1999. **116**(1-2): p. 207-219

[49] Rumminger, M.D. and Linteris, G.T., *"Inhibition of premixed carbon monoxide-hydrogen-oxygen-nitrogen flames by iron pentacarbonyl".* Combustion and Flame, 2000. **120**(4): p. 451-464

[50] Rumminger, M.D. and Linteris, G.T., *"The role of particles in the inhibition of premixed flames by iron pentacarbonyl".* Combustion and Flame, 2000. **123**(1-2): p. 82-94

[51] Rumminger, M.D. and Linteris, G.T., *"The role of particles in the inhibition of counterflow diffusion flames by iron pentacarbonyl".* Combustion and Flame, 2002. **128**(1-2): p. 145-164

[52] Gerasimov, I.E., Knyazkov, D.A., Shmakov, A.G., Paletsky, A.A., Shvartsberg, V.M., Bolshova, T.A. and Korobeinichev, O.P., *"Inhibition of hydrogen-oxygen flames by iron pentacarbonyl at atmospheric pressure".* Proceedings of the Combustion Institute, 2011. **33**(2): p. 2523-2529

[53] Staude, S., Hecht, C., Wlokas, I., Schulz, C. and Atakan, B., *"Experimental and Numerical Investigation of Fe(CO)5 Addition to a Laminar Premixed Hydrogen/Oxygen/Argon Flame".* Zeitschrift für Physikalische Chemie, 2009. **223**(4-5): p. 639-649

[54] Tanaka, S., Ayala, F., C. Keck, J. and Heywood, J.B., *"Two-stage ignition in HCCI combustion and HCCI control by fuels and additives".* Combustion and Flame, 2003. **132**: p. 219-239

[55] Mack, J.H., Dibble, R.W., Buchholz, B.A. and Flowers, D.L. *"The Effect of the Di-Tertiary Butyl Peroxide (DTBP) additive on HCCI Combustion of Fuel Blends of Ethanol and Diethyl Ether"*. Paper SAE 2005-01-2135

[56] Gong, X., *"The Effects of DTBP on the Oxidation of SI Primary Reference Fuels - A Study in an HCCI Engine and in a Pressurized Flow Reactor"*. 2005, Drexel University: Philadelphia.

[57] Aceves, M.S., Flowers, D., Martinez-Frias, J., Espinosa-Loza, F., Pitz, J.W. and Dibble, R. *"Fuel and Additive Characterization for HCCI Combustion"*. Paper SAE 2003-01-1814

[58] Mehl, M., Curran, H.J., Pitz, W.J. and Westbrook, C.K. *"iso-Octane, Version 3"*. 2009; Available from: https://www-pls.llnl.gov/

[59] Mehl, M., Curran, H.J., Pitz, W.J. and Westbrook, C.K. *"Chemical kinetic modeling of component mixtures relevant to gasoline"*. Paper LLNL-CONF-410968

[60] Ombrello, T., Won, S.H., Ju, Y. and Williams, S., *"Flame propagation enhancement by plasma excitation of oxygen. Part I: Effects of O3".* Combustion and Flame, 2010. **157**(Compendex): p. 1906-1915

[61] Ombrello, T., Wona, S.H., Ju, Y. and Williams, S., *"Flame propagation enhancement by plasma excitation of oxygen. Part II: Effects of O2(a1Dg)".* Combustion and Flame 2010. **157**: p. 1916–1928

[62] Wiberg, E., Wiberg, N. and Holleman, A.F., *"Inorganic chemistry"*. 2001. ISBN: 978-0123526519

[63] OSHA. *"Chemical Sampling Information: Nitroethane"*. Available from: http://www.osha.gov/

[64] Dunbeck, P.B. and Reitz, R.D. *"An Experimental Study of Dual Fueling with Gasoline Port Injection in a Single-Cylinder, Air-Cooled HSDI Diesel Generator"*. Paper SAE 2010-01-0869

[65] Hanson, R.M., Kokjohn, S.L., Splitter, D.A. and Reitz, R.D. *"An Experimental Investigation of Fuel Reactivity Controlled PCCI Combustion in a Heavy-Duty Engine"*. Paper SAE 2010-01-0864

[66] Splitter, D., Reitz, R. and Hanson, R. *"High Efficiency, Low Emissions RCCI Combustion by Use of a Fuel Additive"*. Paper SAE 2010-01-2167

[67] Huang, Y. and Mehta, D. *"Investigation of an In-cylinder Ion Sensing Assisted HCCI Control Strategy"*. Paper SAE Paper: 2005-01-0068

[68] Bengtsson, J., Strandh, P., Johansson, R., Tunestål, P. and Johansson, B. *"Multi-Output Control of a Heavy Duty HCCI Engine Using Variable Valve Actuation and Model Predictive Control"*. Paper SAE Paper 2006-01-0873

[69] Epping, K., Aceves, S., Bechtold, R. and Dec, J. *"The Potential of HCCI Combustion for High Efficiency and Low Emissions"*. Paper SAE Paper 2002-01-1923

[70] Yang, Y., Dec, J., Dronniou, N., Sjöberg, M. and Cannella, W., *"Partial Fuel Stratification to Control HCCI Heat Release Rates: Fuel Composition and Other Factors Affecting Pre-Ignition Reactions of Two-Stage Ignition Fuels".* SAE Int. J. Engines, 2011. **4**(1): p. 1903-1920

[71] Vressner, A., Lundin, A., Christensen, M., Tunestål, P. and Johansson, B. *"Pressure Oscillations During Rapid HCCI Combustion"*. Paper SAE Paper 2003-01-3217

[72] Hansen, A.C., Zhang, Q. and Lyne, P.W.L., *"Ethanol-diesel fuel blends - A review".* Bioresource Technology, 2005. **96**(Compendex): p. 277-285

[73] Cui, X., Helmantel, A., Golovichev, V. and Denbratt, I. *"Combustion and Emissions in a Light-Duty Diesel Engine Using Diesel-Water Emulsion and Diesel-Ethanol Blends"*. Paper SAE 2009-01-2695

[74] Cole, R.L., Poola, R.B., Sekar, R., Schaus, J.E. and McPartlin, P. *"Effects of Ethanol Additives on Diesel Particulate and NOx Emissions"*. Paper SAE 2001-01-1937

[75] Rakopoulos, D.C., Rakopoulos, C.D., Kakaras, E.C. and Giakoumis, E.G., *"Effects of ethanol-diesel fuel blends on the performance and exhaust emissions of heavy duty DI diesel engine".* Energy Conversion and Management, 2008. **49**(Compendex): p. 3155-3162

[76] Qi, D.H., Chen, H., Geng, L.M. and Bian, Y.Z., *"Effect of diethyl ether and ethanol additives on the combustion and emission characteristics of biodiesel-diesel blended fuel engine".* Renewable Energy, 2011. **36**(Copyright 2011, The Institution of Engineering and Technology): p. 1252-8

[77] Yan, Y., Yu-sheng, Z., Si-ping, R., Rui, Z. and Dong-dong, W. *"Study on Combustion and Emission Characteristics of Diesel Engines Fueled with Ethanol/Diesel Blended Fuel"*. Paper SAE 2009-01-2675

[78] Pidol, L., Lecointe, B. and Jeuland, N. *"Ethanol as a Diesel Base Fuel: Managing the Flash Point Issue - Consequences on Engine Behavior"*. Paper SAE 2009-01-1807

[79] Pidol, L., Lecointe, B., Pesant, L. and Jeuland, N. *"Ethanol as a Diesel Base Fuel – Potential in HCCI Mode"*. Paper SAE 2008-01-2506

[80] Hu, C., Jian-Xin, W., Shi-Jin, S., Xin-Liang, A. and Wen-Miao, C. *"Effects of Ethanol in Ester-Ethanol-Diesel Blended Fuels on Spray Behavior and PM Emission"*. Paper SAE 2006-01-0236

[81] He, B.-Q., Wang, J.-X., Shuai, S.-J. and Yan, X.-G. *"Homogeneous Charge Combustion and Emissions of Ethanol Ignited by Pilot Diesel on Diesel Engines"*. Paper SAE 2004-01-0094

[82] Kamio, J., Kurotani, T., Kuzuoka, K., Kubo, Y., Taniguchi, H. and Hashimoto, K. *"Study on HCCI-SI Combustion Using Fuels Containing Ethanol"*. Paper SAE 2007-01-4051

[83] Gjirja, S., Olsson, E. and Karlström, A. *"Considerations on Engine Design and Fuelling Technique Effects on Qualitative Combustion in Alcohol Diesel Engines"*. Paper SAE 982530

[84] Träger, F., *"Springer Handbook of Lasers and Optics"*. 2006: Springer, New York. ISBN: 9780387955797

[85] Taylor, W.E., *"Correlation of the Mohs's scale of hardness with the Vickers' s hardness numbers".* Mineralogical Magazine, 1949. **28**: p. 718

[86] Brown, B. *"catool - Combustion Analysis Tool - User Guide"*. 2010; Available from: http://catool.org

[87] Stuart, B.H., *"Infrared spectroscopy: fundamentals and applications"*. 2004: John Wiley and Sons. ISBN: 0470854286

[88] Zha, K., Florea, R.-C. and Jansons, M. *"Comparison of Soot Evolution using High-Speed CMOS Color Camera and Two-Color Thermometry in an Optical Diesel Engine fueled with B20 Biodiesel Blend and Ultra-Low Sulfur Diesel"*. Paper ASME: ICEF2011-60146

[89] Zha, K., Florea, R.-C. and Jansons, M. *"Novel Implementation of Two-Color Soot Temperature Measurement in Optical Diesel Engine with High-speed CMOS Digital Color Camera"*. Paper ICARAME'11: Oral Presentation

[90] *"Princeton Instruments PI-MAX2: 512 ICCD Camera Datasheet"*. Available from: http://www.roperscientific.de

[91] Li, F.M. and Nathan, A., *"CCD image sensors in deep-ultraviolet: degradation behavior and damage mechanisms"*. 2005: Springer. ISBN: 354022680X

[92] *"Princeton Instruments Application Technical Note: Selecting the Right ICCD Camera, The latest advances in intensified CCD camera technology."*. 2008; Available from: http://www.roperscientific.de

[93] *"Princeton Instruments PI-MAX3: 1024i ICCD Camera Datasheet"*. Available from: http://www.roperscientific.de

[94] Lerner, J.M., Gat, N. and Wachman, E., *"Approaches to Spectral Imaging Hardware"*, in *Current Protocols in Cytometry*. 2001, John Wiley & Sons, Inc.

[95] Collin, R., Nygren, J., Richter, M., Aldén, M., Hildingsson, L. and Johansson, B. *"Simultaneous OH- and Formaldehyde-LIF Measurements in an HCCI Engine"*. Paper SAE Paper 2003-01-3218

[96] Idicheria, C.A. and Pickett, L.M. *"Formaldehyde Visualization Near Lift-off Location in a Diesel Jet"*. Paper SAE Paper 2006-01-3434

[97] Donkerbroek, A.J., van Vliet, A.P., Somers, L.M.T., Frijters, P.J.M., Klein-Douwel, R.J.H., Dam, N.J., Meerts, W.L. and ter Meulen, J.J., *"Time- and space-resolved quantitative LIF measurements of formaldehyde in a heavy-duty diesel engine".* Combustion and Flame, 2010. **157**(1): p. 155-166

[98] Marinov, N.M., *"A detailed chemical kinetic model for high temperature ethanol oxidation".* International Journal of Chemical Kinetics, 1999. **31**(3): p. 183-220

[99] Soyhan, H.S., Mauss, F. and Sorusbay, C., *"Chemical kinetic modeling of combustion in internal combustion engines using reduced chemistry".* Combustion Science and Technology, 2002. **174**(11-12): p. 73-91

[100] *"DARS chemical kinetics solver"*. 2011; Available from: http://www.loge.se/

[101] Zeuch, T., Moréac, G., Ahmed, S.S. and Mauss, F., *"A comprehensive skeletal mechanism for the oxidation of n-heptane generated by chemistry-guided reduction".* Combustion and Flame, 2008. **155**(4): p. 651-674

[102] Lu, T. and Law, C.K., *"Linear time reduction of large kinetic mechanisms with directed relation graph: n-Heptane and iso-octane".* Combustion and Flame, 2006. **144**(1-2): p. 24-36

[103] Pepiot-Desjardins, P. and Pitsch, H., *"An efficient error-propagation-based reduction method for large chemical kinetic mechanisms".* Combustion and Flame, 2008. **154**(1-2): p. 67-81

[104] Nori, V. and Seitzman, J. *"Evaluation of Chemiluminescence as a Combustion Diagnostic under Varying Operating Condition"*. Paper

[105] Torres, D.J. and Trujillo, M.F., *"KIVA-4: An unstructured ALE code for compressible gas flow with sprays".* J. Comput. Phys., 2006. **219**(2): p. 943-975

[106] Amsden, A.A., O'Rourke, P.J. and Butler, T.D., *"KIVA-II: A Computer Program for Chemically Reactive Flows with Sprays"*. 1989.

[107] Goodwin, D.G., *"An Open-Source, Extensible Software Suite for CVD Process Simulation".* Chemical Vapor Deposition XVI and EUROCVD 14, ECS Proceedings, 2003. **2003-08**: p. 155-162

[108] *"Message Passing Interface Forum. MPI2: A Message Passing Interface standard".* International Journal of High Performance Computing Applications, 1998. **12**(1-2): p. 1-299

[109] Balaji, P., Buntinas, D., Butler, R., Chan, A., Goodell, D., Gropp, W., Krishna, J., Latham, R., Lusk, E., Mercier, G., Ross, R. and Thaku, R., *"MPICH2 User's Guide"*. 2010: Mathematics and Computer Science Division - Argonne National Laborator. ISBN:

[110] Torres, D.J. and Trujillo, M.F., *"KIVA-4: An unstructured ALE code for compressible gas flow with sprays".* Journal of Computational Physics, 2006. **219**(2): p. 943-975

[111] O'Rourke, P.J. and Amsden, A.A. *"A Spray/Wall Interaction Submodel for the KIVA-3 Wall Film Model"*. Paper SAE 2000-01-0271

[112] O'Rourke, P.J. and Amsden, A.A. *"The TAB Model for Numerical Calculation of Spray Droplet Breakup"*. Paper SAE 872089

[113] Amsden, A.A., O'Rourke, P.J. and Butler, T.D., *"KIVA-II: A Computer Program for Chemically Reactive Flows with Sprays"*. 1989.

[114] Ceriani, L. and Verme, P., *"The origins of the Gini index: extracts from Variabilità e Mutabilità (1912) by Corrado Gini".* Journal of Economic Inequality: p. 1-23

[115] *"Handbook on Income Inequality Measurement"*, ed. J. Silber. 1999. ISBN: ISBN 978-0-7923-8574-5

[116] Herold, R.E., *"Optical Investigations of the Effects of Stratification on Homogeneous Charge Compression Ignition Combustion"*, in *Engine Research Center*. 2008, Wisconsin: Madison.

[117] Gaydon, A.G., *"The Spectroscopy of Flames"*. 2nd ed. 1974. ISBN: 9780412128707

[118] Donkerbroek, A.J., van Vliet, A.P., Somers, L.M.T., Dam, N.J. and ter Meulen, J.J., *"Relation between hydroxyl and formaldehyde in a direct-injection heavy-duty diesel engine".* Combustion and Flame, 2011. **158**(3): p. 564-572

[119] Kashdan, J.T., Docquier, N. and Bruneaux, G. *"Mixture Preparation and Combustion via LIEF and LIF of Combustion Radicals in a Direct-Injection, HCCI Diesel Engine"*. Paper SAE 2004-01-2945

[120] Seitzman, J.M., Haumann, J. and Hanson, R.K., *"Quantitative two-photon LIF imaging of carbon monoxide in combustion gases".* Appl. Opt., 1987. **26**(14): p. 2892-2899

[121] Takashi, H. and Kimitoshi, T. *"Laminar Flame Speeds of Ethanol, n-Heptane, Isooctane Air Mixtures"*. Paper FISITA F2006SC40

[122] Musculus, M. *"Heavy-Duty Low-Temperature and Diesel Combustion & Heavy-Duty Combustion Modeling"*. 2011; Available from: http://www1.eere.energy.gov/vehiclesandfuels/pdfs/merit_review_2011/adv_combustion/ace001_musculus_2011_o.pdf

ABSTRACT

OPTICAL INVESTIGATION OF ETHANOL AND N-HEPTANE DUAL-FUEL PARTIALLY PREMIXED COMBUSTION IN A RECIPROCATING ENGINE

by

RADU FLOREA

August 2012

Advisor: Dr. Dinu Taraza

Major: Mechanical Engineering

Degree: Doctor of Philosophy

The details of the dual-fuel combustion of n-heptane and ethanol were investigated in an optically accessible engine representative of light-duty applications. Experimental work involved the application of optical diagnostics such as high-speed imaging of combustion chemiluminescence and soot radiation, spectral measurements and laser induced fluorescence. At the same time, the experimental conditions have been replicated using numerical simulation of chemically reactive in-cylinder flow.

The numerical simulation results, which showed good agreement with the experimental data across several validation approaches, provided an improved understanding of the mechanism responsible for the control of the rate of combustion for dual-fuel operation. The comparison of ethanol/heptane dual-fuel operation with an n-heptane baseline investigated two possible combustion rate control mechanisms previously identified in literature. The first mechanism relies

on the direct impact of auto-ignition characteristics stratification on the rate of combustion and could be termed kinetically controlled. The second mechanism is based on the formation of fast propagating flame fronts and is termed flame propagation control.

While previous studies have identified the kinetic stratification as being the dominant control mechanism, under the conditions used in the current investigation, the opposite conclusion has been reached. This seems to suggest, that the mechanism responsible for control of the rate of combustion shifts as a function of the value of local state variables such as temperature, pressure and equivalence ratio and further investigation is warranted.

AUTOBIOGRAPHICAL STATEMENT

I was born and raised in the Carpathian hills of Romania. I have always shown inclination towards science and engineering and thus I pursued a mechanical engineering undergraduate program at Transylvania University of Brasov. In 2005, as I was preparing my graduation thesis, I spent the last semester of my undergraduate studies at the Rheinisch-Westfälische Technische Hochschule Aachen, Germany where I was involved in finding practical solutions to real-world problems associated with propulsion of underground mining transportation systems.

I continued my academic career by pursuing a PhD degree at Wayne State University's Center for Automotive Research. The research goals focused on optical diagnostics of combustion, the investigation of chemical kinetic processes responsible for combustion instability during diesel engine cold starting and dual-fuel combustion.

Upon completing the requirements of the PhD degree in early 2012 I accepted a research position with San Antonio, TX based Southwest Research Institute where I'm currently working on high-efficiency internal combustion engines.